

Planck 2018 results

VI. Cosmological parameters

Planck Collaboration: N. Aghanim⁵⁴, Y. Akrami^{15,57,59}, M. Ashdown^{65,5}, J. Aumont⁹⁵, C. Baccigalupi⁷⁸, M. Ballardini^{21,41}, A. J. Banday^{95,8}, R. B. Barreiro⁶¹, N. Bartolo^{29,62}, S. Basak⁸⁵, R. Battye⁶⁴, K. Benabed^{155,90}, J.-P. Bernard^{195,8}, M. Bersanelli^{32,45}, P. Bielewicz^{75,78}, J. J. Bock^{63,10}, J. R. Bond⁷, J. Borrill^{12,93}, F. R. Bouchet^{55,90}, F. Boulanger^{89,54,55}, M. Bucher^{2,6}, C. Burigana^{44,30,47}, R. C. Butler⁴¹, E. Calabrese⁸², J.-F. Cardoso^{55,90}, J. Carron²³, A. Challinor^{58,65,11}, H. C. Chiang^{25,6}, J. Chluba⁶⁴, L. P. L. Colombo³², C. Combet⁶⁸, D. Contreras²⁰, B. P. Crill^{63,10}, F. Cuttaia⁴¹, P. de Bernardis³¹, G. de Zotti⁴², J. Delabrouille², J.-M. Delouis⁶⁷, E. Di Valentino⁶⁴, J. M. Diego⁶¹, O. Doré^{63,10}, M. Douspis⁵⁴, A. Ducout⁶⁶, X. Dupac³⁵, S. Dusini⁶², G. Efstathiou^{65,58,*}, F. Elsner⁷², T. A. Enßlin⁷², H. K. Eriksen⁵⁹, Y. Fantaye^{3,19}, M. Farhang⁷⁶, J. Fergusson¹¹, R. Fernandez-Cobos⁶¹, F. Finelli^{41,47}, F. Forastieri^{30,48}, M. Frailis⁴³, A. A. Fraisse²⁵, E. Franceschi⁴¹, A. Frolov⁸⁷, S. Galeotta⁴³, S. Galli^{55,90,*}, K. Ganga², R. T. Génova-Santos^{60,16}, M. Gerbino³⁸, T. Ghosh^{81,9}, J. González-Nuevo¹⁷, K. M. Górski^{63,97}, S. Gratton^{65,58}, A. Gruppuso^{41,47}, J. E. Gudmundsson^{94,25}, J. Hamann⁸⁶, W. Handley^{65,5}, F. K. Hansen⁵⁹, D. Herranz⁶¹, S. R. Hildebrandt^{63,10}, E. Hivon^{55,90}, Z. Huang⁸³, A. H. Jaffe⁵³, W. C. Jones²⁵, A. Karakci⁵⁹, E. Keihänen²⁴, R. Keskitalo¹², K. Kiiveri^{24,40}, J. Kim⁷², T. S. Kisner⁷⁰, L. Knox²⁷, N. Krachmalnicoff⁷⁸, M. Kunz^{14,54,3}, H. Kurki-Suonio^{24,40}, G. Lagache⁴, J.-M. Lamarre⁸⁹, A. Lasenby^{5,65}, M. Lattanzi^{48,30}, C. R. Lawrence⁶³, M. Le Jeune², P. Lemos^{58,65}, J. Lesgourgues⁵⁶, F. Levrier⁸⁹, A. Lewis^{23,*}, M. Liguori^{29,62}, P. B. Lilje⁵⁹, M. Lilley^{55,90}, V. Lindholm^{24,40}, M. López-Cañiego³⁵, P. M. Lubin²⁸, Y.-Z. Ma^{77,80,74}, J. F. Macías-Pérez⁶⁸, G. Maggio⁴³, D. Maino^{32,45,49}, N. Mandolesi^{41,30}, A. Mangilli⁸, A. Marcos-Caballero⁶¹, M. Maris⁴³, P. G. Martin⁷, M. Martinelli⁹⁶, E. Martínez-González⁶¹, S. Matarrese^{29,62,37}, N. Mauri⁴⁷, J. D. McEwen⁷³, P. R. Meinhold²⁸, A. Melchiorri^{31,50}, A. Mennella^{32,45}, M. Migliaccio^{34,51}, M. Millea^{27,88,55}, S. Mitra^{52,63}, M.-A. Miville-Deschênes^{1,54}, D. Molinari^{30,41,48}, L. Montier^{95,8}, G. Morgante⁴¹, A. Moss⁸⁴, P. Natoli^{30,92,48}, H. U. Nørgaard-Nielsen¹³, L. Pagano^{30,48,54}, D. Paoletti^{41,47}, B. Partridge³⁹, G. Patanchon², H. V. Peiris²², F. Perrotta⁷⁸, V. Pettorino¹, F. Piacentini³¹, L. Polastri^{30,48}, G. Polenta⁹², J.-L. Puget^{54,55}, J. P. Rachen¹⁸, M. Reinecke⁷², M. Remazeilles⁶⁴, A. Renzi⁶², G. Rocha^{63,10}, C. Rossetti², G. Roudier^{2,89,63}, J. A. Rubiño-Martín^{60,16}, B. Ruiz-Granados^{60,16}, L. Salvati⁵⁴, M. Sandri⁴¹, M. Savelainen^{24,40,71}, D. Scott²⁰, E. P. S. Shellard¹¹, C. Sirignano^{29,62}, G. Sirri⁴⁷, L. D. Spencer⁸², R. Sunyaev^{72,91}, A.-S. Suur-Uski^{24,40}, J. A. Tauber³⁶, D. Tavagnacco^{43,33}, M. Tenti⁴⁶, L. Toffolatti^{17,41}, M. Tomasi^{32,45}, T. Trombetti^{44,48}, L. Valenziano⁴¹, J. Valiviita^{24,40}, B. Van Tent⁶⁹, L. Vibert^{54,55}, P. Vielva⁶¹, F. Villa⁴¹, N. Vittorio³⁴, B. D. Wandelt^{55,90}, I. K. Wehus⁵⁹, M. White²⁶, S. D. M. White⁷², A. Zacchei⁴³, and A. Zonca⁷⁹

(Affiliations can be found after the references)

Received 20 July 2018 / Accepted 20 March 2020

ABSTRACT

We present cosmological parameter results from the final full-mission *Planck* measurements of the cosmic microwave background (CMB) anisotropies, combining information from the temperature and polarization maps and the lensing reconstruction. Compared to the 2015 results, improved measurements of large-scale polarization allow the reionization optical depth to be measured with higher precision, leading to significant gains in the precision of other correlated parameters. Improved modelling of the small-scale polarization leads to more robust constraints on many parameters, with residual modelling uncertainties estimated to affect them only at the 0.5σ level. We find good consistency with the standard spatially-flat 6-parameter Λ CDM cosmology having a power-law spectrum of adiabatic scalar perturbations (denoted “base Λ CDM” in this paper), from polarization, temperature, and lensing, separately and in combination. A combined analysis gives dark matter density $\Omega_c h^2 = 0.120 \pm 0.001$, baryon density $\Omega_b h^2 = 0.0224 \pm 0.0001$, scalar spectral index $n_s = 0.965 \pm 0.004$, and optical depth $\tau = 0.054 \pm 0.007$ (in this abstract we quote 68% confidence regions on measured parameters and 95% on upper limits). The angular acoustic scale is measured to 0.03% precision, with $100\theta_* = 1.0411 \pm 0.0003$. These results are only weakly dependent on the cosmological model and remain stable, with somewhat increased errors, in many commonly considered extensions. Assuming the base- Λ CDM cosmology, the inferred (model-dependent) late-Universe parameters are: Hubble constant $H_0 = (67.4 \pm 0.5) \text{ km s}^{-1} \text{ Mpc}^{-1}$; matter density parameter $\Omega_m = 0.315 \pm 0.007$; and matter fluctuation amplitude $\sigma_8 = 0.811 \pm 0.006$. We find no compelling evidence for extensions to the base- Λ CDM model. Combining with baryon acoustic oscillation (BAO) measurements (and considering single-parameter extensions) we constrain the effective extra relativistic degrees of freedom to be $N_{\text{eff}} = 2.99 \pm 0.17$, in agreement with the Standard Model prediction $N_{\text{eff}} = 3.046$, and find that the neutrino mass is tightly constrained to $\sum m_\nu < 0.12 \text{ eV}$. The CMB spectra continue to prefer higher lensing amplitudes than predicted in base Λ CDM at over 2σ , which pulls some parameters that affect the lensing amplitude away from the Λ CDM model; however, this is not supported by the lensing reconstruction or (in models that also change the background geometry) BAO data. The joint constraint with BAO measurements on spatial curvature is consistent with a flat universe, $\Omega_K = 0.001 \pm 0.002$. Also combining with Type Ia supernovae (SNe), the dark-energy equation of state parameter is measured to be $w_0 = -1.03 \pm 0.03$, consistent with a cosmological constant. We find no evidence for deviations from a purely power-law primordial spectrum, and combining with data from BAO, BICEP2, and Keck Array data, we place a limit on the tensor-to-scalar ratio $r_{0.002} < 0.06$. Standard big-bang nucleosynthesis predictions for the helium and deuterium abundances for the base- Λ CDM cosmology are in excellent agreement with observations. The *Planck* base- Λ CDM results are in good agreement with BAO, SNe, and some galaxy lensing observations, but in slight tension with the Dark Energy Survey’s combined-probe results including galaxy clustering (which prefers lower fluctuation amplitudes or matter density parameters), and in significant, 3.6σ , tension with local measurements of the Hubble constant (which prefer a higher value). Simple model extensions that can partially resolve these tensions are not favoured by the *Planck* data.

Key words. cosmic background radiation – cosmological parameters

* Corresponding authors: G. Efstathiou, e-mail: gpe@ast.cam.ac.uk; S. Galli, e-mail: gallis@iap.fr; A. Lewis, e-mail: antony@cosmologist.info

1. Introduction

Since their discovery (Smoot et al. 1992), temperature anisotropies in the cosmic microwave background (CMB) have become one of the most powerful ways of studying cosmology and the physics of the early Universe. This paper reports the final results on cosmological parameters from the Planck Collaboration¹. Our first results were presented in Planck Collaboration XVI (2014, hereafter PCP13). These were based on temperature (TT) power spectra and CMB lensing measurements from the first 15.5 months of *Planck* data combined with the Wilkinson Microwave Anisotropy Probe (WMAP) polarization likelihood at multipoles $\ell \leq 23$ (Bennett et al. 2013) to constrain the reionization optical depth τ . Planck Collaboration XIII (2016, hereafter PCP15) reported results from the full *Planck* mission (29 months of observations with the High Frequency Instrument, HFI), with substantial improvements in the characterization of the *Planck* beams and absolute calibration (resolving a difference between the absolute calibrations of WMAP and *Planck*). The focus of PCP15, as in PCP13, was on temperature observations, though we reported preliminary results on the high-multipole TE and EE polarization spectra. In addition, we used polarization measurements at low multipoles from the Low Frequency Instrument (LFI) to constrain the value of τ .

Following the completion of PCP15, a concerted effort by the *Planck* team was made to reduce systematics in the HFI polarization data at low multipoles. First results were presented in Planck Collaboration Int. XLVI (2016), which showed evidence for a lower value of the reionization optical depth than in the 2015 results. Further improvements to the HFI polarization maps prepared for the 2018 data release are described in Planck Collaboration III (2020). In this paper, we constrain τ using a new low-multipole likelihood constructed from these maps. The improvements in HFI data processing since PCP15 have very little effect on the TT , TE , and EE spectra at high multipoles. However, this paper includes characterizations of the temperature-to-polarization leakage and relative calibrations of the polarization spectra enabling us to produce a combined TT, TE, EE likelihood that is of sufficient fidelity to be used to test cosmological models (although with some limitations, which will be described in detail in the main body of this paper). The focus of this paper, therefore, is to present updated cosmological results from *Planck* power spectra and CMB lensing measurements using temperature and polarization.

PCP13 showed that the *Planck* data were remarkably consistent with a spatially-flat Λ CDM cosmology with purely adiabatic, Gaussian initial fluctuations, as predicted in simple inflationary models. We refer to this model, which can be specified by six parameters, as “base” Λ CDM in this paper. Note that in the base Λ CDM cosmology we assume a single minimal-mass neutrino eigenstate. We investigated a grid of one- and two-parameter extensions to the base- Λ CDM cosmology (varying, for example, the sum of neutrino masses, effective number of relativistic degrees of freedom N_{eff} , spatial curvature Ω_K , or dark-energy equation of state w_0), finding no statistically significant preference for any departure from the base model. These conclusions were reinforced using the full *Planck* mission data in PCP15.

The analyses reported in PCP13 and PCP15 revealed some discrepancies (often referred to as “tensions”) with non-*Planck* data in the context of Λ CDM models (e.g., distance-ladder measurements of the Hubble constant and determinations of the present-day amplitude of the fluctuation spectrum), including other CMB experiments (Story et al. 2013). As a result, it is important to test the fidelity of the *Planck* data as thoroughly as possible. First, we would like to emphasize that where it has been possible to compare data between different experiments at the map level (therefore eliminating cosmic variance), they have been found to be consistent within the levels set by instrument noise, apart from overall differences in absolute calibration; comparisons between WMAP and *Planck* are described by Huang et al. (2018), between the Atacama Cosmology Telescope (ACT) and *Planck* by Louis et al. (2014), and between the South Pole Telescope (SPT) and *Planck* by Hou et al. (2018). There have also been claims of internal inconsistencies in the *Planck* TT power spectrum between frequencies (Spergel et al. 2015) and between the Λ CDM parameters obtained from low and high multipoles (Addison et al. 2016). In addition, the *Planck* TT spectrum preferred more lensing than expected in the base- Λ CDM model (quantified by the phenomenological A_L parameter defined in Sect. 2.3) at moderate statistical significance, raising the question of whether there are unaccounted for systematic effects lurking within the *Planck* data. These issues were largely addressed in Planck Collaboration XI (2016), PCP15, and in an associated paper, Planck Collaboration Int. LI (2017). We revisit these issues in this paper at the cosmological parameter level, using consistency with the *Planck* polarization spectra as an additional check. Since 2013, we have improved the absolute calibration (fixing the amplitudes of the power spectra), added *Planck* polarization, full-mission *Planck* lensing, and produced a new low-multipole polarization likelihood from the *Planck* HFI. Nevertheless, the key parameters of the base- Λ CDM model reported in this paper, agree to better than $1\sigma_{2013}$ ² with those determined from the nominal mission temperature data in PCP13, with the exception of τ (which is lower in the 2018 analysis by $1.1\sigma_{2013}$). The cosmological parameters from *Planck* have remained remarkably stable since the first data release in 2013.

The results from *Planck* are in very good agreement with simple single-field models of inflation (Planck Collaboration XXII 2014; Planck Collaboration XX 2016). We have found no evidence for primordial non-Gaussianity (Planck Collaboration XXIV 2014; Planck Collaboration XVII 2016), setting stringent upper limits. Nor have we found any evidence for isocurvature perturbations or cosmic defects (see PCP15 and Planck Collaboration XX 2016). *Planck*, together with Bicep/Keck (BICEP2, Keck Array and Planck Collaborations 2015) polarization measurements, set tight limits on the amplitude of gravitational waves generated during inflation. These results are updated in this paper and in the companion papers, describing more comprehensive tests of inflationary models (Planck Collaboration X 2020) and primordial non-Gaussianity (Planck Collaboration IX 2020). The *Planck* results require adiabatic, Gaussian initial scalar fluctuations, with a red-tilted spectrum. The upper limits on gravitational waves then require flat inflationary potentials, which has stimulated new developments in inflationary model building (see e.g., Ferrara et al. 2013; Kallosh et al. 2013; Galante et al. 2015; Akrami et al. 2018, and references therein). Some authors (Ijjas et al. 2013; Ijjas & Steinhardt 2016)

¹ *Planck* (<https://www.esa.int/Planck>) is a project of the European Space Agency (ESA) with instruments provided by two scientific consortia funded by ESA member states and led by Principal Investigators from France and Italy, telescope reflectors provided through a collaboration between ESA and a scientific consortium led and funded by Denmark, and additional contributions from NASA (USA).

² Here σ_{2013} is the standard deviation quoted on parameters in PCP13.

have come to a very different conclusion, namely that the *Planck*/Bicep/Keck results require special initial conditions and therefore disfavour inflation. This controversy lies firmly in the theoretical domain (see e.g., Guth et al. 2014; Linde 2018), since observations of the CMB constrain only a limited number of e -folds during inflation, not the initial conditions. Post *Planck*, inflation remains a viable and attractive mechanism for accounting for the structure that we see in the Universe.

The layout of this paper is as follows. Section 2 describes changes to our theoretical modelling since PCP15 and summarizes the likelihoods used in this paper. More comprehensive descriptions of the power-spectrum likelihoods are given in Planck Collaboration V (2020), while the 2018 *Planck* CMB lensing likelihood is described in detail in Planck Collaboration VIII (2020). Section 3 discusses the parameters of the base- Λ CDM model, comparing parameters derived from the *Planck* TT , TE , and EE power spectra. Our best estimates of the base- Λ CDM cosmological parameters are derived from the full *Planck* TT, TE, EE likelihood combined with *Planck* CMB lensing and an HFI-based low-multipole polarization likelihood to constrain τ . We compare the *Planck* TE and EE spectra with power spectra measured from recent ground-based experiments in Sect. 4.

The *Planck* base- Λ CDM cosmology is compared with external data sets in Sect. 5. CMB power spectrum measurements suffer from a “geometric degeneracy” (see Efstathiou & Bond 1999) which limits their ability to constrain certain extensions to the base cosmology (for example, allowing Ω_K or w_0 to vary). *Planck* lensing measurements partially break the geometric degeneracy, but it is broken very effectively with the addition of baryon acoustic oscillation (BAO) measurements from galaxy surveys. As in PCP13 and PCP15 we use BAO measurements as the primary external data set to combine with *Planck*. We adopt this approach for two reasons. Firstly, BAO-scale determinations are relatively simple geometric measurements, with little scope for bias from systematic errors. Secondly, the primary purpose of this paper is to present and emphasize the *Planck* results. We therefore make minimal use of external data sets in reporting our main results, rather than combining with many different data sets. Exploration of multiple data sets can be done by others using the Monte Carlo Markov chains and *Planck* likelihoods released through the *Planck* Legacy Archive (hereafter PLA)³. Nevertheless, Sect. 5 presents a comprehensive survey of the consistency of the *Planck* base- Λ CDM cosmology with different types of astrophysical data, including Type Ia supernovae, redshift-space distortions, galaxy shear surveys, and galaxy cluster counts. These data sets are consistent with the *Planck* base- Λ CDM cosmology with, at worst, moderate tensions at about the 2.5σ level. Distance-ladder measurements of the Hubble constant, H_0 , are an exception, however. The latest measurement from Riess et al. (2019) is discrepant with the *Planck* base- Λ CDM value for H_0 at about the 4.4σ level. This large discrepancy, and its possible implications for cosmology, is discussed in Sect. 5.4.

Section 6 investigates the internal consistency of the *Planck* base- Λ CDM parameters, presenting additional tests using the TE and EE spectra, as well as a discussion of systematic uncertainties. Results from our main grid of parameter constraints on one- or two-parameter extensions to the base- Λ CDM cosmology are presented in Sect. 7. That section also includes discussions of more complex models of dark energy and modified gravity (updating the results presented in Planck Collaboration XIV

2016), primordial nucleosynthesis, reionization, recombination, and dark matter annihilation. Section 8 summarizes our main conclusions.

2. Methodology and likelihoods

2.1. Theoretical model

The definitions, methodology, and notation used in this paper largely follow those adopted in the earlier Planck Collaboration papers dealing with cosmological parameters (PCP13, PCP15). Our baseline assumption is the Λ CDM model with purely adiabatic scalar primordial perturbations with a power-law spectrum. We assume three neutrino species, approximated as two massless states and a single massive neutrino of mass $m_\nu = 0.06$ eV. We put flat priors on the baryon density $\omega_b \equiv \Omega_b h^2$, cold dark matter density $\omega_c \equiv \Omega_c h^2$, an approximation to the observed angular size of the sound horizon at recombination θ_{MC} , the reionization optical depth τ , the initial super-horizon amplitude of curvature perturbations A_s at $k = 0.05$ Mpc⁻¹, and the primordial spectral index n_s . Other parameter definitions, prior limits, and notation are described explicitly in Table 1 of PCP13; the only change is that we now take the amplitude prior to be flat in $\log A_s$ over the range $1.61 < \log(10^{10} A_s) < 3.91$ (which makes no difference to *Planck* results, but is consistent with the range used for some external data analyses).

Changes in our physical modelling compared with PCP15 are as follows.

- For modelling the small-scale nonlinear matter power spectrum, and calculating the effects of CMB lensing, we use the *halofit* technique (Smith et al. 2003) as before, but now replace the Takahashi et al. (2012) approach with *HMcode*, the fitting method of Mead et al. (2015, 2016), as implemented in *camb* (Lewis et al. 2000).

- For each model in which the fraction of baryonic mass in helium Y_P is *not* varied independently of other parameters, the value is now set using an updated big-bang nucleosynthesis (BBN) prediction by interpolation on a grid of values calculated using version 1.1 of the *PARthENoPE* BBN code (Pisanti et al. 2008, version 2.0 gives identical results). We now use a fixed fiducial neutron decay-constant value of $\tau_n = 880.2$ s, neglecting uncertainties. Predictions from *PARthENoPE* for the helium mass fraction ($Y_P \approx 0.2454$, nucleon fraction $Y_P^{\text{BBN}} \approx 0.2467$ from *Planck* in Λ CDM) are lower than those from the code of Pitrou et al. (2018) for the same value of τ_n by $\Delta Y_P \approx 0.0005$; however, other parameter results would be consistent to well within 0.1σ . See Sect. 7.6 for further discussion of BBN parameter uncertainties and code variations.

Building upon many years of theoretical effort, the computation of CMB power spectra and the related likelihood functions has now become highly efficient and robust. Our main results are based upon the lensed CMB power spectra computed with the August 2017 version of the *camb*⁴ Boltzmann code (Lewis et al. 2000) and parameter constraints are based on the July 2018 version of *CosmoMC*⁵ (Lewis & Bridle 2002; Lewis 2013). We have checked that there is very good consistency between these results and equivalent results computed using the *class* Boltzmann code (Blas et al. 2011) and *MontePython* sampler (Audren et al. 2013; Brinckmann & Lesgourgues 2019). Marginalized densities, limits, and contour plots are generated using updated adaptive kernel density estimates (with corrections for boundary

⁴ <https://camb.info>

⁵ <https://cosmologist.info/cosmomc/>

³ <https://pla.esac.esa.int>

and smoothing biases) as calculated using the `getdist` package (Lewis 2019)⁶ (also part of CosmoMC), which improves average accuracy for a given number of posterior samples compared to the version used in our previous analyses.

A few new derived parameters have been added to the output of the CosmoMC chains to allow comparisons and combinations with external data sets. A full description of all parameters is provided in the tables presented in the Explanatory Supplement (Planck Collaboration 2018), and parameter chains are available on the PLA.

2.2. Power spectra and likelihoods

Since the 2015 *Planck* data release, most of the effort on the low-level data processing has been directed to improving the fidelity of the polarization data at low multipoles. The first results from this effort were reported in Planck Collaboration Int. XLVI (2016) and led to a new determination of the reionization optical depth, τ . The main results presented in this paper are based on the 2018 HFI maps produced with the SRoll mapmaking algorithm described in detail in Planck Collaboration III (2020), supplemented with LFI data described in Planck Collaboration II (2020).

Because *Planck*-HFI measures polarization by differencing the signals measured by polarization-sensitive bolometers (PSBs), a number of instrumental effects need to be controlled to achieve high precision in the absolute calibrations of each detector. These include: effective gain variations arising from nonlinearities in the analogue-to-digital electronics and thermal fluctuations; far-field beam characterization, including long bolometer time constants; and differences in detector bandpasses. The SRoll mapmaking solution for the 100–353 GHz channels minimizes map residuals between all HFI detectors at a given frequency, using absolute calibrations based on the orbital dipole, together with a bandpass-mismatch model constructed from spatial templates of the foregrounds and a parametric model characterizing the remaining systematics. We refer the reader to Planck Collaboration III (2020) for details of the implementation of SRoll. The fidelity of the SRoll maps can be assessed using various null tests (e.g., splitting the data by half-mission, odd-even surveys, and different detector combinations) and by the consistency of the recovered Solar dipole solution. These tests are described in Planck Collaboration III (2020) and demonstrate that the Solar dipole calibration is accurate to about one part in 10^4 for the three lowest-frequency HFI channels. Large-scale intensity-to-polarization leakage, caused by calibration mismatch in the SRoll maps, is then reduced to levels $\lesssim 10^{-6} \mu\text{K}^2$ at $\ell > 3$.

The low-multipole polarization likelihood used in this paper is based on the SRoll polarization maps and series of end-to-end simulations that are used to characterize the noise properties and remaining biases in the SRoll maps. This low-multipole likelihood is summarized in Sect. 2.2.3 and is described in more detail in Planck Collaboration V (2020).

As in previous *Planck* papers, the baseline likelihood is a hybrid, patching together a low-multipole likelihood at $\ell < 30$ with a Gaussian likelihood constructed from pseudo-cross-spectrum estimates at higher multipoles. Correlations between the low and high multipoles are neglected. In this paper, we have used two independent high-multipole TT,TE,EE

likelihoods⁷. The Plik likelihood, which is adopted as the baseline in this paper, is described in Sect. 2.2.1, while the CamSpec likelihood is described in Sect. 2.2.2 and Appendix A. These two likelihoods are in very good agreement in TT, but show small differences in TE and EE, as described below and in the main body of this paper. Section 2.3 summarizes the *Planck* CMB lensing likelihood, which is described in greater detail in Planck Collaboration VIII (2020).

Before summarizing the high-multipole likelihoods, we make a few remarks concerning the 2018 SRoll maps. The main aim of the SRoll processing is to reduce the impact of systematics at low multipoles and hence the main differences between the 2015 and 2018 HFI maps are at low multipoles. Compared to the 2015 HFI maps, the SRoll maps eliminate the last 1000 HFI scanning rings (about 22 days of observations) because these were less thermally stable than the rest of the mission. SRoll uses higher resolution maps to determine the destriping offsets compared to the 2015 maps, leading to a reduction of about 12% in the noise levels at 143 GHz (see Fig. 10 of Planck Collaboration III 2020). A tighter requirement on the reconstruction of Q and U values at each pixel leads to more missing pixels in the 2018 maps compared to 2015. These and other changes to the 2018 *Planck* maps have very little impact on the temperature and polarization spectra at high multipoles (as will be demonstrated explicitly in Fig. 9 below).

There are, however, data-processing effects that need to be accounted for to create an unbiased temperature+polarization likelihood at high multipoles from the SRoll maps. In simplified form, the power absorbed by a detector at time t on the sky is

$$P(t) = G \{ I + \rho [Q \cos 2(\psi(t) + \psi_0) + U \sin 2(\psi(t) + \psi_0)] \} + n(t), \quad (1)$$

where I , Q , and U are the beam-convolved Stokes parameters seen by the detector at time t , G is the effective gain (setting the absolute calibration), ρ is the detector polarization efficiency, $\psi(t)$ is the roll angle of the satellite, ψ_0 is the detector polarization angle, and $n(t)$ is the noise. For a perfect polarization-sensitive detector, $\rho = 1$, while for a perfect unpolarized detector, $\rho = 0$. The polarization efficiencies and polarization angles for the HFI bolometers were measured on the ground and are reported in Rosset et al. (2010). For polarization-sensitive detectors the ground-based measurements of polarization angles were measured to an accuracy of approximately 1° and the polarization efficiencies to a quoted accuracy of 0.1–0.3%. The SRoll mapmaking algorithm assumes the ground-based measurements of polarization angles and efficiencies, which cannot be separated because they are degenerate with each other. Errors in the polarization angles induce leakage from E to B modes, while errors in the polarization efficiencies lead to gain mismatch between I , Q and U . Analysis of the *Planck* TB and EB spectra (which should be zero in the absence of parity-violating physics) reported in Planck Collaboration III (2020), suggest errors in the polarization angles of $\lesssim 0.5^\circ$, within the error estimates reported in Rosset et al. (2010). However, systematic errors in the polarization efficiencies are found to be several times larger than the Rosset et al. (2010) determinations (which were limited to characterizations of the feed and detector sub-assemblies and did not characterize the system in combination with the telescope) leading to effective calibration offsets

⁷ We use roman letters, such as TT,TE,EE, to refer to particular likelihood combinations, but use italics, such as *TT*, when discussing power spectra more generally.

⁶ <https://getdist.readthedocs.io/>

in the polarization spectra. These polarization efficiency differences, which are detector- and hence frequency-dependent, need to be calibrated to construct a high-multipole likelihood. To give some representative numbers, the Rosset et al. (2010) ground-based measurements estimated polarization efficiencies for the PSBs, with typical values of 92–96% at 100 GHz, 83–93% at 143 GHz, and 94–95% at 217 GHz (the three frequencies used to construct the high-multipole polarization likelihoods). From the SRoll maps, we find evidence of systematic errors in the polarization efficiencies of order 0.5–1% at 100 and 217 GHz and up to 1.5% at 143 GHz. Differences between the main beams of the PSBs introduce temperature-to-polarization leakage at high multipoles. We use the QuickPol estimates of the temperature-polarization beam transfer function matrices, as described in Hivon et al. (2017), to correct for temperature-to-polarization leakage. Inaccuracies in the corrections for effective polarization efficiencies and temperature-to-polarization leakage are the main contributors to systematic errors in the *Planck* polarization spectra at high multipoles.

In principle, *B*-mode polarization spectra contain information about lensing and primordial tensor modes. However, for *Planck*, *B*-mode polarization spectra are strongly noise dominated on all angular scales. Given the very limited information contained in the *Planck* *B*-mode spectra (and the increased complexity involved) we do not include *B*-mode power spectra in the likelihoods; however, for an estimate of the lensing *B*-mode power spectrum (see Planck Collaboration VIII 2020, hereafter PL2018).

2.2.1. The baseline Plik likelihood

The Plik high-multipole likelihood (described in detail in Planck Collaboration V 2020, hereafter PPL18) is a Gaussian approximation to the probability distributions of the *TT*, *EE*, and *TE* angular power spectra, with semi-analytic covariance matrices calculated assuming a fiducial cosmology. It includes multipoles in the range $30 \leq \ell \leq 2508$ for *TT* and $30 \leq \ell \leq 1996$ for *TE* and *EE*, and is constructed from half-mission cross-spectra measured from the 100-, 143-, and 217 GHz HFI frequency maps.

The *TT* likelihood uses four half-mission cross-spectra, with different multipole cuts to avoid multipole regions where noise dominates due to the limited resolution of the beams and to ensure foreground contamination is correctly handled by our foreground model: 100×100 ($\ell = 30\text{--}1197$); 143×143 ($\ell = 30\text{--}1996$); 143×217 ($\ell = 30\text{--}2508$); and 217×217 ($\ell = 30\text{--}2508$). The *TE* and *EE* likelihoods also include the 100×143 and 100×217 cross-spectra to improve the signal-to-noise ratio, and have different multipole cuts: 100×100 ($\ell = 30\text{--}999$); 100×143 ($\ell = 30\text{--}999$); 100×217 ($\ell = 505\text{--}999$); 143×143 ($\ell = 30\text{--}1996$); 143×217 ($\ell = 505\text{--}1996$); and 217×217 ($\ell = 505\text{--}1996$). The 100-, 143-, and 217 GHz intensity maps are masked to reduce Galactic dust, CO, extended sources, and point-source contamination (a different point-source mask is used at each frequency), as well as badly-conditioned/missing pixels, effectively retaining 66, 57, and 47% of the sky after apodization, respectively (see Eq. (10) in PCP15 for a definition of the effective sky fraction). The apodization is applied to reduce the mask-induced correlations between modes, and reduces the effective sky fraction by about 10% compared to the unapodized masks. The 100-, 143-, and 217 GHz maps in polarization are masked only for Galactic contamination and badly-conditioned or missing pixels, effectively retaining 70, 50, and 41% of the sky after apodization, respectively.

The baseline likelihood uses the different frequency power spectra without coadding them, modelling the foreground and instrumental effects with nuisance parameters that are marginalized over at the parameter estimation level, both in temperature and in polarization. To reduce the size of the covariance matrix and data vector, the baseline Plik likelihood uses binned band powers, which give an excellent approximation to the unbinned likelihood for smooth theoretical power spectra. Unbinned versions of the likelihoods are also available and provide almost identical results to the binned spectra for all of the theoretical models considered in our main parameter grid (Sect. 7.1).

The major changes with respect to the 2015 Plik likelihood are the following.

Beams. In 2015, the effective beam window functions were calculated assuming the same average sky fraction at all frequencies. In this new release, we apply beam window functions calculated for the specific sky fraction retained at each frequency. The impact on the spectra is small, at the level of approximately 0.1% at $\ell = 2000$.

Dust modelling in *TT*. The use of intensity-thresholded point-source masks modifies the power spectrum of the Galactic dust emission, since such masks include point-like bright Galactic dust regions. Because these point-source masks are frequency dependent, a different dust template is constructed from the 545 GHz maps for each power spectrum used in the likelihood. This differs from the approach adopted in 2015, which used a Galactic dust template with the same shape at all frequencies. As in 2015, the Galactic dust amplitudes are then left free to vary, with priors determined from cross-correlating the frequency maps used in the likelihood with the 545 GHz maps. These changes produce small correlated shifts in the dust, cosmic infrared background (CIB), and point-source amplitudes, but have negligible impact on cosmological parameters.

Dust modelling in *TE* and *EE*. Dust amplitudes in *TE* are varied with Gaussian priors as in 2015, while in *EE* we fix the dust amplitudes to the values obtained using the cross-correlations with 353 GHz maps, for the reasons detailed in PPL18. The choice of fixing the dust amplitudes in *EE* has a small impact (of the order of 0.2σ) on the base- Λ CDM results when combining into the full “*TT,TE,EE*,” Plik likelihood because *EE* has lower statistical power compared to *TT* or *TE*; however, dust modelling in *EE* has a greater effect when parameters are estimated from *EE* alone (e.g., fixing the dust amplitude in *EE* lowers n_s by 0.8σ , compared to allowing the dust amplitude to vary.)

Correction of systematic effects in the polarization spectra. In the 2015 *Planck* analysis, small differences in the inter-frequency comparisons of *TE* and *EE* foreground-corrected polarization power spectra were identified and attributed to systematics such as temperature-to-polarization leakage and polarization efficiencies, which had not been characterized adequately at the time. For the 2018 analysis we have applied the following corrections to the Plik spectra.

– **Beam-leakage correction.** The *TE* and *EE* pseudo-spectra are corrected for temperature-to-polarization leakage caused by beam mismatch, using polarized beam matrices computed with the QuickPol code described in Hivon et al. (2017). The beam-leakage correction template is calculated using fiducial theoretical spectra computed from the best-fit Λ CDM cosmology fitted to the *TT* data, together with QuickPol estimates of the HFI polarized beam transfer-function matrices. This template is then included in our data model. The correction for beam

leakage has a larger impact on TE than on EE . For base- Λ CDM cosmology, correcting for the leakage induces shifts of $\lesssim 1\sigma$ when constraining parameters with TT,TE,EE, namely $+1.1\sigma$ for ω_b , -0.7σ for ω_c , $+0.7\sigma$ for θ_{MC} , and $+0.5\sigma$ for n_s , with smaller changes for other parameters.

– Effective polarization efficiencies. We estimate the effective polarization efficiencies of the SRoll maps by comparing the frequency polarization power spectra to fiducial spectra computed from the best-fit base- Λ CDM model determined from the temperature data. The details and limitations of this procedure are described in PPL18 and briefly summarized further below. Applying these polarization efficiency estimates, we find relatively small shifts to the base- Λ CDM parameters determined from the TT,TE,EE likelihood, with the largest shifts in ω_b ($+0.4\sigma$), ω_c ($+0.2\sigma$), and n_s ($+0.2\sigma$). The parameter shifts are small because the polarization efficiencies at different frequencies partially average out in the coadded TE spectra (see also Fig. 9, discussed in Sect. 3).

– Correlated noise in auto-frequency cross-spectra and sub-pixel effects. The likelihood is built using half-mission cross-spectra to avoid noise biases from auto-spectra. However, small residual correlated noise contributions may still be present. The pixelization of the maps introduces an additional noise term because the centroid of the “hits” distribution of the detector samples in each pixel does not necessarily lie at the pixel centre. The impact of correlated noise is evaluated using the end-to-end simulations described in Planck Collaboration III (2020), while the impact of subpixel effects is estimated with analytic calculations. Both effects are included in the Plik data model, but have negligible impact on cosmological parameters. Of the systematic effects listed above, correction for the polarization efficiencies has the largest uncertainty. We model these factors as effective polarization calibration parameters c_v^{EE} , defined at the power spectrum level for a frequency spectrum $\nu \times \nu$ ⁸. To correct for errors in polarization efficiencies and large-scale beam-transfer function errors, we recalibrate the TE and EE spectra against a fiducial theoretical model to minimize

$$\chi^2 = (C^D - GC^{\text{Th}})M^{-1}(C^D - GC^{\text{Th}}), \quad (2a)$$

with respect to the c_v^{EE} parameters contained in the diagonal calibration matrix G with elements

$$G_{i,i} = \left(\frac{1}{\sqrt{c_v^{XX}c_v^{YY}}} + \frac{1}{\sqrt{c_v^{XX}c_v^{YY}}} \right)_{i,i}, \quad (2b)$$

where the index $i = 1, N$ runs over the multipoles ℓ and frequencies $\nu \times \nu'$ of the spectra contained in the C^D data vector of dimension N ; C^D contains the C_ℓ frequency spectra either for $XY = TE$ or $XY = EE$, fit separately. In Eq. (2a), M is the covariance matrix for the appropriate spectra included in the fit, while the c_v^{TT} temperature calibration parameters are fixed. We perform the fit only using multipoles $\ell = 200$ – 1000 to minimize the impact of inaccuracies in the foreground modelling or noise, and we test the stability of the results by fitting either one frequency spectrum or all the frequency spectra at the same time. The recalibration is computed with respect to a fiducial model vector C^{Th} because the *Planck* polarization spectra are noisy and it is not possible to inter-calibrate the spectra to a precision of better than 1% without invoking a reference model. The fiducial theoretical spectra C_ℓ^{Th} contained in C^{Th} are derived from

⁸ Thus, the polarization efficiency for a cross-frequency spectrum $\nu \times \nu'$ in, e.g., EE is $\sqrt{c_v^{EE} \times c_{\nu'}^{EE}}$.

the best-fit temperature data alone, assuming the base- Λ CDM model, adding the beam-leakage model and fixing the Galactic dust amplitudes to the central values of the priors obtained from using the 353 GHz maps. This is clearly a model-dependent procedure, but given that we fit over a restricted range of multipoles, where the TT spectra are measured to cosmic variance, the resulting polarization calibrations are insensitive to small changes in the underlying cosmological model.

In principle, the polarization efficiencies found by fitting the TE spectra should be consistent with those obtained from EE . However, the polarization efficiency at 143×143 , c_{143}^{EE} , derived from the EE spectrum is about 2σ lower than that derived from TE (where the σ is the uncertainty of the TE estimate, of the order of 0.02). This difference may be a statistical fluctuation or it could be a sign of residual systematics that project onto calibration parameters differently in EE and TE . We have investigated ways of correcting for effective polarization efficiencies: adopting the estimates from EE (which are about a factor of 2 more precise than TE) for both the TE and EE spectra (we call this the “map-based” approach); or applying independent estimates from TE and EE (the “spectrum-based” approach). In the baseline Plik likelihood we use the map-based approach, with the polarization efficiencies fixed to the efficiencies obtained from the fits on EE : $(c_{100}^{EE})_{EE \text{ fit}} = 1.021$; $(c_{143}^{EE})_{EE \text{ fit}} = 0.966$; and $(c_{217}^{EE})_{EE \text{ fit}} = 1.040$. The CamSpec likelihood, described in the next section, uses spectrum-based effective polarization efficiency corrections, leaving an overall temperature-to-polarization calibration free to vary within a specified prior.

The use of spectrum-based polarization efficiency estimates (which essentially differs by applying to EE the efficiencies given above, and to TE the efficiencies obtained fitting the TE spectra, $(c_{100}^{EE})_{TE \text{ fit}} = 1.04$, $(c_{143}^{EE})_{TE \text{ fit}} = 1.0$, and $(c_{217}^{EE})_{TE \text{ fit}} = 1.02$), also has a small, but non-negligible impact on cosmological parameters. For example, for the Λ CDM model, fitting the Plik TT,TE,EE+lowE likelihood, using spectrum-based polarization efficiencies, we find small shifts in the base- Λ CDM parameters compared with ignoring spectrum-based polarization efficiency corrections entirely; the largest of these shifts are $+0.5\sigma$ in ω_b , $+0.1\sigma$ in ω_c , and $+0.3\sigma$ in n_s (to be compared to $+0.4\sigma$ in ω_b , $+0.2\sigma$ in ω_c , and $+0.2\sigma$ in n_s for the map-based case). Furthermore, if we introduce the phenomenological A_L parameter (discussed in much greater detail in Sect. 6.2), using the baseline TT,TE,EE+lowE likelihood gives $A_L = 1.180 \pm 0.065$, differing from unity by 2.7σ (the value of A_L is unchanged with respect to the case where we ignore polar efficiencies entirely, 1.180 ± 0.065). Switching to spectrum-based polarization efficiency corrections changes this estimate to $A_L = 1.142 \pm 0.066$ differing from unity by 2.1σ . Readers of this paper should therefore not over-interpret the *Planck* polarization results and should be aware of the sensitivity of these results to small changes in the specific choices and assumptions made in constructing the polarization likelihoods, which are not accounted for in the likelihood error model. To emphasize this point, we also give results from the CamSpec likelihood (see, e.g., Table 1), described in the next section, which has been constructed independently of Plik. We also note that if we apply the CamSpec polarization masks and spectrum-based polarization efficiencies in the Plik likelihood, then the cosmological parameters from the two likelihoods are in close agreement.

The coadded 2018 Plik temperature and polarization power spectra and residuals with respect to the base- Λ CDM model are shown in Figs. 1 and 2.

Table 1. Base- Λ CDM cosmological parameters from *Planck* TT,TE,EE+lowE+lensing.

Parameter	Plik best fit	Plik [1]	CamSpec [2]	([2] – [1])/ σ_1	Combined
$\Omega_b h^2$	0.022383	0.02237 ± 0.00015	0.02229 ± 0.00015	–0.5	0.02233 ± 0.00015
$\Omega_c h^2$	0.12011	0.1200 ± 0.0012	0.1197 ± 0.0012	–0.3	0.1198 ± 0.0012
$100\theta_{MC}$	1.040909	1.04092 ± 0.00031	1.04087 ± 0.00031	–0.2	1.04089 ± 0.00031
τ	0.0543	0.0544 ± 0.0073	$0.0536^{+0.0069}_{-0.0077}$	–0.1	0.0540 ± 0.0074
$\ln(10^{10} A_s)$	3.0448	3.044 ± 0.014	3.041 ± 0.015	–0.3	3.043 ± 0.014
n_s	0.96605	0.9649 ± 0.0042	0.9656 ± 0.0042	+0.2	0.9652 ± 0.0042
$\Omega_m h^2$	0.14314	0.1430 ± 0.0011	0.1426 ± 0.0011	–0.3	0.1428 ± 0.0011
H_0 [km s $^{-1}$ Mpc $^{-1}$]	67.32	67.36 ± 0.54	67.39 ± 0.54	+0.1	67.37 ± 0.54
Ω_m	0.3158	0.3153 ± 0.0073	0.3142 ± 0.0074	–0.2	0.3147 ± 0.0074
Age [Gyr]	13.7971	13.797 ± 0.023	13.805 ± 0.023	+0.4	13.801 ± 0.024
σ_8	0.8120	0.8111 ± 0.0060	0.8091 ± 0.0060	–0.3	0.8101 ± 0.0061
$S_8 \equiv \sigma_8(\Omega_m/0.3)^{0.5}$	0.8331	0.832 ± 0.013	0.828 ± 0.013	–0.3	0.830 ± 0.013
z_{re}	7.68	7.67 ± 0.73	7.61 ± 0.75	–0.1	7.64 ± 0.74
$100\theta_*$	1.041085	1.04110 ± 0.00031	1.04106 ± 0.00031	–0.1	1.04108 ± 0.00031
r_{drag} [Mpc]	147.049	147.09 ± 0.26	147.26 ± 0.28	+0.6	147.18 ± 0.29

Notes. Results for the parameter best fits, marginalized means and 68% errors from our default analysis using the Plik likelihood are given in the first two numerical columns. The CamSpec likelihood results give some idea of the remaining modelling uncertainty in the high- ℓ polarization, though parts of the small shifts are due to slightly different sky areas in polarization. The ‘‘Combined’’ column give the average of the Plik and CamSpec results, assuming equal weight. The combined errors are from the equal-weighted probabilities, hence including some uncertainty from the systematic difference between them; however, the differences between the high- ℓ likelihoods are so small that they have little effect on the 1σ errors. The errors do not include modelling uncertainties in the lensing and low- ℓ likelihoods or other modelling errors (such as temperature foregrounds) common to both high- ℓ likelihoods. A total systematic uncertainty of around 0.5σ may be more realistic, and values should not be overinterpreted beyond this level. The best-fit values give a representative model that is an excellent fit to the baseline likelihood, though models nearby in the parameter space may have very similar likelihoods. The first six parameters here are the ones on which we impose flat priors and use as sampling parameters; the remaining parameters are derived from the first six. Note that Ω_m includes the contribution from one neutrino with a mass of 0.06 eV. The quantity θ_{MC} is an approximation to the acoustic scale angle, while θ_* is the full numerical result.

2.2.2. The CamSpec likelihood

The CamSpec temperature likelihood was used as the baseline for the first analysis of cosmological parameters from *Planck*, reported in PCP13, and was described in PPL13. A detailed description of CamSpec and its generalization to polarization is given in Efstathiou & Gratton (2019). For PCP15, the CamSpec temperature likelihood was unaltered from that adopted in PPL13, except that we used half-mission cross-spectra instead of detector-set cross-spectra and made minor modifications to the foreground model. For this set of papers, the CamSpec temperature analysis uses identical input maps and masks as Plik and is unaltered from PCP15, except for the following details.

- In previous versions we used half-ring difference maps (constructed from the first and second halves of the scanning rings within each pointing period) to estimate noise. In this release we have used differences between maps constructed from odd and even rings. The use of odd-even differences makes almost no difference to the temperature analysis, since the temperature spectra that enter the likelihood are signal dominated over most of the multipole range. However, the odd-even noise estimates give higher noise levels than half-ring difference estimates at multipoles $\lesssim 500$ (in qualitative agreement with end-to-end simulations), and this improves the χ^2 of the polarization spectra. This differs from the Plik likelihood, which uses the half-ring difference maps to estimate the noise levels, together with a correction to compensate for correlated noise, as described in PPL18.

- In PCP15, we used power-spectrum templates for the CIB from the halo models described in Planck Collaboration XXX (2014). The overall amplitude of the CIB power spectrum at 217 GHz was allowed to vary as one of the ‘‘nuisance’’ parameters in the likelihood, but the relative amplitudes at 143×217

and 143×143 were fixed to the values given by the model. In the 2018 analysis, we retain the template shapes from Planck Collaboration XXX (2014), but allow free amplitudes at 217×217 , 143×217 , and 143×143 . The CIB is ignored at 100 GHz. We made these changes to the 2018 CamSpec likelihood to reduce any source of systematic bias associated with the specific model of Planck Collaboration XXX (2014), since this model is uncertain at low frequencies and fails to match *Herschel*-SPIRE measurements (Viero et al. 2013) of the CIB anisotropies at 350 and 500 μm for $\ell \gtrsim 3000$ (Mak et al. 2017). This change was implemented to see whether it had any impact on the value of the lensing parameter A_L (see Sect. 6.2); however, it has a negligible effect on A_L or on other cosmological parameters. The Plik likelihood retains the 2015 model for the CIB.

- In PCP15 we used a single functional form for the Galactic dust power spectrum template, constructed by computing differences of 545×545 power spectra determined using different masks. The dust template was then rescaled to match the dust amplitudes at lower frequencies for the masks used to form the likelihood. In the 2018 CamSpec likelihood we use dust templates computed from the 545×545 spectra, using masks with exactly the same point-source holes as those used to compute the 100×100 , 143×143 , 143×217 , and 217×217 power spectra that are used in the likelihood. The Plik likelihood adopts a similar approach and the CamSpec and Plik dust templates are in very good agreement.

In forming the temperature likelihood, we apply multipole cuts to the temperature spectra as follows: $\ell_{\min} = 30$, $\ell_{\max} = 1200$ for the 100×100 spectrum; $\ell_{\min} = 30$, $\ell_{\max} = 2000$ for the 143×143 spectrum; and $\ell_{\min} = 500$, $\ell_{\max} = 2500$ for 143×217 and 217×217 . As discussed in previous papers, the ℓ_{\min} cuts applied to the 143×217 and 217×217 spectra are imposed to reduce any potential systematic biases arising from Galactic dust at these frequencies. A foreground model is included in

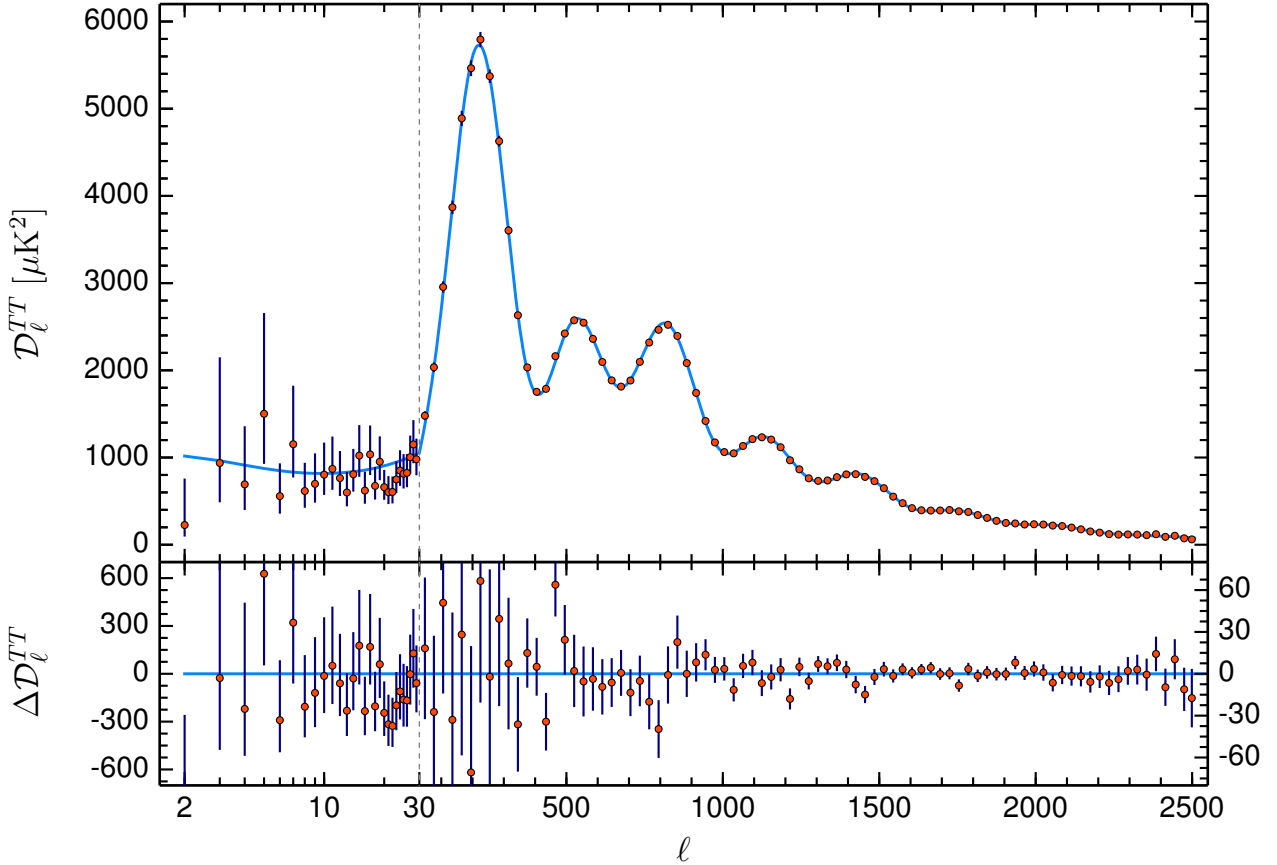


Fig. 1. *Planck* 2018 temperature power spectrum. At multipoles $\ell \geq 30$ we show the frequency-coadded temperature spectrum computed from the Plik cross-half-mission likelihood, with foreground and other nuisance parameters fixed to a best fit assuming the base- Λ CDM cosmology. In the multipole range $2 \leq \ell \leq 29$, we plot the power spectrum estimates from the Commander component-separation algorithm, computed over 86% of the sky. The base- Λ CDM theoretical spectrum best fit to the *Planck* TT,TE,EE+lowE+lensing likelihoods is plotted in light blue in the upper panel. Residuals with respect to this model are shown in the lower panel. The error bars show $\pm 1\sigma$ diagonal uncertainties, including cosmic variance (approximated as Gaussian) and not including uncertainties in the foreground model at $\ell \geq 30$. Note that the vertical scale changes at $\ell = 30$, where the horizontal axis switches from logarithmic to linear.

computing the covariance matrices, assuming that foregrounds are isotropic and Gaussian. This model underestimates the contribution of Galactic dust to the covariances, since this component is anisotropic on the sky. However, dust always makes a very small contribution to the covariance matrices in the CamSpec likelihood. Mak et al. (2017) describe a simple model to account for the Galactic dust contributions to covariance matrices.

It is important to emphasize that these changes to the 2018 CamSpec TT likelihood are largely cosmetic and have very little impact on cosmological parameters. This can be assessed by comparing the CamSpec TT results reported in this paper with those in PCP15. The main changes in cosmological parameters from the TT likelihood come from the tighter constraints on the optical depth, τ , adopted in this paper.

In polarization, CamSpec uses a different methodology to Plik. In temperature, there are a number of frequency-dependent foregrounds at high multipoles that are described by a physically motivated parametric model containing “nuisance” parameters. These nuisance parameters are sampled, along with cosmological parameters, during Markov chain Monte Carlo (MCMC) exploration of the likelihood. The TT likelihood is therefore a power-spectrum-based component-separation tool and it is essential to retain cross-power spectra for each distinct frequency combination. For the *Planck* TE and EE spec-

tra, however, Galactic dust is by far the dominant foreground contribution. At the multipoles and sensitivities accessible to *Planck*, polarized point sources make a negligible contribution to the foreground (as verified by ACTPol and SPTpol; Louis et al. 2017; Henning et al. 2018), so the only foreground that needs to be subtracted is polarized Galactic dust emission. As described in PCP15, we subtract polarized dust emission from each TE/ET and EE spectrum using the 353 GHz half-mission maps. This is done in an analogous way to the construction of 545 GHz-cleaned temperature maps described in PCP15 and Appendix A. Since the 353 GHz maps are noisy at high multipoles we use the cleaned spectra at multipoles ≤ 300 and extrapolate the dust model to higher multipoles by fitting power laws to the dust estimates at lower multipoles.

The polarization spectra are then corrected for temperature-to-polarization leakage and effective polarization efficiencies as described below, assuming a fiducial theoretical power spectrum. The corrected TE/ET spectra and EE spectra for all half-mission cross-spectra constructed from 100-, 143-, and 217 GHz maps are then coadded to form a single TE spectrum and a single EE spectrum for the CamSpec likelihood. The polarization part of the CamSpec likelihood therefore contains no nuisance parameters other than overall calibration factors c_{TE} and c_{EE} for the TE and EE spectra. Since the CamSpec likelihood uses coadded TE and EE spectra, we do not need to bin the spectra to form

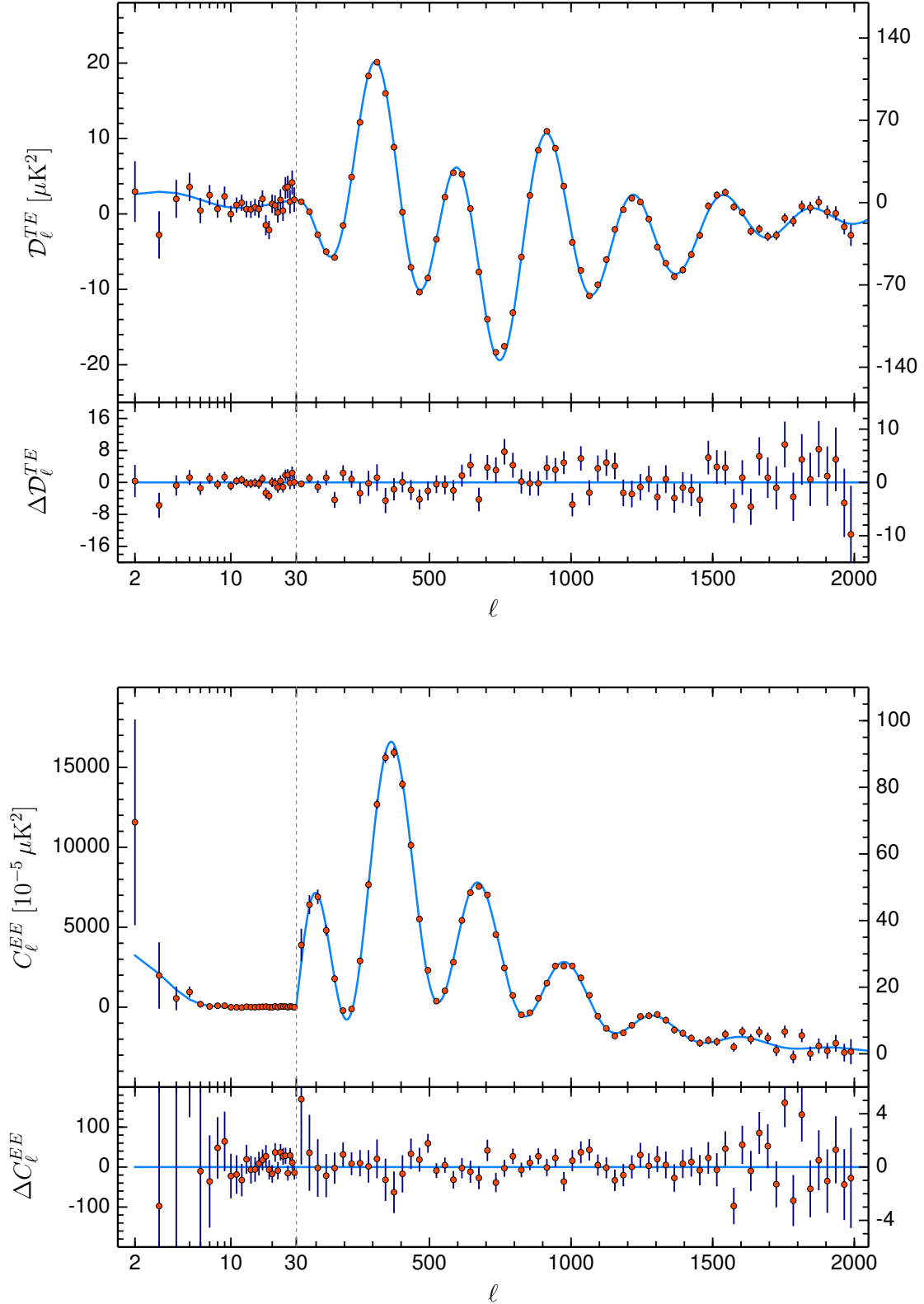


Fig. 2. *Planck* 2018 *TE* (top) and *EE* (bottom) power spectra. At multipoles $\ell \geq 30$ we show the coadded frequency spectra computed from the *Planck* cross-half-mission likelihood with foreground and other nuisance parameters fixed to a best fit assuming the base- Λ CDM cosmology. In the multipole range $2 \leq \ell \leq 29$, we plot the power spectra estimates from the *SimAll* likelihood (though only the *EE* spectrum is used in the baseline parameter analysis at $\ell \leq 29$). The best-fit base- Λ CDM theoretical spectrum fit to the *Planck* TT,TE,EE+lowE+lensing likelihood is plotted in light blue in the upper panels. Residuals with respect to this model are shown in the lower panels. The error bars show Gaussian $\pm 1\sigma$ diagonal uncertainties including cosmic variance. Note that the vertical scale changes at $\ell = 30$, where the horizontal axis switches from logarithmic to linear.

a TT,TE,EE likelihood. The polarization masks used in CamSpec are based on 353–143 GHz polarization maps that are degraded in resolution and thresholded on $P = (Q^2 + U^2)^{1/2}$. The default CamSpec polarization mask used for the 2018 analysis preserves a fraction $f_{\text{sky}} = 57.7\%$ and is apodized to give an effective sky fraction (see equation 10 of PCP15) of $f_{\text{sky}}^{\text{W}} = 47.7\%$. We use the same polarization mask for all frequencies. The CamSpec polarization masks differ from those used in the Plik likelihood, which uses intensity-thresholded masks in polarization (and therefore a larger effective sky area in polarization, as described in the previous section).

To construct covariance matrices, temperature-to-polarization leakage corrections, and effective polarization efficiencies, we need to adopt a fiducial model. For the 2018 analysis, we adopted the best-fit CamSpec base- Λ CDM model from PCP15 to construct a likelihood from the 2018 temperature maps. We then ran a minimizer on the TT likelihood, imposing a prior of $\tau = 0.05 \pm 0.02$, and the best-fit base- Λ CDM cosmology was adopted as our fiducial model. To deal with temperature-to-polarization leakage, we used the QuickPol polarized beam matrices to compute corrections to the TE and EE spectra assuming the fiducial model. The temperature-to-polarization leakage corrections are relatively small for TE spectra (although they have some impact on cosmological parameters, consistent with the behaviour of the Plik likelihood described in the previous section), but are negligible for EE spectra.

To correct for effective polarization efficiencies (including large-scale transfer functions arising from errors in the polarized beams) we recalibrated each TE , ET , and EE spectrum against the fiducial model spectra by minimizing

$$\chi^2 = \sum_{\ell_1 \ell_2} (C_{\ell_1}^{\text{D}} - \alpha_{\text{p}} C_{\ell_1}^{\text{Th}}) M_{\ell_1 \ell_2}^{-1} (C_{\ell_2}^{\text{D}} - \alpha_{\text{p}} C_{\ell_2}^{\text{Th}}), \quad (3)$$

with respect to α_{p} , where C_{ℓ}^{D} is the beam-corrected data spectrum (TE , ET , or EE) corrected for temperature-to-polarization leakage, M is the covariance matrix for the appropriate spectrum, and the sums extend over $200 \leq \ell \leq 1000$. We calibrate each TE and EE spectrum individually, rather than computing map-based polarization calibrations. Although there is a good correspondence between spectrum-based calibrations and map-based calibrations, we find evidence for some differences, particularly for the 143×143 EE spectrum in agreement with the Plik analysis. Unlike Plik, we adopt spectrum-based calibrations of polarization efficiencies in preference to map-based calibrations.

As in temperature, we apply multipole cuts to the polarization spectra prior to coaddition in order to reduce sensitivity to dust subtraction, beam estimation, and noise modelling. For TE/ET spectra we use: $\ell_{\text{min}} = 30$ and $\ell_{\text{max}} = 1200$ for the 100×100 , 100×143 and 100×217 spectra; $\ell_{\text{min}} = 30$ and $\ell_{\text{max}} = 2000$ for 143×143 and 143×217 ; and $\ell_{\text{min}} = 500$ and $\ell_{\text{max}} = 2500$ for the 217×217 cross-spectrum. For EE , we use: $\ell_{\text{min}} = 30$ and $\ell_{\text{max}} = 1000$ for 100×100 ; $\ell_{\text{min}} = 30$ and $\ell_{\text{max}} = 1200$ for 100×143 ; $\ell_{\text{min}} = 200$ and $\ell_{\text{max}} = 1200$ for 100×217 ; $\ell_{\text{min}} = 30$ and $\ell_{\text{max}} = 1500$ for 143×143 ; $\ell_{\text{min}} = 300$ and $\ell_{\text{max}} = 2000$ for 143×217 ; and $\ell_{\text{min}} = 500$ and $\ell_{\text{max}} = 2000$ for 217×217 . Since dust is subtracted from the polarization spectra, we do not include a dust model in the polarization covariance matrices. Note that at low multipoles, $\ell \lesssim 300$, Galactic dust dominates over the CMB signal in EE at all frequencies. We experimented with different polarization masks and different multipole cuts and found stable results from the CamSpec polarization likelihood.

To summarize, for the TT data Plik and CamSpec use very similar methodologies and a similar foreground model, and the power spectra used in the likelihoods only differ in the handling of missing pixels. As a result, there is close agreement between the two temperature likelihoods. In polarization, different polarization masks are applied and different methods are used for correcting Galactic dust, effective polarization calibrations, and temperature-to-polarization leakage. In addition, the polarization covariance matrices differ at low multipoles. As described in Appendix A, the two codes give similar results in polarization for base Λ CDM and most of the extensions of Λ CDM considered in this paper, and there would be no material change to most of the science conclusions in this paper were one to use the CamSpec likelihood in place of Plik. However, in cases where there are differences that could have an impact on the scientific interpretation (e.g., for A_{L} , $\sum m_{\nu}$, and Ω_{K}) we show results from both codes. This should give the reader an impression of the sensitivity of the science results to different methodologies and choices made in constructing the polarization blocks of the high-multipole likelihoods.

2.2.3. The low- ℓ likelihood

The HFI low- ℓ polarization likelihood is based on the full-mission HFI 100 GHz and 143 GHz Stokes Q and U low-resolution maps, cleaned through a template-fitting procedure using LFI 30 GHz (Planck Collaboration II 2020) and HFI 353 GHz maps⁹, which are used as tracers of polarized synchrotron and thermal dust, respectively (for details about the cleaning procedure see PPL18). Power spectra are calculated based on a quadratic maximum-likelihood estimation of the cross-spectrum between the 100- and 143 GHz data, and the multipole range used spans $\ell = 2$ to $\ell = 29$.

We only use the EE likelihood (“lowE”) for the main parameter results in this paper. The likelihood code, called SimAll, is based on the power spectra. It is constructed using an extension of the SimBaL algorithm presented in Planck Collaboration Int. XLVI (2016), using 300 end-to-end simulations characterizing the HFI noise and residual systematics (see Planck Collaboration III 2020, for details) to build an empirical probability distribution of the EE spectra (ignoring the off-diagonal correlations). The TE spectrum at low multipoles does not provide tight constraints compared to EE because of cosmic variance. However, PPL18 discusses the TE spectra at low multipoles constructed by cross-correlating the Commander component-separated map with the 100- and 143 GHz maps. The TE spectra show excess variance compared to simulations at low multipoles, most notably at $\ell = 5$ and at $\ell = 18$ and 19, for reasons that are not understood. No attempt has been made to fold in Commander component-separation errors in the statistical analysis. We have therefore excluded the TE spectrum at low multipoles (with the added benefit of simplifying the construction of the SimAll likelihood). Little information is lost by discarding the TE spectrum. Evidently, further work is required to understand the behaviour of TE at low

⁹ The polarized synchrotron component is fitted only at 100 GHz, being negligible at 143 GHz. For the polarized dust component, following the prescription contained in Planck Collaboration III (2020), the low- ℓ HFI polarization likelihood uses the 353 GHz polarization-sensitive-bolometer-only map.

multipoles; however, as discussed in PPL18, the τ constraint derived from TE to $\ell_{\max} = 10$ ($\tau = 0.051 \pm 0.015$) is consistent with results derived from the SimAll EE likelihood summarized below.

Using the SimAll likelihood combined with the low- ℓ temperature Commander likelihood (see Planck Collaboration IV 2020), varying $\ln(10^{10}A_s)$ and τ , but fixing other cosmological parameters to those of a fiducial base- Λ CDM model (with parameters very close to those of the baseline Λ CDM cosmology in this paper), PPL18 reports the optical depth measurement¹⁰

$$\tau = 0.0506 \pm 0.0086 \quad (68\%, \text{lowE}). \quad (4)$$

This is significantly tighter than the LFI-based constraint used in the 2015 release ($\tau = 0.067 \pm 0.022$), and differs by about half a sigma from the result of Planck Collaboration Int. XLVI (2016) ($\tau = 0.055 \pm 0.009$). The latter change is driven mainly by the removal of the last 1000 scanning rings in the 2018 SRoll maps, higher variance in the end-to-end simulations, and differences in the 30 GHz map used as a synchrotron tracer (see Appendix A of Planck Collaboration II 2020). The impact of the tighter optical depth measurement on cosmological parameters compared to the 2015 release is discussed in Sect. 3.6. The error model in the final likelihood does not fully include all modelling uncertainties and differences between likelihood codes, but the different approaches lead to estimates of τ that are consistent within their respective 1σ errors.

In addition to the default SimAll lowE likelihood used in this paper, the LFI polarization likelihood has also been updated for the 2018 release, as described in detail in PPL18. It gives consistent results to SimAll, but with larger errors ($\tau = 0.063 \pm 0.020$); we give a more detailed comparison of the various τ constraints in Sect. 7.8.

The low- ℓ temperature likelihood is based on maps from the Commander component-separation algorithm, as discussed in detail in Planck Collaboration IV (2020), with a Gibbs-sample-based Blackwell-Rao likelihood that accurately accounts for the non-Gaussian shape of the posterior at low multipoles, as in 2015. The CMB maps that are used differ in several ways from the 2015 analysis. Firstly, since the 2018 analysis does not produce individual bolometer maps (since it is optimized to reduce large-scale polarization systematics) the number of foreground components that can be constrained is reduced compared to 2015. The 2018 Commander analysis only fits the CMB, a single general low-frequency power-law component, thermal dust, and a single CO component with spatially constant line ratios between 100, 217, and 353 GHz. Secondly, the 2018 analysis is based only on *Planck* data and so does not include the WMAP and Haslam 408 MHz maps. Finally, in order to be conservative with respect to CO emission, the sky fraction has been reduced to 86% coverage, compared to 93% in 2015. The net effect is a small increase in errors, and the best-fit data points are correspondingly slightly more scattered compared to 2015. The

(arbitrary) normalization of the Commander likelihood was also changed, so that a theory power spectrum equal to the best-fit power spectrum points will, by definition, give $\chi_{\text{eff}}^2 = 0$.

2.2.4. Likelihood notation

Throughout this paper, we adopt the following labels for likelihoods: (i) *Planck* TT+lowE denotes the combination of the high- ℓ TT likelihood at multipoles $\ell \geq 30$, the low- ℓ temperature-only Commander likelihood, and the low- ℓ EE likelihood from SimAll; (ii) labels such as *Planck* TE+lowE denote the TE likelihood at $\ell \geq 30$ plus the low- ℓ EE SimAll likelihood; and (iii) *Planck* TT,TE,EE+lowE denotes the combination of the combined likelihood using TT , TE , and EE spectra at $\ell \geq 30$, the low- ℓ temperature Commander likelihood, and the low- ℓ SimAll EE likelihood. For brevity we sometimes drop the “*Planck*” qualifier where it should be clear, and unless otherwise stated high- ℓ results are based on the *Planck* likelihood. TE correlations at $\ell \leq 29$ are not included in any of the results presented in this paper.

2.2.5. Uncertainties on cosmological parameters

To maximize the accuracy of the results, various choices can be made in the construction of the high-multipole likelihoods. Examples of these are the sky area, noise models, multipole ranges, frequencies, foreground parameterization, and priors, as detailed for this release of *Planck* data in PPL18. The cosmological parameters and their uncertainties depend on these options. It is therefore necessary to test the sensitivity of the results with respect to such choices. In particular, when removing or adding independent information (e.g., by lifting or adding priors, or by measuring parameters from different multipole ranges), we *do expect* cosmological parameters to shift. The crucial question, however, is whether these are in agreement with statistical expectations. If they are consistent with being statistical excursions, then the noise model, along with foreground and instrumental nuisance parameters (e.g., polarization efficiencies), may be a consistent representation of the data. In this case, the uncertainties quoted in this paper should accurately describe the combined noise and sample variance due to finite data. Different choices of sky area, multipole range, etc., will produce changes in the parameters, but they will be adequately described by the quoted uncertainties. On the other hand, if the shifts *do not* agree with statistical expectations, they might be an indication of unmodelled systematic effects.

In PPL18 we discuss a series of tests indicating the overall robustness of our results. Internal to the *Planck* likelihood code, we consider the CMB spectra, errors, and resulting parameters as we vary the input data, ℓ range, sky area, etc. We also consider the effect of known sources of systematic uncertainty, such as high-frequency oscillations in the raw time-ordered data and temperature-to-polarization leakage. We further test the baseline likelihood using extensive simulations; these tests demonstrate the solidity of our results. As a specific example, when lifting all priors on nuisance parameters (such as calibration and foregrounds), the posterior mean on the number of relativistic species N_{eff} shifts upwards by about 1σ . We quantify in PPL18 that this is statistically not anomalous, since lifting priors reduces information and, as a consequence, error bars also increase.

Only in a small number of areas, do such tests show mild internal disagreements at the level of spectra and parameters.

¹⁰ The corresponding marginalized amplitude parameter is $\ln(10^{10}A_s) = 2.924 \pm 0.052$, which gives A_s about 10% lower than the value obtained from the joint fits in Sect. 3. The τ constraints quoted here are lower than the joint results, since the small-scale power has a preference for higher A_s (and hence higher τ for the well-measured $A_s e^{-2\tau}$ combination) at high multipoles, related to the preference for more lensing discussed in Sect. 6.

One example is the higher than expected χ^2 of the Plik TE frequency-likelihood, which can be traced back to a small mismatch between the different cross-frequency spectra. When we co-add the foreground-cleaned frequency TE spectra into one CMB spectrum (which is less sensitive to such a mismatch), the related χ^2 is in better agreement with expectations. A second example is the choice of polarization-efficiency corrections, which has a small impact on the final results and is further discussed below.

We have also compared the results from the Plik likelihood with those obtained with CamSpec in Sects. 2.2.1 and 2.2.2 and Appendix A, as well as in PPL18 (see also Efstathiou & Gratton 2019). Some of the likelihood choices (e.g., sky area and multipole range) will give different detailed results within the expected sample variance. Others, such as the models for noise (bias-corrected half-ring difference for Plik versus odd-even rings for CamSpec) and polarization efficiency, may give a hint of residual systematic uncertainties. If we restrict ourselves to temperature, the Plik and CamSpec likelihoods are in excellent accord, with most parameters agreeing to better than 0.5σ (0.2σ on the Λ CDM model). On the other hand, we find indications (discussed in more detail in PPL18) that the polarization efficiencies of the frequency-channel maps differ when measured in the TE or EE spectra, and the Plik and CamSpec likelihoods have explored different choices of polarization efficiency corrections. This and polarization-noise modelling may be responsible for differences in the details of the resulting polarization spectra and parameters.

For the base- Λ CDM model, the results from Plik and CamSpec for the TT,TE,EE likelihoods are in good agreement (see Table 1), again with most parameters agreeing to better than 0.5σ . We also find differences between the Plik and CamSpec TTTEEE likelihoods for some extended models, especially for the single-parameter extensions with A_L (at 0.7σ) and Ω_K (at 0.5σ); these differences are discussed in Sects. 6.2 and 7.3, respectively, where we show results for both likelihoods. For both A_L and Ω_K , the Plik TT,TE,EE likelihood pulls away from the base- Λ CDM model with a slightly higher significance than the CamSpec TT,TE,EE likelihood. The is due, at least in part, to the choice of how to model polarization efficiencies, as discussed in PPL18. For the Ω_K case, for example, the $\Delta\chi^2$ between the Λ CDM and Λ CDM+ Ω_K models for TT,TE,EE+lowE is $\Delta\chi^2 = 11$, of which $8.3 \Delta\chi$ points are due to the improvement of the Plik TT,TE,EE likelihood. Using spectrum-based polarization efficiencies, instead of map-based ones¹¹ reduces that total difference to $\Delta\chi^2 = 5.2$, of which $\Delta\chi^2 = 4.6$ is due to the Plik likelihood. This is in agreement with the $\Delta\chi^2$ value obtained for these models by CamSpec, which uses spectrum-based polarization efficiencies, with $\Delta\chi^2 = 4.3$.

Other details of choices in the likelihood functions impact the difference in parameters; however, these comprise both expected statistical fluctuations (due to differing raw data cuts and sky coverage) and possible residual systematic errors. For both extended models the Planck TTTEEE likelihoods are usually combined with other data to break parameter degeneracies. For these parameters, the addition of either Planck lensing or BAO data overwhelms any differences between the Plik and CamSpec likelihoods and so we find almost identical results.

¹¹ As explained in Sects. 2.2.1 and 2.2.2, the “map-based” approach applies the same polarization efficiency corrections estimated from EE to both the TE and EE spectra, while the “spectrum-based” approach applies independent estimates obtained from TE and EE to the TE and EE spectra, respectively.

In this paper we therefore do not explicitly model an increase in error bars due to these residual systematic errors – any such characterization would inevitably be incomplete, and it would also be impossible to give the necessary probabilistic characterization required for meaningful quantitative error bars. Instead our best-fit values, posterior means, errors and limits should (as always) be considered as conditional on the cosmological model and our best knowledge of the Planck instruments and astrophysical foregrounds, as captured by the baseline likelihoods.

2.3. The CMB lensing likelihood

The CMB photons that arrive here today traverse almost the entire observable Universe. Along the way their paths are deflected by gradients in the gravitational potentials associated with inhomogeneities in the Universe (Blanchard & Schneider 1987). The dominant effects (e.g., Lewis & Challinor 2006; Hanson et al. 2010) are a smoothing of the acoustic peaks, conversion of E-mode polarization to B-mode polarization, and generation of a connected 4-point function, each of which can be measured in high angular resolution, low-noise observations, such as those from Planck.

Planck was the first experiment to measure the lensing signal to sufficient precision for it to become important for the determination of cosmological parameters, providing sensitivity to parameters that affect the late-time expansion, geometry, and clustering (Planck Collaboration XVII 2014, hereafter PL2013). In Planck Collaboration XV (2016, hereafter PL2015) the Planck lensing reconstruction was improved by including polarization information. The Planck lensing measurement is still the most significant detection of CMB lensing to date. In this final data release we report a measurement of the power spectrum of the lensing potential, $C_L^{\phi\phi}$, from the 4-point function, with a precision of around 2.6% on the amplitude, as discussed in detail in PL2018. We demonstrate the robustness of the reconstruction to a variety of tests over lensing multipoles $8 \leq L \leq 400$, and conservatively restrict the likelihood to this range to reduce the impact of possible systematics. Compared to 2015, the multipole range is extended from $L_{\min} = 40$ down to $L_{\min} = 8$, with other analysis changes mostly introducing random fluctuations in the band powers, due to improvements in the noise modelling and the somewhat different mixture of frequencies being used in the foreground-cleaned SMICA maps (see Planck Collaboration IV 2020). The signal-to-noise per multipole is almost the same as in 2015, which, combined with the wider multipole range, makes the likelihood just slightly more powerful than in 2015. CMB lensing can provide complementary information to the Planck CMB power spectra, since it probes much lower redshifts, including $z \lesssim 2$, when dark energy becomes important. The lensing effect depends on the propagation of photons on null geodesics, and hence depends on the background geometry and Weyl potential (the combination of scalar metric perturbations that determines the Weyl spacetime curvature tensor; see e.g. Lewis & Challinor (2006)).

We approximate the lensing likelihood as Gaussian in the estimated band powers, making perturbative corrections for the small dependence of band powers on the cosmology, as described in PL2015. We neglect correlations between the 2- and 4-point functions, which are negligible at Planck sensitivity (Schmittfull et al. 2013; Peloton et al. 2017). As in PL2015, band powers at multipoles $L > 400$ are less robust than over $8 \leq L \leq 400$, with some evidence for a curl-test failure, and possibly also systematic differences between individual frequencies that we were unable to resolve. Multipoles at $L < 8$ are very

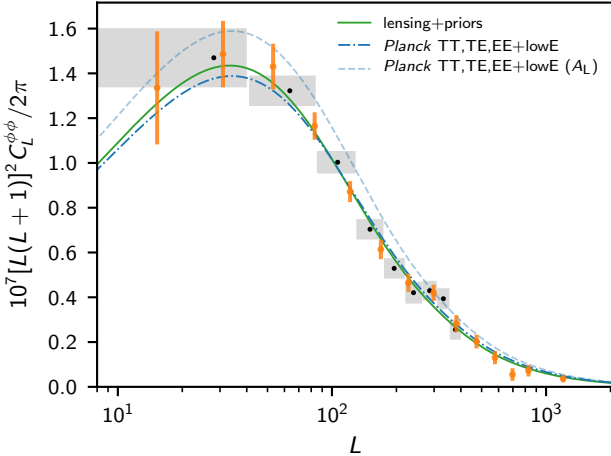


Fig. 3. CMB lensing-potential power spectrum, as measured by *Planck* (see PL2018 for a detailed description of this measurement). Orange points show the full range of scales reconstructed with a logarithmic binning, while grey bands show the error and multipole range of the conservative band powers used for the likelihood, with black points showing the average multipole of the band weight. The solid line shows the best Λ CDM fit to the conservative points alone, and the dot-dashed line shows the prediction from the best fit to the *Planck* CMB power spectra alone. The dashed line shows the prediction from the best fit to the CMB power spectra when the lensing amplitude A_L is also varied ($A_L = 1.19$ for the best-fit model; see Sect. 6.2 for a detailed discussion of A_L).

sensitive to the large mean-field correction on these scales, and hence are sensitive to the fidelity of the simulations used to estimate the mean field. As described above, our baseline cosmological results therefore conservatively use only the multipole range $8 \leq L \leq 400$.

The *Planck* measurements of $C_L^{\phi\phi}$ are plotted in Fig. 3, where they are compared to the predicted spectrum from the best-fitting base- Λ CDM model of Sect. 3, and Fig. 4 shows the corresponding broad redshift ranges that contribute to the lensing band powers in the Λ CDM model. Figure 3 shows that the lensing data are in excellent agreement with the predictions inferred from the CMB power spectra in the base- Λ CDM model ($\chi_{\text{eff}}^2 = 8.9$ for 9 binned conservative band-power measurements, $\chi_{\text{eff}}^2 = 14.0$ for 14 bins over the full multipole range; we discuss agreement in extensions to the Λ CDM model in more detail below). The lensing data prefer lensing power spectra that are slightly tilted towards less power on small scales compared to the best fit to the CMB power spectra. This small tilt pulls joint constraints a small fraction of an error bar towards parameters that give a lower lensing amplitude on small scales. Parameter results from the full multipole range would be a little tighter and largely consistent with the conservative band powers, although preferring slightly lower fluctuation amplitudes (see PL2018).

As described in detail in PL2018, the lensing likelihood (in combination with some weak priors) can alone provide Λ CDM parameter constraints that are competitive with current galaxy lensing and clustering, measuring

$$\sigma_8 \Omega_m^{0.25} = 0.589 \pm 0.020 \quad (68\%, \text{Planck lensing}). \quad (5)$$

Combined with BAO (see Sect. 5.1 below) and a baryon density prior to break the main degeneracy between H_0 , Ω_m , and σ_8 (described in PL2015), individual parameters H_0 , Ω_m , and σ_8 can also separately be constrained to a precision of a few per-

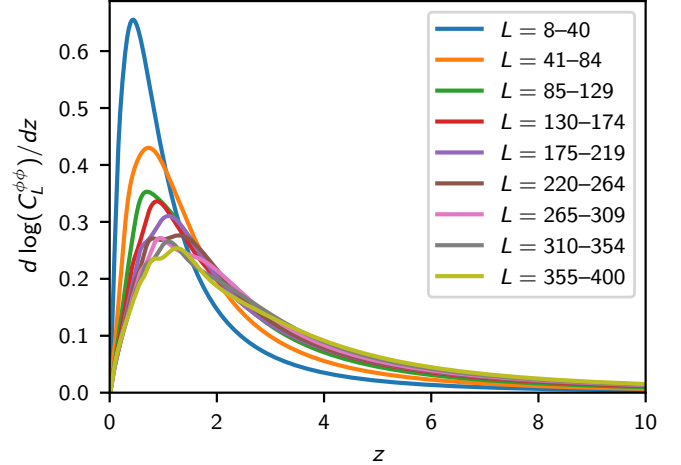


Fig. 4. Contributions to the conservative CMB lensing band powers (see text and Fig. 3) as a function of redshift in the base- Λ CDM model (evaluated here, and only here, using the Limber approximation (LoVerde & Afshordi 2008) on all scales). Multipole ranges of the corresponding band powers are shown in the legend.

cent. We use $\Omega_b h^2 = 0.0222 \pm 0.0005$ (motivated by the primordial deuterium abundance measurements of Cooke et al. 2018, see also Sect. 7.6), which gives

$$\left. \begin{aligned} H_0 &= 67.9_{-1.3}^{+1.2} \text{ km s}^{-1} \text{ Mpc}^{-1}, \\ \sigma_8 &= 0.811 \pm 0.019, \\ \Omega_m &= 0.303_{-0.018}^{+0.016}, \end{aligned} \right\} 68\%, \text{ lensing + BAO}. \quad (6)$$

The constraints of Eq. (5) and (6) are in very good agreement with the estimates derived from the *Planck* power spectra and are independent of how the *Planck* power spectra depend on the cosmological model at high multipoles. This is a strong test of the internal consistency of the *Planck* data. The *Planck* lensing constraints in Eqs. (5) and (6), and the consistency of these results with the *Planck* power spectrum likelihoods, should be borne in mind when comparing *Planck* results with other astrophysical data (e.g., direct measurements of H_0 and galaxy shear surveys, see Sect. 5).

In this paper, we focus on joint constraints with the main *Planck* power spectrum results, where the lensing power spectrum tightens measurements of the fluctuation amplitude and improves constraints on extended models, especially when allowing for spatial curvature.

A peculiar feature of the *Planck* TT likelihood, reported in PCP13 and PCP15, is the favouring of high values for the lensing consistency parameter A_L (at about 2.5σ). This result is discussed in detail in Sect. 6.2. It is clear from Fig. 3, however, that the *Planck* lensing likelihood prefers values of A_L close to unity and cosmological parameters that are close to those of the best-fit base- Λ CDM parameters derived from the *Planck* TT,TE,EE+lowE+lensing likelihood (i.e., without allowing A_L to vary).

3. Constraints on base Λ CDM

The *Planck* measurement of seven acoustic peaks in the CMB temperature power spectrum allows cosmological parameters to be constrained extremely accurately. In previous papers, we have focussed on parameters derived from the *TT* power spectrum.

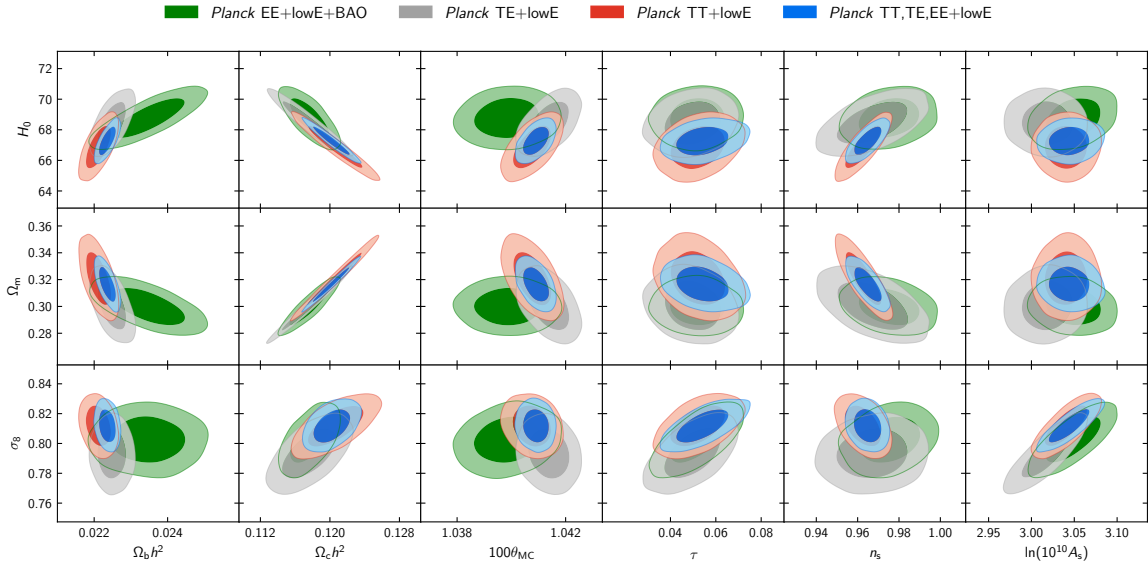


Fig. 5. Constraints on parameters of the base- Λ CDM model from the separate *Planck* EE, TE, and TT high- ℓ spectra combined with low- ℓ polarization (lowE), and, in the case of EE also with BAO (described in Sect. 5.1), compared to the joint result using *Planck* TT,TE,EE+lowE. Parameters on the bottom axis are our sampled MCMC parameters with flat priors, and parameters on the left axis are derived parameters (with H_0 in $\text{km s}^{-1} \text{Mpc}^{-1}$). Contours contain 68% and 95% of the probability.

The *TE* and *EE* polarization spectra provide a powerful consistency check on the underlying model and also help to break some partial parameter degeneracies. The goal of this section is to explore the consistency of cosmological parameters of the base- Λ CDM cosmology determined from *TT*, *TE*, and *EE* spectra and to present results from the combinations of these spectra, which are significantly more precise than those determined using *TT* alone.

Figure 5 shows 2-dimensional marginalized constraints on the six MCMC sampling parameters of the base- Λ CDM model used to explore the parameter posteriors, plotted against the following derived parameters: the Hubble constant H_0 , late-time clustering amplitude σ_8 and matter density parameter Ω_m (defined including a 0.06 eV mass neutrino). Table 1 gives individual parameter constraints using our baseline parameter combination *Planck* TT,TE,EE+lowE+lensing. These represent the legacy results on the cosmological Λ CDM parameters from the *Planck* satellite, and are currently the most precise measurements coming from a single CMB experiment. We give the best-fit values, as well as the marginalized posterior mean values, along with the corresponding 68% probability intervals. Table 1 also quantifies the small changes in parameters that are found when using the Plik and CamSpec high- ℓ polarization analyses described in Sect. 2.2 and Appendix A. Table 2 gives marginalized parameter constraints from the various CMB spectra, individually and without CMB lensing, including a wider variety of derived parameters of physical interest.

We now discuss in more detail the parameters that are most directly measured by the data and how these relate to constraints on individual parameters of more general interest.

3.1. Acoustic scale

The acoustic oscillations in ℓ seen in the CMB power spectra correspond to a sharply-defined acoustic angular scale on the sky, given by $\theta_* \equiv r_*/D_M$ where r_* is the comoving sound horizon at recombination quantifying the distance the photon-baryon perturbations can influence, and D_M is the comoving angular diam-

eter distance¹² that maps this distance into an angle on the sky. *Planck* measures

$$100\theta_* = 1.04097 \pm 0.00046 \quad (68\%, \textit{Planck} \text{ TT+lowE}), \quad (7)$$

corresponding to a precise 0.05% measurement of the angular scale $\theta_* = (0^\circ.59643 \pm 0^\circ.00026)$. The angular scales of the peaks in the polarization spectrum and cross-spectrum are different, since the polarization at recombination is sourced by quadrupolar flows in the photon fluid, which are out of phase with the density perturbations. The polarization spectra can, however, be used to measure the same acoustic scale parameter, giving a stringent test on the assumption of purely adiabatic perturbation driving the oscillations. From the polarization spectra we find

$$100\theta_* = 1.04156 \pm 0.00049 \quad (68\%, \textit{Planck} \text{ TE+lowE}), \quad (8a)$$

$$100\theta_* = 1.04001 \pm 0.00086 \quad (68\%, \textit{Planck} \text{ EE+lowE}), \quad (8b)$$

in excellent agreement with the temperature measurement. The constraint from *TE* is of similar precision to that from *TT*: although the polarization data are much noisier, the *TE* and *EE* spectra have more distinct acoustic peaks, which helps improve the signal-to-noise ratio of the acoustic scale measurement. Using the combined likelihood we find:

$$100\theta_* = 1.04109 \pm 0.00030 \quad (68\%, \text{TT,TE,EE+lowE}), \quad (9)$$

a measurement with 0.03% precision.¹³

Because of its simple geometrical interpretation, θ_* is measured very robustly and almost independently of the cosmological model (see Table 5). It is the CMB analogue of the transverse baryon acoustic oscillation scale r_{drag}/D_M measured from galaxy

¹² The quantity D_M is $(1+z)D_A$, where D_A is the usual angular diameter distance.

¹³ Doppler aberration due to the Earth's motion means that θ_* is expected to vary over the sky at the 10^{-3} level; however, averaged over the likelihood masks, the expected bias for *Planck* is below 0.1σ .

Table 2. Parameter 68% intervals for the base- Λ CDM model from *Planck* CMB power spectra, in combination with CMB lensing reconstruction and BAO.

Parameter	TT+lowE 68% limits	TE+lowE 68% limits	EE+lowE 68% limits	TT,TE,EE+lowE 68% limits	TT,TE,EE+lowE+lensing 68% limits	TT,TE,EE+lowE+lensing+BAO 68% limits
$\Omega_b h^2$	0.02212 ± 0.00022	0.02249 ± 0.00025	0.0240 ± 0.0012	0.02236 ± 0.00015	0.02237 ± 0.00015	0.02242 ± 0.00014
$\Omega_c h^2$	0.1206 ± 0.0021	0.1177 ± 0.0020	0.1158 ± 0.0046	0.1202 ± 0.0014	0.1200 ± 0.0012	0.11933 ± 0.00091
$100\theta_{MC}$	1.04077 ± 0.00047	1.04139 ± 0.00049	1.03999 ± 0.00089	1.04090 ± 0.00031	1.04092 ± 0.00031	1.04101 ± 0.00029
τ	0.0522 ± 0.0080	0.0496 ± 0.0085	0.0527 ± 0.0090	$0.0544^{+0.0070}_{-0.0081}$	0.0544 ± 0.0073	0.0561 ± 0.0071
$\ln(10^{10} A_s)$	3.040 ± 0.016	$3.018^{+0.020}_{-0.018}$	3.052 ± 0.022	3.045 ± 0.016	3.044 ± 0.014	3.047 ± 0.014
n_s	0.9626 ± 0.0057	0.967 ± 0.011	0.980 ± 0.015	0.9649 ± 0.0044	0.9649 ± 0.0042	0.9665 ± 0.0038
H_0 [km s ⁻¹ Mpc ⁻¹]	66.88 ± 0.92	68.44 ± 0.91	69.9 ± 2.7	67.27 ± 0.60	67.36 ± 0.54	67.66 ± 0.42
Ω_Λ	0.679 ± 0.013	0.699 ± 0.012	$0.711^{+0.033}_{-0.026}$	0.6834 ± 0.0084	0.6847 ± 0.0073	0.6889 ± 0.0056
Ω_m	0.321 ± 0.013	0.301 ± 0.012	$0.289^{+0.026}_{-0.033}$	0.3166 ± 0.0084	0.3153 ± 0.0073	0.3111 ± 0.0056
$\Omega_m h^2$	0.1434 ± 0.0020	0.1408 ± 0.0019	$0.1404^{+0.0034}_{-0.0039}$	0.1432 ± 0.0013	0.1430 ± 0.0011	0.14240 ± 0.00087
$\Omega_m h^3$	0.09589 ± 0.00046	0.09635 ± 0.00051	$0.0981^{+0.0016}_{-0.0018}$	0.09633 ± 0.00029	0.09633 ± 0.00030	0.09635 ± 0.00030
σ_8	0.8118 ± 0.0089	0.793 ± 0.011	0.796 ± 0.018	0.8120 ± 0.0073	0.8111 ± 0.0060	0.8102 ± 0.0060
$S_8 \equiv \sigma_8 (\Omega_m / 0.3)^{0.5}$	0.840 ± 0.024	0.794 ± 0.024	$0.781^{+0.052}_{-0.060}$	0.834 ± 0.016	0.832 ± 0.013	0.825 ± 0.011
$\sigma_8 \Omega_m^{0.25}$	0.611 ± 0.012	0.587 ± 0.012	0.583 ± 0.027	0.6090 ± 0.0081	0.6078 ± 0.0064	0.6051 ± 0.0058
z_{re}	7.50 ± 0.82	$7.11^{+0.91}_{-0.75}$	$7.10^{+0.87}_{-0.73}$	7.68 ± 0.79	7.67 ± 0.73	7.82 ± 0.71
$10^9 A_s$	2.092 ± 0.034	2.045 ± 0.041	2.116 ± 0.047	$2.101^{+0.031}_{-0.034}$	2.100 ± 0.030	2.105 ± 0.030
$10^9 A_s e^{-2\tau}$	1.884 ± 0.014	1.851 ± 0.018	1.904 ± 0.024	1.884 ± 0.012	1.883 ± 0.011	1.881 ± 0.010
Age [Gyr]	13.830 ± 0.037	13.761 ± 0.038	$13.64^{+0.16}_{-0.14}$	13.800 ± 0.024	13.797 ± 0.023	13.787 ± 0.020
z_e	1090.30 ± 0.41	1089.57 ± 0.42	$1087.8^{+1.6}_{-1.7}$	1089.95 ± 0.27	1089.92 ± 0.25	1089.80 ± 0.21
r_s [Mpc]	144.46 ± 0.48	144.95 ± 0.48	144.29 ± 0.64	144.39 ± 0.30	144.43 ± 0.26	144.57 ± 0.22
$100\theta_*$	1.04097 ± 0.00046	1.04156 ± 0.00049	1.04001 ± 0.00086	1.04109 ± 0.00030	1.04110 ± 0.00031	1.04119 ± 0.00029
z_{drag}	1059.39 ± 0.46	1060.03 ± 0.54	1063.2 ± 2.4	1059.93 ± 0.30	1059.94 ± 0.30	1060.01 ± 0.29
r_{drag} [Mpc]	147.21 ± 0.48	147.59 ± 0.49	146.46 ± 0.70	147.05 ± 0.30	147.09 ± 0.26	147.21 ± 0.23
k_D [Mpc ⁻¹]	0.14054 ± 0.00052	0.14043 ± 0.00057	0.1426 ± 0.0012	0.14090 ± 0.00032	0.14087 ± 0.00030	0.14078 ± 0.00028
z_{eq}	3411 ± 48	3349 ± 46	3340^{+81}_{-92}	3407 ± 31	3402 ± 26	3387 ± 21
k_{eq} [Mpc ⁻¹]	0.01041 ± 0.00014	0.01022 ± 0.00014	$0.01019^{+0.00025}_{-0.00028}$	0.010398 ± 0.000094	0.010384 ± 0.000081	0.010339 ± 0.000063
$100\theta_{s,eq}$	0.4483 ± 0.0046	0.4547 ± 0.0045	0.4562 ± 0.0092	0.4490 ± 0.0030	0.4494 ± 0.0026	0.4509 ± 0.0020
f_{2000}^{143}	31.2 ± 3.0			29.5 ± 2.7	29.6 ± 2.8	29.4 ± 2.7
$f_{2000}^{143 \times 217}$	33.6 ± 2.0			32.2 ± 1.9	32.3 ± 1.9	32.1 ± 1.9
f_{2000}^{217}	108.2 ± 1.9			107.0 ± 1.8	107.1 ± 1.8	106.9 ± 1.8

Notes. The top group of six rows are the base parameters, which are sampled in the MCMC analysis with flat priors. The middle group lists derived parameters. The bottom three rows show the temperature foreground amplitudes $f_{\ell=2000}^{TT}$ for the corresponding frequency spectra (expressed as the contribution to $D_{\ell=2000}^{TT}$ in units of $(\mu\text{K})^2$). In all cases the helium mass fraction used is predicted by BBN (posterior mean $Y_p \approx 0.2454$, with theoretical uncertainties in the BBN predictions dominating over the *Planck* error on $\Omega_b h^2$). The reionization redshift mid-point z_{re} and optical depth τ here assumes a simple tanh model (as discussed in the text) for the reionization of hydrogen and simultaneous first reionization of helium. Our baseline results are based on *Planck* TT,TE,EE+lowE+lensing (as also given in Table 1).

surveys, where r_{drag} is the comoving sound horizon at the end of the baryonic-drag epoch (see Sect. 5.1). In Λ CDM, the CMB constraint can be expressed as a tight 0.04%-precision relation between $r_{drag} h$ and Ω_m as

$$\left(\frac{r_{drag} h}{\text{Mpc}}\right) \left(\frac{\Omega_m}{0.3}\right)^{0.4} = 101.056 \pm 0.036 \quad (68\%, \text{TT,TE,EE} + \text{lowE}). \quad (10)$$

The sound horizon r_{drag} depends primarily on the matter, baryon, and radiation densities, which for fixed observed CMB temperature today¹⁴, gives a 0.05% constraint on the combination

$$\Omega_m^{0.3} h (\Omega_b h^2)^{-0.16} = 0.87498 \pm 0.00052 \quad (68\%, \text{TT,TE,EE} + \text{lowE}). \quad (11)$$

Marginalizing out the dependence on the baryon density, the remaining degeneracy between the matter density and Hubble parameters is well approximated by a constraint on the parameter combination $\Omega_m h^3$ (Percival et al. 2002). We find a 0.3% constraint from *Planck*:

$$\Omega_m h^3 = 0.09633 \pm 0.00029 \quad (68\%, \text{TT,TE,EE} + \text{lowE}), \quad (12)$$

corresponding to an anti-correlation between the matter density $\Omega_m h^2$ and the Hubble parameter. This correlation can also be seen in Fig. 5 as an anti-correlation between the dark-matter density $\Omega_c h^2$ and H_0 , and a corresponding positive correlation between $\Omega_c h^2$ and Ω_m .

3.2. Hubble constant and dark-energy density

The degeneracy between Ω_m and H_0 is not exact, but the constraint on these parameters individually is substantially less precise than Eq. (12), giving

$$\left. \begin{aligned} H_0 &= (67.27 \pm 0.60) \text{ km s}^{-1} \text{ Mpc}^{-1}, \\ \Omega_m &= 0.3166 \pm 0.0084, \end{aligned} \right\} (68\%, \text{TT,TE,EE} + \text{lowE}). \quad (13)$$

It is important to emphasize that the values given in Eq. (13) assume the base- Λ CDM cosmology with minimal neutrino mass. These estimates are highly model dependent and this needs to be borne in mind when comparing with other measurements, for example the direct measurements of H_0 discussed in Sect. 5.4. The values in Eq. (13) are in very good agreement with

¹⁴ We take $T_0 = 2.7255\text{K}$ (Fixsen 2009), with the $\pm 0.0006\text{K}$ error having negligible impact on results.

the independent constraints of Eq. (6) from *Planck* CMB lensing+BAO. Including CMB lensing sharpens the determination of H_0 to a 0.8% constraint:

$$H_0 = (67.36 \pm 0.54) \text{ km s}^{-1} \text{ Mpc}^{-1} \quad (68\%, \text{ TT, TE, EE} + \text{lowE+lensing}). \quad (14)$$

This value is our “best estimate” of H_0 from *Planck*, assuming the base- Λ CDM cosmology.

Since we are considering a flat universe in this section, a constraint on Ω_m translates directly into a constraint on the dark-energy density parameter, giving

$$\Omega_\Lambda = 0.6847 \pm 0.0073 \quad (68\%, \text{ TT, TE, EE} + \text{lowE+lensing}). \quad (15)$$

In terms of a physical density, this corresponds to $\Omega_\Lambda h^2 = 0.3107 \pm 0.0082$, or cosmological constant $\Lambda = (4.24 \pm 0.11) \times 10^{-66} \text{ eV}^2 = (2.846 \pm 0.076) \times 10^{-122} m_{\text{Pl}}^2$ in natural units (where m_{Pl} is the Planck mass).

3.3. Optical depth and the fluctuation amplitude

Since the CMB fluctuations are linear up to lensing corrections, and the lensing corrections are largely oscillatory, the average observed CMB power spectrum amplitude scales nearly proportionally with the primordial comoving curvature power spectrum amplitude A_s (which we define at the pivot scale $k_0 = 0.05 \text{ Mpc}^{-1}$). The sub-horizon CMB anisotropies are however scattered by free electrons that are present after reionization, so the observed amplitude actually scales with $A_s e^{-2\tau}$, where τ is the reionization optical depth (see Sect. 7.8 for further discussion of reionization constraints). This parameter combination is therefore well measured, with the 0.6% constraint

$$A_s e^{-2\tau} = (1.884 \pm 0.012) \times 10^{-9} \quad (68\%, \text{ TT, TE, EE} + \text{lowE}). \quad (16)$$

In this final *Planck* release the optical depth is well constrained by the large-scale polarization measurements from the *Planck* HFI, with the joint constraint

$$\tau = 0.0544_{-0.0081}^{+0.0070} \quad (68\%, \text{ TT, TE, EE+lowE}). \quad (17)$$

Assuming simple tanh parameterization of the ionization fraction¹⁵, this implies a mid-point redshift of reionization

$$z_{\text{re}} = 7.68 \pm 0.79 \quad (68\%, \text{ TT, TE, EE+lowE}), \quad (18)$$

and a one-tail upper limit of $z_{\text{re}} < 9.0$ (95%). This is consistent with observations of high-redshift quasars that suggest the Universe was fully reionized by $z \approx 6$ (Bouwens et al. 2015). We do not include the astrophysical constraint that $z_{\text{re}} \gtrsim 6.5$ in our default parameter results, but if required results including this prior are part of the published tables on the PLA. A more detailed

¹⁵ For reference, the ionization fraction $x_e = n_e/n_{\text{H}}$ in the tanh model is assumed to have the redshift dependence (Lewis 2008):

$$x_e = \frac{1 + n_{\text{He}}/n_{\text{H}}}{2} \left[1 + \tanh \left(\frac{y(z_{\text{re}}) - y(z)}{\Delta y} \right) \right],$$

where $y(z) = (1+z)^{3/2}$, $\Delta y = \frac{3}{2}(1+z_{\text{re}})^{1/2}\Delta z$, with $\Delta z = 0.5$. Helium is assumed to be singly ionized with hydrogen at $z \gg 3$, but at lower redshifts we add the very small contribution from the second reionization of helium with a similar tanh transition at $z = 3.5$.

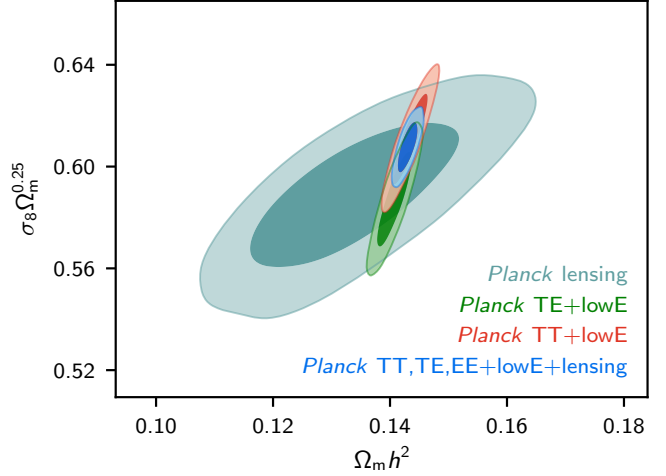


Fig. 6. Base- Λ CDM 68% and 95% marginalized constraint contours for the matter density and $\sigma_8 \Omega_m^{0.25}$, a fluctuation amplitude parameter that is well constrained by the CMB-lensing likelihood. The *Planck* TE, TT, and lensing likelihoods all overlap in a consistent region of parameter space, with the combined likelihood substantially reducing the allowed parameter space.

discussion of reionization histories consistent with *Planck* and results from other *Planck* likelihoods is deferred to Sect. 7.8.

The measurement of the optical depth breaks the $A_s e^{-2\tau}$ degeneracy, giving a 1.5% measurement of the primordial amplitude:

$$A_s = (2.101_{-0.034}^{+0.031}) \times 10^{-9} \quad (68\%, \text{ TT, TE, EE+lowE}). \quad (19)$$

Since the optical depth is reasonably well constrained, degeneracies with other cosmological parameters contribute to the error in Eq. (19). From the temperature spectrum alone there is a significant degeneracy between $A_s e^{-2\tau}$ and $\Omega_m h^2$, since for fixed θ_* , larger values of these parameters will increase and decrease the small-scale power, respectively. This behaviour is mitigated in our joint constraint with polarization because the polarization spectra have a different dependence on $\Omega_m h^2$; polarization is generated by causal sub-horizon quadrupole scattering at recombination, but the temperature spectrum has multiple sources and is also sensitive to non-local redshifting effects as the photons leave the last-scattering surface (see, e.g., Galli et al. 2014, for further discussion).

Assuming the Λ CDM model, the *Planck* CMB parameter amplitude constraint can be converted into a fluctuation amplitude at the present day, conventionally quantified by the σ_8 parameter. The CMB lensing reconstruction power spectrum also constrains the late-time fluctuation amplitude more directly, in combination with the matter density. Figure 6 shows constraints on the matter density and amplitude parameter combination $\sigma_8 \Omega_m^{0.25}$ that is well measured by the CMB lensing spectrum (see PL2015 for details). There is good consistency between the temperature, polarization, and lensing constraints here, and using their combination significantly reduces the allowed parameter space. In terms of the late-time fluctuation amplitude parameter σ_8 we find the combined result

$$\sigma_8 = 0.8111 \pm 0.0060 \quad (68\%, \text{ Planck TT, TE, EE+lowE} + \text{lensing}). \quad (20)$$

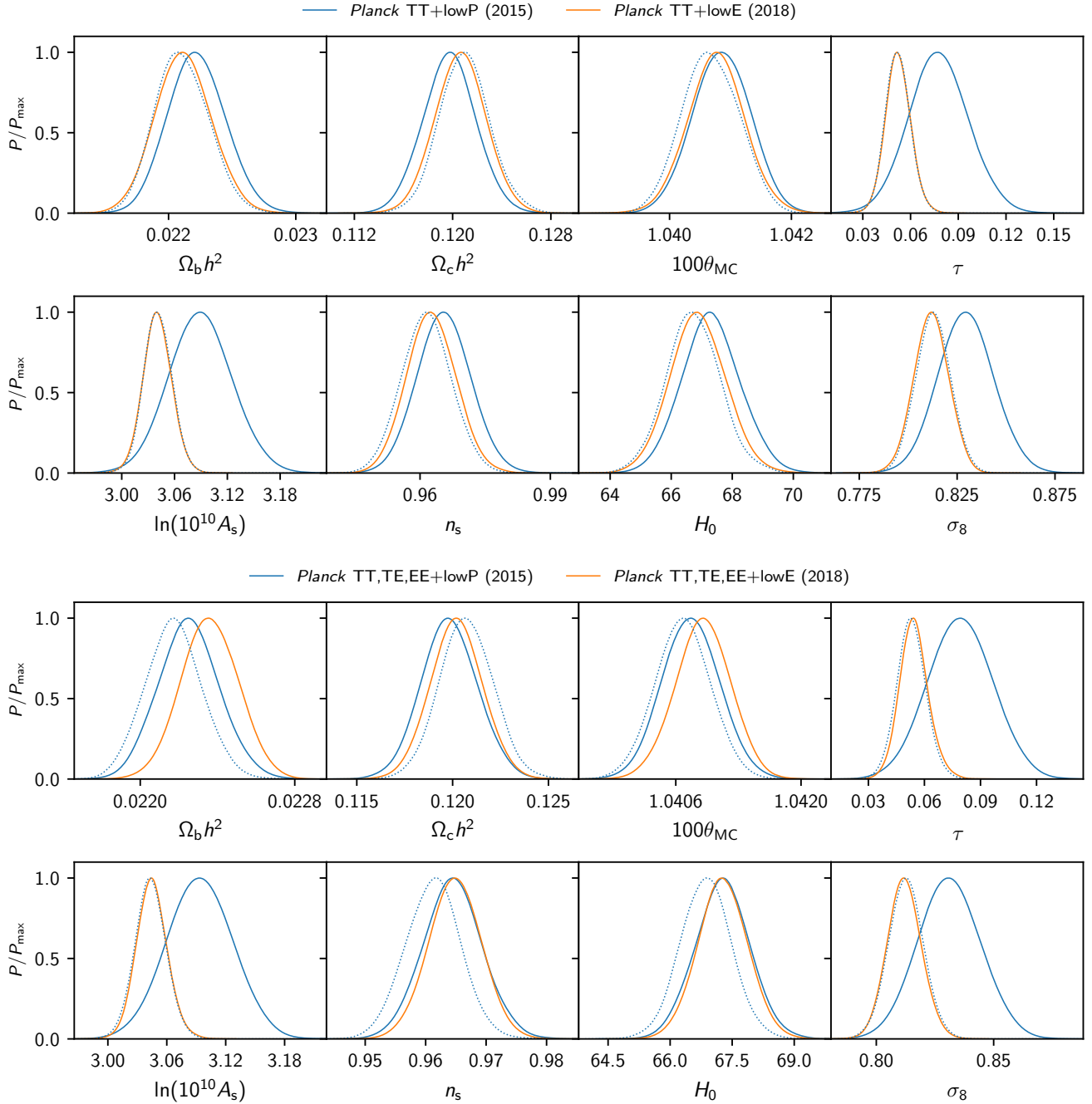


Fig. 7. Comparison between the 2015 and 2018 marginalized Λ CDM parameters. Dotted lines show the 2015 results, replacing the 2015 “lowP” low- ℓ polarization likelihood with the new 2018 “lowE” SimA11 likelihood, isolating the impact of the change in the low- ℓ polarization likelihood (and hence the constraints on τ).

Measurements of galaxy clustering, galaxy lensing, and clusters can also measure σ_8 , and we discuss consistency of these constraints within the Λ CDM model in more detail in Sect. 5.

3.4. Scalar spectral index

The scale-dependence of the CMB power spectrum constrains the slope of the primordial scalar power spectrum, conventionally parameterized by the power-law index n_s , where $n_s = 1$ corresponds to a scale-invariant spectrum. The matter and baryon densities also affect the scale-dependence of the CMB spectra, but in a way that differs from a variation in n_s , leading to

relatively mild degeneracies between these parameters. Assuming that the primordial power spectrum is an exact power law we find

$$n_s = 0.9649 \pm 0.0042 \quad (68\%, \text{Planck TT,TE,EE+lowE+lensing}), \quad (21)$$

which is 8σ away from scale-invariance ($n_s = 1$), confirming the red tilt of the spectrum at high significance in Λ CDM. Section 7.2 and Planck Collaboration X (2020) discuss the implications of this result for models of inflation and include constraints on models with primordial tensor modes and a scale-dependent scalar spectral index.

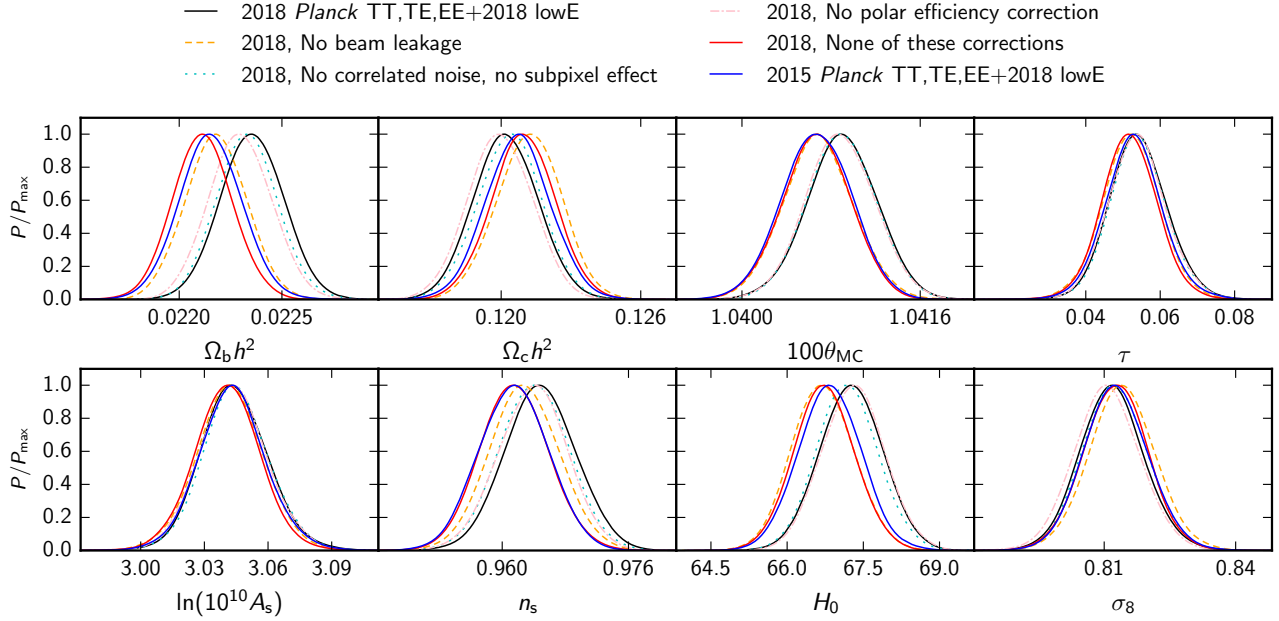


Fig. 8. Impact of corrections for systematic effects on 2018 marginalized Λ CDM parameters from *Planck* TT,TE,EE+lowE. The plot shows the baseline results (black solid line), and the baseline result excluding corrections for various effects: beam leakage (dashed orange); polarization efficiencies (dot-dashed pink); and subpixel effects and correlated noise (dotted cyan). The impact of not including any of these corrections is shown in solid blue, and agree fairly well with the 2015 results if the 2015 low- ℓ polarization likelihood is replaced with 2018 lowE likelihood (2015 *Planck* TT,TE,EE+2018 lowE). This shows that corrections for polarization systematics account for most of the small changes between the 2015 and 2018 results that are not caused by the change in optical depth.

3.5. Matter densities

The matter density can be measured from the CMB spectra using the scale-dependence of the amplitude, since for fixed θ_* a larger matter density reduces the small-scale CMB power. The matter density also affects the amount of lensing in the CMB spectra and the amplitude of the CMB-lensing reconstruction spectrum. The matter density is well constrained to be

$$\Omega_m h^2 = 0.1430 \pm 0.0011 \quad (68\%, \text{Planck TT,TE,EE+lowE+lensing}). \quad (22)$$

The matter mostly consists of cold dark matter, with density constrained at the percent level:

$$\Omega_c h^2 = 0.1200 \pm 0.0012 \quad (68\%, \text{Planck TT,TE,EE+lowE+lensing}). \quad (23)$$

Changes in the baryon density affect the spectrum in characteristic ways, modifying the relative heights of the even and odd acoustic peaks, due to the effect of baryons on the depth of first and subsequent acoustic (de)compressions. Despite comprising less than a sixth of the total matter content, the baryon effects on the power spectra are sufficiently distinctive that the baryon-density parameter is measured at sub-percent level accuracy with *Planck*:

$$\Omega_b h^2 = 0.02237 \pm 0.00015 \quad (68\%, \text{Planck TT,TE,EE+lowE+lensing}). \quad (24)$$

There is a partial degeneracy with n_s , which can also affect the relative heights of the first few peaks. This is most evident in *TE*, but is reduced in *TT* because of the larger range of scales that are measured by *Planck* with low noise.

3.6. Changes in the base- Λ CDM parameters between the 2015 and 2018 data releases

Figure 7 compares the parameters of the base- Λ CDM model measured from the final data release with those reported in PCP15. To differentiate between changes caused by the new lowE polarization likelihood, and therefore generated by the change in the measured optical depth to reionization, we also show the result of using the 2015 likelihoods in combination with the 2018 lowE polarization likelihood at low multipoles. Figure 7 includes the results for both *Planck* TT+lowE and *Planck* TT,TE,EE+lowE¹⁶

The main differences in Λ CDM parameters between the 2015 and the 2018 releases are caused by the following effects.

- New polarization low- ℓ likelihood. The use of the new HFI low- ℓ polarization likelihood in place of the 2015 LFI likelihood is the largest cause of shifts between the 2015 and 2018 parameters. The lowering and tightening of the constraint on τ is responsible for a 1σ decrease of $\ln(10^{10}A_s)$ through the $A_s e^{-2\tau}$ degeneracy. This in turn decreases the smoothing due to gravitational lensing at high multipoles, which is compensated by an increase of about 1σ in ω_c . This decreases the amplitude of the first acoustic peak, so n_s shifts to a lower value by about 0.5σ to restore power. Further adjustments are then achieved by the changes of θ_* and ω_b by about 0.5σ .
- Polarization corrections in the high- ℓ likelihood. As described in detail in Sect. 2.2, the largest changes from 2015 are caused by corrections applied to the polarization spectra. To isolate the causes of shifts introduced by changes in the high- ℓ likelihood, Fig. 8 compares 2018 results neglecting

¹⁶ The published 2015 parameter constraints and chains had a small error in the priors for the polarization Galactic foregrounds, which was subsequently corrected in the published likelihoods. The impact on cosmological parameters was very small. Here we compare with the uncorrected 2015 chains, not the published 2015 likelihood.

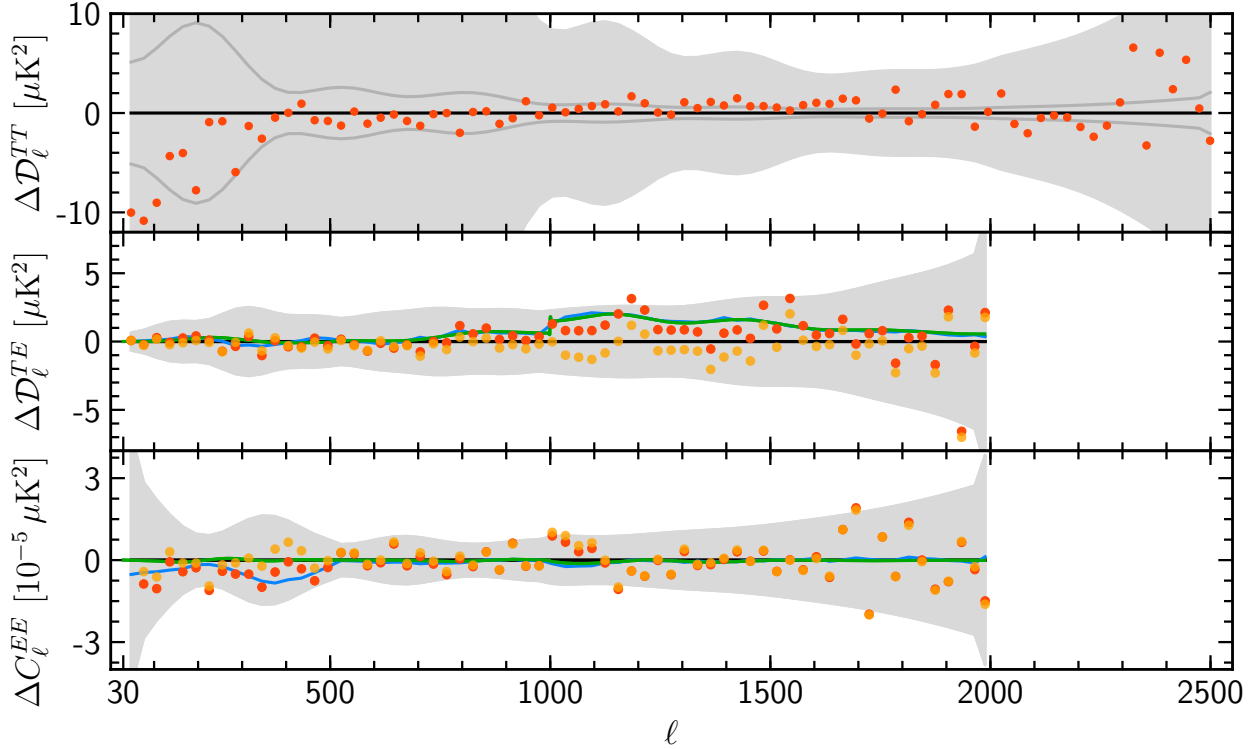


Fig. 9. Differences between the 2018 and 2015 coadded power spectra at high ℓ in TT , TE , and EE from top to bottom (red points). The 2015 TT spectrum has been recalibrated by a factor of 1.00014. For TE and EE , the orange points show the same differences but without applying the polar-efficiency and beam-leakage corrections to the 2018 spectra. This shows that the differences between the two data releases in polarization are caused mainly by these two effects. Finally, the green line shows the coadded beam-leakage correction, while the blue line shows the sum of the beam-leakage and polar-efficiency corrections. The grey band shows the $\pm 1\sigma$ errors of the 2018 power spectra (for TT , the grey line also shows error bars scaled down by a factor of 10).

corrections to the polarization spectra with results from the 2015 high- ℓ likelihood combined with the 2018 low- ℓ likelihood (so that both sets of results are based on similar constraints on τ). The shift towards larger values in ω_b by around 1σ is mainly caused by the beam-leakage correction in the TE high- ℓ likelihood, which is also responsible for an increase of approximately 0.5σ in n_s , compensating for the shift in n_s as a result of the change in τ since 2015. The beam-leakage correction also changes ω_c (by -0.7σ) and θ_{MC} ($+0.7\sigma$). The other corrections implemented in 2018 have a smaller impact on the Λ CDM parameters, as described in detail in [Planck Collaboration V \(2020\)](#).

Figure 9 presents the differences between the coadded spectra from 2018 and 2015. This plot shows the stability of the TT spectra, while also demonstrating that the main differences in polarization between the 2015 and 2018 releases are caused by the 2018 corrections for polarization efficiencies and beam leakage.

4. Comparison with high-resolution experiments

As discussed in [PCP13](#) and [PCP15](#), *Planck* TT spectra are statistically much more powerful than temperature data from current high-resolution experiments such as the Atacama Cosmology Telescope (ACT, e.g., [Das et al. 2014](#)) and the South Pole Telescope (SPT, e.g., [Story et al. 2013](#); [George et al. 2015](#)). As a result, the *Planck* temperature data dominate if they are combined with ACT and SPT data. In [PCP15](#), the high-resolution temperature data were used only to constrain low-amplitude components of the foreground model, which are

otherwise weakly constrained by *Planck* data alone (with very little impact on cosmological parameters). We adopt the same approach in this paper.

Since the publication of [PCP15](#), [Hou et al. \(2018\)](#) have performed a direct map-based comparison of the SPT temperature data at 150 GHz with the *Planck* 143 GHz maps over the same area of sky (covering 2540 deg²), finding no evidence for any systematic error in either data set after accounting for an overall difference in calibration. Temperature power spectrum comparisons between *Planck* and SPT are reported in a companion paper by [Aylor et al. \(2017\)](#). They find cosmological parameters for base Λ CDM derived from *Planck* and SPT over the same patch of sky and multipole range to be in excellent agreement. In particular, by comparing parameters determined over the multipole range 650–2000 from both experiments, the reduction in sample variance allows a test that is sensitive to systematic errors that could cause shifts in parameter posteriors comparable to the widths of the [PCP15](#) posteriors. The parameters determined over the SPT sky area differ slightly, but not significantly, from the best-fit Λ CDM parameters reported in [PCP15](#) based on a much larger area of sky. [Aylor et al. \(2017\)](#) also find a tendency for the base- Λ CDM parameters derived from SPT to shift as the multipole range is increased, but at low statistical significance.

Polarization measurements have become a major focus for ground-based CMB experiments. High resolution TE and EE spectra have been measured by the ACT Polarimeter (ACTPol) and the polarization-sensitive receiver of SPT (SPTpol). Following two seasons of observations, ACTPol has covered 548 deg² along the celestial equator at 149 GHz with data and analysis presented in [Naess et al. \(2014\)](#) and [Louis et al. \(2017\)](#). The

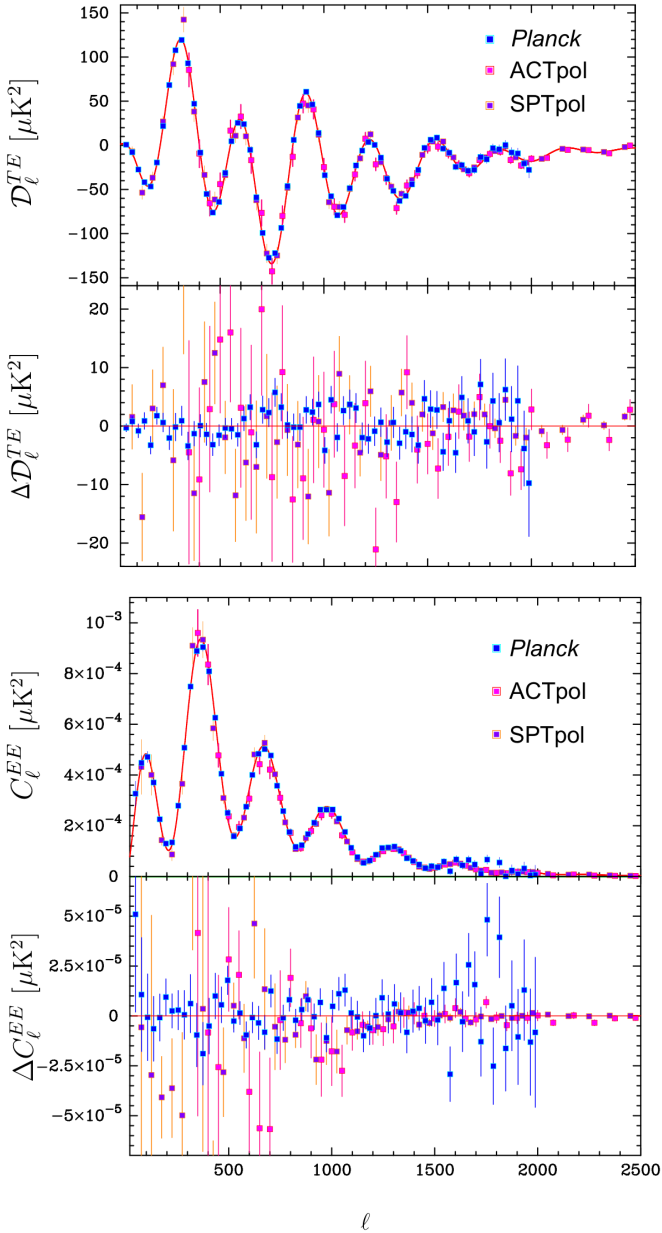


Fig. 10. Comparison of the *Planck* P1k, ACTPol, and SPTpol *TE* and *EE* power spectra. The solid lines show the best-fit base- Λ CDM model for *Planck* TT,TE,EE+lowE+lensing. The lower panel in each pair of plots shows the residuals relative to this theoretical model. The ACTPol and SPTpol *TE* and *EE* spectra are as given in [Louis et al. \(2017\)](#) and [Henning et al. \(2018\)](#), i.e., without adjusting nuisance parameters to fit the *Planck* theoretical model. The error bars show $\pm 1\sigma$ uncertainties.

ACTPol spectra span the multipole range $350 < \ell < 9000$. SPTpol polarization spectra from 100 deg^2 in the southern hemisphere at 150 GHz were first reported in [Crites et al. \(2015\)](#) and recently extended to 500 deg^2 ([Henning et al. 2018](#)). The SPTpol spectra span the multipole range $50 < \ell < 8000$. In contrast, the *Planck* *TE* and *EE* power spectra lose statistical power at multipoles ≥ 1500 . The ACTPol and SPTpol spectra are compared with the *Planck* *TE* and *EE* spectra in Fig. 10. The polarization spectra measured from these three very different experiments are in excellent agreement.

For the base- Λ CDM cosmology, the cosmological parameters should have converged close to their true values by multipoles ~ 2000 . Since ACTPol and SPTpol cover a much smaller

sky area than *Planck* the errors on their *TE* and *EE* spectra are larger than those of *Planck* at low multipoles (see Fig. 10). As a consequence, the current ACTPol and SPTpol polarization constraints on the parameters of the base- Λ CDM cosmology are much weaker than those derived from *Planck*. The ACTPol results ([Louis et al. 2017](#)) are consistent with the *Planck* base- Λ CDM parameters and showed a small improvement in constraints on extensions to the base cosmology that affect the damping tail. Similar results were found by SPTpol, though [Henning et al. \(2018\)](#) noted a $\geq 2\sigma$ tension with the base- Λ CDM model and found a trend for the parameters of the base- Λ CDM model to drift away from the *Planck* solution as the SPTpol likelihood is extended to higher multipoles. To assess these results we have performed some tests of the consistency of the latest *Planck* results and the SPTpol spectra.

As a reference model for SPTpol we adopt the base- Λ CDM parameters for the combined *TE* + *EE* fit to the SPTpol data from Table 5 of [Henning et al. \(2018\)](#). It is worth noting that the best-fit SPTpol cosmology is strongly excluded by the *Planck* *TT* spectra and by the *Planck* *TE* + *EE* spectra. We use the *Planck* TT,TE,EE+lowE+lensing base- Λ CDM best-fit cosmology (as plotted in Fig. 10) as a reference model for *Planck*. For each model, we ran the public version of the SPTpol likelihood code¹⁷ sampling the nuisance parameters using the same priors as in [Henning et al. \(2018\)](#). The best-fit values of χ^2 are listed in Table 3. As in [Henning et al. \(2018\)](#), in assigning significance levels to these values, we take the number of degrees of freedom to be equal to the number of band powers minus eight, corresponding to five cosmological parameters (ω_b , ω_c , θ_{MC} , n_s , $A_s e^{-2\tau}$) and three nuisance parameters with flat priors.

As found by [Henning et al. \(2018\)](#), the SPTpol *TE* spectrum gives nearly identical values of χ^2 for both the SPTpol and *Planck* cosmologies and so does not differentiate between them; however, the χ^2 values are high, at the 2.3σ level. The SPTpol *EE* spectrum provides weaker constraints on cosmological parameters than the *TE* spectrum and is clearly better fit by the SPTpol cosmology. If the SPTpol covariance matrix is accurate, the combined TE+EE SPTpol data disfavour the *Planck* Λ CDM cosmology quite strongly and disfavour any 6-parameter Λ CDM cosmology. For Λ CDM models, outliers distributed over a wide range of multipoles contribute to the high χ^2 values, notably at $\ell = 124, 324, 1874, 2449$, and 3249 in *TE*, and $\ell = 1974$ and 6499 in *EE*.

We can assess consistency of the parameter differences, $\Delta\mathbf{p}$, between the two experiments by computing,

$$\chi_p^2 = \Delta\mathbf{p}^T C_p^{-1} \Delta\mathbf{p}, \quad (25)$$

where C_p is the covariance matrix for SPTpol parameters (we neglect the errors in the *Planck* parameters, which are much smaller). Values for χ_p^2 are given in Table 3 together with probabilities to exceed (PTEs) computed from a χ^2 distribution with five degrees of freedom. We find no evidence for any statistically significant inconsistency between the two sets of parameters, even for the combined *TE* + *EE* SPTpol likelihood. We also note that the parameter $A_s e^{-2\tau}$ makes quite a large contribution to χ_p^2 for the *TE* + *EE* and *EE* spectra, but is sensitive to possible systematic errors in the SPTpol polarization efficiency calibration (which, as discussed, is not well understood [Henning et al. 2018](#)). Varying the maximum multipole used in

¹⁷ Downloaded from <http://pole.uchicago.edu/public/data/henning17/>. Note that we discovered errors in the way that the covariances matrices were loaded for separate *TE* and *EE* analyses, which have been corrected in the analysis presented here.

Table 3. Minimum χ^2 values fitting the SPTpol spectra to the best-fit *Planck* and SPTpol Λ CDM cosmologies (as described in the text).

SPTpol spectrum	N_b	<i>Planck</i> cosmology		SPT cosmology			PTE
		χ^2_{\min}	N_σ	χ^2_{\min}	N_σ	χ^2_p	
<i>TE</i> + <i>EE</i>	112	146.1	2.91	137.4	2.31	9.85	0.08
<i>TE</i>	56	71.4	2.38	70.3	2.27	3.38	0.64
<i>EE</i>	56	67.3	1.96	61.4	1.37	8.21	0.15

Notes. N_b gives the number of band powers in each spectrum. The deviation of χ^2_{\min} from the expectation $\langle \chi^2_{\min} \rangle = N_{\text{d.o.f.}}$ is given by the columns labelled N_σ , where $N_\sigma = (\chi^2_{\min} - N_{\text{d.o.f.}}) / \sqrt{2N_{\text{d.o.f.}}}$, and $N_{\text{d.o.f.}} = N_b - 8$. The last two columns give χ^2_p for parameter differences (Eq. (25)) and the associated PTEs.

the SPTpol likelihood (ℓ_{\max}), we find that the parameters of the SPTpol *TE* + *EE* cosmology converge by $\ell_{\max} = 2500$; higher multipoles do not contribute significantly to the SPTpol base- Λ CDM solution.

Henning et al. (2018) reported a trend for the parameters of the base- Λ CDM cosmology to change as the SPTpol likelihood is extended to higher multipoles, which they suggested may be an indication of new physics. However, this effect is not of high statistical significance and cannot be tested by the *Planck* spectra, which become less sensitive than the SPTpol spectra at multipoles $\gtrsim 1500$. The consistency of the base- Λ CDM cosmology at high multipoles in polarization should become clearer in the near future as more polarization data are accumulated by ACT-Pol and SPTpol.

5. Comparison with other astrophysical data sets

5.1. Baryon acoustic oscillations

As in PCP13 and PCP15 baryon acoustic oscillation (BAO) measurements from galaxy redshift surveys are used as the primary non-CMB astrophysical data set in this paper. The acoustic scale measured by BAOs, at around 147 Mpc, is much larger than the scale of virialized structures. This separation of scales makes BAO measurements insensitive to nonlinear physics, providing a robust geometrical test of cosmology. It is for this reason that BAO measurements are given high weight compared to other non-CMB data in this and in previous *Planck* papers. BAO features in the galaxy power spectrum were first detected by Cole et al. (2005) and Eisenstein et al. (2005). Since their discovery, BAO measurements have improved in accuracy via a number of ambitious galaxy surveys. As demonstrated in PCP13 and PCP15 BAO results from galaxy surveys have been consistently in excellent agreement with the best-fit base- Λ CDM cosmology inferred from *Planck*. More recently, the redshift reach of BAO measurements has been increased using quasar redshift surveys and Lyman- α absorption lines detected in quasar spectra.

Figure 11 summarizes the latest BAO results, updating Fig. 14 of PCP15. This plot shows the acoustic-scale distance ratio $D_V(z)/r_{\text{drag}}$ measured from surveys with effective redshift z , divided by the mean acoustic-scale ratio in the base- Λ CDM cosmology using *Planck* TT,TE,EE+lowE+lensing. Here r_{drag} is the comoving sound horizon at the end of the baryon drag epoch and D_V is a combination of the comoving angular diameter distance $D_M(z)$ and Hubble parameter $H(z)$:

$$D_V(z) = \left[D_M^2(z) \frac{cz}{H(z)} \right]^{1/3}. \quad (26)$$

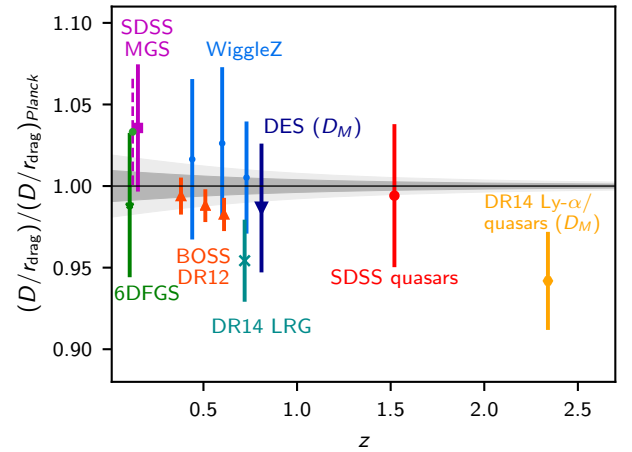


Fig. 11. Acoustic-scale distance measurements divided by the corresponding mean distance ratio from *Planck* TT,TE,EE+lowE+lensing in the base- Λ CDM model. The points, with their 1σ error bars are as follows: green star, 6dFGS (Beutler et al. 2011); magenta square, SDSS MGS (Ross et al. 2015); red triangles, BOSS DR12 (Alam et al. 2017); small blue circles, WigggleZ (as analysed by Kazin et al. 2014); large dark blue triangle, DES (DES Collaboration 2019); cyan cross, DR14 LRG (Bautista et al. 2018); red circle, SDSS quasars (Ata et al. 2018); and orange hexagon, which shows the combined BAO constraints from BOSS DR14 Lyman- α (de Sainte Agathe et al. 2019) and Lyman- α cross-correlation with quasars, as cited in Blomqvist et al. (2019). The green point with magenta dashed line is the 6dFGS and MGS joint analysis result of Carter et al. (2018). All ratios are for the averaged distance $D_V(z)$, except for DES and BOSS Lyman- α , where the ratio plotted is D_M (results for $H(z)$ are shown separately in Fig. 16). The grey bands show the 68% and 95% confidence ranges allowed for the ratio $D_V(z)/r_{\text{drag}}$ by *Planck* TT,TE,EE+lowE+lensing (bands for D_M/r_{drag} are very similar).

The grey bands in the figure show the $\pm 1\sigma$ and $\pm 2\sigma$ ranges allowed by *Planck* in the base- Λ CDM cosmology.

Compared to Fig. 14 of PCP15, we have replaced the Baryon Oscillation Spectroscopic Survey (BOSS) LOWZ and CMASS results of Anderson et al. (2014) with the latest BOSS data release 12 (DR12) results summarized by Alam et al. (2017). That paper reports “consensus” results on BAOs (weighting together different BAO analyses of BOSS DR12) reported by Ross et al. (2017), Vargas-Magaña et al. (2018), and Beutler et al. (2017a) in three redshift slices with effective redshifts $z_{\text{eff}} = 0.38, 0.51, \text{ and } 0.61$. These new measurements, shown by the red triangles in Fig. 11, are in good agreement with the *Planck* base- Λ CDM cosmology.

By using quasars, it has become possible to extend BAO measurements to redshifts greater than unity. Ata et al. (2018) have measured the BAO scale D_V at an effective redshift of

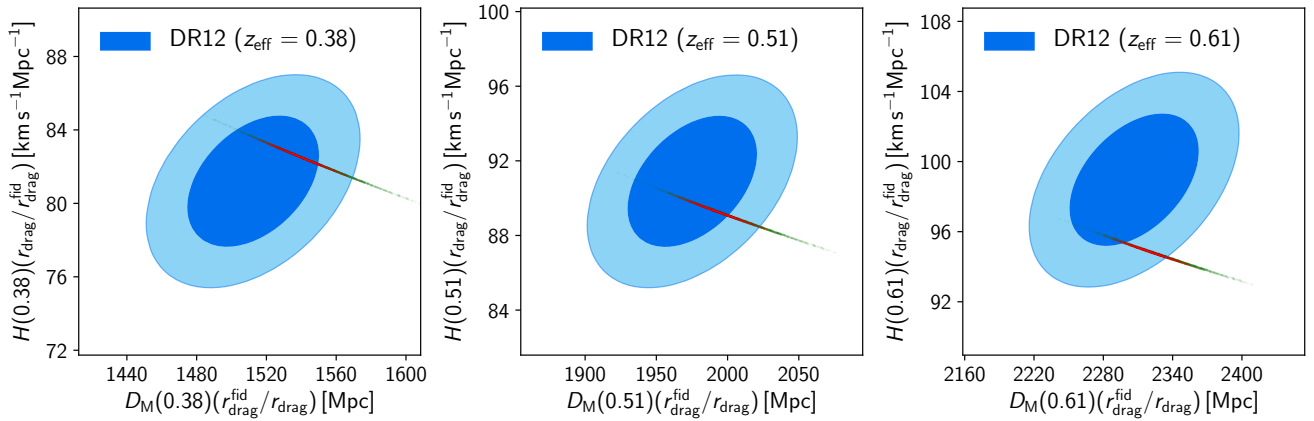


Fig. 12. Constraints on the comoving angular diameter distance $D_M(z)$ and Hubble parameter $H(z)$ at the three central redshifts of the Alam et al. (2017) analysis of BOSS DR12. The dark blue and light blue regions show 68% and 95% CL, respectively. The fiducial sound horizon adopted by Alam et al. (2017) is $r_{\text{drag}}^{\text{fid}} = 147.78$ Mpc. Green points show samples from *Planck* TT+lowE chains, and red points corresponding samples from *Planck* TT,TE,EE+lowE+lensing, indicating good consistency with BAOs; one can also see the shift towards slightly lower D_M and higher H as more CMB data are added.

$z_{\text{eff}} = 1.52$ using a sample of quasars from the extended Baryon Oscillation Survey (eBOSS). This measurement is shown by the red circle in Fig. 11 and is also in very good agreement with *Planck*. The results of the Ata et al. (2018) analysis also agree well with other analyses of the eBOSS quasar sample (e.g., Gil-Marín et al. 2018).

At even higher redshifts BAOs have been measured in the Lyman α spectra of quasars (Delubac et al. 2015; Font-Ribera et al. 2014; Bautista et al. 2017; du Mas des Bourboux et al. 2017; de Sainte Agathe et al. 2019; Blomqvist et al. 2019). In the first preprint version of this paper, we compared the *Planck* results with those from BAO features measured from the flux-transmission correlations of Sloan Digital Sky Survey (SDSS) DR12 quasars (Bautista et al. 2017) and with the cross-correlation of the Ly α forest with SDSS quasars (du Mas des Bourboux et al. 2017). The combined result on D_M/r_{drag} from these analyses was about 2.3σ lower than expected from the best-fit *Planck* base- Λ CDM cosmology. The Bautista et al. (2017) and du Mas des Bourboux et al. (2017) analyses have been superseded by equivalent studies of a larger sample of SDSS DR14 quasars reported in de Sainte Agathe et al. (2019) and Blomqvist et al. (2019). The combined result for D_M/r_{drag} from these analyses (as quoted by Blomqvist et al. 2019) is plotted as the orange hexagon on Fig. 11 and lies within 1.7σ of the *Planck* best-fit model. The errors on these high-redshift BAO measurements are still quite large in comparison with the galaxy measurements and so we do not include them in our default BAO compilation¹⁸.

The more recent BAO analyses solve for the positions of the BAO feature in both the line-of-sight and transverse directions (the distortion in the transverse direction caused by the background cosmology is sometimes called the Alcock-Paczynski effect, Alcock & Paczynski 1979), leading to joint constraints on the angular diameter distance $D_M(z_{\text{eff}})$ and the Hubble parameter $H(z_{\text{eff}})$. These constraints for the BOSS DR12 analysis are plotted in Fig. 12. Samples from the *Planck* TT+lowE and *Planck*

TT,TE,EE+lowE+lensing likelihood are shown in green and red, respectively, demonstrating that BAO and *Planck* polarization data with lensing consistently pull parameters in the same direction (towards slightly lower $\Omega_c h^2$). We find the same behaviour for *Planck* when adding polarization and lensing to the TT likelihood separately. This demonstrates the remarkable consistency of the *Planck* data, including polarization and CMB lensing with the galaxy BAO measurements. Evidently, the *Planck* base- Λ CDM parameters are in good agreement with both the isotropized D_V BAO measurements plotted in Fig. 11, and with the anisotropic constraints plotted in Fig. 12.

In this paper, we use the 6dFGS and SDSS-MGS measurements of D_V/r_{drag} (Beutler et al. 2011; Ross et al. 2015) and the final DR12 anisotropic BAO measurements of Alam et al. (2017). Since the WiggleZ volume partially overlaps that of the BOSS-CMASS sample, and the correlations have not been quantified, we do not use the WiggleZ results in this paper. It is clear from Fig. 11 that the combined BAO likelihood for the lower redshift points is dominated by the BOSS measurements.

In the base- Λ CDM model, the *Planck* data constrain the Hubble constant H_0 and matter density Ω_m to high precision:

$$\left. \begin{aligned} H_0 &= (67.36 \pm 0.54) \text{ km s}^{-1} \text{ Mpc}^{-1}, \\ \Omega_m &= 0.3158 \pm 0.0073, \end{aligned} \right\} \begin{array}{l} (68\%, \text{ TT,TE,EE+} \\ \text{lowE+lensing}). \end{array} \quad (27)$$

With the addition of the BAO measurements, these constraints are strengthened to

$$\left. \begin{aligned} H_0 &= (67.66 \pm 0.42) \text{ km s}^{-1} \text{ Mpc}^{-1}, \\ \Omega_m &= 0.3111 \pm 0.0056, \end{aligned} \right\} \begin{array}{l} (68\%, \text{ TT,TE,EE+} \\ \text{lowE+lensing}) \\ \text{BAO.} \end{array} \quad (28)$$

These numbers are in very good agreement with the constraints given in Eq. (6), which exclude the high-multipole *Planck* likelihood. Section 5.4 discusses the consistency of direct measurements of H_0 with these estimates and Hubble parameter measurements from the line-of-sight component of BAOs at higher redshift.

As discussed above, we have excluded Ly α BAOs from our default BAO compilation. The full likelihood for the combined Ly α and Ly α -quasar cross-correlations reported in du Mas des Bourboux et al. (2017) is not yet available; nevertheless, we can

¹⁸ The first preprint version of this paper showed that the inclusion of the Bautista et al. (2017) and du Mas des Bourboux et al. (2017) Ly α BAO results had a minor impact on the parameters of the base- Λ CDM cosmology. The impact of the more recent Ly α results of de Sainte Agathe et al. (2019) and Blomqvist et al. (2019) will be even lower, since they are in closer agreement with the *Planck* best-fit cosmology.

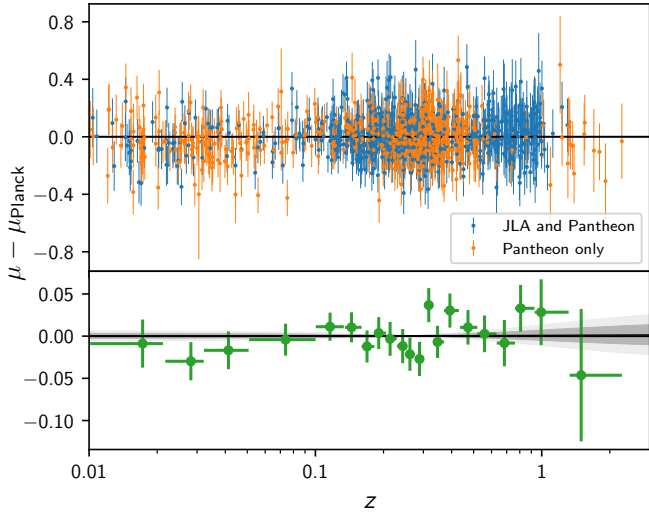


Fig. 13. Distance modulus $\mu = 5 \log_{10}(D_L) + \text{constant}$ (where D_L is the luminosity distance) for supernovae in the Pantheon sample (Scolnic et al. 2018) with 1σ errors, compared to the *Planck* TT,TE,EE+lowE+lensing Λ CDM best fit. Supernovae that were also in the older Joint Lightcurve Analysis (JLA; Betoule et al. 2014) sample are shown in blue. The peak absolute magnitudes of the SNe, corrected for light-curve shape, colour, and host-galaxy mass correlations (see Eq. (3) of Scolnic et al. 2018), are fixed to an absolute distance scale using the H_0 value from the *Planck* best fit. The lower panel shows the binned errors, with equal numbers of supernovae per redshift bin (except for the two highest redshift bins). The grey bands show the ± 1 and $\pm 2\sigma$ bounds from the *Planck* TT,TE,EE+lowE+lensing chains, where each model is calibrated to the best fit, as for the data.

get an indication of the impact of including these measurements by assuming uncorrelated Gaussian errors on D_M/r_{drag} and $r_{\text{drag}}H$. Adding these measurements to *Planck* TT,TE,EE+lowE and our default BAO compilation shifts H_0 higher, and $\Omega_m h^2$ and σ_8 lower, by approximately 0.3σ . The joint *Planck*+BAO result then gives D_M/r_{drag} and $r_{\text{drag}}H$ at $z = 2.4$ lower by 0.25 and 0.3 of *Planck*'s σ , leaving the overall 2.3σ tension with these results almost unchanged. As shown by Aubourg et al. (2015), it is difficult to construct well-motivated extensions to the base- Λ CDM model that can resolve the tension with the Ly α BAOs. Further work is needed to assess whether the discrepancy between *Planck* and the Ly α BAO results is a statistical fluctuation, is caused by small systematic errors, or is a signature of new physics.

5.2. Type Ia supernovae

The use of type Ia supernovae (SNe) as standard candles has been of critical importance to cosmology, leading to the discovery of cosmic acceleration (Riess et al. 1998; Perlmutter et al. 1999). For Λ CDM models, however, SNe data have little statistical power compared to *Planck* and BAO and in this paper they are used mainly to test models involving evolving dark energy and modified gravity. For these extensions of the base cosmology, SNe data are useful in fixing the background cosmology at low redshifts, where there is not enough volume to allow high precision constraints from BAO.

In PCP15 we used the ‘‘Joint Light-curve Analysis’’ (JLA) sample constructed from the SNLS and SDSS SNe plus several samples of low redshift SNe described in Betoule et al. (2013, 2014) and Moshir et al. (2014). In this paper, we use the new ‘‘Pantheon’’ sample of Scolnic et al. (2018), which adds

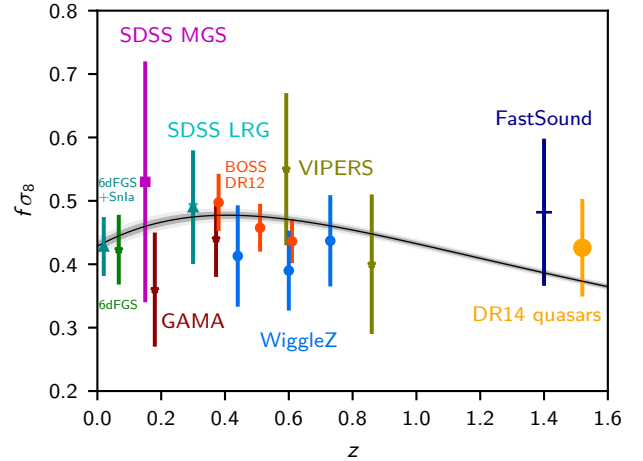


Fig. 14. Constraints on the growth rate of fluctuations from various redshift surveys in the base- Λ CDM model: dark cyan, 6dFGS and velocities from SNe Ia (Huterer et al. 2017); green, 6dFGRS (Beutler et al. 2012); purple square, SDSS MGS (Howlett et al. 2015); cyan cross, SDSS LRG (Oka et al. 2014); dark red, GAMA (Blake et al. 2013); red, BOSS DR12 (Alam et al. 2017); blue, WiggleZ (Blake et al. 2012); olive, VIPERS (Pezzotta et al. 2017); dark blue, FastSound (Okumura et al. 2016); and orange, BOSS DR14 quasars (Zarrouk et al. 2018). Where measurements are reported in correlation with other variables, we here show the marginalized posterior means and errors. Grey bands show the 68% and 95% confidence ranges allowed by *Planck* TT,TE,EE+lowE+lensing.

276 supernovae from the Pan-STARRS1 Medium Deep Survey at $0.03 < z < 0.65$ and various low-redshift and HST samples to give a total of 1048 supernovae spanning the redshift range $0.01 < z < 2.3$. The Pantheon compilation applies cross-calibrations of the photometric systems of all of the sub-samples used to construct the final catalogue (Scolnic et al. 2015), reducing the impact of calibration systematics on cosmology¹⁹. The Pantheon data are compared to the predictions of the *Planck* TT,TE,EE+lowE+lensing base- Λ CDM model best fit in Fig. 13. The agreement is excellent. The JLA and Pantheon samples are consistent with each other (with Pantheon providing tighter constraints on cosmological parameters) and there would be no significant change to our science conclusions had we chosen to use the JLA sample in this paper. To illustrate this point we give results for a selection of models using both samples in the parameter tables available in the PLA; Fig. 17, illustrating inverse-distance-ladder constraints on H_0 (see Sect. 5.4), shows a specific example.

5.3. Redshift-space distortions

The clustering of galaxies observed in a redshift survey exhibits anisotropies induced by peculiar motions (known as redshift-space distortions, RSDs). Measurement of RSDs can provide constraints on the growth rate of structure and the amplitude of the matter power spectrum (e.g., Percival & White 2009). Since it uses non-relativistic tracers, RSDs are sensitive to the time-time component of the metric perturbation or the Newtonian potential. A comparison of the amplitude inferred from RSDs with that inferred from lensing (sensitive to the Weyl potential, see Sect. 7.4), provides a test of General Relativity.

¹⁹ We use the November 2018 data file available from <https://github.com/dscolnic/Pantheon/>, which includes heliocentric redshifts and no bulk-flow corrections for $z > 0.08$.

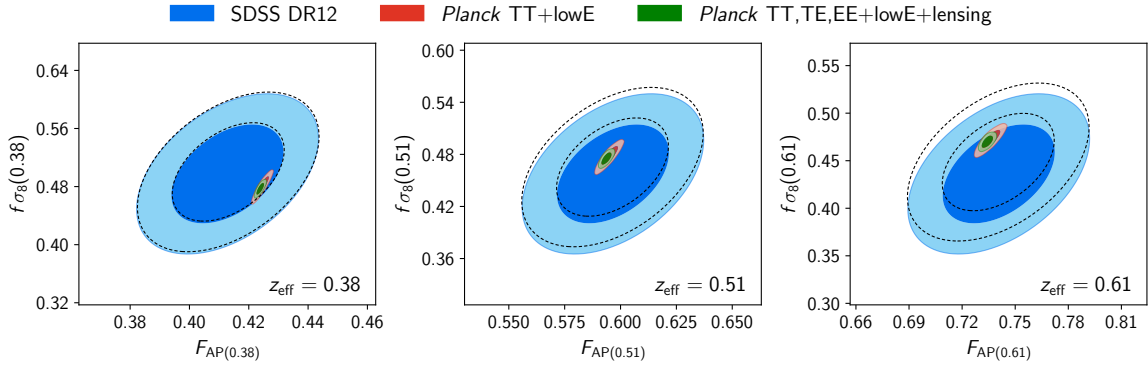


Fig. 15. Constraints on $f\sigma_8$ and F_{AP} (see Eqs. (29) and (30)) from analysis of redshift-space distortions. The blue contours show 68% and 95% confidence ranges on $(f\sigma_8, F_{\text{AP}})$ from BOSS-DR12, marginalizing over D_V . Constraints from *Planck* for the base- Λ CDM cosmology are shown by the red and green contours. The dashed lines are the 68% and 95% contours for BOSS-DR12, conditional on the *Planck* TT,TE,EE+lowE+lensing constraints on D_V .

Measurements of RSDs are usually quoted as constraints on $f\sigma_8$, where for models with scale-independent growth $f = d \ln D / d \ln a$. For Λ CDM, $d \ln D / d \ln a \approx \Omega_m^{0.55}(z)$. We follow PCP15, defining

$$f\sigma_8 \equiv \frac{[\sigma_8^{(\text{vd})}(z)]^2}{\sigma_8^{(\text{dd})}(z)}, \quad (29)$$

where $\sigma_8^{(\text{vd})}$ is the density-velocity correlation in spheres of radius $8 h^{-1}$ Mpc in linear theory.

Measuring $f\sigma_8$ requires modelling nonlinearities and scale-dependent bias and is considerably more complicated than estimating the BAO scale from galaxy surveys. One key problem is deciding on the precise range of scales that can be used in an RSD analysis, since there is a need to balance potential systematic errors associated with modelling nonlinearities against reducing statistical errors by extending to smaller scales. In addition, there is a partial degeneracy between distortions caused by peculiar motions and the Alcock-Paczynski effect. Nevertheless, there have been substantial improvements in modelling RSDs in the last few years, including extensive tests of systematic errors using numerical simulations. Different techniques for measuring $f\sigma_8$ are now consistent to within a few percent (Alam et al. 2017).

Figure 14, showing $f\sigma_8$ as a function of redshift, is an update of Fig. 16 from PCP15. The most significant changes from PCP15 are the new high precision measurements from BOSS DR12, shown as the red points. These points are the ‘‘consensus’’ BOSS D12 results from Alam et al. (2017), which averages the results from four different ways of analysing the DR12 data (Beutler et al. 2017b; Grieb et al. 2017; Sánchez et al. 2017; Satpathy et al. 2017). These results are in excellent agreement with the *Planck* base Λ CDM cosmology (see also Fig. 15) and provide the tightest constraints to date on the growth rate of fluctuations. We have updated the VIPERS constraints to those of the second public data release (Pezzotta et al. 2017) and added a data point from the Galaxy and Mass Assembly (GAMA) redshift survey (Blake et al. 2012). Two new surveys have extended the reach of RSD measurements (albeit with large errors) to redshifts greater than unity: the deep FASTSOUND emission line redshift survey (Okumura et al. 2016); and the BOSS DR14 quasar survey (Zarrouk et al. 2018). We have also added a new low redshift estimate of $f\sigma_8$ from Huterer et al. (2017) at an effective redshift of $z_{\text{eff}} = 0.023$, which is based on correlating deviations

from the mean magnitude-redshift relation of SNe in the Pantheon sample with estimates of the nearby peculiar velocity field determined from the 6dF Galaxy Survey (Springob et al. 2014). As can be seen from Fig. 14, these growth rate measurements are consistent with the *Planck* base- Λ CDM cosmology over the entire redshift range $0.023 < z_{\text{eff}} < 1.52$.

Since the BOSS-DR12 estimates provide the strongest constraints on RSDs, it is worth comparing these results with *Planck* in greater detail. Here we use the ‘‘full-shape consensus’’ results²⁰ on D_V , $f\sigma_8$, and F_{AP} for each of the three redshift bins from Alam et al. (2017) and the associated 9×9 covariance matrix, where F_{AP} is the Alcock-Paczynski parameter,

$$F_{\text{AP}}(z) = D_M(z) \frac{H(z)}{c}. \quad (30)$$

Figure 15 shows the constraints from BOSS-DR12 on $f\sigma_8$ and F_{AP} marginalized over D_V . *Planck* base- Λ CDM constraints are shown by the red and green contours. For each redshift bin, the *Planck* best-fit values of $f\sigma_8$ and F_{AP} lie within the 68% contours from BOSS-DR12. Figure 15 highlights the impressive consistency of the base- Λ CDM cosmology from the high redshifts probed by the CMB to the low redshifts sampled by BOSS.

5.4. The Hubble constant

Perhaps the most controversial tension between the *Planck* Λ CDM model and astrophysical data is the discrepancy with traditional distance-ladder measurements of the Hubble constant H_0 . PCP13 reported a value of $H_0 = (67.3 \pm 1.2) \text{ km s}^{-1} \text{ Mpc}^{-1}$ for the base- Λ CDM cosmology, substantially lower than the distance-ladder estimate of $H_0 = (73.8 \pm 2.4) \text{ km s}^{-1} \text{ Mpc}^{-1}$ from the SH0ES²¹ project (Riess et al. 2011) and other H_0 studies (e.g., Freedman et al. 2001, 2012). Since then, additional data acquired as part of the SH0ES project (Riess et al. 2016, 2018a, hereafter R18) has exacerbated the tension. R18 conclude that $H_0 = (73.48 \pm 1.66) \text{ km s}^{-1} \text{ Mpc}^{-1}$, compared to our *Planck* TT,TE,EE+lowE+lensing estimate from Table 1 of $H_0 = (67.27 \pm 0.60) \text{ km s}^{-1} \text{ Mpc}^{-1}$. Using *Gaia* parallaxes Riess et al. (2018b) slightly tightened their measurement to $H_0 = (73.52 \pm 1.62) \text{ km s}^{-1} \text{ Mpc}^{-1}$. Recently Riess et al. (2019)

²⁰ When using RSDs to constraint dark energy in Sect. 7.4, we use the alternative D_M , H , and $f\sigma_8$ parameterization from Alam et al. (2017) for consistency with the DR12 BAO-only likelihood that we use elsewhere.

²¹ SN, H_0 , for the Equation of State of dark energy.

then used improved measurements of LMC Cepheids to further tighten²² the constraint to $H_0 = (74.03 \pm 1.42) \text{ km s}^{-1} \text{ Mpc}^{-1}$. Interestingly, the central values of the SHOES and *Planck* estimates have hardly changed since the appearance of PCP13, but the errors on both estimates have shrunk so that the discrepancy has grown from around 2.5σ in 2013 to 3.5σ today (4.4σ using Riess et al. 2019). This discrepancy has stimulated a number of investigations of possible systematic errors in either the *Planck* or SHOES data, which have failed to identify any obvious problem with either analysis (e.g., Spergel et al. 2015; Addison et al. 2016; Planck Collaboration Int. LI 2017; Efstathiou 2014; Cardona et al. 2017; Zhang et al. 2017; Follin & Knox 2018). It has also been argued that the Gaussian likelihood assumption used in the SHOES analysis leads to an overestimate of the statistical significance of the discrepancy (Feeney et al. 2018).

Recently, Freedman et al. (2019) have reported a determination of H_0 using the tip of the red giant branch as a distance estimator. This analysis gives $H_0 = (69.8 \pm 1.9) \text{ km s}^{-1} \text{ Mpc}^{-1}$, i.e., intermediate between the SHOES measurement and the *Planck* base- Λ CDM value. There has been some controversy (see Yuan et al. 2019) concerning the calibration of the tip of the red giant branch adopted in Freedman et al. (2019), though a recent reanalysis by Freedman et al. (2020) yields a value of H_0 that is almost identical to that reported in Freedman et al. (2019).

Measurements of the Hubble constant using strong gravitational-lensing time delays are also higher than the *Planck* base- Λ CDM value. The most recent results, based on six strongly lensed quasars, give $H_0 = 73.3^{+1.7}_{-1.8} \text{ km s}^{-1} \text{ Mpc}^{-1}$ (Wong et al. 2019), which is about 3.2σ higher than the *Planck* value. A number of other techniques have been used to infer H_0 , including stellar ages (e.g., Jimenez & Loeb 2002; Gómez-Valent & Amendola 2018), distant megamasers (Reid et al. 2013; Kuo et al. 2013; Gao et al. 2016) and gravitational-wave standard sirens Abbott et al. (2017b). These measurements span a range of values. Nevertheless, there is a tendency for local determinations to sit high compared to the *Planck* base- Λ CDM value, with the SHOES Cepheid-based measurement giving the most statistically significant discrepancy.

In this paper, we take the R18 estimate at face value and include it as a prior in combination with *Planck* in some of the parameter tables available on the PLA. The interested reader can then assess the impact of the R18 measurement on a wide range of extensions to the base- Λ CDM cosmology.

We already mentioned in Sect. 5.1 that BAO measurements along the line of sight constrain $H(z)r_{\text{drag}}$. *Planck* constrains r_{drag} to a precision of 0.2% for the base- Λ CDM model and so the BAO measurements can be accurately converted into absolute measurements of $H(z)$. This is illustrated by Fig. 16, which shows clearly how well the *Planck* base- Λ CDM cosmology fits the BAO measurements of $H(z)$ over the redshift range 0.3–2.5, yet fails to match the R18 measurement of H_0 at $z = 0$. The model is also consistent with the most recent Ly α BAO measurements at $z \approx 2.3$.

PCP13 and PCP15 emphasized that this mismatch between BAO measurements and forward distance-ladder measurements of H_0 is not sensitive to the *Planck* data at high multipoles. For example, combining WMAP with BAO measurements leads to $H_0 = (68.14 \pm 0.73) \text{ km s}^{-1} \text{ Mpc}^{-1}$ for the base- Λ CDM cosmology, which is discrepant with the R18 value at the 2.9σ level.

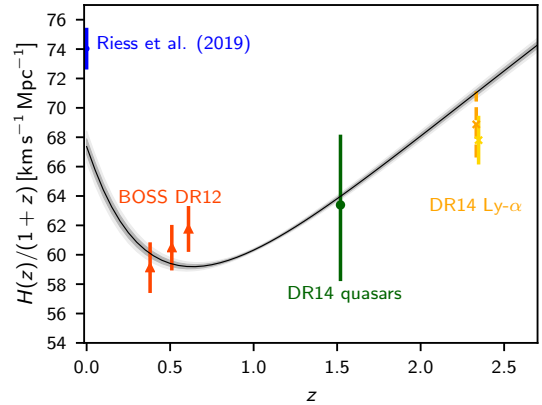


Fig. 16. Comoving Hubble parameter as a function of redshift. The grey bands show the 68% and 95% confidence ranges allowed by *Planck* TT,TE,EE+lowE+lensing in the base- Λ CDM model, clearly showing the onset of acceleration around $z = 0.6$. Red triangles show the BAO measurements from BOSS DR12 (Alam et al. 2017), the green circle is from BOSS DR14 quasars (Zarrouk et al. 2018), the orange dashed point is the constraint from the BOSS DR14 Ly α auto-correlation at $z = 2.34$ (de Sainte Agathe et al. 2019), and the solid gold point is the joint constraint from the Ly α auto-correlation and cross-correlation with quasars from Blomqvist et al. (2019). All BOSS measurements are used in combination with the *Planck* base-model measurements of the sound horizon r_{drag} , and the DR12 points are correlated. The blue point at redshift zero shows the inferred forward-distance-ladder Hubble measurement from Riess et al. (2019).

Heavens et al. (2014), Cuesta et al. (2015), Aubourg et al. (2015) showed that the combination of CMB, BAO, and SNe data provides a powerful “inverse-distance-ladder” approach to constructing a physically calibrated distance-redshift relation down to very low redshift. For the base- Λ CDM model, this inverse-distance-ladder approach can be used to constrain H_0 without using any CMB measurements at all, or by only using constraints on the CMB parameter θ_{MC} (see also Bernal et al. 2016; Addison et al. 2018; DES Collaboration 2018a; Lemos et al. 2019). This is illustrated in Fig. 17, which shows how the constraints on H_0 and Ω_m converge to the *Planck* values as more data are included. The green contours show the constraints from BAO and the Pantheon SNe data, together with a BBN constraint on the baryon density ($\Omega_b h^2 = 0.0222 \pm 0.0005$) based on the primordial deuterium abundance measurements of Cooke et al. (2018, see Sect. 7.6). The dashed contours in this figure show how the green contours shift if the Pantheon SNe data are replaced by the JLA SNe sample. Adding *Planck* CMB lensing (grey contours) constrains $\Omega_m h^2$ and shifts H_0 further away from the R18 measurement. Using a “conservative” *Planck* prior of $100\theta_{\text{MC}} = 1.0409 \pm 0.0006$ (which is consistent with all of the variants of Λ CDM considered in this paper to within 1σ , see Table 5) gives the red contours, with $H_0 = (67.9 \pm 0.8) \text{ km s}^{-1} \text{ Mpc}^{-1}$ and $\Omega_m = 0.305 \pm 0.001$, very close to the result using the full *Planck* likelihood (blue contours). Evidently, there is a significant problem in matching the base- Λ CDM model to the R18 results and this tension is not confined exclusively to the *Planck* results.

The question then arises of whether there is a plausible extension to the base- Λ CDM model that can resolve the discrepancy. Table 5 summarizes the *Planck* constraints on H_0 for variants of Λ CDM considered in this paper. H_0 remains discrepant with R18 in all of these cases, with the exception of models in which we allow the dark energy equation of state to vary. For models with either a fixed dark energy equation-of-state parameter, w_0 ,

²² By default in this paper (and in the PLA) we use the Riess et al. (2018a) number (available at the time we ran our parameter chains) unless otherwise stated; using the updated number would make no significant difference to our conclusions.

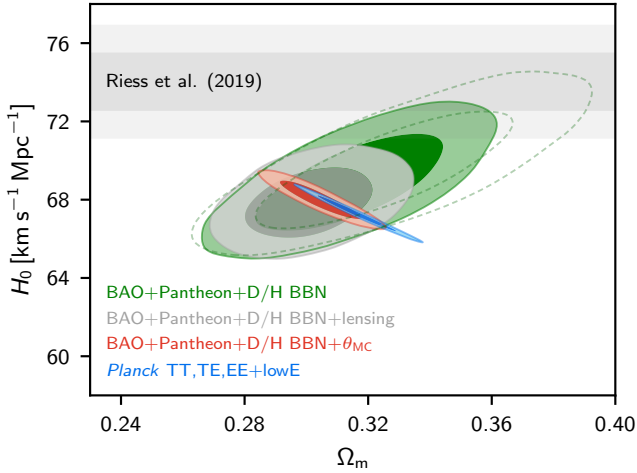


Fig. 17. Inverse-distance-ladder constraints on the Hubble parameter and Ω_m in the base- Λ CDM model, compared to the result from the full *Planck* CMB power-spectrum data. BAO data constrain the ratio of the sound horizon at the epoch of baryon drag and the distances; the sound horizon depends on the baryon density, which is constrained by the conservative prior of $\Omega_b h^2 = 0.0222 \pm 0.0005$, based on the measurement of D/H by [Cooke et al. \(2018\)](#) and standard BBN with modelling uncertainties. Adding *Planck* CMB lensing constrains the matter density, or adding a conservative *Planck* CMB “BAO” measurement ($100\theta_{MC} = 1.0409 \pm 0.0006$) gives a tight constraint on H_0 , comparable to that from the full CMB data set. Grey bands show the local distance-ladder measurement of [Riess et al. \(2019\)](#). Contours contain 68% and 95% of the probability. Marginalizing over the neutrino masses or allowing dark energy equation of state parameters $w_0 > -1$ would only lower the inverse-distance-ladder constraints on H_0 . The dashed contours show the constraints from the data combination BAO+JLA+D/H BBN.

or time-varying equation of state parameterized by w_0 and w_a (see Sect. 7.4.1 for definitions and further details), *Planck* data alone lead to poor constraints on H_0 . However, for most physical dark energy models where $p_{de} \geq -\rho_{de}$ (so $w_0 > -1$), and the density is only important after recombination, H_0 can only decrease with respect to Λ CDM if the measured CMB acoustic scale is maintained, making the discrepancy with R18 worse. If we allow for $w_0 < -1$, then adding BAO and SNe data is critical to obtain a useful constraint (as pointed out by [Aubourg et al. 2015](#)), and we find

$$H_0 = (68.34 \pm 0.81) \text{ km s}^{-1} \text{ Mpc}^{-1}, \quad (w_0 \text{ varying}), \quad (31a)$$

$$H_0 = (68.31 \pm 0.82) \text{ km s}^{-1} \text{ Mpc}^{-1}, \quad (w_0, w_a \text{ varying}), \quad (31b)$$

for the parameter combination *Planck* TT,TE,EE+lowE+lensing+BAO+Pantheon. Modifying the dark energy sector in the late universe does not resolve the discrepancy with R18.

If the difference between base Λ CDM and the R18 measurement of H_0 is caused by new physics, then it is unlikely to be through some change to the late-time distance-redshift relationship. Another possibility is a change in the sound horizon scale. If we use the R18 measurement of H_0 , combined with Pantheon supernovae and BAO, the acoustic scale is $r_{\text{drag}} = (136.4 \pm 3.5) \text{ Mpc}$. The difficulty is to find a model that can give this much smaller value of the sound horizon (compared to $r_{\text{drag}} = (147.05 \pm 0.3) \text{ Mpc}$ from *Planck* TT,TE,EE+lowE in Λ CDM), while preserving a good fit to the CMB power spectra and a baryon density consistent with BBN. We discuss some extensions to Λ CDM in Sect. 7.1 that allow larger H_0 values (e.g., $N_{\text{eff}} > 3.046$); however, these models are not preferred by

the *Planck* data, and tend to introduce other tensions, such as a higher value of σ_8 ²³.

The tension between base Λ CDM and the SHOES H_0 measurement is intriguing and emphasizes the need for independent measurements of the distance scale. It will be interesting in the future to compare the Cepheid distance scale in more detail with other distance indicators, such as the tip of the red giant branch ([Freedman et al. 2019](#)), and with completely different techniques such as gravitational-lensing time delays ([Suyu et al. 2013](#)) and gravitational-wave standard sirens ([Holz & Hughes 2005](#); [Abbott et al. 2017b](#); [Chen et al. 2018](#); [Feeney et al. 2019](#)).

5.5. Weak gravitational lensing of galaxies

The distortion of the shapes of distant galaxies by lensing due to large-scale structure along the line of sight is known as galaxy lensing or cosmic shear (see e.g., [Bartelmann & Schneider 2001](#), for a review). It constrains the gravitational potentials at lower redshift than CMB lensing, with tomographic information and completely different systematics, so the measurements are complementary. Since the source galaxy shapes and orientations are in general unknown, the lensing signal is a small effect that can only be detected statistically. If it can be measured robustly it is a relatively clean way of measuring the Weyl potential (and hence, in GR, the total matter fluctuations); however, the bulk of the statistical power comes from scales where the signal is significantly nonlinear, complicating the cosmological interpretation. The measurement is also complicated by several other issues. Intrinsic alignment between the shape of lensed galaxies and their surrounding potentials means that the galaxy shape correlation functions actually measure a combination of lensing and intrinsic alignment effects ([Hirata & Seljak 2004](#)). Furthermore, to get a strong statistical detection, a large sample of galaxies is needed, so most current results use samples that rely mainly on photometric redshifts; accurate calibration of the photometric redshifts and modelling of the errors are required in order to use the observed lensing signal for cosmology.

Cosmic shear measurements are available from several collaborations, including CFHTLenS ([Heymans et al. 2012](#); [Erben et al. 2013](#), which we discussed in PCP15), DLS ([Jee et al. 2016](#)), and more recently the Dark Energy Survey (DES, [DES Collaboration 2018b](#)), Hyper Suprime-Cam (HSC, [Hikage et al. 2019](#); [Hamana et al. 2020](#)), and KiDS ([Hildebrandt et al. 2017](#); [Köhlinger et al. 2017](#); [Hildebrandt et al. 2020](#)). The CFHTLenS and KiDS results found a modest tension with the *Planck* Λ CDM cosmology, preferring lower values of Ω_m or σ_8 . A combined analysis of KiDS with GAMA ([van Uitert et al. 2018](#)) galaxy clustering has found results consistent with *Planck*, whereas a similar analysis combining KiDS lensing measurements with spectroscopic data from the 2-degree Field Lensing Survey and BOSS claims a 2.6σ discrepancy with *Planck* ([Joudaki et al. 2018](#)). [Troxel et al. \(2018a\)](#) have shown that a more accurate

²³ To obtain simultaneously higher values of H_0 , lower values of σ_8 , and consistent values of Ω_m it is necessary to invoke less common extensions of the Λ CDM model, such as models featuring non-standard interactions in the neutrino, dark-matter, dark-radiation, and/or dark-energy sector (see e.g., [Pettorino 2013](#); [Lesgourgues et al. 2016](#); [Planck Collaboration XIV 2016](#); [Archidiacono et al. 2016](#); [Lancaster et al. 2017](#); [Oldengott et al. 2017](#); [Di Valentino et al. 2018](#); [Buen-Abad et al. 2018](#); [Poulin et al. 2019](#); [Kreisch et al. 2020](#); [Agrawal et al. 2019](#); [Lin et al. 2019](#); [Archidiacono et al. 2019](#)). Such models are likely to be highly constrained by the *Planck*, BAO, and supernova data used in this paper and by future CMB observations and surveys of large-scale structure.

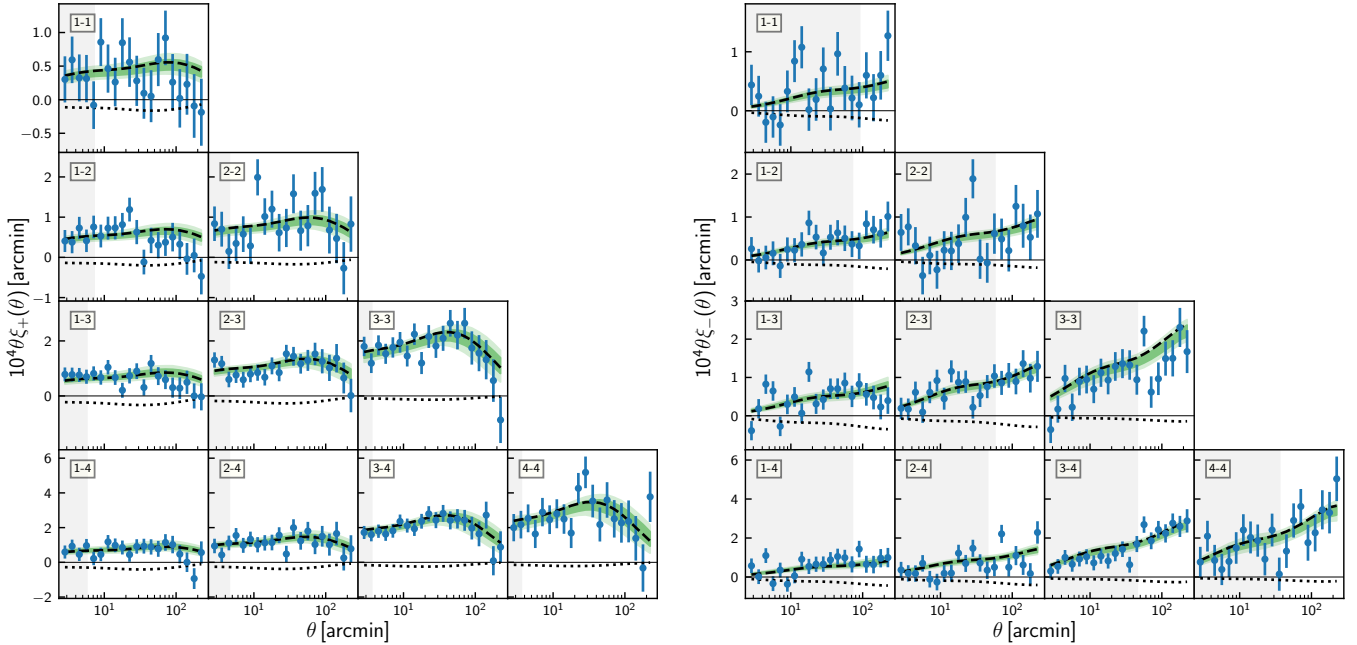


Fig. 18. Dark Energy Survey (DES) shear correlation functions, ξ_+ (left) and ξ_- (right), for the auto- and cross-correlation between the four DES source redshift bins (Troxel et al. 2018b). Green bands show the 68% and 95% distribution of model fits in the DES lensing-only base- Λ CDM parameter fits. The dashed line shows the DES lensing parameter best fit when the cosmological parameters are fixed to the best fit model for *Planck* TT,TE,EE+lowE only; dotted lines show the size of the contribution of intrinsic alignment terms to the dashed lines. Grey bands show the scales excluded from the DES analysis, in order to reduce sensitivity to nonlinear effects.

treatment of the intrinsic galaxy shape noise, multiplicative shear calibration uncertainty, and angular scale of each bin can significantly change earlier KiDS results (by about 1σ), making them more consistent with *Planck*. At the time of running our chains the DES lensing results had been published and included this improved modelling, while an updated analysis from KiDS was not yet available; we therefore only consider the DES results in detail here. Troxel et al. (2018a) reports consistent results from DES and their new analysis of KiDS, and HSC also report results consistent with *Planck*. However, the more recent KiDS analysis by Hildebrandt et al. (2020) still finds a 2.3σ discrepancy with *Planck*, and Joudaki et al. (2020) claim that a recalibration of the DES redshifts gives results compatible with KiDS and a combined 2.5σ tension with *Planck*.

The DES collaboration analysed 1321 deg^2 of imaging data from the first year of DES. They analysed the cosmic shear correlation functions of 26 million source galaxies in four redshift bins (Troxel et al. 2018b), and also considered the auto- (Elvin-Poole et al. 2018) and cross-spectrum (Prat 2018) of 650 000 lens galaxies in five redshift bins. To be conservative they restricted their parameter analysis to scales that are only weakly affected by nonlinear modelling (at the expense of substantially reducing the statistical power of the data). To account for modelling uncertainties, the cosmic shear analysis marginalizes over 10 nuisance parameters, describing uncertainties in the photometric redshift distributions, shear calibrations, and intrinsic alignments; the joint analysis adds an additional 10 nuisance parameters describing the bias and redshift uncertainty of the lens galaxies.

We use the first-year DES lensing (cosmic shear) likelihood, data cuts, nuisance parameters, and nuisance parameter priors, as described by Troxel et al. (2018b), DES Collaboration (2018b), Krause et al. (2017). We implement the theory model code independently, but use the same physical model and assumptions

as the DES analysis,²⁴ treating the nuisance parameters as fast parameters for sampling in CosmoMC. In this section we adopt the cosmological parameter priors assumed by Troxel et al. (2018b), but to be consistent with our other Λ CDM analyses, we assume a single minimal-mass eigenstate rather than marginalizing over the neutrino mass, and use HMcode for the nonlinear corrections²⁵. The shear correlation data points and parameter fits are shown in Fig. 18. Note that intrinsic alignments contribute significantly to the observed shear correlation functions (as shown by the dotted lines in the figure). This introduces additional modelling uncertainty and a possible source of bias if the intrinsic alignment model is not correct. The DES model is validated in Troxel et al. (2018b), Krause et al. (2017).

Figure 19 shows the constraints in the $\Omega_m - \sigma_8$ plane from DES lensing, compared to the constraints from the CMB power spectra and CMB lensing. The DES cosmic shear constraint is of comparable statistical power to CMB lensing, but due to the significantly lower mean source redshift, the degeneracy directions are different (with DES cosmic shear approximately constraining $\Omega_m \sigma_8^{0.5}$ and CMB lensing constraining $\Omega_m \sigma_8^{0.25}$). The correlation between the DES cosmic shear and CMB lensing results is relatively small, since the sky area of the CMB reconstruction is much larger than that for DES, and it is also mostly not at high signal-to-noise ratio. Neglecting the cross-correlation, we combine the DES and *Planck* lensing results to break a large

²⁴ Except for the modified-gravity models in Sect. 7.4 where we calculate the lensing spectrum directly from the power spectrum of the Weyl potential (rather than from the matter power spectrum assuming standard GR).

²⁵ The results are quite sensitive to the choice of cosmological parameter priors, see PL2018 for an analysis using the different priors assumed by the *Planck* CMB lensing analysis. Here we assume consistent (DES) priors for DES and CMB lensing results; however, the *Planck* power spectrum constraints are much less sensitive to priors and we use our default priors for those.

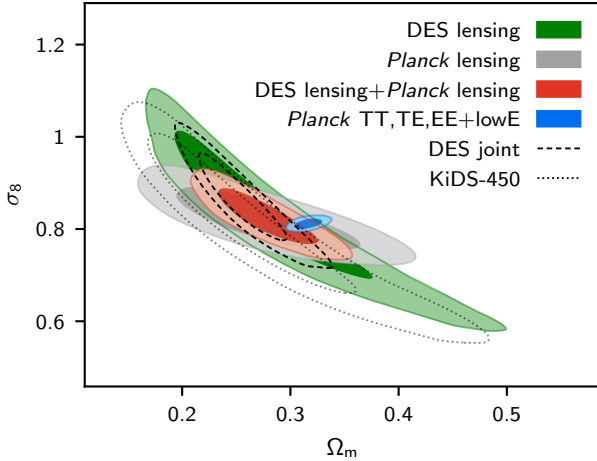


Fig. 19. Base- Λ CDM model 68% and 95% constraint contours on the matter-density parameter Ω_m and fluctuation amplitude σ_8 from DES lensing (Troxel et al. 2018b, green), *Planck* CMB lensing (grey), and the joint lensing constraint (red). For comparison, the dashed line shows the constraint from the DES cosmic shear plus galaxy-clustering joint analysis (DES Collaboration 2018b), the dotted line the constraint from the original KiDS-450 analysis (Hildebrandt et al. 2017, without the corrections considered in Troxel et al. 2018a), and the blue filled contour shows the independent constraint from the *Planck* CMB power spectra.

part of the degeneracy, giving a substantially tighter constraint than either alone. The lensing results separately, and jointly, are both consistent with the main *Planck* power-spectrum results, although preferring σ_8 and Ω_m values at the lower end of those allowed by *Planck*. The DES joint analysis of lensing and clustering is also marginally consistent, but with posteriors preferring lower values of Ω_m (see the next subsection). Overlap of contours in a marginalized 2D subspace does not of course guarantee consistency in the full parameter space. However, the values of the Hubble parameter in the region of Ω_m - σ_8 parameter space consistent with *Planck* Ω_m and σ_8 are also consistent with *Planck*'s value of H_0 . A joint analysis of DES with BAO and a BBN baryon-density constraint gives values of the Hubble parameter that are very consistent with the *Planck* power spectrum analysis (DES Collaboration 2018a).

5.6. Galaxy clustering and cross-correlation

The power spectrum of tracers of large-scale structure can yield a biased estimate of the matter power spectrum, which can then be used as a probe of cosmology. For adiabatic Gaussian initial perturbations the bias is expected to be constant on large scales where the tracers are out of causal contact with each other, and nearly constant on scales where nonlinear growth effects are small. Much more information is available if small scales can also be used, but this requires detailed modelling of perturbative biases out to $k \approx 0.3$ – 0.6 Mpc^{-1} , and fully nonlinear predictions beyond that. Any violation of scale-invariant bias on super-horizon scales would be a robust test for non-Gaussian initial perturbations protected by causality (Dalal et al. 2008). However, using the shape of the biased-tracer power spectrum on smaller scales to constrain cosmology requires at least a model of constant bias parameters for each population at each redshift, and, as precision is increased, or smaller scales probed, a model for the scale dependence of the bias. Early galaxy surveys provided cosmology constraints that were competitive with

those from CMB power spectrum measurements (e.g., Percival et al. 2001), but as precision has improved, focus has mainly moved away to using the cleaner BAO and RSD measurements and, in parallel, developing ways to get the quasi-linear theoretical predictions under better control. Most recent studies of galaxy clustering have focussed on investigating bias rather than background cosmology, with the notable exception of WiggleZ (Parkinson et al. 2012).

Here we focus on the first-year DES survey measurement of galaxy clustering (Elvin-Poole et al. 2018) and the cross-correlation with galaxy lensing (“galaxy-galaxy lensing” Prat 2018). By simultaneously fitting for the clustering, lensing, and cross-correlation, the bias parameters can be constrained empirically (DES Collaboration 2018b). Similar analyses using KiDS lensing data combined with spectroscopic surveys have been performed by van Uitert et al. (2018) and Joudaki et al. (2018).

To keep the theoretical model under control (nearly in the linear regime), DES exclude all correlations on scales where modelling uncertainties in the nonlinear regime could begin to bias parameter constraints (at the price of substantially reducing the total statistical power available in the data). Assuming a constant bias parameter for each of the given source redshift bins, parameter constraints are obtained after marginalizing over the bias, as well as a photometric redshift window mid-point shift parameter to account for redshift uncertainties. Together with galaxy lensing parameters, the full joint analysis has 20 nuisance parameters. Although this is a relatively complex nuisance-parameter model, it clearly does not fully model all possible sources of error: for example, correlations between redshift bins may depend on photometric redshift uncertainties that are not well captured by a single shift in the mean of each window’s population. However, Troxel et al. (2018b) estimate that the impact on parameters is below 0.5σ for all more complex models they considered. The DES theoretical model for the correlation functions (which we follow) neglects redshift-space distortions, and assumes that the bias is constant in redshift and k across each redshift bin; these may be adequate approximations for current noise levels and data cuts, but will likely need to be re-examined in the future as statistical errors improve.

Using the full combined clustering and lensing DES likelihood, for a total of 457 data points (DES Collaboration 2018b), the best-fit Λ CDM model has $\chi_{\text{eff}}^2 \approx 500$ or 513 with the *Planck* best-fit cosmology. Parameter constraints from the galaxy auto- and cross-correlation are shown in Fig. 20, together with the joint constraint with DES lensing (the comparison with DES galaxy lensing and CMB lensing alone is shown in Fig. 19).

Using the joint DES likelihood in combination with DES cosmological parameter priors gives (for our base- Λ CDM model with $\sum m_\nu = 0.06 \text{ eV}$)

$$\left. \begin{aligned} S_8 \equiv \sigma_8(\Omega_m/0.3)^{0.5} &= 0.793 \pm 0.024, \\ \Omega_m &= 0.256_{-0.031}^{+0.023}, \end{aligned} \right\} 68\%, \text{ DES.} \quad (32)$$

Planck TT,TE,EE+lowE+lensing gives a higher value of $S_8 = 0.832 \pm 0.013$, as well as larger $\Omega_m = 0.315 \pm 0.007$. As shown in the previous section, the DES lensing results are quite compatible with *Planck*, although peaking at lower Ω_m and σ_8 values. The full joint DES likelihood, however, shrinks the error bars in the σ_8 - Ω_m plane so that only 95% confidence contours overlap with *Planck* CMB data, giving a moderate (roughly 2% PTE) tension, as shown in Fig. 20. The dotted contour in Fig. 20 shows the result using the CamSpec *Planck* likelihood, which gives results slightly more consistent with DES than the default Plik likelihood. The *Planck* result is therefore sensitive to the

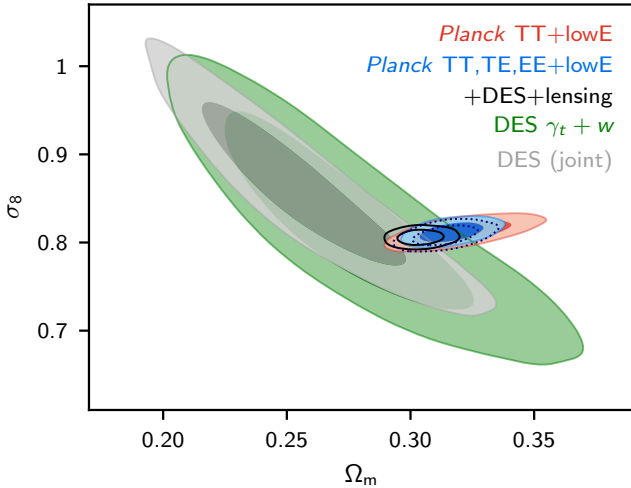


Fig. 20. Base- Λ CDM model constraints from the Dark Energy Survey (DES), using the shear-galaxy correlation and the galaxy auto-correlation data (green) and the joint result with DES lensing (grey), compared with *Planck* results using TT+lowE and TT,TE,EE+lowE. The black solid contours show the joint constraint from *Planck* TT,TE,EE+lowE+lensing+DES, assuming the difference between the data sets is purely statistical. The dotted line shows the *Planck* TT,TE,EE+lowE result using the CamSpec likelihood, which is slightly more consistent with the DES contours than using the default PLik likelihood. Contours contain 68% and 95% of the probability.

details of the polarization modelling at the 0.5σ level, and the tension cannot be quantified robustly beyond this level.

Combining DES with the baseline *Planck* likelihood pulls the *Planck* result to lower Ω_m and slightly lower σ_8 , giving

$$\left. \begin{aligned} \sigma_8 &= 0.811 \pm 0.011, \\ \Omega_m &= 0.3040 \pm 0.0060, \\ \sigma_8 &= 0.8062 \pm 0.0057, \end{aligned} \right\} \begin{array}{l} (68\%, \text{Planck} \\ \text{TT,TE,EE+lowE+} \\ \text{lensing+DES}). \end{array} \quad (33)$$

A similar shift is seen without including *Planck* lensing, and is disfavoured by *Planck* CMB with a total $\Delta\chi_{\text{eff}}^2 \approx 13$ for the CMB likelihoods (comparing the *Planck*-only best fit to the fit when combined with DES). The shift in parameters is also larger than would be expected for Gaussian distributions, given the small change in parameter covariance. The corresponding change in χ_{eff}^2 for the DES likelihood is $\Delta\chi_{\text{eff}}^2 \approx 10$, which is high, but less surprising given the 4–5 contribution expected from the number of parameters that are much better constrained by *Planck*. The summary consistency statistic $\chi_{\text{eff,joint}}^2 - \chi_{\text{eff,DES}}^2 - \chi_{\text{eff,Planck}}^2 \approx 14$, which is high at the roughly 1% PTE level, given the expected value of 4, assuming roughly Gaussian statistics (Raveri & Hu 2019).

In summary, the DES combined probes of Λ CDM parameters are in moderate percent-level tension with *Planck*. Whether this is a statistical fluctuation, evidence for systematics, or new physics is currently unclear. In this paper, we follow the philosophy of PCP13 and PCP15 of making minimal use of other astrophysical data in combination with *Planck*, using BAO as our primary complementary data set. We therefore do not include DES results in most of the parameter constraints discussed in this paper. We do, however, consider the impact of the DES weak lensing results on dark-energy and modified-gravity constraints in Sect. 7.4 and on neutrino masses in Sect. 7.5.1. We also include DES for a wider range of models in the *Planck* parameter tables available on the PLA.

5.7. Cluster counts

Counts of clusters of galaxies provide an additional way of constraining the amplitude of the power spectrum at low redshifts (e.g., Pierpaoli et al. 2001; Komatsu & Seljak 2002, and references therein). *Planck* clusters, selected via the thermal Sunyaev-Zeldovich (tSZ) signature, were used to explore cosmological parameters in *Planck* Collaboration XX (2014). This analysis was revisited using a deeper sample of *Planck* clusters in *Planck* Collaboration XXIV (2016). We have not produced a new tSZ cluster catalogue in the 2018 *Planck* data release and so the results presented in this section are based on the 439 clusters in the MMF3 cluster cosmology sample, as analysed in *Planck* Collaboration XXIV (2016). Comparison with the 2018 CMB *Planck* power spectrum results show differences primarily from changes to the base- Λ CDM model parameters caused by the tighter constraints on τ . The impact of the lower value of τ reported in *Planck* Collaboration Int. XLVI (2016) on the interpretation of cluster counts has been discussed by Salvati et al. (2018).

We first review the main results from *Planck* Collaboration XXIV (2016). There has been increasing recognition that the calibration of cluster masses is the dominant uncertainty in using cluster counts to estimate cosmological parameters. In the analysis of *Planck* clusters, the cluster tSZ observable was related to the cluster mass M_{500}^{26} using X-ray scaling relations (Arnaud et al. 2010), calibrated against a subsample of the *Planck* clusters. The X-ray masses are, however, derived assuming hydrostatic equilibrium and are expected to be biased low (e.g., Nagai et al. 2007). This was accounted for by multiplying the true masses by a so-called ‘‘hydrostatic mass bias’’ factor of $(1 - b)$. The strongest constraints on this bias factor come from weak gravitational lensing estimates of cluster masses. *Planck* Collaboration XXIV (2016) considered three lensing mass calibrations²⁷: $(1 - b) = 0.69 \pm 0.07$ from 22 *Planck* clusters from the Weighing the Giants lensing programme (von der Linden et al. 2014); $(1 - b) = 0.78 \pm 0.08$ from 37 *Planck* clusters calibrated by the Canadian Cluster Comparison Project (Hoekstra et al. 2015); and $1/(1 - b) = 0.99 \pm 0.19$ from *Planck* CMB-lensing mass estimates of the MMF3 cluster sample (*Planck* Collaboration XXIV 2016). More recently, Sereno et al. (2017) have analysed 35 *Planck* clusters with galaxy shear data from the CFHTLenS (Heymans et al. 2012) and RCSLenS (Hilbrandt et al. 2016) surveys, finding $(1 - b) \approx 0.77 \pm 0.11$ for all clusters and $(1 - b) = 0.68 \pm 0.11$ for the 15 clusters in the cosmological sample. Additionally, Penna-Lima et al. (2017) use gravitational lensing measurements from HST images of 21 *Planck* clusters finding $(1 - b) = 0.73 \pm 0.10$.

The determination of cosmological parameters such as σ_8 and Ω_m from *Planck* cluster counts is strongly dependent on the prior adopted for the mass bias parameter. In this paper, we use the *Planck* TT,TE,EE+lowE+lensing likelihood in combination with the *Planck* cluster counts to derive a constraint on $(1 - b)$ (following similar analyses described in *Planck* Collaboration XX 2016 and Salvati et al. 2018). This gives

$$(1 - b) = 0.62 \pm 0.03 \quad \begin{array}{l} (68\%, \text{Planck} \\ \text{TT,TE,EE+lowE+lensing}), \end{array} \quad (34)$$

²⁶ The mass contained within a sphere of radius R_{500} , centred on the cluster, where R_{500} is the radius at which the mean density is 500 times the critical density at the redshift of the cluster.

²⁷ See Sif3n et al. (2016) for a discussion of dynamical mass estimates for SZ-selected clusters.

compared to 0.58 ± 0.04 using the 2015 TT,TE,EE+lowP likelihood (Planck Collaboration XX 2016). The roughly 1σ upward shift in Eq. (34) is mainly caused by the 2018 change in the τ constraint. The mass bias of Eq. (34) is at the lower end of the weak-lensing mass estimates, but is about 2σ lower than the *Planck* CMB-lensing mass calibration reported in Planck Collaboration XX (2016).

Zubeldia & Challinor (2019) have revisited the *Planck* CMB-lensing mass calibration, incorporating the CMB-lensing mass estimates within a likelihood describing the *Planck* cluster counts, together with a *Planck* prior on θ_{MC} . This study corrects for significant biases in the analysis reported in Planck Collaboration XX (2016). Zubeldia & Challinor (2019) find $(1 - b) = 0.71 \pm 0.10$ and $\sigma_8(\Omega_m/0.33)^{0.25} = 0.765 \pm 0.035$. These results, based entirely on *Planck* data, are consistent with the base- Λ CDM parameters from the *Planck* power spectra and with the inferred mass bias of Eq. (34).

Since PCP15 there have been a number of new analyses of cluster counts using other surveys. Two recent studies (Mantz et al. 2015; de Haan et al. 2016), with very different selection criteria, use weak gravitational lensing mass determinations from the Weighing the Giants programme to calibrate cluster scaling relations. de Haan et al. (2016) analysed a sample of 377 clusters at $z > 0.25$ identified with SPT, finding $\sigma_8(\Omega_m/0.27)^{0.3} = 0.797 \pm 0.031$, while Mantz et al. (2015) analysed an X-ray-selected sample of clusters from the ROSAT All-Sky survey, finding $\sigma_8(\Omega_m/0.3)^{0.17} = 0.81 \pm 0.03$. These measurements can be compared to our baseline Λ CDM constraints (*Planck* TT,TE,EE+lowE+lensing) of $\sigma_8(\Omega_m/0.27)^{0.3} = 0.849 \pm 0.010$ and $\sigma_8(\Omega_m/0.3)^{0.17} = 0.817 \pm 0.076$.

Schellenberger & Reiprich (2017) have analysed a sample of 64 of the brightest X-ray clusters using a prior on the hydrostatic mass bias from Biffi et al. (2016). These authors find $\Omega_m = 0.303 \pm 0.009$, $\sigma_8 = 0.790^{+0.030}_{-0.028}$, and $S_8 = \sigma_8(\Omega_m/0.3)^{1/2} = 0.792 \pm 0.054$. Each of these numbers is within about 1σ of the *Planck* base- Λ CDM best-fit cosmology reported in this paper. Finally, we mention the analysis of ROSAT-observed X-ray clusters carried out by Böhringer et al. (2014, 2017). These authors choose a central value for the hydrostatic mass bias of $(1 - b) = 0.9$, although they allow for small variations in the slope (7%) and normalization (14%) of the X-ray luminosity-mass relation; they find constraints the σ_8 - Ω_m plane in tension with *Planck* at about 2.5σ .

In summary, accurate calibrations of cluster masses are essential if cluster counts are to be used as cosmological probes. Given the uncertainties in these calibrations, we do not use cluster counts in our main parameter grid. Consistency of cluster counts with the best-fit *Planck* base- Λ CDM cosmology requires hydrostatic mass biases (Eq. (34)) that are at the lower end, but within about 1σ of bias factors estimated from weak-lensing cluster masses. The combined *Planck* CMB-lensing and cluster-count analysis reported by Zubeldia & Challinor (2019) is in good agreement with the *Planck* base- Λ CDM cosmology. At this time, there is no compelling evidence for a discrepancy between *Planck*-, SPT-, or X-ray-selected cluster counts and the base- Λ CDM model.

6. Internal consistency of Λ CDM model parameters

In this section we briefly discuss a couple of curious features of the *Planck* data that lead to moderate tensions in parameter consistency tests. We first discuss how parameters vary between high and low multipoles, and the relevant features in the power spectra that may be responsible for these shifts. We then discuss

the related issue of how the full multipole range appears to prefer more lensing than predicted by Λ CDM fits. We end this section with a discussion of systematic uncertainties.

6.1. Consistency of high and low multipoles

The *Planck* CMB temperature power spectrum shows a conspicuous dip over the multipole range $20 \lesssim \ell \lesssim 30$ compared to Λ CDM fits, as can be seen in Fig. 1. This feature was first observed by WMAP (Bennett et al. 2003), and was discussed in detail in PCP13. Since it is detected consistently by both WMAP and *Planck* at multiple frequencies, it cannot plausibly be explained by an instrumental systematic or foreground. The large-scale *Planck* temperature map is signal dominated, so the dip feature is almost identical in this final release. PCP13 also noted an approximately 2.7σ mismatch between the best-fit Λ CDM cosmology and the amplitude of the measured temperature power spectrum at $\ell \leq 30$. However, with the tighter optical depth constraints used in this paper and improvements in the high multipole likelihoods we find no strong evidence for an amplitude mismatch. The *Planck* TT,TE,EE+lowE+lensing best-fit Λ CDM model provides a good overall fit to the temperature multipoles at $\ell < 30$ ($\chi^2_{\text{eff}} \approx 23$ for 28 data points), and because of the skewed χ^2 -like distribution of the CMB spectrum estimators, it is expected that typically more than half of the data points are below the theoretical model values (see Fig. 1). The statistical significance of the dip feature is hard to quantify, since it was identified a posteriori, but PPL15 suggest a significance of about 2.8% after maximizing over extremal ℓ ranges found in simulations. This could be an indication of new physics at large scales, for example associated with a sharp feature in the inflationary potential (as considered by Peiris et al. 2003, and many subsequent researchers). Alternatively, it could just be a statistical fluctuation, which is our baseline assumption. However, since the dip is a relatively unusual fluctuation and it is near one end of the multipole range, it tends to pull cosmological parameters more than would be expected in typical realizations of a Λ CDM cosmology. This needs to be borne in mind in assessing parameter shifts between low and high multipoles.

WMAP measured the CMB temperature fluctuations up to $\ell \approx 800$ (Bennett et al. 2013). The higher-resolution data from *Planck* substantially increases the multipole range of the temperature power spectrum out to $\ell \approx 2500$. Cosmological parameters are therefore expected to shift (usually towards the truth) from the mean posterior values measured by WMAP, together with a reduction in the error bars. This is what is seen, with the *Planck* values of H_0 and n_s decreasing, and Ω_m and $\Omega_m h^2$ increasing, along with substantially smaller errors. However as noted in PCP13 the magnitudes of the shifts appear to be slightly larger than might be expected statistically, assuming the base- Λ CDM cosmology. This stimulated additional work on the consistency of the *Planck* power spectra reported in PPL15 and to further investigations of the consistency of cosmological parameters measured from high and low multipoles from *Planck* (Addison et al. 2016; Planck Collaboration Int. LI 2017). As noted in the introduction, there is a very good agreement between *Planck* and WMAP temperature maps on the scales observed by WMAP (Planck Collaboration I 2016; Huang et al. 2018), but an inconsistency with high multipoles could indicate either new physics beyond Λ CDM, or the presence of some unidentified systematics associated with the *Planck* data and/or the foreground model. Planck Collaboration Int. LI (2017) find that although some cosmological parameters differ by more than 2σ between $\ell < 800$ and $\ell > 800$, accounting for the multi-dimensional parameter

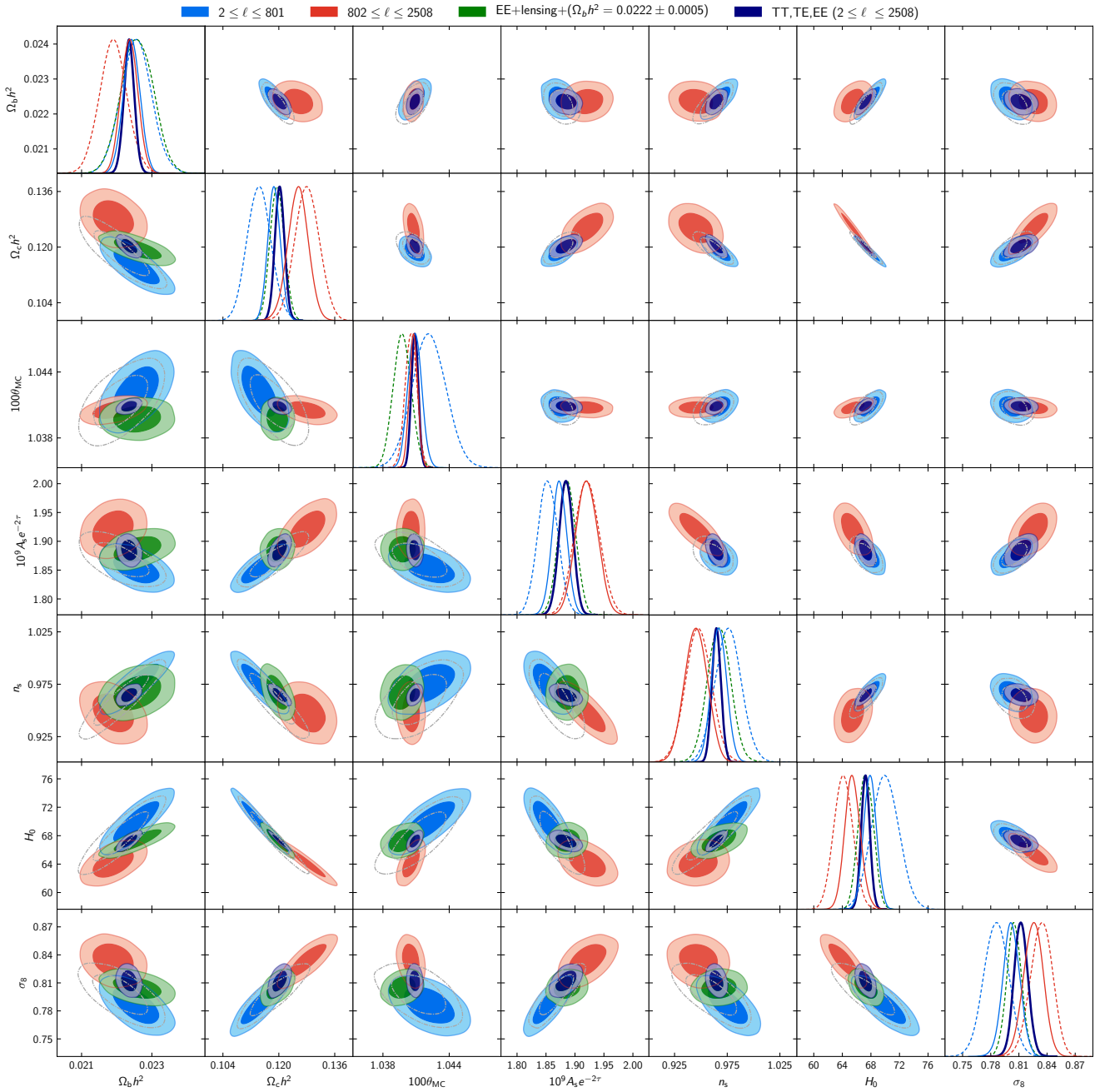


Fig. 21. Base- Λ CDM 68% and 95% parameter constraint contours from the CMB power spectra using $\ell \leq 801$ (blue), compared to $\ell \geq 802$ (red). All results use the `plik_lite` *Planck* likelihood, and also include the low- ℓ `SimAll` “lowE” likelihood to constrain the optical depth τ ; the `Commander` likelihood is used for temperature multipoles $\ell < 30$. The lower triangle contains the *Planck* temperature likelihoods, which show a moderate tension between high and low multipoles; however, they intersect in a region of parameter space consistent with the nearly-independent constraint from EE+lensing combined with a conservative prior $\Omega_b h^2 = 0.0222 \pm 0.0005$, motivated by element-abundance observations (green). The upper triangle shows the equivalent results from *Planck* TT,TE,EE+lowE at low and high multipoles. The full combined result from *Planck* TT,TE,EE+lowE is shown as the navy contours. The unfilled grey contours show the result for multipoles $30 \leq \ell \leq 801$ (that is, removing the low- ℓ `Commander` likelihood that pulls parameters to give lower temperature power, due to the dip below $\ell \approx 30$). The diagonal plots are the marginalized parameter constraints, where results corresponding to the lower triangle are shown dashed, while the upper triangle are the solid curves.

space including correlations between parameters, the shifts are at the 10% level and hence not especially unusual. Nonetheless, parameter shifts, particularly in the fluctuation amplitude and Hubble parameter (which are directly relevant for the Λ CDM-comparison with external data, as discussed in Sect. 5) are worth a brief re-examination using the additional information provided by the *Planck* polarization spectra.

Constraints on cosmological parameters from power spectra at high multipoles require a foreground model. Previous studies have shown that results are not very sensitive to the specific assumptions that are made within the broad context of slowly varying foreground spectra expected on physical grounds (Addison et al. 2016; Planck Collaboration Int. LI 2017). In this section, we use the `plik_lite` *Planck*

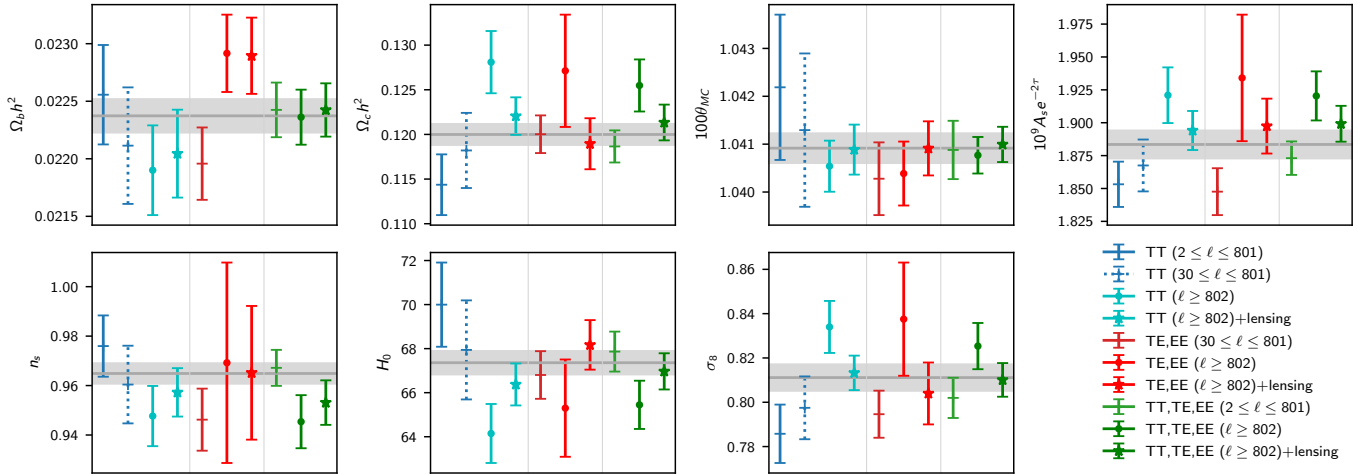


Fig. 22. Base- Λ CDM 68% marginalized parameter constraints for various combinations of power spectrum ranges (all using `plik_lite` and also including low- ℓ polarization “lowE”). Points marked with a cross are from $2 \leq \ell \leq 801$, while points marked with a circle are from $\ell \geq 802$. Dotted errors are the result from $30 \leq \ell \leq 801$, without the `Commander` large-scale temperature likelihood, showing that $\ell < 30$ pulls the low-multipole parameters further from the joint result. Points marked with a star are from $\ell \geq 802$ combined with the lensing likelihood, showing that constraining the lensing amplitude pulls all the results from high multipoles towards better consistency with the results from lower multipoles. The grey horizontal band shows the combined 68% constraint from *Planck* TT,TE,EE+lowE+lensing.

likelihood, described in detail in PPL18, which has the standard *Planck* foreground and nuisance parameters marginalized out without further assumptions on the cosmology²⁸. For standard model extensions `plik_lite` accurately reproduces results from the full *Planck* likelihood. It allows us to explore the high- ℓ likelihood accounting for foreground uncertainties, but with the foregrounds constrained in a sensible way from their spectra over the full multipole range. We consider the multipole ranges $\ell \leq 801$ and $\ell \geq 802$ (corresponding to the boundary of one of the `plik_lite` bins), so that the low-multipole range is roughly comparable to WMAP and the two ranges have similar statistical power on most parameters. Results splitting at $\ell \approx 1000$ are similar, but with larger errors in the high multipole range.

Figure 21 shows a comparison of the high and low multipole ranges, both for temperature (lower triangle, as previously discussed by Addison et al. 2016 and Planck Collaboration Int. LI 2017), and new results for the combined temperature-polarization likelihood (upper triangle). Part of the difference between the low- and high-multipole ranges is caused by the large-scale temperature dip discussed above; if we exclude multipoles $\ell < 30$ (unfilled grey contours), the contours from $\ell \leq 801$ shift towards the area of consistency with the high multipoles. This could indicate that the low-multipole results have been pulled unusually far from the truth by the large-scale power spectrum dip; if so, the WMAP temperature results would also have been pulled at a similar (but not identical) level. The region of overlap of the high- and low-multipole parameter constraints is consistent with constraints from the nearly-independent combination of *EE* polarization and lensing with a conservative $\Omega_b h^2$ prior (green contours). This is consistent with a statistical fluctuation pulling the low and high multipoles in opposite directions, so that their intersection is closer to the truth if Λ CDM is correct.

Figure 22 shows marginalized individual parameter constraints, and also a comparison with the results from the

polarization likelihoods at high and low multipoles. The $\ell \geq 802$ temperature results pull parameters to a region of higher matter density and fluctuation amplitude (and to lower n_s and H_0) than the lower multipole range, and predict a CMB lensing amplitude parameter $\sigma_8 \Omega_m^{0.25} = 0.649 \pm 0.018$. This is in tension with the CMB lensing-reconstruction measurement of $\sigma_8 \Omega_m^{0.25} = 0.589 \pm 0.020$ at 2.2σ (as pointed out by Addison et al. 2016 with 2015 data; also see the closely-related discussion in the next subsection). As shown in Fig. 22, combining the $\ell \geq 802$ CMB likelihood with the lensing reconstruction, all parameter results move back towards the same region of parameter space as combining with $\ell \leq 801$, consistent with the high- ℓ temperature result having fluctuated high along the main degeneracy direction. As discussed in Sects. 2.3 and 3.3, the combined CMB power spectrum results over the full multipole range are consistent with the lensing likelihood.

It is also interesting to compare to parameter constraints from the CMB power spectrum multipoles $\ell \leq 801$ combined with the lensing and BAO, which gives

$$\left. \begin{aligned} H_0 &= (67.85 \pm 0.52) \text{ km s}^{-1} \text{ Mpc}^{-1}, \\ \sigma_8 &= 0.8058 \pm 0.0063, \\ \Omega_m &= 0.3081 \pm 0.0065. \end{aligned} \right\} \begin{array}{l} 68\%, \text{ TT, TE, EE} \\ [\ell \leq 801] \\ +\text{lowE}+ \\ \text{lensing+BAO.} \end{array} \quad (35)$$

These results are entirely independent of the cosmological parameter fit to the $\ell \geq 801$ power spectra, but agree well at the 1σ level with the full joint results in Table 1 (which have similar errors on these parameters). An equivalent result could be obtained using WMAP data after replacing their low- ℓ polarization with the *Planck* HFI measurement (i.e., lowE).

For the temperature likelihoods, the difference between the low- and high-multipole constraints remains evident, with $\Omega_m h^2$ differing at the 2.8σ level. Adding polarization, the results from the multipole ranges are more consistent, as shown in Fig. 22, though the difference in $\Omega_m h^2$ is still unusual at the roughly 2σ level. However, the shifts in the different parameters are all highly correlated, due to partial parameter degeneracies, so the significance of any individual large shift is lower after accounting for the number of parameters (Planck Collaboration Int. LI 2017). The internal tensions between multipole ranges appear to

²⁸ We do not attempt to quantify likelihood modelling differences in this section, but a `CamSpec`-based likelihood gives slightly less tension between high and low multipoles (especially with polarization), associated with the weaker preference for $A_L > 1$, as discussed in more detail in Sect. 6.2.

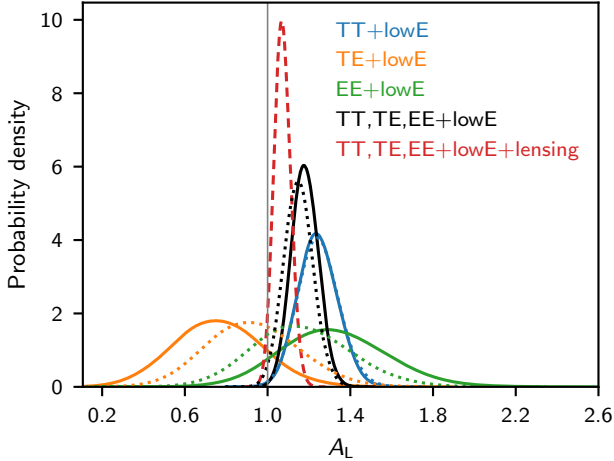


Fig. 23. Constraints on the value of the consistency parameter A_L , as a single-parameter extension to the base- Λ CDM model, using various combinations of *Planck* data. When only power spectrum data are used, $A_L > 1$ is favoured at about 3σ , but including the lensing reconstruction the result is consistent at 2σ with $A_L = 1$. The dotted lines show equivalent results for the CamSpec likelihood, which peak slightly nearer to $A_L = 1$, indicating some sensitivity of the A_L results to choices made in constructing the high-multipole likelihoods.

be consistent with moderate statistical fluctuations, related to the low- ℓ dip at large scales and correlated with the lensing amplitude on small scales. The large-scale feature is well determined by both WMAP and *Planck* and very robustly measured. The internal consistency of the *Planck* power spectra between different frequencies and detectors (PPL15; PPL18) argues against systematics driving large parameter shifts at high multipoles. Equation (35) also demonstrates that any effect from the high-multipole spectra alone cannot be pulling our baseline parameters by more than about 1σ . In the next subsection we describe in more detail the apparent preference for a higher lensing amplitude, and the features in the observed spectrum that could be responsible for it.

6.2. Lensing smoothing and A_L

In addition to the direct measurement of CMB lensing described in Sect. 2.3 and PL2018, lensing can be seen in the *Planck* CMB power spectra via the lensing-induced smoothing of the acoustic peaks and transfer of power to the damping tail. This effect is modelled in our main parameter analysis, and can be calculated accurately from the unlensed CMB power spectra and the CMB lensing potential power spectrum in each model (Seljak 1996; Lewis & Challinor 2006). Interesting consistency checks include testing if the amplitude of the smoothing effect in the CMB power matches expectation and whether the amplitude of the smoothing is consistent with that measured by the lensing reconstruction. To do this, the theoretical prediction for the lensing spectrum in each model is often scaled by an “ A_L ” consistency parameter, where the theoretical expectation is that $A_L = 1$ (Calabrese et al. 2008).

As shown in Fig. 3, the *Planck* lensing-reconstruction power spectrum is consistent with the amplitude expected for Λ CDM models that fit the CMB spectra, so the *Planck* lensing measurement is compatible with $A_L = 1$. However, the distributions of A_L inferred from the CMB power spectra alone are shown in Fig. 23 for various different data combinations, and these

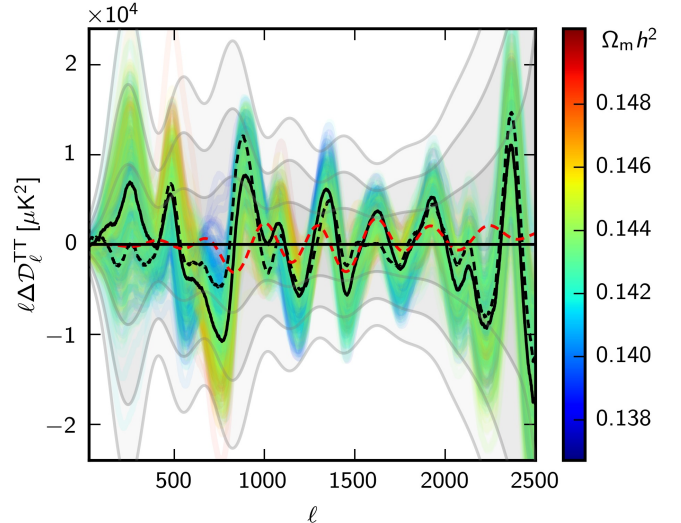


Fig. 24. Base- Λ CDM model ($A_L = 1$) TT power spectrum residuals smoothed with a Gaussian kernel of width $\sigma_\ell = 40$. The black line shows the smoothed difference between the coadded data points and the theoretical model for the *Planck* TT+lowE best-fit model, while coloured lines show the residuals for samples over the allowed parameter space coloured by the value of $\Omega_m h^2$. Grey bands show the 1, 2, and 3σ diagonal range expected for the smoothed residuals in the best-fit model. The red dashed line shows 10% of the lensing-smoothing difference predicted in the best-fit model, displaying the oscillatory signal expected if there were more lensing of the acoustic peaks. The data residuals are not particularly anomalous, but the residuals have a similar pattern to the lensing smoothing difference over the approximate range $\ell = 1100$ – 2000 , giving a preference for around 10% more lensing at fixed cosmological parameters. Allowed models with lower $\Omega_m h^2$ (and hence higher H_0) predict less lensing and give a larger oscillatory residual, preferring relatively more lensing smoothing than models with high matter density. The black dashed line shows the smoothed residual for the *Planck* TT+lowE best fit to Λ CDM+ A_L (with $A_L = 1.19$).

indicate a preference for $A_L > 1$, with

$$A_L = 1.243 \pm 0.096 \quad (68\%, \text{Planck TT+lowE}), \quad (36a)$$

$$A_L = 1.180 \pm 0.065 \quad (68\%, \text{Planck TT,TE,EE+lowE}), \quad (36b)$$

assuming a Λ CDM+ A_L model. The TE polarization data alone slightly prefer $A_L < 1$, with the EE data slightly preferring $A_L > 1$; however, both are consistent with $A_L = 1$ within 2σ . The joint combined likelihood shifts the value preferred by the TT data downwards towards $A_L = 1$, but the error also shrinks, increasing the significance of $A_L > 1$ to 2.8σ (99.8% of parameter samples have $A_L > 0$, so the one-tailed limit is almost exactly 3σ). Moreover, combining with the lensing likelihood further pulls the constraint towards $A_L = 1$, which is then consistent with the data to within 2σ ; we see that the preference for $A_L > 1$ is driven by the CMB power spectra alone.

The preference for high A_L is not just a volume effect in the full parameter space (see PCP13 for discussion of such effects in multi-parameter fitting), with the best fit improved by $\Delta\chi_{\text{eff}}^2 = -8.7$ when adding A_L for TT+lowE and $\Delta\chi_{\text{eff}}^2 = -9.7$ for TT,TE,EE+lowE. The bulk of the $\Delta\chi_{\text{eff}}^2$ comes from the high- ℓ likelihood (mostly in the range $600 < \ell < 1500$); however, the low- ℓ temperature commander likelihood fit is also improved if A_L is free, with $\Delta\chi_{\text{eff}}^2 = -2.3$ and $\Delta\chi_{\text{eff}}^2 = -1.3$ for the TT+lowE and TT,TE,EE+lowE, respectively, due to the lower amplitude of the A_L fit on large scales. The change in fit to the low- ℓ polarization is not very significant ($\Delta\chi_{\text{eff}}^2 = -0.2$ and $\Delta\chi_{\text{eff}}^2 = -0.4$).

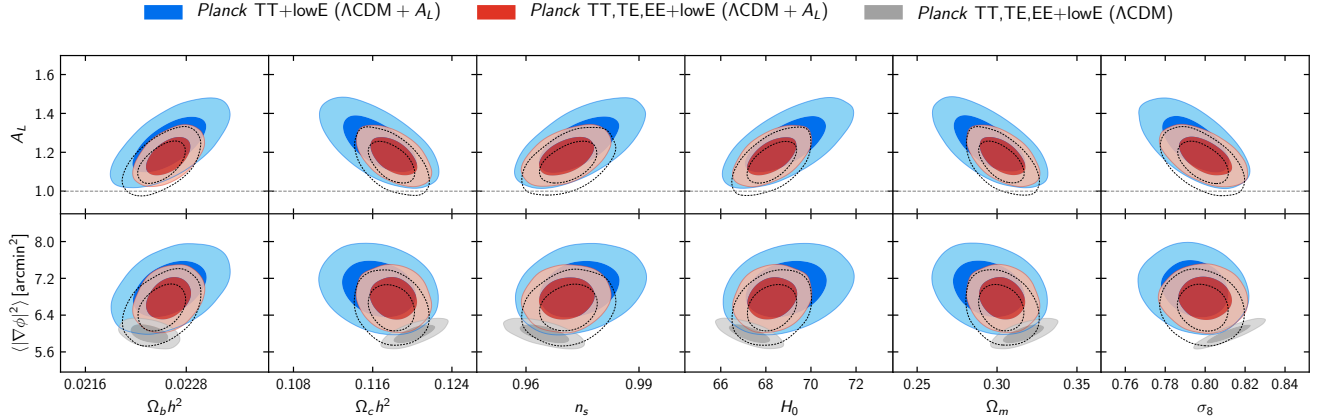


Fig. 25. Marginalized 68% and 95% parameter constraint contours when adding A_L as a single-parameter extension to the base- Λ CDM model, with (red) and without (blue) small-scale polarization, compared to the constraints in the base- Λ CDM model (grey). The dashed contours show equivalent results for *Planck* TT,TE,EE+lowE when using the CamSpec likelihood, which gives results with A_L nearer unity and with slightly larger errors. The *second row* of subplots show, on the left axis, the predicted lensing deflection angle variance (from lensing multipoles $2 \leq \ell \leq 2000$), which is a measure of the amount of actual lensing: the TT,TE,EE+lowE likelihood prefers about 10% more actual lensing power (associated with lensing smoothing), but in the (unphysical) varying- A_L case this can be achieved using cosmological parameters that predict less lensing than in Λ CDM but substantially larger A_L , giving a preference for $A_L \approx 1.2$.

The determination of A_L from the high- ℓ polarization data and the TT,TE,EE+lowE joint combination depends on the calibration of the polarization channels, and is affected by different ways of modelling the polarization efficiencies, as discussed in Sect. 2.2. The results from the CamSpec likelihood (which uses spectrum-based rather than map-based calibrations for *TE* and *EE*) are somewhat shifted with respect to the *Planck* likelihood, as shown by the dotted lines in Fig. 23, and have larger errors, giving

$$A_L = 1.246^{+0.092}_{-0.100} \quad (68\%, \text{ TT+lowE [CamSpec]}), \quad (37a)$$

$$A_L = 1.149 \pm 0.072 \quad (68\%, \text{ TT,TE,EE+lowE [CamSpec]}). \quad (37b)$$

Using CamSpec there is still a clear preference for $A_L > 1$, but the joint result with polarization is now only just over 2σ above $A_L = 1$. The differences between these *Planck* and CamSpec results arise from differences in the methodologies used to create the likelihoods. Although both likelihoods clearly show a preference for $A_L > 1$, this cannot be claimed to be a robust detection at much over 2σ (see also *Efstathiou & Gratton 2019*).

The preference for $A_L > 1$ within the Λ CDM model is a curious feature of the *Planck* CMB power spectrum data, and has already been discussed extensively in *PCP13*, *PCP15*, and *Planck Collaboration Int. LI (2017)*, although it is now slightly more significant. In temperature, over half of the small (approximately 0.02) upward shift in A_L compared to 2015 is explained by the lower optical depth from the 2018 low- ℓ likelihood: lower τ implies lower A_s to match the high- ℓ CMB fluctuation amplitude, and hence larger A_L to yield a lensing amplitude and hence amount of smoothing at the same level as 2015. In polarization about 40% of the shift in A_L is explained by changes in τ , with changes in the maps, modelling for beam leakage, and polarization efficiencies explaining the rest.

The high- ℓ temperature likelihood preference for more lensing smoothing than allowed by Λ CDM can be seen by eye in the smoothed data residuals plotted in Fig. 24; over almost all the allowed Λ CDM parameter space there is an oscillatory residual in the range $1100 \lesssim \ell \lesssim 2000$ that matches the shape of the

lensing smoothing²⁹ (although in other multipole ranges it does not match at all). The residual is not obviously anomalous, with the TT Λ CDM best fit improving by $\Delta\chi^2 \approx 4$ if a best-fit oscillatory residual (with $A_L \approx 1.1$) is added to the best-fit Λ CDM theory model. The stronger preference for $A_L > 1$ when A_L varies arises because degeneracies between A_L , cosmological parameters, and foregrounds improves the fit at both high and lower multipoles, as shown by the black dashed line in Fig. 24. In Λ CDM the lensing amplitude can be increased by increasing $\Omega_m h^2$; however, the model then becomes a bad fit because of the poorer agreement at $\ell < 1000$). Varying A_L allows a high A_L to remove the oscillatory residual at high multipoles that appears in Λ CDM with lower $\Omega_m h^2$, giving best fits with lower $\Omega_m h^2$ and higher H_0 (by 1.5–2.0 σ , depending on the exact combination of data used) that are not favoured in the physical Λ CDM model. Lower values of $\Omega_m h^2$ give higher values of n_s , lowering the theory prediction on large scales, so high A_L models are also slightly preferred by the dip in the $\ell < 30$ *Planck* temperature data. The parameter degeneracies are illustrated in Fig. 25.

The A_L results appear to be robust to changes in foreground modelling in the baseline likelihood, with the CamSpec 545 GHz cleaned likelihood (see Appendix A) giving very similar results. However, the dip in the residuals at $1420 \lesssim \ell \lesssim 1480$, part of the oscillatory feature that looks like additional lensing, nearly coincides with an approximately 3σ discrepancy (for the best-fit foreground cosmology model) between the 143 GHz and 217 GHz power spectra at $1450 \lesssim \ell \lesssim 1510$, with the 217 GHz spectrum pulling the coadded spectrum low compared to 143 GHz by an amount comparable to the coadded residual (at $\ell = 1480$ the 217 GHz spectrum is $\mathcal{D}_\ell \approx 7 \mu\text{K}^2$ lower than 143 GHz with smoothing $\sigma_\ell = 40$; see *PPL18*). This may be an indication that the preference for A_L at high multipoles is partly

²⁹ Although the oscillatory pattern looks most similar to lensing at high multipoles, an increase in the foreground model amplitude can decrease the oscillation amplitude in the theory contribution to the spectrum, and hence appear as an oscillatory difference. For example $\Delta n_s \approx -0.02$, combined with an implausibly large change in the foreground model, gives a difference in the predicted spectrum with an oscillatory component that has similar amplitude to $\Delta A_L \approx 0.1$; see the related discussion in *Planck Collaboration Int. LI (2017)*.

due to unknown systematics or foregrounds. However, tightly cutting the ℓ range that contributes to the 3σ frequency difference does not in itself shift A_L to substantially lower values (though cutting all of $1420 \lesssim \ell \lesssim 1480$ does), and the significance of the oscillatory feature in the Λ CDM CMB residual is in any case not very high. If it is largely a statistical fluctuation, it would be expected to vary with changes in sky area; that is somewhat the case, with around 80% sky area giving a substantially less oscillatory residual to the same best-fit Λ CDM model at $\ell \lesssim 1600$, but still favouring high A_L . Different power spectrum analyses have also shown the preference for A_L (Spergel et al. 2015; Couchot et al. 2017), though with varying significance, which could indicate that our roughly 3σ significance is partly an issue of analysis choices, e.g., the sky areas included and foreground priors chosen.

The dashed line in Fig. 3 shows the lensing power spectrum in the *Planck* TT,TE,EE+lowE best-fit Λ CDM+ A_L model, which is clearly inconsistent with the lensing reconstruction, since it lies above almost all of the measured data points. Because the amplitude of the lensing smoothing effect can be calculated from the lensing potential power spectrum alone, which we can also empirically measure, it is impossible to increase the lensing smoothing of the CMB peaks without also increasing the measured lensing reconstruction amplitude. This remains true if the lensing power spectrum is allowed to vary in shape (Motloch & Hu 2018). The actual lensing smoothing effect can also partly be removed by delensing, as shown by Larsen et al. (2016) and Carron et al. (2017). In PL2018 we update these delensing analyses, and show (using the internal lensing reconstruction, a *Planck* CIB map as a tracer of the lensing potential, and a combined estimate) that the amount of peak sharpening observed after delensing is consistent with theoretical expectations (e.g., for the *TT* spectrum, we measure a reduction in lensing smoothing of 0.411 ± 0.028 , compared to the expected value of 0.375 when using a combination of CIB and *Planck* lensing reconstruction).

Although the residuals shown in Fig. 24 between the data and the Λ CDM best fit temperature spectrum show what looks like an oscillatory lensing residual at high ℓ , the fit itself is determined by the entire range of multipoles (and the low- ℓ polarization than constrains τ). The preference for $A_L > 1$ could therefore be attributed to other scales when considering the CMB spectra alone. For example, after removing $\ell < 30$ in both temperature and polarization, A_L from *TT* is consistent with unity to within 1σ . However, in this case the Λ CDM lensing amplitudes are still large, giving a value of $\Omega_m \sigma_8^{0.25}$, in 2σ tension with the lensing reconstruction. This is another reflection of the tension noted in Sect. 6.1 between the lensing reconstruction and the lensing amplitude predicted using temperature multipoles $\ell \gtrsim 800$: the two tensions are therefore not independent and largely driven by the same features of the Λ CDM fit to the temperature and low- ℓ polarization data.

If $A_L > 1$ is not just a statistical fluctuation, but comes from new physics changing the theoretical predictions, it could be something that mimics the smoothing effect in the CMB peaks. The *lensing* smoothing effect comes from averaging over the sky a spectrum that is locally varying (due to magnification and shear locally changing the scale and shape of the CMB peaks). Conceptually, the temperature lensing reconstruction works by looking for this spatial variation in scale and shear of the local power. Any non-lensing isotropic change in the amplitude of the small-scale peaks and troughs, either from new physics or random fluctuations, would therefore only have a small effect on the lensing reconstruction, which is sensitive to scale and shape, not amplitude.

One locally anisotropic physical effect that has been considered as a possible explanation is the presence of large-scale compensated isocurvature modes, discussed in detail in Planck Collaboration X (2020). Because the large-scale isocurvature modes locally vary the baryon-to-photon ratio, they can partially mimic the lensing smoothing effect by spatially varying the acoustic scale (Muñoz et al. 2016; Valiviita 2017). However, because they have a similar local effect to lensing, they also affect the large-scale lensing reconstruction (Smith et al. 2017). Combining with the *Planck* 2018 lensing reconstruction, which now extends down to $L = 8$, as shown in Planck Collaboration X (2020) this model therefore does not offer a significant improvement in overall fit ($\Delta\chi_{\text{eff}}^2 = -3.3$ with *Planck* TT,TE,EE+lowE+lensing).

If the $A_L > 1$ preference is simply a statistical excursion (perhaps the most likely explanation), this indicates that there are random features in the spectrum that are pulling some parameters unusually far from expected values³⁰. There are several theoretical models that can fit the CMB power spectra and also predict larger lensing amplitudes. These include Λ CDM models with spatial curvature, for which we find $\Omega_K < 0$ at over 3σ (Sect. 7.3) from the CMB power spectra, and some dark energy and modified gravity models (Sect. 7.4). For extensions to base- Λ CDM, parameters that decrease the lensing amplitude are more constrained by the *Planck* power spectra than might otherwise be expected; for example, higher neutrino masses lower the predicted lensing power compared to base Λ CDM, leading to surprisingly tight constraints (Sect. 7.5.1). Adding the lensing-reconstruction information significantly reduces the parameter space of larger lensing amplitudes and partially mitigates these effects. However, the statistical power of the *Planck* power spectra is sufficiently high that the joint constraints prefer lensing amplitudes in the higher range allowed by the lensing data.

Even within Λ CDM, the fact that the data prefer more lensing leads to a preference for higher fluctuation amplitudes, hence the high- ℓ data yield higher A_s and higher τ than we infer in combination with large-scale E-mode polarization (Sect. 2.2.3) or lensing reconstruction. Since these preferences are degenerate with $\Omega_m h^2$, n_s , and H_0 (see PCP13, PCP15), these parameters are also pulled ($\Omega_m h^2$ higher, n_s and H_0 lower). Our baseline best-fit results include both the “lowE” data and the lensing reconstruction, each of which restrict the range of allowed variation, so the remaining pulls should be modest; however, it should not perhaps be too much of a surprise if the central values of the parameters inferred from *Planck* turn out to be slightly more shifted than typical with respect to the ultimate truth if the base- Λ CDM model is correct.

7. Extensions to the base- Λ CDM model

7.1. Grid of extended models

We have studied a range of extension to the base Λ CDM model. A full grid of results from standard parameter extensions is available online through the PLA³¹. Figure 26 and Table 4 summarize

³⁰ It is not trivial to assess how unlikely a fluctuation in a consistency parameter like this is given the number of different cosmological and consistency test parameters we might have looked at. We are only discussing A_L in detail here because it comes out high; other consistency parameters, for example the relative amplitude of ISW, Doppler, and Sachs-Wolfe contributions to the temperature spectrum, come out perfectly consistent with expectations.

³¹ Chains are available at <https://pla.esac.esa.int>, with description and parameter tables in Planck Collaboration (2018).

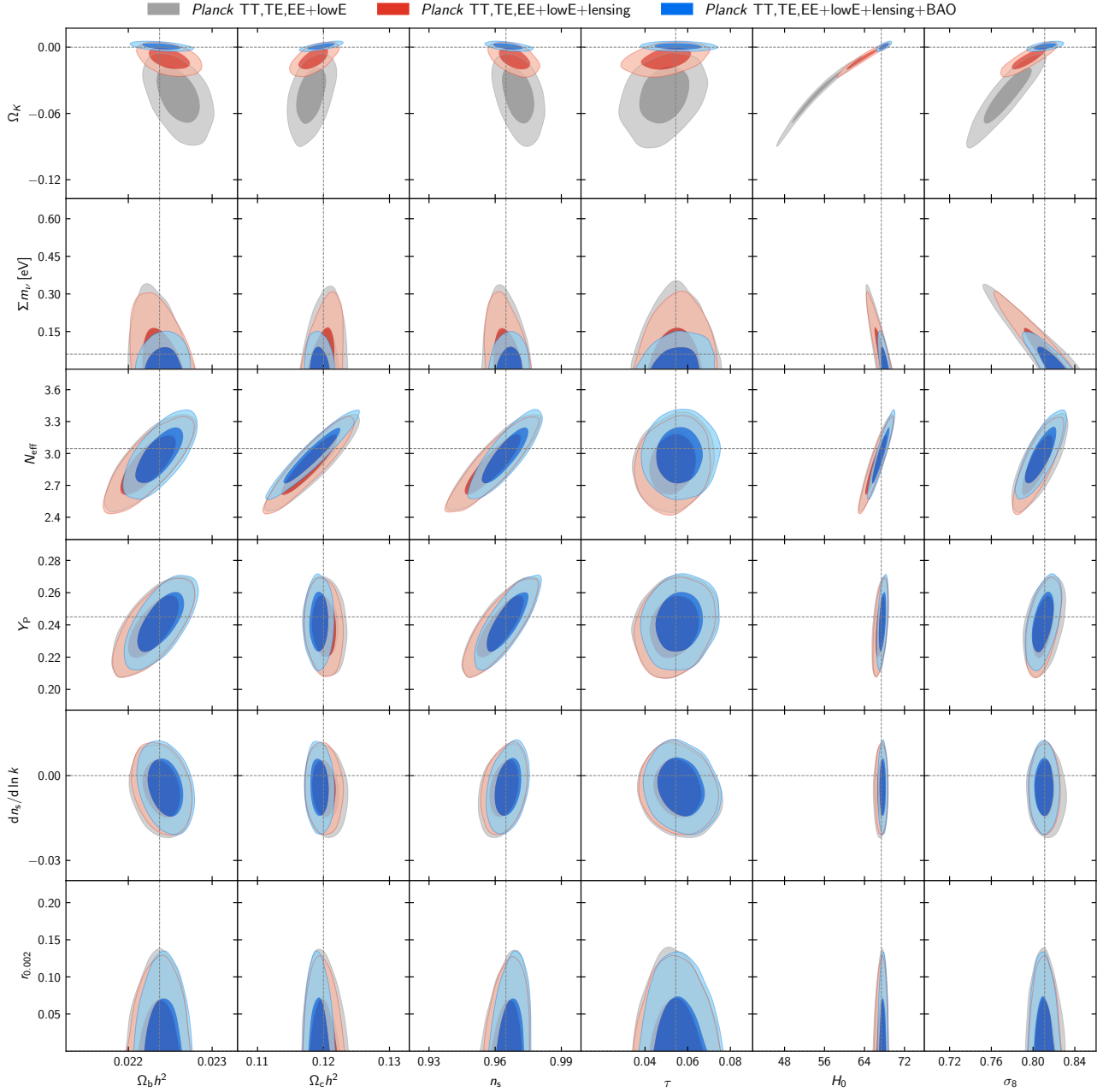


Fig. 26. Constraints on 1-parameter extensions to the base- Λ CDM model. Contours show 68% and 95% confidence regions for *Planck* TT,TE,EE+lowE (grey), *Planck* TT,TE,EE+lowE+lensing (red), and *Planck* TT,TE,EE+lowE+lensing+BAO (blue). Horizontal dashed lines correspond to the parameter values assumed in the base- Λ CDM cosmology, while vertical dashed lines show the mean posterior values in the base model for *Planck* TT,TE,EE+lowE+lensing.

Table 4. Constraints on 1-parameter extensions to the base- Λ CDM model for combinations of *Planck* power spectra, *Planck* lensing, and BAO (equivalent results using the CamSpec likelihood are given in Table A.2).

Parameter	TT+lowE	TT, TE, EE+lowE	TT, TE, EE+lowE+lensing	TT, TE, EE+lowE+lensing+BAO
Ω_K	$-0.056^{+0.044}_{-0.050}$	$-0.044^{+0.033}_{-0.034}$	$-0.011^{+0.013}_{-0.012}$	$0.0007^{+0.0037}_{-0.0037}$
Σm_ν [eV]	< 0.537	< 0.257	< 0.241	< 0.120
N_{eff}	$3.00^{+0.57}_{-0.53}$	$2.92^{+0.36}_{-0.37}$	$2.89^{+0.36}_{-0.38}$	$2.99^{+0.34}_{-0.33}$
Y_P	$0.246^{+0.039}_{-0.041}$	$0.240^{+0.024}_{-0.025}$	$0.239^{+0.024}_{-0.025}$	$0.242^{+0.023}_{-0.024}$
$dn_s/d \ln k$	$-0.004^{+0.015}_{-0.015}$	$-0.006^{+0.013}_{-0.013}$	$-0.005^{+0.013}_{-0.013}$	$-0.004^{+0.013}_{-0.013}$
$r_{0.002}$	< 0.102	< 0.107	< 0.101	< 0.106
w_0	$-1.56^{+0.60}_{-0.48}$	$-1.58^{+0.52}_{-0.41}$	$-1.57^{+0.50}_{-0.40}$	$-1.04^{+0.10}_{-0.10}$

Notes. We quote 95% limits here.

Table 5. Constraints on standard cosmological parameters from *Planck* TT,TE,EE+lowE+lensing when the base- Λ CDM model is extended by varying additional parameters.

Parameter(s)	$\Omega_b h^2$	$\Omega_c h^2$	$100\theta_{MC}$	H_0	n_s	$\ln(10^{10} A_s)$
Base Λ CDM	0.02237 ± 0.00015	0.1200 ± 0.0012	1.04092 ± 0.00031	67.36 ± 0.54	0.9649 ± 0.0042	3.044 ± 0.014
r	0.02237 ± 0.00014	0.1199 ± 0.0012	1.04092 ± 0.00031	67.40 ± 0.54	0.9659 ± 0.0041	3.044 ± 0.014
$dn_s/d \ln k$	0.02240 ± 0.00015	0.1200 ± 0.0012	1.04092 ± 0.00031	67.36 ± 0.53	0.9641 ± 0.0044	3.047 ± 0.015
$dn_s/d \ln k, r$	0.02243 ± 0.00015	0.1199 ± 0.0012	1.04093 ± 0.00030	67.44 ± 0.54	0.9647 ± 0.0044	3.049 ± 0.015
$d^2 n_s/d \ln k^2, dn_s/d \ln k$	0.02237 ± 0.00016	0.1202 ± 0.0012	1.04090 ± 0.00030	67.28 ± 0.56	0.9625 ± 0.0048	3.049 ± 0.015
N_{eff}	0.02224 ± 0.00022	0.1179 ± 0.0028	1.04116 ± 0.00043	66.3 ± 1.4	0.9589 ± 0.0084	3.036 ± 0.017
$N_{\text{eff}}, dn_s/d \ln k$	0.02216 ± 0.00022	0.1157 ± 0.0032	1.04144 ± 0.00048	65.2 ± 1.6	0.950 ± 0.011	3.034 ± 0.017
Σm_ν	0.02236 ± 0.00015	0.1201 ± 0.0013	1.04088 ± 0.00032	$67.1^{+1.2}_{-0.67}$	0.9647 ± 0.0043	3.046 ± 0.015
$\Sigma m_\nu, N_{\text{eff}}$	0.02221 ± 0.00022	$0.1179^{+0.0027}_{-0.0030}$	1.04116 ± 0.00044	$65.9^{+1.8}_{-1.6}$	0.9582 ± 0.0086	3.037 ± 0.017
$m_{\nu, \text{sterile}}^{\text{eff}}, N_{\text{eff}}$	$0.02242^{+0.00014}_{-0.00016}$	$0.1200^{+0.0032}_{-0.0020}$	$1.04074^{+0.00033}_{-0.00029}$	$67.11^{+0.63}_{-0.79}$	$0.9652^{+0.0045}_{-0.0056}$	$3.050^{+0.014}_{-0.016}$
α_{-1}	0.02238 ± 0.00015	0.1201 ± 0.0015	1.04087 ± 0.00043	67.30 ± 0.67	0.9645 ± 0.0061	3.045 ± 0.014
w_0	0.02243 ± 0.00015	0.1193 ± 0.0012	1.04099 ± 0.00031	...	0.9666 ± 0.0041	3.038 ± 0.014
Ω_K	0.02249 ± 0.00016	0.1185 ± 0.0015	1.04107 ± 0.00032	$63.6^{+2.1}_{-2.3}$	0.9688 ± 0.0047	$3.030^{+0.017}_{-0.015}$
Y_p	0.02230 ± 0.00020	0.1201 ± 0.0012	1.04067 ± 0.00055	67.19 ± 0.63	0.9621 ± 0.0070	3.042 ± 0.016
Y_p, N_{eff}	0.02224 ± 0.00022	$0.1171^{+0.0042}_{-0.0049}$	1.0415 ± 0.0012	$66.0^{+1.7}_{-1.9}$	0.9589 ± 0.0085	3.036 ± 0.018
A_L	0.02251 ± 0.00017	0.1182 ± 0.0015	1.04110 ± 0.00032	68.16 ± 0.70	0.9696 ± 0.0048	$3.029^{+0.018}_{-0.016}$

Notes. The constraint on τ is also stable but not shown for brevity; however, we include H_0 (in $\text{km s}^{-1} \text{Mpc}^{-1}$) as a derived parameter (which is very poorly constrained from *Planck* alone in the $\Lambda\text{CDM}+w_0$ extension). Here α_{-1} is a matter isocurvature amplitude parameter, following PCP15. All limits are 68% in this table. The results assume standard BBN except when varying Y_p independently (which requires non-standard BBN). Varying A_L is not a physical model (see Sect. 6.2).

the constraints on 1-parameter extensions to the base- Λ CDM model. As in 2013 and 2015 we find no strong evidence in favour of any of these extensions, using either the *Planck* data alone or *Planck* combined with BAO. We also find that constraints on the base- Λ CDM parameters are remarkably robust to a variety of possible extensions to the Λ CDM model, as shown in Table 5: many of these parameters are constrained to high precision in a nearly model-independent way.

We now discuss some specific extensions in more detail.

7.2. Early Universe

CMB observations probe the state of the universe at the earliest time that is directly observable with the electromagnetic spectrum. The physics of the anisotropies is well understood, and can be predicted accurately with linear theory given a set of initial conditions. *Planck* observations can therefore be used to give powerful constraints on the initial conditions, i.e., the perturbations present at the start of the hot big bang. We discuss in turn constraints on the scalar and tensor perturbations, allowing for deviations from a purely power-law scalar spectrum, and discuss the interpretation within the context of the most popular inflationary models.

7.2.1. Primordial scalar power spectrum

The *Planck* data are consistent with purely adiabatic primordial scalar curvature perturbations, with no evidence for isocurvature modes (see [Planck Collaboration X 2020](#)), as predicted by the simplest single-field inflation models. The primordial power spectrum is then just a function of scale. In this section, we characterize the scalar fluctuation spectrum in terms of a spectral index n_s and its first two derivatives with respect to $\ln k$ (the ‘‘running’’ and ‘‘running of the running’’ of the spectral

index):

$$\mathcal{P}_{\mathcal{R}}(k) = A_s \left(\frac{k}{k_0} \right)^{n(k)}, \quad (38a)$$

$$n(k) = n_s - 1 + (1/2)(dn_s/d \ln k) \ln(k/k_0) + (1/6)(d^2 n_s/d \ln k^2)(\ln(k/k_0))^2. \quad (38b)$$

In the absence of any running of the spectral index, our constraint on n_s for the base- Λ CDM model (Eq. (21)) shows an 8σ tilt away from scale invariance. Adding BAO tightens the constraint to nearly 9σ :

$$n_s = 0.9665 \pm 0.0038 \quad (68\%, \text{TT,TE,EE+lowE+lensingBAO}). \quad (39)$$

The need for a red-tilted scalar spectrum is quite robust to extensions to base Λ CDM, as summarized in Table 5. In all cases, we find $n_s < 1$ at $\geq 3\sigma$.

Adding running of the spectral index, $dn_s/d \ln k$, as a single additional parameter to base Λ CDM, we find

$$\left. \begin{aligned} dn_s/d \ln k &= -0.0045 \pm 0.0067, \\ n_s &= 0.9641 \pm 0.0044, \\ n_{s,0.002} &= 0.979 \pm 0.021, \end{aligned} \right\} \quad (68\%, \text{TT,TE,EE+lowE+lensing}), \quad (40a)$$

$$\left. \begin{aligned} dn_s/d \ln k &= -0.0041 \pm 0.0067, \\ n_s &= 0.9659 \pm 0.0040, \\ n_{s,0.002} &= 0.979 \pm 0.021, \end{aligned} \right\} \quad (68\%, \text{TT,TE,EE+lowE+lensing+BAO}). \quad (40b)$$

where n_s is defined by default at $k = 0.05 \text{Mpc}^{-1}$ and $n_{s,0.002}$ is the corresponding tilt at $k = 0.002 \text{Mpc}^{-1}$. The slight

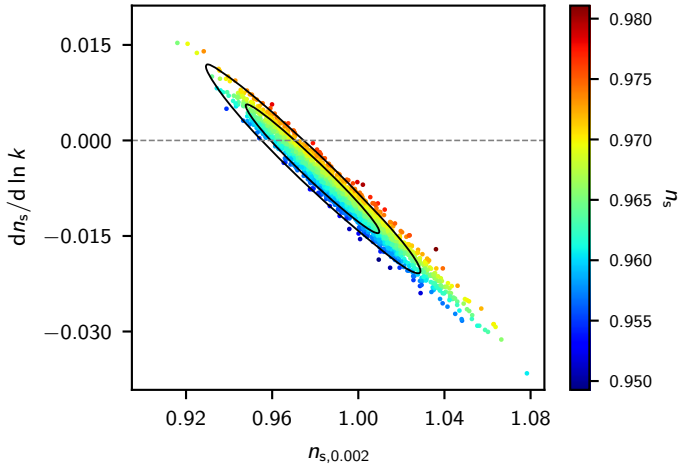


Fig. 27. Constraints on the running of the scalar spectral index in the Λ CDM model, using *Planck* TT,TE,EE+lowE+lensing when marginalizing over r (samples, coloured by the spectral index at $k = 0.05 \text{ Mpc}^{-1}$), and the equivalent result when $r = 0$ (black contours). The *Planck* data are consistent with zero running, but also allow for significant negative running, which gives a positive tilt $n_{s,0.002}$, and hence less power, on large scales ($k \approx 0.002 \text{ Mpc}^{-1}$).

preference for negative running is driven by the mild tension between the CMB temperature power spectrum at high and low multipoles discussed in Sect. 6.1, with negative running allowing higher large-scale tilt, giving less power on large scales (see Fig. 27 and the extensive discussions in PCP13 and PCP15). The measurements of the tilt and running around the pivot scale of $k \approx 0.05 \text{ Mpc}^{-1}$ are robust to allowing even more freedom for the spectrum to vary with scale. For example, allowing for running of the running we find

$$\left. \begin{aligned} d^2 n_s / d \ln k^2 &= 0.009 \pm 0.012, \\ dn_s / d \ln k &= 0.0011 \pm 0.0099, \\ n_s &= 0.9647 \pm 0.0043, \end{aligned} \right\} \begin{array}{l} 68\%, \text{ TT,TE,EE+lowE} \\ \text{+lensing+BAO.} \end{array} \quad (41)$$

Here the slight preference for negative running has almost disappeared, and there is instead a slight preference for lower large-scale power by having positive running of the running, leaving a near power-law solution on small scales. There is no evidence for any significant deviation from a power law on small scales. This is consistent with the simplest slow-roll inflation models where the running (and higher derivatives of the spectral index) are higher order in slow-roll (so that $dn_s/d \ln k = \mathcal{O}(|n_s - 1|^2)$, $d^2 n_s / d \ln k^2 = \mathcal{O}(|n_s - 1|^3)$) and all deviations from a constant spectral index can be neglected at *Planck* sensitivity.

An analysis of more general parameterizations of the primordial power spectrum are presented in Sect. 6 of *Planck Collaboration X (2020)*, including various specific physically motivated models, as well as general parametric reconstructions. Models with many more free parameters can provide better fits to the data, but none are favoured; in all cases the small-scale spectrum is found to be consistent with a power law over the range $0.008 \text{ Mpc}^{-1} \lesssim k \lesssim 0.1 \text{ Mpc}^{-1}$, with low-significance hints of larger-scale features corresponding to the dip in the low- ℓ temperature power spectrum. The introduction of the additional degrees of freedom in the initial power spectrum had no significant impact on the determination of the main cosmological parameters for the parameterizations considered.

7.2.2. Tensor modes

Primordial gravitational waves³², or tensor modes, source a distinctive curl-like (“*B*-mode”) pattern in the CMB polarization and add additional power to the large-scale temperature power spectrum (Kamionkowski et al. 1997; Seljak & Zaldarriaga 1997). *Planck*’s *B*-mode measurement is noise and systematics limited and provides a relative weak constraint on the tensor-to-scalar ratio $r_{0.002} < 0.41$ (95% CL, *Planck Collaboration V 2020*). As with the 2013 and 2015 releases, the strongest constraint on tensor modes from the *Planck* data alone comes from the *TT* spectrum at $\ell \lesssim 100$.

The precision of the *Planck* temperature constraint remains limited by cosmic variance from the scalar component and is model dependent. The tightest and least model-dependent constraints on the tensor amplitude come from the Ade et al. (2018; BK15) analysis of the BICEP2/Keck field, in combination with *Planck* and WMAP maps to remove polarized Galactic dust emission. The BK15 observations measure the *B*-mode polarization power spectrum in nine bins at $\ell \lesssim 300$, with the tensor amplitude information coming mainly from scales $\ell \approx 100$, where the *B*-mode spectrum from scattering at recombination is expected to peak. The *Planck* CMB power spectrum measurements use a much larger sky area, and are useful to convert this measurement into a constraint on the tensor-to-scalar ratio r at a given scale with little additional cosmic variance error. To relate the tensor measurement to constraints on specific inflation models (which usually predict a region in the n_s - r plane), combining with the *Planck* data is also essential, although model dependent.

Figure 28 shows the constraints in the n_s - r plane, with r added as a single additional parameter to the base model and plotted at pivot scale 0.002 Mpc^{-1} . We assume the tensor-mode spectrum is close to scale invariant, with spectral index given by the inflation consistency relation to second order in slow-roll parameters. *Planck* alone gives

$$r_{0.002} < 0.10, \quad (95\%, \text{ TT,TE,EE+lowE+lensing}), \quad (42)$$

with $n_s = 0.9659 \pm 0.0041$ at 1σ . Adding BK15 to directly measure the tensor amplitude significantly tightens the r constraint, and adding BAO data tightens (slightly) the n_s constraint. Using the *Planck* temperature likelihoods we find

$$r_{0.002} < 0.055 \quad (95\%, \text{ TT+lowE+lensing+BK15+BAO}), \quad (43)$$

with $n_s = 0.9661 \pm 0.0040$ at 1σ , or adding polarization

$$r_{0.002} < 0.058 \quad (95\%, \text{ TT,TE,EE+lowE+lensing+BK15+BAO}), \quad (44)$$

with $n_s = 0.9668 \pm 0.0037$ at 1σ . However, the small change when adding polarization is not stable to the choice of polarization likelihood; when using the CamSpec TT,TE,EE+lowE likelihood in place of Plik, we find the weaker constraint $r_{0.002} < 0.065$ for the same data combination as that used in Eq. (44).

All the combined n_s - r contours exclude convex potentials at about the 95% confidence (marginally less if we use the CamSpec likelihood, see Fig. 28), which substantially restricts the range of allowed inflation models and disfavours all simple integer power law potentials. More generally, since r depends on the slope of the potential, the smallness of the empirical upper

³² The polarization anisotropies generated by gravitational waves was discussed first by Polnarev (1985).

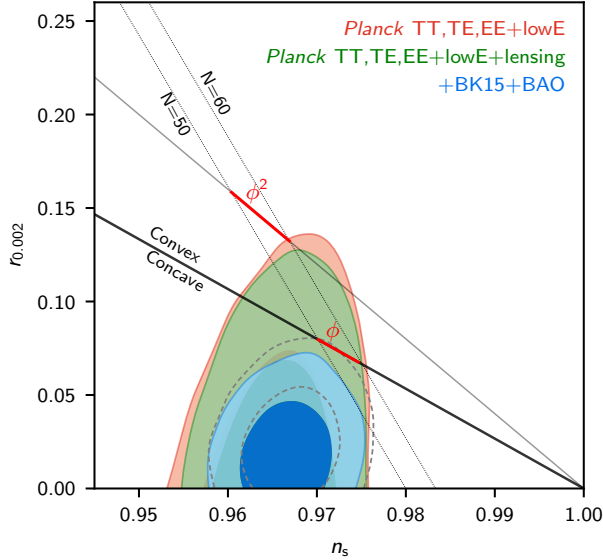


Fig. 28. Constraints on the tensor-to-scalar ratio $r_{0.002}$ in the Λ CDM model, using *Planck* TT,TE,EE+lowE and *Planck* TT,TE,EE+lowE+lensing (red and green, respectively), and joint constraints with BAO and BICEP2/Keck (blue, including *Planck* polarization to determine the foreground components, Ade et al. 2018). This assumes the inflationary consistency relation and negligible running. Dashed grey contours show the joint constraint when using CamSpec instead of Plik as the high- ℓ *Planck* likelihood, indicating the level of modelling uncertainty in the polarization results. Dotted lines show the loci of approximately constant e -folding number N , assuming simple $V \propto (\phi/m_{\text{Pl}})^p$ single-field inflation. Solid lines show the approximate n_s - r relation for locally quadratic and linear potentials to first order in slow roll; red lines show the approximate allowed range assuming $50 < N < 60$ and a power-law potential for the duration of inflation. The solid black line (corresponding to a linear potential) separates concave and convex potentials.

limit on r implies that the inflationary potential must have been nearly flat when modes exited the horizon. The measured n_s must then be determined largely by the second derivative of the potential, suggesting a hierarchy in the magnitudes of the slow-roll parameters, favouring hilltop-like potentials. For a detailed discussion of the implications for specific inflation models see Planck Collaboration X (2020).

If we allow running of the spectral index in addition to tensor modes, the constraint on $r_{0.002}$ weakens if we use only the *Planck* likelihood; a negative running allows n_s at large scales to shift to higher values, lowering the large-scale scalar amplitude, and hence allowing a larger tensor contribution. Inclusion of the BK15 likelihood significantly reduces the extent of this degeneracy by constraining the tensor amplitude more directly, giving

$$\left. \begin{array}{l} r_{0.002} < 0.16, \\ dn_s/d \ln k = -0.008^{+0.014}_{-0.015}, \end{array} \right\} \begin{array}{l} 95\%, \text{ TT,TE,EE+lowE} \\ \text{+lensing,} \end{array} \quad (45a)$$

$$\left. \begin{array}{l} r_{0.002} < 0.066, \\ dn_s/d \ln k = -0.006 \pm 0.013, \end{array} \right\} \begin{array}{l} 95\%, \text{ TT,TE,EE+lowE} \\ \text{+lensing+BK15+BAO.} \end{array} \quad (45b)$$

The combination of *Planck* and BK15 robustly constrain the tensor ratio to be small, with $r_{0.002} \lesssim 0.06$. The implications for inflation are slightly more model dependent as a result of degeneracies between n_s and additional parameters in extended Λ CDM models. However, as shown in

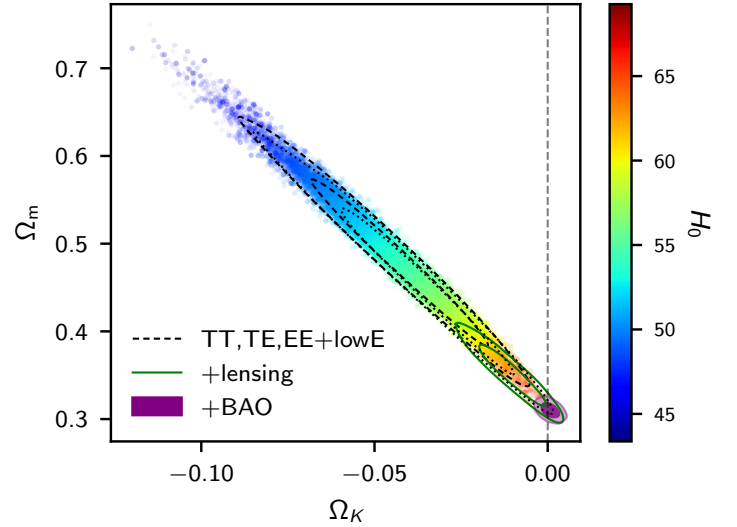


Fig. 29. Constraints on a non-flat universe as a minimal extension to the base- Λ CDM model. Points show samples from the *Planck* TT,TE,EE+lowE chains coloured by the value of the Hubble parameter and with transparency proportional to the sample weight. Dashed lines show the corresponding 68% and 95% confidence contours that close away from the flat model (vertical line), while dotted lines are the equivalent contours from the alternative CamSpec likelihood. The solid dashed line shows the constraint from adding *Planck* lensing, which pulls the result back towards consistency with flat (within 2σ). The filled contour shows the result of also adding BAO data, which makes the full joint constraint very consistent with a flat universe.

Table 5, the extensions of Λ CDM that we consider in this paper cannot substantially shift the value of the spectral index when the tensor amplitude is small, so the overall conclusions are unlikely to change substantially in extended models.

7.3. Spatial curvature

The base- Λ CDM model assumes that the spatial hypersurfaces are flat, such as would be predicted (to within measurable precision) by the simplest inflationary models. This is a prediction that can be tested to high accuracy by the combination of CMB and BAO data (the CMB alone suffers from a geometric degeneracy, which is weakly broken with the addition of CMB lensing). This is illustrated in Fig. 29.

The combination of the *Planck* temperature and polarization power spectra give

$$\Omega_K = -0.056^{+0.028}_{-0.018} \quad (68\%, \text{ Planck TT+lowE}), \quad (46a)$$

$$\Omega_K = -0.044^{+0.018}_{-0.015} \quad (68\%, \text{ Planck TT,TE,EE+lowE}), \quad (46b)$$

an apparent detection of curvature at well over 2σ . The 99% probability region for the TT,TE,EE+lowE result is $-0.095 < \Omega_K < -0.007$, with only about 1/10 000 samples at $\Omega_K \geq 0$. This is not entirely a volume effect, since the best-fit χ^2 changes by $\Delta\chi^2_{\text{eff}} = -11$ compared to base Λ CDM when adding the one additional curvature parameter. The reasons for the pull towards negative values of Ω_K are discussed at length in PCP15 and Sect. 6.2. They are essentially the same as those that lead to the preference for $A_L > 1$, although slightly exacerbated in the case of curvature, since the low multipoles also fit the low- ℓ temperature likelihood slightly better if $\Omega_K < 0$. As with the $A_L > 1$

preference, the joint *Planck* polarization result is not robust at the approximately 0.5σ level to modelling of the polarization likelihoods, with the CamSpec TT,TE,EE+lowE likelihood giving $\Omega_K = -0.037^{+0.019}_{-0.014}$.

Closed models predict substantially higher lensing amplitudes than in Λ CDM, so combining with the lensing reconstruction (which is consistent with a flat model) pulls parameters back into consistency with a spatially flat universe to well within 2σ :

$$\Omega_K = -0.0106 \pm 0.0065 \quad (68\%, \text{TT,TE,EE+lowE+lensing}). \quad (47a)$$

The constraint can be further sharpened by combining the *Planck* data with BAO data; this convincingly breaks the geometric degeneracy to give

$$\Omega_K = 0.0007 \pm 0.0019 \quad (68\%, \text{TT,TE,EE+lowE+lensing+BAO}). \quad (47b)$$

The joint results suggests our Universe is spatially flat to a 1σ accuracy of 0.2%.

7.4. Dark energy and modified gravity

The late-time accelerated expansion of the Universe (Riess et al. 1998; Perlmutter et al. 1999) is still considered one of the most mysterious aspects of the standard cosmology. In the base Λ CDM model the acceleration is driven by a cosmological constant, added into the Einstein equations of General Relativity (GR, Einstein 1917). Although Λ CDM fits the data well, Λ is a phenomenological parameter without an underlying theoretical basis to explain its value (though see Weinberg 1987). In addition, the empirically required value of Λ marks our epoch as a special time in the evolution of the Universe. Attempts have therefore been made to find a dynamical mechanism that leads to cosmic acceleration, with evolving background energy densities close to Λ CDM. Such dynamics is usually associated with a fluid (a scalar field) which we refer to as “dark energy” (DE), or with modifications of GR, which we refer to as “modified gravity” (MG).

A detailed analysis of the impact of *Planck* data on dark energy and modified gravity was presented in a dedicated paper that accompanied the 2015 *Planck* release, Planck Collaboration XIV (2016, hereafter PDE15). We refer the reader to this paper for a review of different cosmological models, and for constraints from *Planck* on its own and in combination with galaxy weak lensing (WL) and redshift-space distortions (RSDs). In PDE15 it was shown that although the base- Λ CDM model fits *Planck* data, there were some tensions (at levels as high as 3σ) when *Planck* was combined with RSD and WL data, even when conservative cuts were applied to exclude nonlinear scales. However, the addition of *Planck* lensing data was found to reduce these tensions. Updated constraints on a few specific models, using more recent WL data, are presented in DES Collaboration (2018b).

In this paper, we follow a similar methodology to PDE15, distinguishing between models that directly affect only the background (and impact perturbations predominantly through changes in the expansion rate) and those that directly affect perturbations. However, we restrict the analysis to a smaller range of models here. As in the rest of this paper, we show results for the baseline *Planck* TT,TE,EE+lowE+lensing data set and for combinations with other relevant data sets. Such external data are particularly useful for constraining DE and MG mod-

els because the largest deviations from Λ CDM are usually at late times, which are not well constrained by the CMB power-spectra and CMB lensing. However, CMB lensing provides important information that mitigates the preference for $A_L > 1$ seen in the *Planck* temperature power spectra (Sect. 6.2), so we explicitly comment on the impact of CMB lensing wherever relevant. We recall here that the lensing likelihood assumes a fiducial Λ CDM model, but linear corrections to the fiducial mode are accounted for self-consistently. PL2018 explicitly tested that this procedure is unbiased, even when the lensing spectrum differs from the fiducial spectrum by as much as 20% (which is much larger than differences allowed by the CMB lensing data).

We consider the following external data sets:

- SNe + BAO (see Sects. 5.1, 5.2, and 5.4 for discussions of the data sets and comments on why we do not combine *Planck* data with direct measurements of H_0);
- RSDs (as described in Sect. 5.3), where we specifically use BOSS-DR12 data from Alam et al. (2017), adopting the $f\sigma_8-H-D_M$ parameterization;
- WL data from DES (as described in Sect. 5.5), except that here we use the Weyl potential to obtain theoretical predictions for the lensing correlation functions, rather than assuming the matter-sourced Poisson equation to relate the lensing potential power spectrum to the matter power spectrum.

We calculate all results both fixing and varying the neutrino mass. Neutrino masses are known to be degenerate with DE and MG and should be varied consistently when testing such models (as discussed in Dirian 2017); fixing the neutrino mass to the minimal value of 0.06 eV (as for our baseline Λ CDM results) gives tighter constraints than allowing the neutrino mass to vary and partly shifts results towards Λ CDM. These shifts are usually small, often negligible, and always less than 1σ for marginalized results. We model the small-scale nonlinear power spectrum using HMcode (Mead et al. 2015, 2016) as in the main parameter grid of extensions to base- Λ CDM, neglecting any differences arising from modified gravity. In using the DES weak-lensing correlation functions, we exclude scales where nonlinear modelling uncertainties are important, but since the modified gravity models introduce an additional level of uncertainty, we also marginalize over the feedback amplitude B with a flat prior, $2 \leq B \leq 4$. This parameter is used by HMcode to introduce an additional uncertainty in the nonlinear correction due to the modelling of the baryonic effects on the matter power spectrum at small scales, modifying the halo mass-concentration relation and the shape of the halo density profile. In this context, however, we marginalize over this parameter in order to reduce the residual sensitivity of our results on the nonlinear modelling in modified gravity theories; marginalizing over B reduces the constraining power coming from nonlinear scales, where the correction recipe used by HMcode may not correctly reproduce the perturbation evolution for all the models included in our parameterization.

Throughout this section we will adopt the metric given by the line element

$$ds^2 = a^2 \left[-(1 + 2\Psi)d\tau^2 + (1 - 2\Phi)dx^2 \right], \quad (48)$$

with the speed of light c set to 1. The functions $\Phi(\tau, x)$ and $\Psi(\tau, x)$ are the gauge-invariant gravitational potentials, which are very nearly equal at late times in Λ CDM. For the background parameterization we use the standard CAMB code, while for the

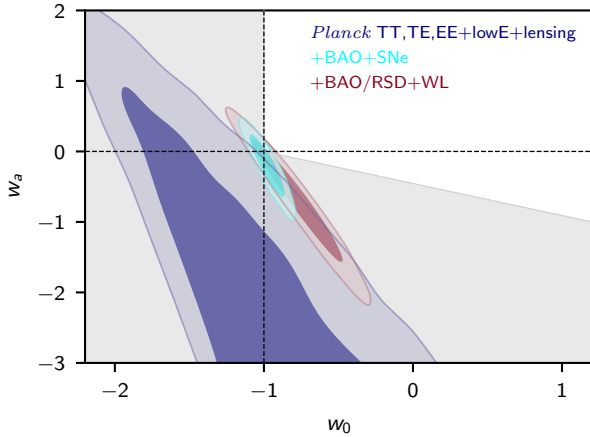


Fig. 30. Marginalized posterior distributions of the (w_0, w_a) parameters for various data combinations. The tightest constraints come from the combination *Planck* TT,TE,EE+lowE+lensing+SNe+BAO and are compatible with Λ CDM. Using *Planck* TT,TE,EE+lowE+lensing alone is considerably less constraining and allows for an area in parameter space that corresponds to large values of the Hubble constant (as already discussed in *Planck* Collaboration XIII 2016 and PDE15). The dashed lines indicate the point corresponding to the Λ CDM model. The parametric equation of state given by Eq. (49) stays out of the phantom regime (i.e., has $w \geq -1$) at all times only in the (upper-right) unshaded region.

perturbation parameterization we use the publicly available code MGCAMB³³ (Zhao et al. 2009; Hojjati et al. 2011) integrated into the latest version of CosmoMC. For the effective field theory (EFT) models of Sect. 7.4.3 we use EFTCAMB³⁴ (Hu et al. 2014; Raveri et al. 2014).

7.4.1. Background parameterization: w_0, w_a

If the DE is a generic dynamical fluid, its equation of state parameter $w \equiv p/\rho$ will in general be a function of time. Here p and ρ are the spatially-averaged (background) DE pressure and density.

To test a time-varying equation of state we adopt the functional form

$$w(a) = w_0 + (1 - a)w_a, \quad (49)$$

where w_0 and w_a are assumed to be constants. In Λ CDM, $w_0 = -1$ and $w_a = 0$. We use the parameterized post-Friedmann (PPF) model of Fang et al. (2008) to explore expansion histories where w crosses -1 . The PPF equations are modelled on the perturbations of quintessence dark energy, i.e., they correspond to a fluid with vanishing anisotropic stress and a rest-frame speed of sound approximately equal to the speed of light. Because of the high sound speed, dark-energy density perturbations are suppressed inside the horizon and are irrelevant compared to the matter perturbations, except on the very largest scales. While this is the standard procedure adopted in the literature, we should emphasize that a single minimally-coupled canonical scalar field (quintessence) *cannot* cross $w = -1$ (Vikman 2005). Such a crossing could happen in models with two scalar fields (one of which would have to be a phantom field with the opposite sign

of the kinetic term); in such models the perturbations remain close to the quintessence case (see e.g., Kunz & Sapone 2006). Alternatively, the phantom “barrier” can be crossed with a sound speed that vanishes in the phantom domain (Creminelli et al. 2009) or in models with additional terms in the action, such as in kinetic-gravity-braiding (Deffayet et al. 2010), or with non-minimal couplings (Amendola 2000; Pettorino & Baccigalupi 2008). These and other modified gravity models, typically also change the behaviour of the perturbations.

Marginalized contours of the posterior distributions for w_0 and w_a are shown in Fig. 30. Note that CMB lensing has only a small effect on the constraints from *Planck* alone (see the parameter grid tables in the PLA). Using *Planck* data alone, a wide volume of dynamical dark-energy parameter space is allowed, with contours cut off by our priors ($-3 < w_0 < 1$, $-5 < w_a < 5$, and $0.4 < h < 1$; note that Fig. 30 does not show the complete prior range). However, most of the allowed region of parameter space corresponds to phantom models with very high values of H_0 (as discussed in PDE15); such models are inconsistent with the late-time evolution constrained by SNe and BAO data. This is illustrated in Fig. 30 which also shows constraints if we add BAO/RSD+WL and BAO+SNe to the *Planck* TT,TE,EE+lowE+lensing likelihood. The addition of external data sets narrows the constraints towards the Λ CDM values of $w_0 = -1$, $w_a = 0$. The tightest constraints are found for the data combination *Planck* TT,TE,EE+lowE+lensing+BAO+SNe; the difference in χ^2 between the best-fit DE and Λ CDM models for this data combination is only $\Delta\chi^2 = -1.4$ (which is not significant given the two additional parameters). Numerical constraints for these data combinations, as well as χ^2 differences, are presented in Table 6. It is also apparent that for the simple w_0, w_a parameterization of evolving DE, *Planck* combined with external data sets does not allow significantly lower values of S_8 or higher values of H_0 compared to the base- Λ CDM cosmology.

Fixing the evolution parameter $w_a = 0$, we obtain the tight constraint

$$w_0 = -1.028 \pm 0.031 \quad (68\%, \text{Planck TT,TE,EE+lowE+lensing+SNe+BAO}), \quad (50)$$

and restricting to $w_0 > -1$ (i.e., not allowing phantom equations of state), we find

$$w_0 < -0.95 \quad (95\%, \text{Planck TT,TE,EE+lowE+lensing+SNe+BAO}). \quad (51)$$

Here we only quote two significant figures, so that the result is robust to differences between the PlIk and CamSpec likelihoods.

For the remainder of this section, we assume Λ CDM at the background level (i.e., $w = -1$ at all times), but instead turn our attention to constraining the behaviour of the dark sector perturbations.

7.4.2. Perturbation parameterization: μ, η

In the types of DE or MG models considered here, changes to observables only arise via the impact on the geometry of the Universe. At the level of perturbations, it is then sufficient to model the impact on the gravitational potentials Φ and Ψ , or, equivalently, on two independent combinations of these potentials (e.g., Zhang et al. 2007; Amendola et al. 2008). Following PDE15 we consider two phenomenological functions, μ and η , defined as follows.

³³ Available at <http://www.sfu.ca/~aha25/MGCAMB.html> (February 2014 version, but updated to correctly output the power spectrum of the Weyl potential).

³⁴ Available at <http://eftcamb.org/> (version 2.0).

Table 6. Marginalized values and 68% confidence limits for cosmological parameters obtained by combining *Planck* TT,TE,EE+lowE+lensing with other data sets, assuming the (w_0, w_a) parameterization of $w(a)$ given by Eq. (49).

Parameter	<i>Planck</i> +SNe+BAO	<i>Planck</i> +BAO/RSD+WL
w_0	-0.957 ± 0.080	-0.76 ± 0.20
w_a	$-0.29^{+0.32}_{-0.26}$	$-0.72^{+0.62}_{-0.54}$
H_0 [km s ⁻¹ Mpc ⁻¹]	68.31 ± 0.82	66.3 ± 1.8
σ_8	0.820 ± 0.011	$0.800^{+0.015}_{-0.017}$
S_8	0.829 ± 0.011	0.832 ± 0.013
$\Delta\chi^2$	-1.4	-1.4

Notes. The $\Delta\chi^2$ values for best fits are computed with respect to the Λ CDM best fits computed from the corresponding data set combination.

1. $\mu(a, k)$: a modification of the Poisson equation for Ψ ,

$$k^2\Psi = -\mu(a, k)4\pi G a^2 [\rho\Delta + 3(\rho + P)\sigma], \quad (52)$$

where $\rho\Delta = \rho_m\Delta_m + \rho_r\Delta_r$, using comoving fractional density perturbations Δ , and where σ is the anisotropic stress from relativistic species (photons and neutrinos).

2. $\eta(a, k)$: an effective additional anisotropic stress, leading to a difference between the gravitational potentials Φ and Ψ , defined implicitly through

$$k^2 [\Phi - \eta(a, k)\Psi] = \mu(a, k)12\pi G a^2 (\rho + P)\sigma. \quad (53)$$

At late times, σ from standard particles is negligible and we find

$$\eta(a, k) \approx \Phi/\Psi. \quad (54)$$

These definitions are phenomenological, in the sense that they are not derived from a theoretical action. However, they are able to capture a generic deviation of the perturbation evolution from Λ CDM that does not need to correspond to a known model. This approach is complementary to constraints on action-based models, which are the topic of the next subsection. When $\eta = \mu = 1$ we recover GR at all times, including when there are non-zero contribution from photons and neutrinos to the density perturbation or anisotropic stress. In the parameterization adopted here (described further below), the MG contribution to η is only relevant at late times, when the anisotropic stress from relativistic particles is negligible.

In this section we fix the background evolution to that of Λ CDM ($w = -1$ at all times), so that any significant deviation of μ or η from unity would indicate a deviation from Λ CDM. We also consider constraints on the derived quantity Σ , defined as

$$k^2 [\Phi + \Psi] = -\Sigma(a, k)4\pi G a^2 [2\rho\Delta - 3(\rho + P)\sigma]. \quad (55)$$

Since Σ measures deviations of the lensing potential from the GR prediction, it is better constrained by WL data than μ and η separately.

For simplicity we only allow μ and η to vary with time (as in PDE15). Scale dependence increases the number of degeneracies in parameter space and may require, for example, higher-order statistics in WL observables (Peel et al. 2018) to break the degeneracies. We use the late-time DE parameterization of PDE15 and Casas et al. (2017), where the time evolution of all quantities is assumed to be proportional to the relative dark-energy density:

$$\mu(z) = 1 + E_{11}\Omega_{DE}(z); \quad (56a)$$

$$\eta(z) = 1 + E_{21}\Omega_{DE}(z). \quad (56b)$$

This defines the constants E_{11} and E_{21} . We report results in terms of $\mu_0 \equiv \mu(z = 0)$ and $\eta_0 \equiv \eta(z = 0)$, which are determined from E_{11} and E_{21} , given the dark-energy density parameter today. This parameterization is motivated by the assumption that the impact of dark energy depends on its density and therefore allows for more deviation of μ and η from Λ CDM at late times. The alternative early-time parameterization included in PDE15 led to similar results and is not discussed here for brevity. Our choice of parameterization, of course, limits the nature of possible deviations from Λ CDM; however, the choices of Eqs. (56a) and (56b) allow us to compare our results directly with those of PDE15.

Figure 32 shows the marginalized constraints on μ_0 and η_0 from different combinations of data, and also compares with the results from PDE15. Marginalized mean values and errors for cosmological parameters are presented in Table 7. This table also lists results for $\langle d^2 \rangle^{1/2}$, the root-mean-square CMB lensing deflection angle, and the parameter combination $\Sigma_0 S_8$ that is well-constrained by the DES WL data. These quantities allow the reader to assess the impact of lensing data on the parameter constraints. The μ parameter affects the growth of structure, so, for example, higher μ gives larger values of σ_8 . The CMB only constrains MG via the integrated Sachs-Wolfe effect (on large scales, where there is large cosmic variance) and CMB lensing. Lensing observations do not constrain the fluctuation amplitude directly, but the amplitude scaled by Σ (as defined in Eq. (55)). The degeneracy direction shown in Fig. 32 corresponds to approximately constant lensing amplitude, with higher μ_0 requiring lower Σ_0 and hence lower η_0 . The thickness of the degeneracy contour and its location depends on the constraint on lensing. With *Planck* data alone, or *Planck*+SNe+BAO, the lensing amplitude is pulled to high values by the preference for more lensing discussed in Sect. 6.2, so the contours are slightly shifted with respect to Λ CDM. The inclusion of WL³⁵ data shrinks the contour, and reduces the offset with respect to Λ CDM; DES WL data disfavour higher lensing amplitudes than predicted by the *Planck* Λ CDM cosmology. DES also measures lensing at much lower redshift than CMB lensing, so it is a more powerful probe of MG models where changes to GR only appear at late times (as we have assumed).

The BAO/RSD data constrain μ_0 directly, since redshift distortions are a probe of structure growth. The lower panel of Fig. 32 shows constraints with BAO/RSD alone, and also demonstrates that removing the CMB lensing reconstruction data shifts the contour further from Λ CDM; this is consistent with the pull away from Λ CDM being driven by the preference for more lensing in the high- ℓ CMB power spectra.

We can further demonstrate the effect of CMB lensing by varying the consistency parameter A_L within MG models. Figure 31 shows the degeneracy between A_L and $\Sigma_0 - 1$, which is computed as a derived parameter in our (μ, η) parameterization. Here A_L affects lensing of the CMB power spectra only, while Σ_0 encodes modifications to the lensing amplitude caused by modifications of gravity. The contours show that MG models

³⁵ Tests during the writing of this paper revealed a bug in MGCAMB that was also present in 2015. This bug reduced the constraining power of WL data for the (μ, η) parameterization (which in 2015 was suppressed by the very conservative excision of nonlinear scales). The CMB and BAO/RSD constraints and other cosmological models were not affected by this bug.

Table 7. Marginalized values and 68% confidence regions for cosmological parameters obtained combining *Planck* TT,TE,EE+lowE with other data sets, assuming the (μ, η) parameterization of modified gravity.

Parameter	With CMB lensing			Without CMB lensing		
	<i>Planck</i>	<i>Planck</i> +SNe+BAO	<i>Planck</i> +BAO/RSD+WL	<i>Planck</i>	<i>Planck</i> +SNe+BAO	<i>Planck</i> +BAO/RSD+WL
$\mu_0 - 1$	$0.10^{+0.30}_{-0.42}$	$0.05^{+0.26}_{-0.39}$	$-0.07^{+0.19}_{-0.32}$	$0.12^{+0.29}_{-0.51}$	$0.10^{+0.30}_{-0.50}$	$-0.12^{+0.17}_{-0.32}$
$\eta_0 - 1$	$0.22^{+0.55}_{-1.0}$	$0.32^{+0.63}_{-0.89}$	$0.32^{+0.63}_{-0.89}$	$0.55^{+0.78}_{-1.2}$	$0.62^{+0.79}_{-1.2}$	$0.52^{+0.67}_{-0.86}$
$\Sigma_0 - 1$	0.100 ± 0.093	0.106 ± 0.086	$0.018^{+0.059}_{-0.048}$	$0.27^{+0.15}_{-0.13}$	$0.27^{+0.15}_{-0.13}$	$0.017^{+0.058}_{-0.050}$
τ	$0.0481^{+0.0087}_{-0.0072}$	$0.0487^{+0.0088}_{-0.0074}$	0.0524 ± 0.0075	0.0504 ± 0.0080	0.0505 ± 0.0080	0.0526 ± 0.0079
H_0 [km s ⁻¹ Mpc ⁻¹]	68.20 ± 0.63	68.19 ± 0.45	68.09 ± 0.45	68.23 ± 0.71	68.26 ± 0.48	68.09 ± 0.46
σ_8	$0.812^{+0.034}_{-0.040}$	$0.807^{+0.029}_{-0.039}$	$0.799^{+0.023}_{-0.033}$	$0.817^{+0.032}_{-0.053}$	$0.814^{+0.033}_{-0.052}$	$0.794^{+0.020}_{-0.032}$
S_8	0.817 ± 0.037	$0.812^{+0.033}_{-0.038}$	$0.806^{+0.027}_{-0.034}$	$0.822^{+0.040}_{-0.051}$	$0.819^{+0.037}_{-0.052}$	$0.801^{+0.025}_{-0.034}$
$\langle d^2 \rangle^{1/2}$ [arcmin]	$2.531^{+0.046}_{-0.052}$	2.529 ± 0.049	2.453 ± 0.032	$2.697^{+0.095}_{-0.082}$	$2.695^{+0.099}_{-0.080}$	2.456 ± 0.043
$\Sigma_0 S_8$	0.898 ± 0.067	$0.897^{+0.068}_{-0.061}$	$0.820^{+0.043}_{-0.035}$	$1.04^{+0.12}_{-0.099}$	$1.04^{+0.12}_{-0.098}$	$0.814^{+0.044}_{-0.038}$
$\Delta\chi^2$	-4.6	-5.5	-1.2	-10.2	-11.0	-0.7

Notes. The $\Delta\chi^2$ values are computed with respect to the best-fit Λ CDM cosmology, using the same data combination. The quantity $\langle d^2 \rangle^{1/2}$ is the root-mean-square CMB lensing deflection angle, which is pulled high by the CMB data unless galaxy lensing (WL) or CMB lensing are included. The combination $\Sigma_0 S_8$ is approximately the lensing amplitude parameter best constrained by the DES WL data at lower redshift.

($\Sigma_0 \neq 1$) are preferred by the *Planck* power spectra (although not strongly) if $A_L = 1$. The preference for higher Σ_0 values is reduced by allowing larger A_L ; the preference for MG that we find is therefore largely another reflection of the preference for $A_L > 1$ discussed in Sect. 6.2. Adding *Planck* CMB lensing measurements shifts the contours back into consistency with Λ CDM (blue contours). Adding BAO/RSD + WL tightens the constraints (red contours) which remain consistent with Λ CDM. Using the CamSpec likelihood gives slightly less preference for high A_L , and the results for *Planck* TT,TE,EE+lowE+lensing shift by about 0.2σ towards better consistency with Λ CDM.

7.4.3. Effective field theory description of dark energy

To investigate action-based models that can give interesting values of μ and η , we limit ourselves to a sub-class of effective field theories (EFTs, Cheung et al. 2008; Creminelli et al. 2009; Gubitosi et al. 2013). The EFTs we consider contain models with a single scalar field and at most second-order equations of motion, a restriction that is in general necessary to avoid the so-called Ostrogradski instability. In addition, EFTs typically assume a universal coupling to gravity; models with non-universal couplings (Amendola 2000; Pettorino & Baccigalupi 2008), multiple scalar fields, additional vector (Hellings & Nordtvedt 1973) or tensor fields (Hassan et al. 2012), or non-local models (Belgacem et al. 2018) do not fall into this class and are not considered here. Nevertheless EFTs provide a general set of models for which we can, in principle, compute all quantities of interest, including μ and η (which will span a restricted part of the μ - η space considered in the previous section.)

As described in Sect. 5.2.1 of PDE15, the degrees of freedom in actions of this class of models can be reduced to the expansion rate H and five additional functions of time (Gleyzes et al. 2013; Bellini & Sawicki 2014) $\{\alpha_M, \alpha_K, \alpha_B, \alpha_T, \alpha_H\}$. However, measurements of the speed of gravitational waves (Abbott et al. 2017a) imply that $\alpha_T(z=0) \simeq 0$, which reduces the space of acceptable models (Lombriser & Taylor 2016; McManus et al.

2016; Creminelli & Vernizzi 2017; Ezquiaga & Zumalacáregui 2017; Sakstein & Jain 2017; Baker et al. 2017).

Apart from models where gravitational wave propagation is not modified at all, which would necessarily limit us to $\eta = 1$ (Saltas et al. 2014), only conformally (non-minimally) coupled models³⁶ with $\alpha_B = -\alpha_M$ (and $\alpha_H = 0$) naturally lead to $\alpha_T = 0$. For these reasons we focus on this latter class of models (and for simplicity we assume $\alpha_T(z) \simeq 0$ at all times), and in addition choose the kinetic terms of the scalar (set by α_K) to keep the scalar sound speed equal to the speed of light (current observational data are not able to constrain the sound speed significantly, see e.g., the k -essence model constraints in PDE15). We finally end up with a non-minimally coupled k -essence model described by the single function α_M that determines the running of the Planck mass. The background expansion is chosen to be the same as in Λ CDM, as in our analysis of the μ - η parameterization described in the previous section. The main difference relative to PDE15 is that we now allow for $\alpha_M < 0$, which corresponds to a Planck mass decreasing with time.

As in PDE15 we adopt the parameterization $\alpha_M = \alpha_{M0} a^\beta$, where α_{M0} is the value of α_M today and where $\beta > 0$ determines how quickly the absolute value of α_M decreases at high redshift. In terms of the non-minimal coupling function Ω multiplying the Ricci scalar R in the action, this corresponds to³⁷

$$\Omega^{\text{EFT}}(a) = \exp\left\{\frac{\alpha_{M0}}{\beta} a^\beta\right\} - 1 = \exp\left\{\Omega_0^{\text{EFT}} a^\beta\right\} - 1, \quad (57)$$

which agrees with the exponential model built-in to EFTCAMB (Raveri et al. 2014) (which we use to compute the model

³⁶ Recently the EFT action has been extended to include degenerate higher-order theories (DHOST, Zumalacáregui & García-Bellido 2014; Gleyzes et al. 2015; Ben Achour et al. 2016), which feature an additional parameter called β_1 (Langlois et al. 2017). DHOST models can also give $\alpha_T \simeq 0$, but α_H and β_1 are constrained to be small from astrophysical tests of gravity (Crisostomi & Koyama 2018; Langlois et al. 2018; Dima & Vernizzi 2018; Saltas et al. 2018).

³⁷ This notation is conventional; note that Ω^{EFT} here is not the contribution to the critical density, and Ω_0^{EFT} is not the value of $\Omega^{\text{EFT}}(a)$ at $a = 1$.

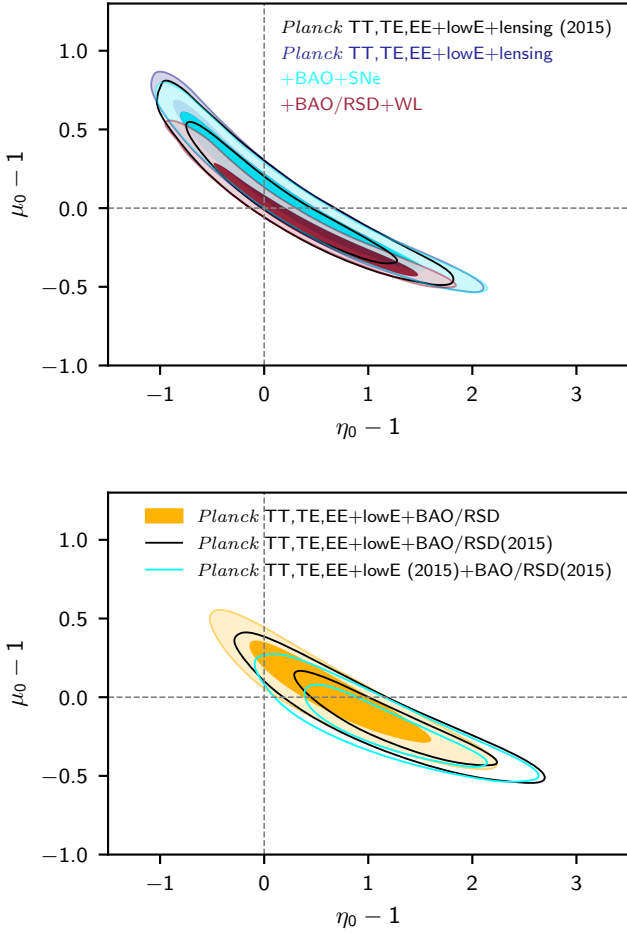


Fig. 31. *Top:* marginalized posterior distributions of the MG parameters μ and η for *Planck* TT,TE,EE+lowE+lensing data alone and in combination with external data (as indicated in the legend), using the late-time parameterization and neglecting any scale dependence. The dashed lines show the standard Λ CDM model. *Bottom:* impact of the BAO/RSD and *Planck* TT,TE,EE+lowE data, compared to the 2015 results. For the 2018 *Planck* data, the contours shift towards lower values of $\eta_0 - 1$, along the maximum degeneracy line (black versus cyan contours) and shift in the same direction when using the BAO/RSD data (yellow versus black contours).

predictions presented here). The resulting posterior distribution on Ω_0^{EFT} , marginalized over β and other parameters, is shown in Fig. 33. The Λ CDM limit lies at $\Omega_0^{\text{EFT}} = 0$ (vertical dashed line). We see that the posterior distribution prefers negative values of Ω_0^{EFT} , with a shift of 1.6σ for the baseline *Planck* TT,TE,EE+lowE+lensing likelihood and 2.1σ if CMB lensing is excluded. These shifts are reduced to 0.8σ with the addition of BAO/RSD+WL to the *Planck* TT,TE,EE+lowE+lensing likelihood and to 0.9σ if *Planck* lensing is excluded. Table 8 gives the parameter constraints for these data combinations and lists the changes in χ^2 of the best fits relative to base Λ CDM. As was the case for the (μ, η) parameterization, DES WL measurements pull the contours towards Λ CDM. If we determine μ_0 and η_0 that correspond to the mean values of the EFT parameters for a specific scale choice, we find that the parameters lie in the top-left quadrant of the (μ, η) parameter space shown in Fig. 32. Another class of models that predicts values of (μ, η) in the top-left quadrant of Fig. 32 are the non-local models, specifically the RR model of Dirian et al. (2016); these models are not discussed here.

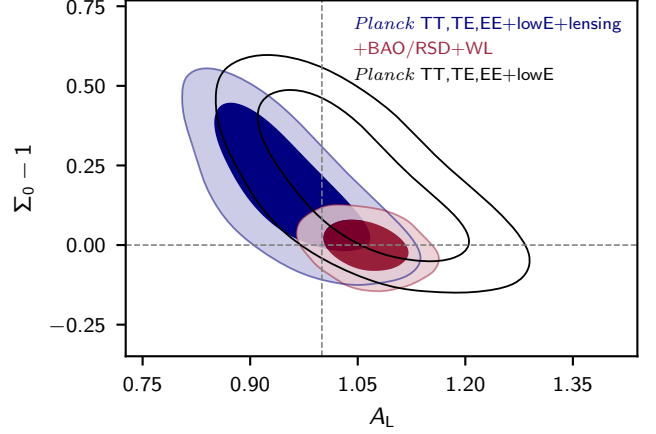


Fig. 32. Degeneracy between A_L and $\Sigma_0 - 1$, computed as a derived parameter in our (μ, η) parameterization. The horizontal dashed line includes Λ CDM (but is also marginalized over one of the two degrees of freedom in the μ - η space). The vertical dashed line shows $A_L = 1$. The filled contours use the *Planck* TT,TE,EE+lowE+lensing likelihood, alone and in combination with WL+BAO/RSD data. The unfilled contours show the constraints from *Planck* TT,TE,EE+lowE. Note that A_L only affects CMB lensing of the *Planck* power spectra by definition, as discussed in Sect. 6.2.

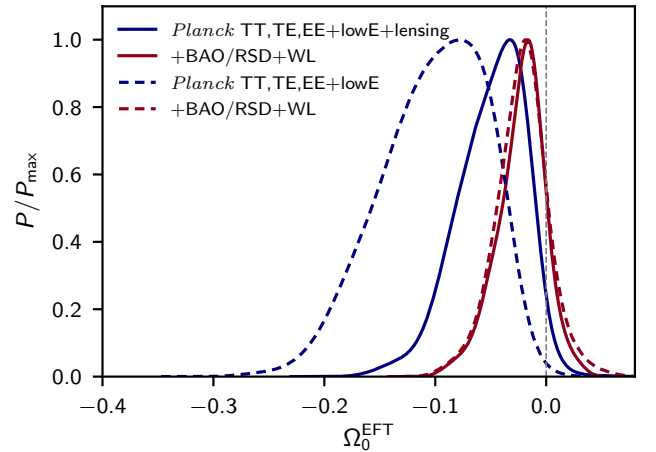


Fig. 33. Marginalized posterior distribution of Ω_0^{EFT} that parameterizes the evolution of the *Planck* mass according to Eq. (57) in the EFT model. We show constraints for *Planck* TT,TE,EE+lowE+lensing data (solid lines), as well as *Planck* TT,TE,EE+lowE data without CMB lensing (dashed lines), both alone and in combination with WL+BAO/RSD data. The Λ CDM limit lies at $\Omega_0^{\text{EFT}} = 0$ (vertical dashed line).

Overall, the EFT sub-class of non-minimally coupled k -essence models considered here is not preferred by current data. Without using CMB and galaxy WL lensing, *Planck* gives a moderate preference for models that predict more lensing compared to Λ CDM (as found in our investigation of the (μ, η) parameterization). However, combining *Planck* with CMB and DES WL lensing measurements disfavors high lensing amplitudes and pulls the parameters towards Λ CDM.

7.4.4. General remarks

Planck alone provides relatively weak constraints on dark energy and modified gravity, but *Planck* does constrain other cosmological parameters extremely well. By combining *Planck* with

external data we then obtain tight constraints on these models. We find no strong evidence for deviations from Λ CDM, either at the background level or when allowing for changes to the perturbations. At the background level, Λ CDM is close to the best fit. In the simple μ - η and EFT parameterizations of perturbation-level deviations from GR, we do find better fits to the *Planck* TT,TE,EE+lowE data compared to Λ CDM, but this is largely associated with the preference in the CMB power spectra for higher lensing amplitudes (as discussed in Sect. 6.2), rather than a distinctive preference for modified gravity. Adding weak lensing data disfavors the large lensing amplitudes and our results are consistent with Λ CDM to within 1σ . Since neutrino masses are in general degenerate with DE and MG parameters, it is also worth testing the impact of varying neutrino masses versus fixing them to our base- Λ CDM value of $m_\nu = 0.06$ eV. We find similar trends, with slightly larger posteriors when varying the neutrino mass.

7.5. Neutrinos and extra relativistic species

7.5.1. Neutrino masses

The *Planck* base- Λ CDM model assumes a normal mass hierarchy with the minimal mass $\sum m_\nu = 0.06$ eV allowed by neutrino flavour oscillation experiments. However, current observations are consistent with many neutrino mass models, and there are no compelling theoretical reasons to strongly prefer any one of them. Since the masses are already known to be non-zero, allowing for larger $\sum m_\nu$ is one of the most well-motivated extensions of the base model. The normal hierarchy, in which the lowest two mass eigenstates have the smallest mass splitting, can give any $\sum m_\nu \gtrsim 0.06$ eV; an inverted hierarchy, in which the two most massive eigenstates have the smallest mass separation, requires $\sum m_\nu \gtrsim 0.1$ eV. A constraint that $\sum m_\nu < 0.1$ eV would therefore rule out the inverted hierarchy. For a review of neutrino physics and the impact on cosmology see e.g., [Lesgourgues et al. \(2013\)](#).

As in [PCP13](#) and [PCP15](#), we quote constraints assuming three species of neutrino with degenerate mass, a Fermi-Dirac distribution, and zero chemical potential. At *Planck* sensitivity the small mass splittings can be neglected to good accuracy (see e.g., [Lesgourgues & Pastor 2006](#)). Neutrinos that become non-relativistic around recombination produce distinctive signals in the CMB power spectra, which *Planck* and other experiments have already ruled out. If the neutrino mass is low enough that they became non-relativistic after recombination ($m_\nu \ll 1$ eV), the main effect on the CMB power spectra is a change in the angular diameter distance that is degenerate with decreasing H_0 . The *Planck* data then mainly constrain lower masses via the lensing power spectrum and the impact of lensing on the CMB power spectra. Since the CMB power spectra prefer slightly more lensing than in the base- Λ CDM model, and neutrino mass can only suppress the power, we obtain somewhat stronger constraints than might be expected in typical realizations of a minimal-mass neutrino model.

In [PCP15](#) no preference for higher neutrino masses was found, but a tail to high neutrino masses was still allowed, with relatively high primordial amplitudes A_s combining with high neutrino mass to give acceptable lensing power. The tighter 2018 constraint on the optical depth from polarization at low multipoles restricts the primordial A_s to be smaller, to match the same observed high- ℓ power ($C_\ell \propto A_s e^{-2\tau}$); this reduces the parameter space with larger neutrino masses, giving tighter constraints on the mass. With only temperature information at high ℓ , the

95% CL upper bound moved from 0.72 eV ([PCP15](#) TT+lowP) to 0.59 eV (using the SimLow polarization likelihood of [Planck Collaboration Int. XLVI 2016](#), at low ℓ). This now further tightens to

$$\sum m_\nu < 0.54 \text{ eV} \quad (95\%, \text{Planck TT+lowE}). \quad (58a)$$

Adding high- ℓ polarization further restricts residual parameter degeneracies, and the limit improves to

$$\sum m_\nu < 0.26 \text{ eV} \quad (95\%, \text{Planck TT,TE,EE+lowE}). \quad (58b)$$

Although the high- ℓ TT spectrum prefers more lensing than in base Λ CDM, the lensing reconstruction is very consistent with expected amplitudes. In [PCP15](#), the 2015 lensing likelihood weakened joint neutrino mass constraints because it preferred substantially less lensing than the temperature power spectrum. The 2018 lensing construction gives a slightly (1–2%) higher lensing power spectrum amplitude than in 2015, which, combined with the decrease in the range of higher lensing amplitudes allowed by the new TT+lowE likelihood, means that the constraints are more consistent. Adding lensing therefore now slightly tightens the constraints to

$$\sum m_\nu < 0.44 \text{ eV} \quad (95\%, \text{TT+lowE+lensing}), \quad (59a)$$

$$\sum m_\nu < 0.24 \text{ eV} \quad (95\%, \text{TT,TE,EE+lowE+lensing}). \quad (59b)$$

The joint constraints using polarization are however sensitive to the details of the high- ℓ polarization likelihoods, with the CamSpec likelihood giving significantly weaker constraints with polarization:

$$\sum m_\nu < 0.38 \text{ eV} \quad (95\%, \text{TT,TE,EE+lowE} \\ \text{[CamSpec]}) \quad (60a)$$

$$\sum m_\nu < 0.27 \text{ eV} \quad (95\%, \text{TT,TE,EE+lowE} \\ \text{+lensing [CamSpec]}). \quad (60b)$$

As discussed in Sect. 6.2, the CamSpec TT,TE,EE+lowE likelihood shows a weaker preference for higher lensing amplitude A_L than the default Plik likelihood, and this propagates directly into a weaker constraint on the neutrino mass, since for small masses the constraint is largely determined by the lensing effect. The differences between Plik and CamSpec are much smaller if we add CMB lensing, since the lensing measurements restrict the lensing amplitude to values closer to those expected in base Λ CDM.

The combination of the acoustic scale measured by the CMB (θ_{MC}) and BAO data is sufficient to largely determine the background geometry in the Λ CDM+ $\sum m_\nu$ model, since the lower-redshift BAO data break the geometric degeneracy. Combining BAO data with the CMB lensing reconstruction power spectrum (with priors on $\Omega_b h^2$ and n_s , following [PL2015](#)), the neutrino mass can also be constrained to be

$$\sum m_\nu < 0.60 \text{ eV} \quad (95\%, \text{Planck lensing+BAO+}\theta_{MC}). \quad (61)$$

This number is consistent with the tighter constraints using the CMB power spectra, and almost independent of lensing effects in the CMB spectra; it would hold even if the A_L tension discussed in Sect. 6.2 were interpreted as a sign of unknown residual systematics. Since the constraint from the CMB power spectra is strongly limited by the geometrical degeneracy,

Table 8. Marginalized values and 68% confidence regions for cosmological parameters obtained by combining *Planck* TT,TE,EE+lowE with other data sets, assuming the EFT parameterization $\Omega_0^{\text{EFT}}(a)$.

Parameter	With CMB lensing		Without CMB lensing	
	<i>Planck</i>	<i>Planck</i> +BAO/RSD+WL	<i>Planck</i>	<i>Planck</i> +BAO/RSD+WL
Ω_0^{EFT}	$-0.049^{+0.037}_{-0.024}$ (1.6 σ)	$-0.019^{+0.024}_{-0.019}$ (0.8 σ)	$-0.101^{+0.059}_{-0.038}$ (2.1 σ)	-0.021 ± 0.025 (0.9 σ)
α_{M0}	$-0.040^{+0.041}_{-0.016}$	$-0.015^{+0.019}_{-0.017}$	$-0.075^{+0.073}_{-0.028}$	$-0.014^{+0.017}_{-0.014}$
β	$0.72^{+0.38}_{-0.14}$	$0.66^{+0.44}_{-0.21}$	$0.66^{+0.38}_{-0.16}$	$0.62^{+0.45}_{-0.24}$
τ	$0.0489^{+0.0083}_{-0.0072}$	$0.0549^{+0.0096}_{-0.011}$	0.0497 ± 0.0082	0.0528 ± 0.0086
H_0 [km s ⁻¹ Mpc ⁻¹] ...	68.19 ± 0.67	68.22 ± 0.46	68.30 ± 0.71	68.16 ± 0.46
σ_8	0.8198 ± 0.0074	0.8151 ± 0.0067	$0.845^{+0.013}_{-0.015}$	$0.8164^{+0.0087}_{-0.010}$
S_8	0.826 ± 0.013	0.8205 ± 0.0098	0.849 ± 0.017	0.823 ± 0.011
$\Delta\chi^2$	-4.3	-2.1	-9.7	-2.9

Notes. The $\Delta\chi^2$ values are computed with respect to the best-fit Λ CDM model using the same data combination. Values in brackets give the significance of the deviation from zero assuming a Gaussian posterior distribution.

adding BAO data to the *Planck* likelihood significantly tightens the neutrino mass constraints. Without CMB lensing we find

$$\sum m_\nu < 0.16 \text{ eV} \quad (95\%, \text{Planck TT+lowE+BAO}), \quad (62a)$$

$$\sum m_\nu < 0.13 \text{ eV} \quad (95\%, \text{Planck TT,TE,EE+lowE+BAO}), \quad (62b)$$

and combining with lensing the limits further tighten to

$$\sum m_\nu < 0.13 \text{ eV} \quad (95\%, \text{Planck TT+lowE+BAO}), \quad (63a)$$

$$\sum m_\nu < 0.12 \text{ eV} \quad (95\%, \text{Planck TT,TE,EE+lowE+BAO}). \quad (63b)$$

These combined constraints are almost immune to high- ℓ polarization modelling uncertainties, with the CamSpec likelihood giving the 95% limit $\sum m_\nu < 0.13 \text{ eV}$ for *Planck* TT,TE,EE+lowE+lensing+BAO.

Adding the Pantheon SNe data marginally tightens the bound to $\sum m_\nu < 0.11 \text{ eV}$ (95%, *Planck* TT,TE,EE+lowE+lensing+BAO+Pantheon). In contrast the full DES 1-year data prefer a slightly lower σ_8 value than the *Planck* Λ CDM best fit, so DES slightly favours higher neutrino masses, relaxing the bound to $\sum m_\nu < 0.14 \text{ eV}$ (95%, *Planck* TT,TE,EE+lowE+lensing+BAO+DES).

Increasing the neutrino mass leads to lower values of H_0 , and hence aggravates the tension with the distance-ladder determination of Riess et al. (2018a, see Fig. 34). Adding the Riess et al. (2018a) H_0 measurement to *Planck* will therefore give even tighter neutrino mass constraints (see the parameter tables in the PLA), but such constraints should be interpreted cautiously until the Hubble tension is better understood.

The remarkably tight constraints using CMB and BAO data are comparable with the latest bounds from combining with Ly α forest data (Palanque-Delabrouille et al. 2015; Yèche et al. 2017). Although Ly α is a more direct probe of the neutrino mass (in the sense that it is sensitive to the matter power spectrum on scales where the suppression caused by neutrinos is expected to be significant) the measurements are substantially more difficult to model and interpret than the CMB and BAO data. Our 95% limit of $\sum m_\nu < 0.12 \text{ eV}$ starts to put pressure

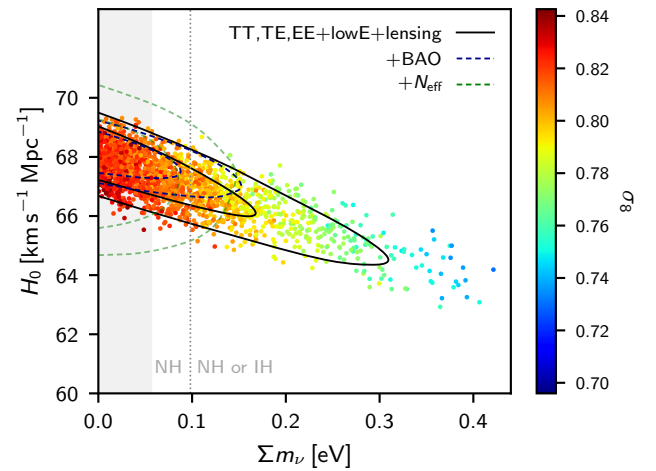


Fig. 34. Samples from *Planck* TT,TE,EE+lowE chains in the $\sum m_\nu$ - H_0 plane, colour-coded by σ_8 . Solid black contours show the constraints from *Planck* TT,TE,EE+lowE+lensing, while dashed blue lines show the joint constraint from *Planck* TT,TE,EE+lowE+lensing+BAO, and the dashed green lines additionally marginalize over N_{eff} . The grey band on the left shows the region with $\sum m_\nu < 0.056 \text{ eV}$ ruled out by neutrino oscillation experiments. Mass splittings observed in neutrino oscillation experiments also imply that the region left of the dotted vertical line can only be a normal hierarchy (NH), while the region to the right could be either the normal hierarchy or an inverted hierarchy (IH).

on the inverted mass hierarchy (which requires $\sum m_\nu \gtrsim 0.1 \text{ eV}$) independently of Ly α data. This is consistent with constraints from neutrino laboratory experiments which also slightly prefer the normal hierarchy at 2–3 σ (Adamson et al. 2017; Abe et al. 2018; Capozzi et al. 2018; de Salas et al. 2018a,b).

7.5.2. Effective number of relativistic species

New light particles appear in many extensions of the Standard Model of particle physics. Additional dark relativistic degrees of freedom are usually parameterized by N_{eff} , defined so that the total relativistic energy density well after electron-positron annihilation is given by

$$\rho_{\text{rad}} = N_{\text{eff}} \frac{7}{8} \left(\frac{4}{11} \right)^{4/3} \rho_\gamma. \quad (64)$$

The standard cosmological model has $N_{\text{eff}} \approx 3.046$, slightly larger than 3 since the three standard model neutrinos were not completely decoupled at electron-positron annihilation (Gnedin & Gnedin 1998; Mangano et al. 2005; de Salas & Pastor 2016).

We can treat any additional massless particles produced well before recombination (that neither interact nor decay) as simply an additional contribution to N_{eff} . Any species that was initially in thermal equilibrium with the Standard Model particles produces a $\Delta N_{\text{eff}} (\equiv N_{\text{eff}} - 3.046)$ that depends only on the number of degrees of freedom and decoupling temperature. Using conservation of entropy, fully thermalized relics with g degrees of freedom contribute

$$\Delta N_{\text{eff}} = g \left[\frac{43}{4g_s} \right]^{4/3} \times \begin{cases} 4/7 & \text{boson,} \\ 1/2 & \text{fermion,} \end{cases} \quad (65)$$

where g_s is the effective degrees of freedom for the entropy of the other thermalized relativistic species that are present when they decouple.³⁸ Examples range from a fully thermalized sterile neutrino decoupling at $1 \lesssim T \lesssim 100$ MeV, which produces $\Delta N_{\text{eff}} = 1$, to a thermalized boson decoupling before top quark freeze-out, which produces $\Delta N_{\text{eff}} \approx 0.027$.

Additional radiation does not need to be fully thermalized, in which case ΔN_{eff} must be computed on a model-by-model basis. We follow a phenomenological approach in which we treat N_{eff} as a free parameter. We allow $N_{\text{eff}} < 3.046$ for completeness, corresponding to standard neutrinos having a lower temperature than expected, even though such models are less well motivated theoretically.

The 2018 *Planck* data are still entirely consistent with $N_{\text{eff}} \approx 3.046$, with the new low- ℓ polarization constraint lowering the 2015 central value slightly and with a corresponding 10% reduction in the error bar, giving

$$N_{\text{eff}} = 3.00^{+0.57}_{-0.53} \quad (95\%, \text{Planck TT+lowE}), \quad (66a)$$

$$N_{\text{eff}} = 2.92^{+0.36}_{-0.37} \quad (95\%, \text{Planck TT,TE,EE+lowE}), \quad (66b)$$

with similar results including lensing. Modifying the relativistic energy density before recombination changes the sound horizon, which is partly degenerate with changes in the late-time geometry. Although the physical acoustic scale measured by BAO data changes in the same way, the low-redshift BAO geometry helps to partially break the degeneracies. Despite improvements in both BAO data and *Planck* polarization measurements, the joint *Planck*+BAO constraints remain similar to PCP15:

$$N_{\text{eff}} = 3.11^{+0.44}_{-0.43} \quad (95\%, \text{TT+lowE+lensing+BAO}); \quad (67a)$$

$$N_{\text{eff}} = 2.99^{+0.34}_{-0.33} \quad (95\%, \text{TT,TE,EE+lowE+lensing+BAO}). \quad (67b)$$

For $N_{\text{eff}} > 3.046$ the *Planck* data prefer higher values of the Hubble constant and fluctuation amplitude, σ_8 , than for the base- Λ CDM model. This is because higher N_{eff} leads to a smaller sound horizon at recombination and H_0 must rise to keep the acoustic scale, $\theta_* = r_*/D_M$, fixed at the observed value. Since the change in the allowed Hubble constant with N_{eff} is associated with a change in the sound horizon, BAO data do not help

³⁸ For most of the thermal history $g_s \approx g_*$, where g_* is the effective degrees of freedom for density, but they can differ slightly, for example during the QCD phase transition (Borsanyi et al. 2016).

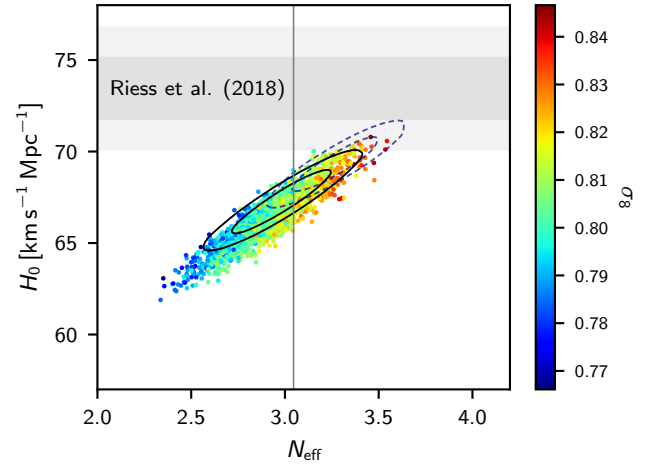


Fig. 35. Samples from *Planck* TT,TE,EE+lowE chains in the $N_{\text{eff}}-H_0$ plane, colour-coded by σ_8 . The grey bands show the local Hubble parameter measurement $H_0 = (73.45 \pm 1.66)$ km s⁻¹ Mpc⁻¹ from Riess et al. (2018a). Solid black contours show the constraints from *Planck* TT,TE,EE+lowE+lensing+BAO, while dashed lines the joint constraint also including Riess et al. (2018a). Models with $N_{\text{eff}} < 3.046$ (left of the solid vertical line) require photon heating after neutrino decoupling or incomplete thermalization.

to strongly exclude larger values of N_{eff} . Thus varying N_{eff} allows the tension with Riess et al. (2018a, R18) to be somewhat eased, as illustrated in Fig. 35. However, although the 68% error from *Planck* TT,TE,EE+lowE+lensing+BAO on the Hubble parameter is weakened when allowing varying N_{eff} , it is still discrepant with R18 at just over 3σ , giving $H_0 = (67.3 \pm 1.1)$ km s⁻¹ Mpc⁻¹. Interpreting this discrepancy as a moderate statistical fluctuation, the combined result is

$$\left. \begin{aligned} N_{\text{eff}} &= 3.27 \pm 0.15 \\ H_0 &= (69.32 \pm 0.97) \text{ km s}^{-1} \text{ Mpc}^{-1} \end{aligned} \right\} \begin{array}{l} 68\%, \text{ TT,TE,EE+lowE+} \\ \text{lensing+BAO+R18.} \end{array} \quad (68)$$

However, as explained in PCP15, this set of parameters requires an increase in σ_8 and a decrease in Ω_m , potentially increasing tensions with weak galaxy lensing and (possibly) cluster count data. Higher values for N_{eff} also start to come into tension with observational constraints on primordial light element abundances (see Sect. 7.6).

Restricting ourselves to the more physically motivated models with $\Delta N_{\text{eff}} > 0$, the one-tailed *Planck* TT,TE,EE+lowE+lensing+BAO constraint is $\Delta N_{\text{eff}} < 0.30$ at 95%. This rules out light thermal relics that decoupled after the QCD phase transition (although new species are still allowed if they decoupled at higher temperatures and with g not too large). Figure 36 shows the detailed constraint as a function of decoupling temperature, assuming only light thermal relics and other Standard Model particles.

7.5.3. Joint constraints on neutrino mass and N_{eff}

There are various theoretical scenarios in which it is possible to have both sterile neutrinos and neutrino mass. We first consider the case of massless relics combined with the three standard degenerate active neutrinos, varying N_{eff} and $\sum m_\nu$ together. The parameters are not very correlated, so the mass constraint is similar to that obtained when not also varying N_{eff} . We find:

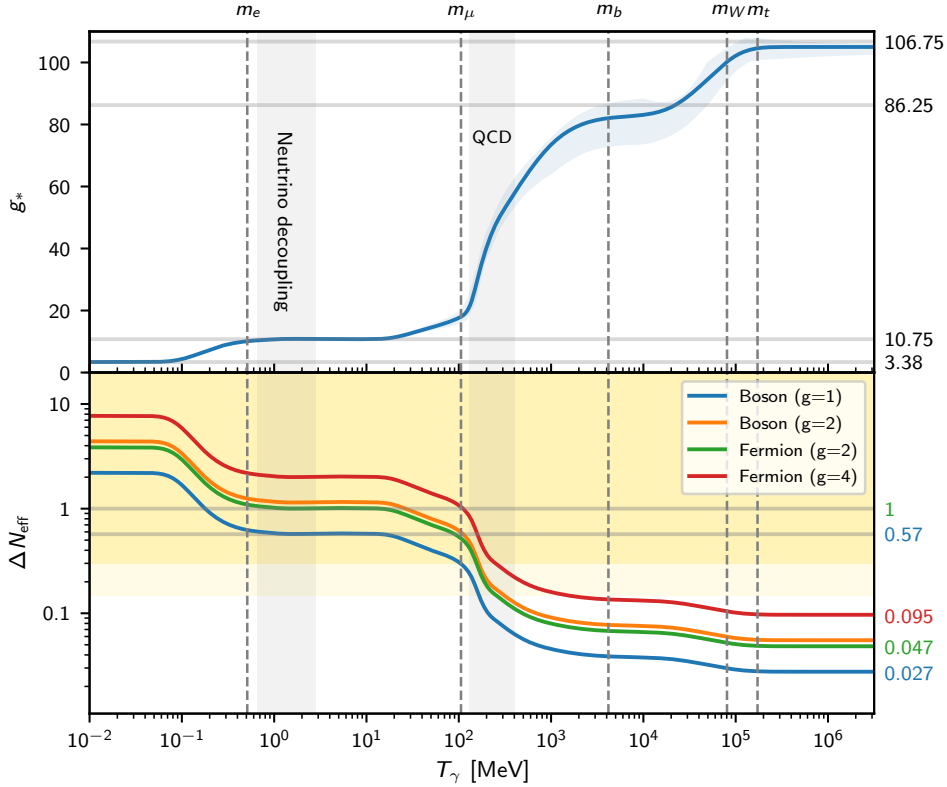


Fig. 36. Constraints on additional relativistic particles. *Top:* evolution of the effective degrees of freedom for Standard Model particle density, g_* , as a function of photon temperature in the early Universe. Vertical bands show the approximate temperature of neutrino decoupling and the QCD phase transition, and dashed vertical lines denote some mass scales at which corresponding particles annihilate with their antiparticles, reducing g_* . The solid line shows the fit of Borsanyi et al. (2016) plus standard evolution at $T_\gamma < 1$ MeV, and the pale blue bands the estimated $\pm 1\sigma$ error region from Saikawa & Shirai (2018). Numbers on the right indicate specific values of g_* expected from simple degrees of freedom counting. *Bottom:* expected ΔN_{eff} today for species decoupling from thermal equilibrium as a function of the decoupling temperature, where lines show the prediction from the Borsanyi et al. (2016) fit assuming a single scalar boson ($g = 1$, blue), bosons with $g = 2$ (e.g., a massless gauge vector boson, orange), a Weyl fermion with $g = 2$ (green), or fermions with $g = 4$ (red). One-tailed 68% and 95% regions excluded by *Planck* TT,TE,EE+lowE+lensing+BAO are shown in gold; this rules out at 95% significance light thermal relics decoupling after the QCD phase transition (where the theoretical uncertainty on g_* is negligible), including specific values indicated on the right axis of $\Delta N_{\text{eff}} = 0.57$ and 1 for particles decoupling between muon and positron annihilation. At temperatures well above the top quark mass and electroweak phase transition, g_* remains somewhat below the naive 106.75 value expected for all the particles in the Standard Model, giving interesting targets for ΔN_{eff} that may be detectable in future CMB experiments (see e.g. Baumann et al. 2018).

$$\left. \begin{array}{l} N_{\text{eff}} = 2.96^{+0.34}_{-0.33}, \\ \sum m_\nu < 0.12 \text{ eV}, \end{array} \right\} \begin{array}{l} 95\%, \text{ Planck} \\ \text{TT,TE,EE+lowE+lensing+BAO.} \end{array} \quad (69)$$

The bounds remain very close to the bounds on either N_{eff} (Eq. (67b)) or $\sum m_\nu$ (Eq. (63b)) in 7-parameter models, showing that the data clearly differentiate between the physical effects generated by the addition of these two parameters. Similar results are found without lensing and BAO data. Although the mass constraint is almost unchanged, varying N_{eff} does allow for larger Hubble parameters, as shown in Fig. 34. However, as discussed in PCP15 and the previous section, this does not substantially help to resolve possible tensions with σ_8 measurements from other astrophysical data.

The second case that we consider is massive sterile neutrinos combined with standard active neutrinos having a minimal-mass hierarchy, parameterizing the sterile mass by $m_{\nu, \text{sterile}}^{\text{eff}} \equiv \Omega_{\nu, \text{sterile}} h^2 (94.1 \text{ eV})$ as in PCP13 and PCP15. The physical mass of the sterile neutrino in this case is $m_{\text{sterile}}^{\text{thermal}} = (\Delta N_{\text{eff}})^{-3/4} m_{\nu, \text{sterile}}^{\text{eff}}$ assuming a thermal sterile neutrino, or $m_{\text{sterile}}^{\text{DW}} = (\Delta N_{\text{eff}})^{-1} m_{\nu, \text{sterile}}^{\text{eff}}$ in the case of production via the mechanism described by Dodelson & Widrow (1994). For low ΔN_{eff} the physical mass can therefore

become large, in which case the particles behave in the same way as cold dark matter. In our grid of parameter chains we adopt a prior that $m_{\text{sterile}}^{\text{thermal}} < 10 \text{ eV}$ (and necessarily $\Delta N_{\text{eff}} \geq 0$) to exclude parameter space that is degenerate with a change in the cold dark matter density; as we show in Fig. 37, detailed constraints will depend on this choice of prior. Assuming $m_{\text{sterile}}^{\text{thermal}} < 10 \text{ eV}$ we find

$$\left. \begin{array}{l} N_{\text{eff}} < 3.29, \\ m_{\nu, \text{sterile}}^{\text{eff}} < 0.65 \text{ eV}, \end{array} \right\} \begin{array}{l} 95\%, \text{ Planck} \\ \text{TT,TE,EE+lowE+lensing+BAO,} \end{array} \quad (70a)$$

or adopting a stronger prior of $m_{\text{sterile}}^{\text{thermal}} < 2 \text{ eV}$, we obtain the stronger constraint

$$\left. \begin{array}{l} N_{\text{eff}} < 3.34, \\ m_{\nu, \text{sterile}}^{\text{eff}} < 0.23 \text{ eV}, \end{array} \right\} \begin{array}{l} 95\%, \text{ Planck} \\ \text{TT,TE,EE+lowE+lensing+BAO.} \end{array} \quad (70b)$$

The mass constraint in Eq. (70a) actually appears weaker than in PCP15; this is because the change in optical depth reduces the

high- N_{eff} parameter space, and the remaining lower- N_{eff} parameter space has significant volume associated with models having relatively large $m_{\nu, \text{sterile}}^{\text{eff}}$ (close to the $m_{\text{sterile}}^{\text{thermal}}$ prior cut). Removing this high-physical-mass parameter space by tightening the prior to 2 eV gives the mass constraint in Eq. (70b), which is substantially tighter than the result quoted in PCP15 without high- ℓ polarization.

One thermalized sterile neutrino with $\Delta N_{\text{eff}} = 1$ is excluded at about 6σ irrespective of its mass, or at about 7σ when assuming a mass $m_{\text{sterile}}^{\text{DW}} \approx 1$ eV. This is especially interesting in the context of the controversial evidence for light sterile neutrinos, invoked to explain the neutrino short baseline (SBL) anomaly. The latest MiniBooNE data on electron-neutrino appearance (Aguilar-Arevalo et al. 2018) support previous anomalous results by LSND (Aguilar-Arevalo et al. 2001), with a combined significance of 6.1σ in favour of electron-neutrino appearance. However, this contradicts recent muon-neutrino disappearance data from MINOS+ and IceCube (Dentler et al. 2018), when considered along with electron-antineutrino disappearance results (Dentler et al. 2017; Gariazzo et al. 2018), and also appears to be excluded by OPERA (Agafonova et al. 2018). The long-standing evidence for electron-neutrino disappearance in reactor experiments has also recently been challenged by new data from STEREO (Almazán et al. 2018) and PROSPECT (Ashenfelter et al. 2018). It is worth noting, however, that removing any *individual* experiment does not relieve the tension between the remaining experiments, and mild tension still persists if all electron (anti-)neutrino appearance (disappearance) data are removed (see Maltoni 2018, for a detailed summary). Several analyses have shown that in order to fit the anomalous data sets with one sterile neutrino, one needs an active-sterile neutrino mixing angle such that the fourth neutrino mass eigenstate would acquire a thermal distribution in the early Universe (see e.g., Hannestad et al. 2013; Bridle et al. 2017; Knee et al. 2018), thus contributing as $\Delta N_{\text{eff}} \approx 1^{39}$. Our *Planck* results confirm that the presence of a light thermalized sterile neutrino is in strong contradiction with cosmological data, and that the production of sterile neutrinos possibly explaining the SBL anomaly would need to be suppressed by some non-standard interactions (Archidiacono et al. 2016; Chu et al. 2015), low-temperature reheating (de Salas et al. 2015), or another special mechanism.

7.6. Big-bang nucleosynthesis

7.6.1. Primordial element abundances

Primordial helium. The latest estimates of the primordial helium abundance come from the data compilations of Aver et al. (2015), giving $Y_{\text{p}}^{\text{BBN}} \equiv 4n_{\text{He}}/n_{\text{b}} = 0.2449 \pm 0.0040$ (68% CL) and Peimbert et al. (2016), giving a slightly tighter constraint $Y_{\text{p}}^{\text{BBN}} = 0.2446 \pm 0.0029$ (68% CL). These two estimates are consistent with each other. Izotov et al. (2014) find a higher value, $Y_{\text{p}}^{\text{BBN}} = 0.2551 \pm 0.0022$ (68% CL) in moderate (2.2σ to 2.9σ) tension with the previous two. Aver et al. (2015) discuss the differences between their results and Izotov et al. (2014), which are caused by modelling differences involving neutral hydrogen collisional emission, corrections for dust absorption, and helium emissivities, amongst other effects. This raises the issue, which has long-plagued helium abundance measurements, of whether the systematic errors are accurately incorporated in the quoted

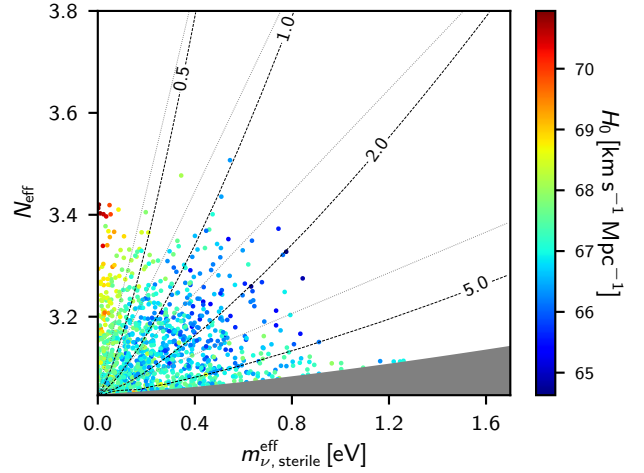


Fig. 37. Samples from *Planck* TT,TE,EE+lowE+lensing, colour coded by the value of the Hubble parameter H_0 , for a model with minimal-mass active neutrinos and one additional sterile neutrino with mass parameterized by $m_{\nu, \text{sterile}}^{\text{eff}}$. The physical mass for thermally-produced sterile neutrinos, $m_{\text{sterile}}^{\text{thermal}}$, is constant along the grey lines labelled by the mass in eV; the equivalent result for sterile neutrinos produced via the Dodelson-Widrow mechanism (Dodelson & Widrow 1994) is shown by the adjacent thinner lines. The dark grey shaded region shows the part of parameter space excluded by our default prior $m_{\text{sterile}}^{\text{thermal}} < 10$ eV, where the sterile neutrinos would start to behave like dark matter for CMB constraints.

uncertainties. In this paper, we will use the more conservative Aver et al. (2015) results as the baseline; however, we will occasionally quote bounds based on the combined Aver et al. (2015) and Peimbert et al. (2016) results ($Y_{\text{p}}^{\text{BBN}} = 0.2447 \pm 0.0023$ (68% CL)) and for the Izotov et al. (2014) results.

Compared to the measurement used in PCP15, the Aver et al. (2015) error bar has decreased by a factor of 2.4. To relate the primordial helium abundance to early Universe parameters under the assumption of standard BBN, we use two public BBN codes: first, version 1.10 of ParthEnoPE⁴⁰ (Pisanti et al. 2008); and second, the recently released PRIMAT code⁴¹ (Pitrou et al. 2018). The most relevant particle physics parameter for helium-abundance calculations is the neutron lifetime. ParthEnoPE 1.10 uses the average value $\tau_n = (880.2 \pm 1.0)$ s (68% CL) taken from the Particle Data Group summary (Patrignani 2016). This is a very small shift with respect to the value of $\tau_n = (880.3 \pm 1.1)$ s used in PCP15. The PRIMAT code uses instead an average over post-2000 measurements only, $\tau_n = (879.5 \pm 0.8)$ s (68% CL, Serebrov et al. 2018). The two codes find (consistently) that uncertainties of $\sigma(\tau_n) = 1.0$ s and 0.8 s correspond to theoretical errors for the helium fraction of $\sigma(Y_{\text{p}}^{\text{BBN}}) = 3.0 \times 10^{-4}$ and 2.4×10^{-4} , respectively. Given the *Planck* result for the baryon density in the base- Λ CDM model,

$$\omega_{\text{b}} = 0.02236 \pm 0.00029 \quad (95\%, \text{TT,TE,EE+lowE}), \quad (71)$$

ParthEnoPE predicts

$$Y_{\text{p}}^{\text{BBN}} = 0.24672_{-(0.00012)0.00061}^{+(0.00011)0.00061} \quad (95\%, \text{TT,TE,EE+lowE}), \quad (72a)$$

⁴⁰ <http://parthenope.na.infn.it>. Note that ParthEnoPE already exists in version 2.0, but the difference with respect to 1.10 is only at the level of numerical methods and performance. The physical input data and results are identical.

⁴¹ <http://www2.iap.fr/users/pitrou/primat.htm>

³⁹ Note that ΔN_{eff} could in principle be reduced if there was a small amount of lepton asymmetry in the early Universe; however, this would raise other types of problems (Saviano et al. 2013).

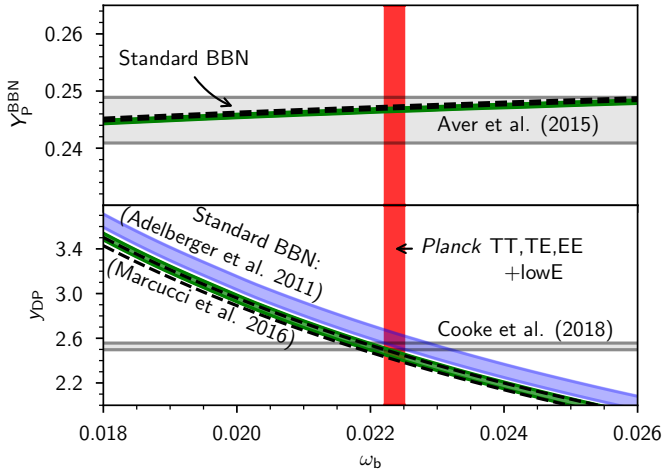


Fig. 38. Summary of BBN results with $N_{\text{eff}} = 3.046$, using *Planck* TT,TE,EE+lowE. All bands are 68% credible intervals. The standard BBN predictions computed with *PARthENoPE* are shown in green (case (b) in the text), while those from *PRIMAT* are in black dashed lines (case (c)). The blue lines show the *PARthENoPE* results based on the experimental determination of nuclear rates by [Adelberger et al. \(2011\)](#), instead of the theoretical rate of [Marcucci et al. \(2016, case \(a\)\)](#).

while *PRIMAT* gives

$$Y_{\text{P}}^{\text{BBN}} = 0.24714_{-(0.00013)0.00049}^{+(0.00012)0.00049} \quad (95\%, \text{TT,TE,EE+lowE}). \quad (72b)$$

The first set of error bars (in parentheses) reflects only the uncertainty on ω_{b} , while the second set includes the theoretical uncertainty $\sigma(Y_{\text{P}}^{\text{BBN}})$ added in quadrature. The two mean values are shifted by $\Delta Y_{\text{P}}^{\text{BBN}} \approx 4.2 \times 10^{-4}$ because of differences in the adopted neutron lifetime and because *PRIMAT* includes a more elaborate treatment of weak interaction rates. However, this shift is quite close to the theoretical errors estimated from both codes, and about an order of magnitude smaller than the observational error quoted by [Aver et al. \(2015\)](#). As shown in Fig. 38, the results from both codes lie well within the region favoured by the [Aver et al. \(2015\)](#) observations. They are also compatible at the 1σ level with the combined [Aver et al. \(2015\)](#) and [Peimbert et al. \(2016\)](#) results, but in 3.6 – 3.8σ tension with the [Izotov et al. \(2014\)](#) results. Evidently, there is an urgent need to resolve the differences between the helium abundance measurements and this tension should be borne in mind when we use the [Aver et al. \(2015\)](#) measurements below.

Primordial deuterium. There has been significant progress related to deuterium abundance determination since the completion of *PCP15*. On the observational side, [Cooke et al. \(2018\)](#) have published a new estimate based on their best seven measurements in metal-poor damped Ly α systems, $y_{\text{DP}} \equiv 10^5 n_{\text{D}}/n_{\text{H}} = 2.527 \pm 0.030$ (68% CL). On the calculational side, the value of the nuclear reaction rate $d(p, \gamma)^3\text{He}$, which has a major impact on BBN computations of the primordial deuterium calculation, has now been calculated ab initio. The most recent theoretical calculation is presented in [Marcucci et al. \(2016\)](#), leading to a smaller value of y_{DP} and differs significantly from previous predictions extrapolated from laboratory experiments by [Adelberger et al. \(2011\)](#). This issue should be settled by forthcoming precise measurements by the LUNA experiment ([Gustavino 2017](#)). In this paper we will compare the results obtained when the deuterium fraction is computed in three different ways:

- with *PARthENoPE*, assuming the experimental rate from [Adelberger et al. \(2011\)](#);
- with *PARthENoPE*, using the theoretical rate of [Marcucci et al. \(2016\)](#);
- with *PRIMAT*, using the rate from [Iliadis et al. \(2016\)](#), based on a hybrid method that consists of assuming the energy dependence of the rate computed ab initio by [Marcucci et al. \(2005\)](#) and normalizing it with a fit to a selection of laboratory measurements.

In addition to the $d(p, \gamma)^3\text{He}$ reaction rates, the current versions of *PARthENoPE*, *PRIMAT*, and other codes (such as that developed by [Nollett & Burles 2000](#); [Nollett & Holder 2011](#)) make different assumptions on other rates, in particular those of the deuterium fusion reactions $d(d, n)^3\text{He}$ and $d(d, p)^3\text{H}$, which also contribute significantly to the error budget of the primordial deuterium fraction. *PARthENoPE* estimates these rates by averaging over all existing measurements, while *PRIMAT* again uses a hybrid method based on a subset of the existing data. When using one of approaches (a), (b), or (c), we adopt different theoretical errors. For (a), [Adelberger et al. \(2011\)](#) estimate that the error in their extrapolated rate propagates to $\sigma(y_{\text{DP}}) = 0.06$. For (b), we rely on the claim by [Marcucci et al. \(2016\)](#) that the error is now dominated by uncertainties on deuterium fusion and propagates to $\sigma(y_{\text{DP}}) = 0.03$. For (c), the error computed by *PRIMAT* (close to the best-fit value of ω_{b}) is similar, $\sigma(y_{\text{DP}}) = 0.032$.

These systematic error estimates are consistent with the differences between different BBN codes. Taking $d(p, \gamma)^3\text{He}$ from [Marcucci et al. \(2016\)](#), the prediction of *PARthENoPE* 1.10 is higher than that of the code by [Nollett & Holder \(2011\)](#) by about $\Delta y_{\text{DP}} = 0.04$, which is comparable to the theoretical error adopted in this paper. [Nollett & Holder \(2011\)](#) attribute this shift to their different assumptions on the deuterium fusion rates. The shift between cases (b) and (c) is smaller, $\Delta y_{\text{DP}} = 0.015$, suggesting that differences in $d(p, \gamma)^3\text{He}$ and in the deuterium fusion rates nearly compensate each other in the final result.

Nuclear rate uncertainties are critically important in the discussion of the compatibility between deuterium measurements and CMB data. [Cooke et al. \(2018\)](#) reported that their measurement of primordial deuterium was in moderate 2.0σ tension with the *Planck* baryon density from *PCP15*. This is based on the predictions of the code of [Nollett & Holder \(2011\)](#) with the nuclear rate of [Marcucci et al. \(2016\)](#). Switching to *PARthENoPE* (b) and including the theoretical error $\sigma(y_{\text{DP}}) = 0.03$, we find consistency to 1.1σ . With our three BBN calculation pipelines, the deuterium abundance measurement of [Cooke et al. \(2018\)](#) translates into the following bounds on ω_{b} ,

$$\left. \begin{array}{l} \text{(a) } \omega_{\text{b}} = 0.02270 \pm 0.00075 \\ \text{(b) } \omega_{\text{b}} = 0.02198 \pm 0.00044 \\ \text{(c) } \omega_{\text{b}} = 0.02189 \pm 0.00046 \end{array} \right\} \begin{array}{l} 95\%, \\ \text{Cooke (2018)}, \end{array} \quad (73)$$

including theoretical errors. In several places in this work and in *PL2018*, we refer to a ‘‘conservative BBN prior,’’ $\omega_{\text{b}} = 0.0222 \pm 0.0005$ (68% CL), set to be compatible with each of these three predictions.

We now update this discussion using the latest *Planck* results. With our three assumptions (a), (b), and (c) on standard BBN, the determination of ω_{b} by *Planck* 2018 for the base- Λ CDM model (see Eq. (71)) implies

$$\left. \begin{array}{l} \text{(a) } y_{\text{DP}} = 2.587_{-(0.052)0.13}^{+(0.055)0.13} \\ \text{(b) } y_{\text{DP}} = 2.455_{-(0.053)0.080}^{+(0.054)0.081} \\ \text{(c) } y_{\text{DP}} = 2.439_{-(0.051)0.081}^{+(0.053)0.082} \end{array} \right\} 95\%, \text{TT,TE,EE+lowE}, \quad (74)$$

with the ω_b -only error between parentheses, followed by the total error including the theoretical uncertainty. These results are in agreement with the [Cooke et al. \(2018\)](#) measurement to within 0.8σ , 1.4σ , and 1.7σ , respectively. Thus no significant tensions are found in any of these cases.

Other light elements. We do not discuss other light elements, such as tritium and lithium, since the observed abundance measurements and their interpretation in terms of the standard models of BBN are more controversial (see [Fields 2011](#); [Fields et al. 2014](#), for reviews). The *Planck* results do not shed any further light on these problems compared to earlier CMB experiments.

Nuclear rates from bounds from Planck. The previous paragraphs highlighted the importance of assumptions on the radiative-capture process $d(p, \gamma)^3\text{He}$ for deuterium abundance predictions. It is worth checking whether the comparison of CMB and deuterium abundance data provides an indirect estimate of this rate. This approach was suggested in [Cooke et al. \(2014\)](#) and implemented in [Di Valentino et al. \(2014\)](#) and [PCP15](#). We can now update it using the latest *Planck* and deuterium data.

We parameterize the thermal rate $R_2(T)$ of the $d(p, \gamma)^3\text{He}$ process in the `PARthENoPE` code by rescaling the rate $R_2^{\text{ex}}(T)$ fitted to experimental data by [Adelberger et al. \(2011\)](#) with a factor A_2 :

$$R_2(T) = A_2 R_2^{\text{ex}}(T). \quad (75)$$

This factor does not account in an exact way for the differences between the experimental fit and the theoretical predictions; it should instead be seen as a consistency parameter, very much like A_L for CMB lensing in Sect. 6.2. The rate $R_2^{\text{th}}(T)$ predicted by [Marcucci et al. \(2005\)](#) has a temperature dependence that is close to what is measured experimentally, and can be very well approximated by a rescaling factor $A_2 = 1.055$. The new theoretical rate obtained by [Marcucci et al. \(2016\)](#) has a slightly different temperature dependence but is well approximated by an effective rescaling factor $A_2^{\text{th}} = 1.16$ ([Mangano & Pisanti, priv. comm.](#)).

Assuming the base- Λ CDM model, we then constrain A_2 using *Planck* data combined with the latest deuterium abundance measurements from [Cooke et al. \(2018\)](#). We still need to take into account theoretical errors on deuterium predictions arising from uncertainties on other rates, and from the difference between various codes. According to [Marcucci et al. \(2016\)](#) and [Pitrou et al. \(2018\)](#), the deuterium fusion uncertainties propagate to an error $\sigma(y_{\text{DP}}) = 0.03$, which encompasses the difference on deuterium predictions between `PARthENoPE` versus `PRIMAT`. Thus we adopt $\sigma(y_{\text{DP}}) = 0.03$ as the theoretical error on deuterium predictions in this analysis. Adding the theoretical error in quadrature to the observational error of [Cooke et al. \(2018\)](#), we obtain a total error of $\sigma(y_{\text{DP}}) = 0.042$ on deuterium, which we use in our joint fits of *Planck*+deuterium (D) data. We find

$$A_2 = 1.138 \pm 0.072 \quad (68\%, \text{Planck TT+lowE+D}), \quad (76a)$$

$$A_2 = 1.080 \pm 0.061 \quad (68\%, \text{Planck TT,TE,EE+lowE+D}). \quad (76b)$$

If we compare these results with those from [PCP15](#), the tension between the *Planck* TT+lowE+D prediction and the experimental rate slightly increases to 1.9σ . However the inclusion of polarization brings the *Planck* TT,TE,EE+lowE+D prediction half-way between the experimental value and the theoretical rate of [Marcucci et al. \(2016\)](#), in agreement with both at the 1.3σ level. The situation is thus inconclusive and highlights the need

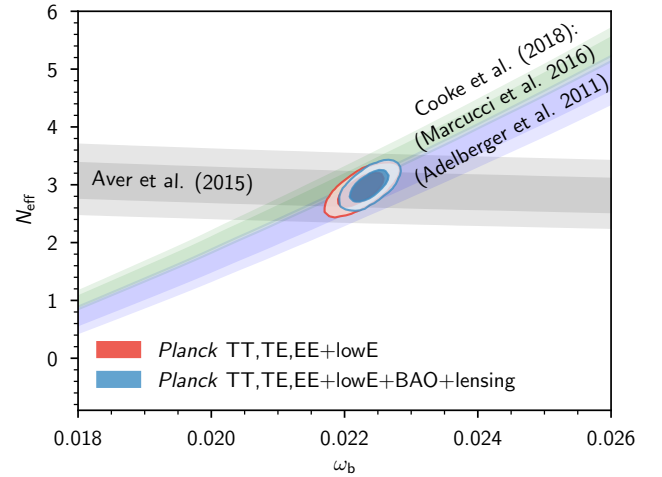


Fig. 39. Constraints in the ω_b - N_{eff} plane from *Planck* TT,TE,EE+lowE and *Planck* TT,TE,EE+lowE+BAO+lensing data (68% and 95% contours) compared to the predictions of BBN combined with primordial abundance measurements of helium ([Aver et al. 2015](#), in grey) and deuterium ([Cooke et al. 2018](#), in green and blue, depending on which reaction rates are assumed). In the CMB analysis, N_{eff} is allowed to vary as an additional parameter to the base- Λ CDM model, while Y_p is inferred from ω_b and N_{eff} according to BBN predictions. For clarity we only show the deuterium predictions based on the `PARthENoPE` code with two assumptions on the nuclear rate $d(p, \gamma)^3\text{He}$ (case (a) in blue, case (b) in green). These constraints assume no significant lepton asymmetry.

for a precise experimental determination of the $d(p, \gamma)^3\text{He}$ rate with LUNA ([Gustavino 2017](#)).

Varying the density of relic radiation. We can also relax the assumption that $N_{\text{eff}} = 3.046$ to check the agreement between CMB and primordial element abundances in the ω_b - N_{eff} plane. Figure 39 shows that this agreement is very good, with a clear overlap of the 95% preferred regions of *Planck* and of the helium+deuterium measurements. This is true with any of our assumptions on the nuclear rates. For clarity in the plot, we only include the predictions of `PARthENoPE` (cases (a) and (b)), but those of `PRIMAT` are very close to case (b). Since all these data sets are compatible with each other, we can combine them to obtain marginalized bounds on N_{eff} , valid in the 7-parameter $\Lambda\text{CDM}+N_{\text{eff}}$ model, with an error bar reduced by up to 30% compared to the *Planck*+BAO bounds of Eq. (67b):

$$\begin{aligned} & \left. \begin{aligned} (a) \quad N_{\text{eff}} = 2.89^{+0.29}_{-0.29} \\ (b) \quad N_{\text{eff}} = 3.05^{+0.27}_{-0.27} \\ (c) \quad N_{\text{eff}} = 3.06^{+0.26}_{-0.28} \end{aligned} \right\} \begin{aligned} & 95\%, \text{Planck} \\ & \text{TT,TE,EE+lowE+Aver (2015)} \\ & \text{Cooke (2018);} \end{aligned} \quad (77) \end{aligned}$$

$$\begin{aligned} & \left. \begin{aligned} (a) \quad N_{\text{eff}} = 2.94^{+0.27}_{-0.27} \\ (b) \quad N_{\text{eff}} = 3.10^{+0.26}_{-0.25} \\ (c) \quad N_{\text{eff}} = 3.12^{+0.25}_{-0.26} \end{aligned} \right\} \begin{aligned} & 95\%, \text{Planck} \\ & \text{TT,TE,EE+lowE+BAO+Aver} \\ & \text{(2015)} \\ & \text{Cooke (2018);} \end{aligned} \quad (78) \end{aligned}$$

The bounds become even stronger if we combine the helium measurements of [Aver et al. \(2015\)](#) and [Peimbert et al. \(2016\)](#):

$$\begin{aligned} & \left. \begin{aligned} (a) \quad N_{\text{eff}} = 2.93^{+0.23}_{-0.23} \\ (b) \quad N_{\text{eff}} = 3.04^{+0.22}_{-0.22} \\ (c) \quad N_{\text{eff}} = 3.06^{+0.22}_{-0.22} \end{aligned} \right\} \begin{aligned} & 95\%, \text{Planck} \\ & \text{TT,TE,EE+lowE+BAO+Aver} \\ & \text{(2015) + Peimbert (2016)} \\ & \text{+ Cooke (2018).} \end{aligned} \quad (79) \end{aligned}$$

However, as noted in the previous section, there is some inconsistency between the helium abundance measurements reported

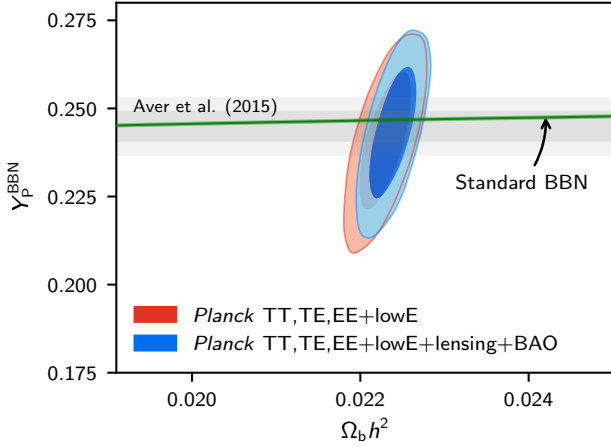


Fig. 40. Constraints on the helium abundance Y_p^{BBN} from *Planck*, assuming the standard value of $N_{\text{eff}} = 3.046$. Results are consistent with the predictions of standard BBN (green line), and also the observed helium abundance (68% and 95% grey bands from *Aver et al. (2015)*).

by different authors. If we use the helium abundance measurement of *Izotov et al. (2014)* in place of *Aver et al. (2015)* and *Peimbert et al. (2016)*, the mean value of N_{eff} shifts by about 0.35 (e.g., for case (b), $N_{\text{eff}} = 3.37 \pm 0.22$ at the 95% level), in 2.9σ tension with the standard model value of 3.046.

Note finally that one can obtain N_{eff} bounds independently of the details of the CMB spectra at high multipoles by combining the helium, deuterium, and BAO data sets with a nearly model-independent prior on the scale of the sound horizon at decoupling inferred from *Planck* data, $100\theta_{\text{MC}} = 1.0409 \pm 0.0006$ (68%). This gives a very conservative bound, $N_{\text{eff}} = 2.95^{+0.56}_{-0.52}$ (95%), when BBN is modelled as in case (b), along with a 68% bound on the Hubble rate, $H_0 = (67.2 \pm 1.7) \text{ km s}^{-1} \text{ Mpc}^{-1}$.

7.6.2. CMB constraints on the helium fraction

We now allow the helium fraction to vary independently of BBN, and compare *Planck* constraints with expectations. In the parameter chains we vary the mass fraction Y_p and compute the nucleon fraction Y_p^{BBN} as a derived parameter, obtaining

$$Y_p^{\text{BBN}} = 0.241 \pm 0.025 \text{ (95\%, Planck TT,TE,EE+lowE)}, \quad (80a)$$

with similar results combined with lensing and BAO,

$$Y_p^{\text{BBN}} = 0.243^{+0.023}_{-0.024} \quad \left. \begin{array}{l} \text{95\%, Planck} \\ \text{TT,TE,EE+lowE+lensing+BAO.} \end{array} \right\} \quad (80b)$$

The *Planck* constraints on Y_p and $\Omega_b h^2$ are shown in Fig. 40, and are in good agreement with standard BBN predictions and the helium abundance measurement of *Aver et al. (2015)*.

Since both helium abundance and relativistic degrees of freedom affect the CMB damping tail, they are partially degenerate. Allowing N_{eff} to also vary in addition to Y_p , we obtain the somewhat weaker constraints:

$$\left. \begin{array}{l} Y_p^{\text{BBN}} = 0.247^{+0.034}_{-0.036}, \\ N_{\text{eff}} = 2.89^{+0.63}_{-0.57}, \end{array} \right\} \text{95\%, Planck TT,TE,EE+lowE,} \quad (81)$$

$$\left. \begin{array}{l} Y_p^{\text{BBN}} = 0.246 \pm 0.035, \\ N_{\text{eff}} = 2.97^{+0.58}_{-0.54}, \end{array} \right\} \left. \begin{array}{l} \text{95\%, Planck} \\ \text{TT,TE,EE+lowE+lensing+BAO.} \end{array} \right\} \quad (82)$$

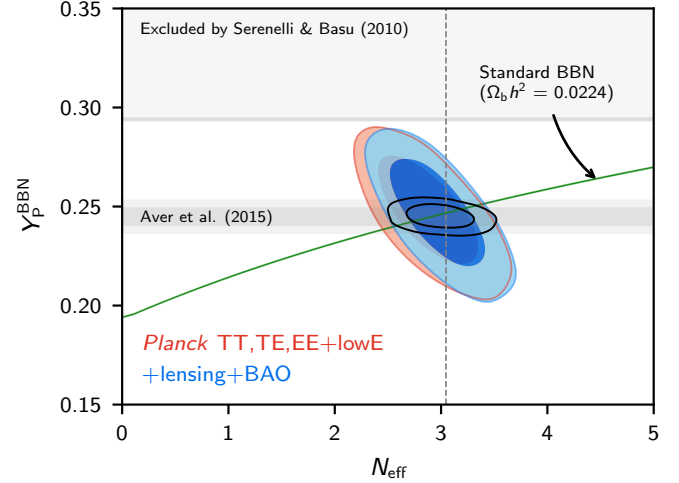


Fig. 41. Constraints on the helium abundance Y_p^{BBN} and number of neutrino species N_{eff} from *Planck* TT,TE,EE+lowE and in combination with lensing and BAO. Results are consistent with the predictions of standard BBN (green line), and also the observed helium abundance (68% and 95% grey bands from *Aver et al. (2015)*). The grey band at the top shows a conservative 95% upper bound inferred from the Solar helium abundance (*Serenelli & Basu (2010)*). The black contours show the joint BBN-independent constraint from combining *Planck* TT,TE,EE+lowE+lensing+BAO and *Aver et al. (2015)*.

These constraints are shown in Fig. 41, and are again entirely consistent with standard assumptions. The direct helium abundance measurement of *Aver et al. (2015)* provides significantly tighter constraints than those from *Planck* CMB measurements. By combining *Planck* with *Aver et al. (2015)* we obtain a slightly tighter BBN-independent constraint on N_{eff} , while substantially improving the Y_p^{BBN} result:

$$\left. \begin{array}{l} Y_p^{\text{BBN}} = 0.2437^{+0.0077}_{-0.0080}, \\ N_{\text{eff}} = 2.99^{+0.43}_{-0.40}, \end{array} \right\} \left. \begin{array}{l} \text{95\%, Planck} \\ \text{TT,TE,EE+lowE+lensing+} \\ \text{BAO+Aver (2015).} \end{array} \right\} \quad (83)$$

In our main grid results we assume that Y_p can be determined accurately using standard BBN predictions from *PARthENoPE* based on a neutron lifetime $\tau_n = (880.2 \pm 1.0) \text{ s}$. This uncertainty on τ_n is sufficiently small that it has negligible impact on constraints for non-BBN parameters.

If the τ_n constraint is relaxed, for example to allow a systematic shift towards the beam measurement $\tau_n = [887 \pm 1.2(\text{stat.}) \pm 1.9(\text{sys.})] \text{ s}$ of *Yue et al. (2013)*, there would be a slight shift in cosmological parameters; however, taking the central value of $\tau_n \approx 887 \text{ s}$ would shift ΛCDM parameters by at most 0.2σ (for θ_{MC}). As shown in Table 5 the base- ΛCDM parameters are very stable to marginalization over Y_p with no constraint, at the expense of only modest increase in uncertainties. There is therefore only very limited scope for shifting the main *Planck* parameters by changing the BBN model, especially given the BBN-independent requirement of consistency with the observed helium abundances of *Aver et al. (2015)*.

Finally, we can assume that standard BBN is an accurate theory, but take τ_n as a free parameter to obtain an indirect constraint on the neutron lifetime from CMB or CMB+helium data. This is potentially interesting in the context of the long-standing difference between neutrino lifetime measurements performed by beam and bottle experiments. The PDG result, $\tau_n = (880.2 \pm 1.0) \text{ s}$, is based on an average over two beam and five bottle experiments (*Patrignani 2016*). The beam-only average

gives $\tau_n = (888.0 \pm 2.0)$ s, while the bottle-only average yields $\tau_n = (879.2 \pm 0.6)$ s; these determinations are in 4.0σ tension. To derive an independent prediction, following the lines of [Salvati et al. \(2016\)](#), we combine our Λ CDM+ Y_p chains with the function $Y_p^{\text{BBN}}(\omega_b, \tau_n)$ predicted by `PARthENOPE` or `PRIMAT` to obtain a posterior probability distribution in (ω_b, τ_n) space⁴². After marginalizing over ω_b , for CMB-only data, we find

$$\tau_n = (851 \pm 60) \text{ s} \quad (68\%, \text{Planck TT,TE,EE+lowE}), \quad (84a)$$

using `PRIMAT` (or, with `PARthENOPE`, $\tau_n = (855 \pm 62)$ s). Adding helium measurements from [Aver et al. \(2015\)](#), we find

$$\tau_n = (867 \pm 18) \text{ s} \quad (68\%, \text{Planck TT,TE,EE+lowE+Aver (2015)}), \quad (84b)$$

using `PRIMAT` (or, with `PARthENOPE`, $\tau_n = (870 \pm 18)$ s). These results do not provide a statistically significant preference for either the beam or bottle values. If we make a similar prediction by combining *Planck* with the helium measurement of [Izotov et al. \(2014\)](#), we obtain a range, $\tau_n = (920 \pm 11)$ s (68%CL), in 3.6σ tension with all direct measurements of the neutron lifetime; this is a potentially interesting result, emphasizing again the need to resolve tensions between different analyses of the primordial helium abundance.

7.7. Recombination history

The cosmological recombination era marks an important phase in the history of the Universe, determining precisely how CMB photons decoupled from baryons around redshift $z \approx 10^3$ ([Sunyaev & Zeldovich 1970](#); [Peebles & Yu 1970](#)). With precision data from *Planck*, we can test physical assumptions of the recombination process ([Hu et al. 1995](#); [Seljak et al. 2003](#)), studying both standard and non-standard physics.

The *Planck* data are sensitive to several subtle atomic physics and radiative-transfer effects (see e.g., [Chluba & Sunyaev 2006](#); [Kholupenko et al. 2007](#); [Switzer & Hirata 2008](#)) that were omitted in earlier calculations of the recombination history ([Zeldovich et al. 1968](#); [Peebles 1968](#); [Seager et al. 2000](#)). These effects can lead to significant biases to several cosmological parameters (e.g., [Rubiño-Martín et al. 2010](#); [Shaw & Chluba 2011](#)); however, as the *Planck* 2015 analysis confirmed, at the present level of precision these can be reliably incorporated within the advanced recombination codes `CosmoRec` ([Chluba & Thomas 2011](#)) and `HyRec` ([Ali-Haimoud & Hirata 2010](#)), as well as the `recfast` code ([Seager et al. 1999](#); [Wong et al. 2008](#)), modified using corrections calculated with the more precise codes.

In this section, we update the `PCP15` search for deviations from the standard recombination history. In particular, improved polarization data provide additional constraining power that warrants revisiting this question. As in 2015, we find no significant indication for departures of the recombination history from the standard prediction.

We use a semi-blind eigen-analysis (often referred to as a principal-component analysis) of deviations of the free-electron fraction, $x_e(z) = n_e/n_H$, where n_H denotes the number density of hydrogen nuclei, away from the standard recombination history ([Farhang et al. 2012, 2013](#)). Specifically, a perturbation, $\delta x_e(z)/x_e^{\text{fid}}(z)$, is expanded in $N_z = 80$ bands of δz , spanning redshifts from well before helium recombination to well past hydro-

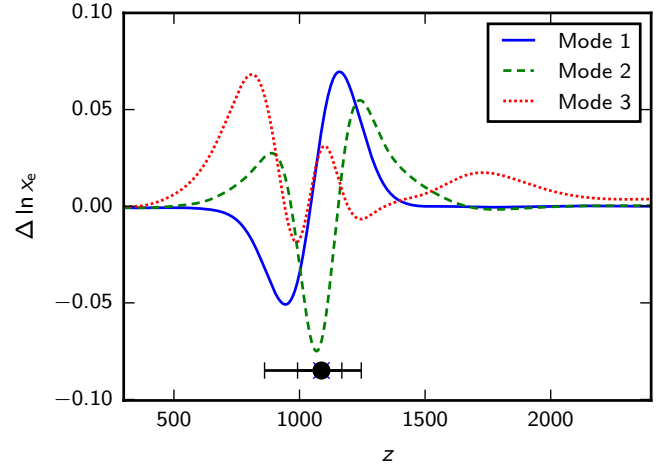


Fig. 42. First three normalized x_e modes constructed using the *Planck* TT,TE,EE+lowE likelihood. The modes are marginalized over standard and nuisance parameters. The forecast measurement uncertainties for the mode amplitudes are $\sigma_{\mu_1} = 0.16$, $\sigma_{\mu_2} = 0.23$, and $\sigma_{\mu_3} = 0.73$. The position and width of the Thomson visibility function are indicated by the error bars at the bottom of the figure.

gen recombination (taken to be $200 \leq z \leq 3500$). Here, $x_e^{\text{fid}}(z)$ describes the ionization history, assuming the standard recombination physics and using the best-fitting cosmological parameters from *Planck* TT,TE,EE+lowE.

We then form the Fisher information matrix for the $N_z + N_{\text{std}} + N_{\text{nuis}}$ parameters, corresponding to the x_e -perturbation, standard cosmological, and nuisance parameters, respectively. The Fisher matrix is then inverted to obtain the parameter-parameter correlation matrix. Our focus is on the $N_z \times N_z$ block of this Fisher inverse, containing the marginalized errors and correlations of the x_e parameters. The x_e block is diagonalized, and the corresponding diagonal variances are rank-ordered from the lowest to highest fluctuation variance (i.e., from the best to worst constrained mode). The rotation diagonalizing the Fisher inverse defines the x_e eigenmodes. Truncation of the eigenmode hierarchy to determine the number of x_e modes used for parameter estimation is performed according to some suitably chosen selection criterion. We refer to these modes as “eXeMs”, the first three of which are shown in Fig. 42. Only a small number are probed by *Planck* 2018 data, even with the addition of the higher quality polarization information. If instead we diagonalized the N_z block of the Fisher matrix before inverting, the modes would be characterized by the fixed best-fitting cosmological and nuisance parameter values, i.e., they would not be marginalized. Those x_e modes differ from the eXeMs, but would give similar results (as discussed in [Farhang et al. 2012](#)).

For our analysis, we use the eXeMs, applying them to the *Planck* TT,TE,EE+lowE+lensing+BAO data combination. By construction, these modes are orthogonal to each other⁴³; however, correlations arise once the standard and nuisance parameters are varied. This slightly modifies the errors and can also cause small parameter biases ([Farhang et al. 2012](#)). Although the lowest order x_e modes given in `PCP15` look similar to those for the 2018 data, the precision of the *Planck* data requires the eigen-analysis to be updated around the new fiducial point in parameter space; indeed, we find subtle differences, e.g., a small

⁴² For simplicity, here we fix the extra relativistic degrees of freedom to the standard value $N_{\text{eff}} = 3.046$; see [Salvati et al. \(2016\)](#) for discussion.

⁴³ In practice, our mode generation method gives slight mode correlations at the level of 3–9% due to the numerical procedure and smoothing of the mode-functions (see [Farhang et al. 2012](#), for details).

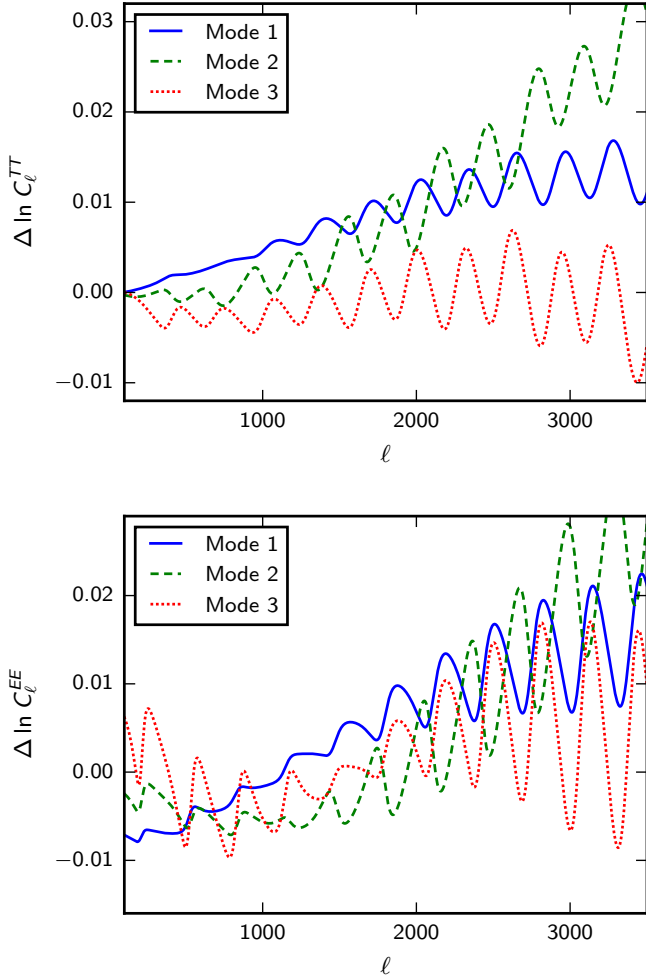


Fig. 43. Power spectrum responses to the first three x_e modes, constructed using *Planck* TT,TE,EE+lowE, shown in Fig. 42. For each curve, the corresponding x_e mode was added to the standard recombination history with an amplitude corresponding to their predicted 1σ uncertainties (i.e., $\sigma_{\mu_1} = 0.16$, $\sigma_{\mu_2} = 0.23$, and $\sigma_{\mu_3} = 0.73$ for the first three eXeMs).

shift in the position of the first mode, to which the data are sensitive.

As discussed in PCP15, the first mode corresponds mainly to a change in the width and height of the Thomson visibility function, while the second mode leads to a change in the position of the visibility peak. The third mode introduces a superposition of the change in the width, height, and position of the visibility peak. Each mode causes a response in $\delta C_\ell / C_\ell^{\text{fid}}$, as illustrated in Fig. 43.

In the eigen-analysis, each eXeM is multiplied by an amplitude, μ_i , which is determined by MCMC sampling along with all of the other standard cosmological and nuisance parameters. These amplitudes and their errors are summarized in Table 9 for the data combination *Planck* TT,TE,EE+lowE+lensing+BAO. There is stability in the amplitudes as the mode number is increased, and all are consistent with no deviation from standard recombination within the errors. We also find that cosmological parameters do not shift with the inclusion of these modes, agreeing well (though with slightly larger errors) with the Λ CDM values computed assuming the standard recombination history. The four-mode case (not reported here) gives similar results, but with slightly larger errors.

Table 9. Standard cosmological parameters, along with the first three x_e -mode amplitudes, as determined using *Planck* TT,TE,EE+lowE+lensing+BAO (all errors are 68% CL).

Parameter	+ 1 mode	+ 2 modes	+ 3 modes
$100\Omega_b h^2$...	2.241 ± 0.016	2.241 ± 0.018	2.239 ± 0.018
$\Omega_c h^2$...	0.1191 ± 0.0009	0.1192 ± 0.0010	0.1192 ± 0.0010
H_0 ...	67.72 ± 0.43	67.72 ± 0.44	67.84 ± 0.45
τ ...	0.054 ± 0.007	0.055 ± 0.007	0.055 ± 0.007
n_s ...	0.9667 ± 0.0051	0.9668 ± 0.0050	0.9657 ± 0.0051
$\ln(10^{10} A_s)$..	3.042 ± 0.015	3.042 ± 0.014	3.040 ± 0.015
μ_1 ...	0.02 ± 0.12	0.01 ± 0.12	$!0.03 \pm 0.13$
μ_2	0.01 ± 0.17	$!0.05 \pm 0.17$
μ_3	-0.84 ± 0.69

In PCP15, an equivalent exercise also showed no evidence for deviations from the standard recombination history. Using the 2015 *Planck* high-multipole temperature power spectra, only two modes were well-constrained; however, adding the preliminary high-multipole polarization data in PCP15 allowed a third mode to be constrained. The 2018 *Planck* temperature and improved polarization data used in this paper provide a more robust analysis. Relative to 2015, we find comparable errors on the first and second mode amplitudes and a small decrease in the uncertainty of the third mode amplitude.

7.8. Reionization

At scales smaller than the horizon size at reionization ($\ell \gtrsim 10$), free electrons generated during reionization can scatter and partially damp the CMB anisotropies. This leads to a mostly scale-independent suppression of power above $\ell \approx 10$ by a factor of $e^{-2\tau}$, where τ is the total integrated optical depth to reionization, related to the free electron fraction $x_e(z) \equiv n_e^{\text{reion}}(z)/n_H(z)$ by

$$\tau = n_H(0)c\sigma_T \int_0^{z_{\text{max}}} dz x_e(z) \frac{(1+z)^2}{H(z)}. \quad (85)$$

Here $n_e^{\text{reion}}(z)$ is the number density of free electrons from reionization, $n_H(z)$ is the total number of hydrogen nuclei, and σ_T is the Thomson scattering cross-section. We set $z_{\text{max}} = 50$, which is early enough to capture the entirety of the expected contribution from reionization. We assume that the first reionization of helium happens at the same time as the reionization of hydrogen, so complete first reionization corresponds to $x_e > 1$. There is an additional increase in x_e at $z \lesssim 3.5$ when the helium is fully ionized; this only has a small contribution to τ and in all cases we model it with a simple smooth transition at $z = 3.5$.

At large scales in polarization ($\ell \lesssim 30$), anisotropies are instead created by the rescattering of the local temperature quadrupole, which varies maximally across Hubble-sized patches. This leads to a ‘‘bump’’ today in the large-scale polarization power spectrum at the Hubble scale during reionization. The amplitude of the bump scales like τ^2 , but the exact shape encodes information on the detailed evolution of the ionization fraction and can therefore constrain $x_e(z)$ (Zaldarriaga et al. 1997; Kaplinghat et al. 2003). Conversely, the inferred value of τ depends on the model assumed for $x_e(z)$, thus the reionization history has implications for other cosmological parameters, which are important to quantify. Throughout the 2018 papers, we use the simple TANH model for reionization (described below and in Sect. 3.3). In this section, we augment this with two other models to check whether our choice has any impact on the τ constraints, and to assess the extent to which *Planck* data can place

model-independent bounds on reionization. The three models we use are the following.

- TANH, which assumes a smooth transition from a neutral to ionized Universe, with a parametric form for $x_e(z)$ based on a hyperbolic tangent (see Footnote 15). This model is not physically motivated, but makes the optical depth approximately independent of the transition width (Lewis 2008). It has been used previously in PCP13 and PCP15, and is the default model in these 2018 papers.

- PCA (principle-component analysis), which decomposes the reionization history into eigenmodes that form a complete basis for any observable history (Hu & Holder 2003). In general, one must also specify a set of bounds to prevent the reconstruction from giving unphysical (e.g., negative) ionization fractions, and for this we use the optimal bounds given in Millea & Bouchet (2018). The PCA model has some deficiencies: firstly, model parameters (the eigenmode amplitudes) do not have a straightforward physical interpretation; secondly, even with the optimal physicality bounds, physicality cannot be enforced exactly (Mortonson & Hu 2008; Millea & Bouchet 2018). Nevertheless, the PCA approach serves as a useful alternative for comparison, and although we do not do so here, it can be used to construct an approximate likelihood that can be convenient way of exploring other models (Heinrich & Hu 2018; Miranda et al. 2017).

- FlexKnot, which reconstructs any arbitrary reionization history using an interpolating function between a varying number of knots, with marginalization over the number of knots (Millea & Bouchet 2018). Here, the model parameters are directly tied to the physical quantity of the ionization fraction, and as such physicality can be enforced by design. This model is the exact analogue of the model used in reconstructing the primordial power spectrum from *Planck* data (Vázquez et al. 2012; Planck Collaboration XX 2016).

For each of these models, we must also specify the prior on the model parameters, which in turn corresponds to some particular prior on τ . Previous analyses of *Planck* data such as Heinrich et al. (2017), Obied et al. (2018), Hazra & Smoot (2017), or Villanueva-Domingo et al. (2018), have not considered the impact of these (sometimes implicit) priors, which differed among the different analyses and consequently caused some partial disagreement between results. To allow direct comparison of τ values, unless otherwise stated we will use a prior that is uniform on τ . Heinrich & Hu (2018) construct a prior that is uniform on τ , but which increases the allowed unphysical parameter space and is chosen a posteriori. Here we instead use the flat prior constructed by the procedure described in Millea & Bouchet (2018) and Handley & Millea (2019), which does not admit extra unphysical models and gives the most generic prior that leaves the prior on τ uniform.

Evidence based on observations of the Gunn-Peterson trough in the spectra of high-redshift quasars show that the inter-galactic medium is highly ionized by $z \approx 6$ (see e.g., Bouwens et al. 2015). We enforce this bound in the case of the TANH model by requiring that the central redshift of reionization be greater than $z = 6.5$; since the assumed duration in the TANH model is $\Delta z = 0.5$, this ensures that reionization is nearly complete by $z \approx 6$. The corresponding lower limit for the optical depth is $\tau \gtrsim 0.0430$, modulo some small dependence on other cosmological parameters. In the case of the FlexKnot model, the Gunn-Peterson bounds are enforced by constraining the knot redshifts to be at $z > 6$. Here, because the duration of reionization is not specified and can effectively be instantaneous, the optical depth can be as low as $\tau = 0.0385$. The PCA model also implicitly

includes the Gunn-Peterson bounds, since the eigenmodes only have support within the range $z \in [6, 30]$, although the imperfect physicality bounds do allow values of τ slightly below 0.0385.

We begin by giving results using only the lowE large-scale polarization likelihood. As discussed in Sect. 2.2.3, this likelihood uses only *EE* information, and is restricted to $\ell \leq 29$; we assume that the reionization information in the polarization spectrum at $\ell \geq 30$ is negligible, which is a good approximation for most models that can fit the low- ℓ data. The lowE data provide constraints on reionization that are largely model independent, i.e., insensitive to other cosmological parameters. For definiteness, we fix these other cosmological parameters to their best-fit values from *Planck* TT,TE,EE, in particular holding $A_s e^{-2\tau}$ rather than A_s fixed, which better reflects the impact that the $\ell \gtrsim 10$ data would have (we will comment at the end of this section on how the high- ℓ data affect τ). We plot posterior constraints from lowE in the top panel of Fig. 44. One can see the moderate extent to which the hard cutoff of the Gunn-Peterson bound informs the posterior in the TANH and FlexKnot cases (it of course also impacts the PCA case, although the imperfect physicality priors in this case lead to the more gradual cutoff visible in the figure). We find in the three cases the 68% constraints:

$$\tau = 0.0519^{+0.0030}_{-0.0079} \quad (\text{lowE; flat } \tau \text{ prior; TANH}); \quad (86a)$$

$$\tau = 0.0504^{+0.0050}_{-0.0079} \quad (\text{lowE; flat } \tau \text{ prior; FlexKnot}); \quad (86b)$$

$$\tau = 0.0487^{+0.0038}_{-0.0081} \quad (\text{lowE; flat } \tau \text{ prior; PCA}). \quad (86c)$$

The three results are in good agreement, showing that the *Planck* data prefer a late and fast transition from a neutral to an ionized universe, which all models can capture equally well. The TANH result gives slightly higher optical depth than the others, which is primarily driven by the fixed duration of reionization assumed. The PCA result is slightly lower, and is partly affected by the imperfect physicality priors that allow unphysical negative ionization fractions. The FlexKnot result represents our best model-independent estimate of the optical depth. Nevertheless, the differences between this and the TANH result, or between the FlexKnot result using either a flat prior on τ or on the knot positions and amplitudes (the dashed line in Fig. 44), are small. For example, these differences correspond to shifts in σ_8 of $< 0.1\sigma$ when used in conjunction with *Planck* TT,TE,EE+lowE data. Thus, although future cosmological inferences will depend somewhat on the details of reionization (Allison et al. 2015; Millea & Bouchet 2018), current *Planck* data are quite robust to how reionization is modelled.

The FlexKnot approach provides a model-independent reconstruction of the entire reionization history, with physicality enforced exactly. This reconstruction is presented in Fig. 45. A comparison against the TANH model is also shown; although this imposes a fixed shape on the evolution, it nevertheless matches the FlexKnot constraint fairly well. We find no preference for any significant high-redshift contribution to the optical depth. This conclusion does not depend qualitatively on our choice of prior either; we have checked both a prior that is uniform on the knot positions and amplitudes, and one that is uniform on the contribution to τ between redshifts 15 and 30, $\tau(15, 30)$. We find:

$$\tau(15, 30) < 0.006 \quad (\text{lowE, flat } \tau(15, 30), \text{ FlexKnot}); \quad (87a)$$

$$\tau(15, 30) < 0.007 \quad (\text{lowE, flat knot, FlexKnot}). \quad (87b)$$

This can be compared with the results of Heinrich et al. (2017) and Obied et al. (2018), who found a roughly 2σ preference for non-zero $\tau(15, 30)$ using *Planck* 2015 data (which included

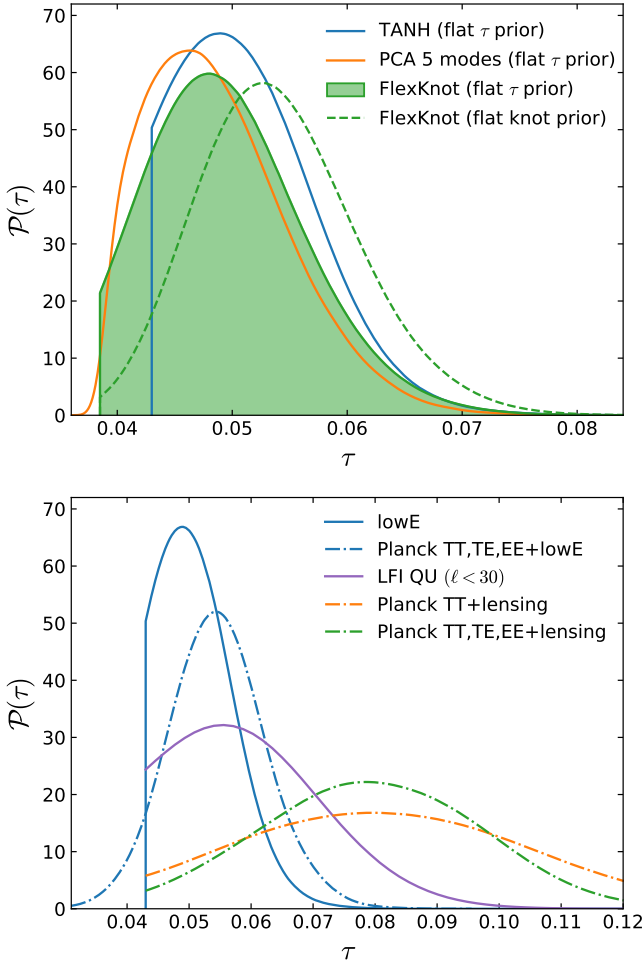


Fig. 44. *Top:* marginalized constraints on the optical depth to reionization from lowE alone, assuming different models of reionization and different priors over the model parameters. Only reionization parameters are varied here, with $A_s e^{-2\tau}$ and other cosmological and instrumental parameters held fixed at their best-fit values from *Planck* TT,TE,EE. The solid lines use a flat prior on τ , while the dashed line uses a flat prior on the knot amplitudes; the difference between the green lines is an example of the level to which these constraints depend on the choice of prior. *Bottom:* constraints from different data sets on the optical depth assuming the TANH model and a flat τ prior (the cases that include high- ℓ data are indicated by dot-dashed lines and also marginalize over Λ CDM parameters, as opposed to fixing them). The *Planck* TT,TE,EE+lowE line is shown without the lower bound due to measurements of the Gunn-Peterson trough, as a reminder that this bound is applied only in this section, resulting in some small extra shifts in the central values of quoted constraints between this section and the remainder of the paper.

a large-scale polarization likelihood from the LFI instrument). Millea & Bouchet (2018) showed that the majority of this preference disappeared when using the lower-noise *Planck* HFI SimLow likelihood (Planck Collaboration Int. XLVI 2016), with an additional sub-dominant effect due to the choice of prior. Here we have used the yet more precise SimAll likelihood, which yields an upper bound in Eq. (87a) that improves on the result given in Millea & Bouchet (2018) by roughly a factor of 3. This is due entirely to changes in the SimAll likelihood compared to SimLow, largely originating from better control of systematics in the HFI polarization data.

The upper bound on the contribution from $z > 15$ to the total optical depth limits some candidate explanations of the

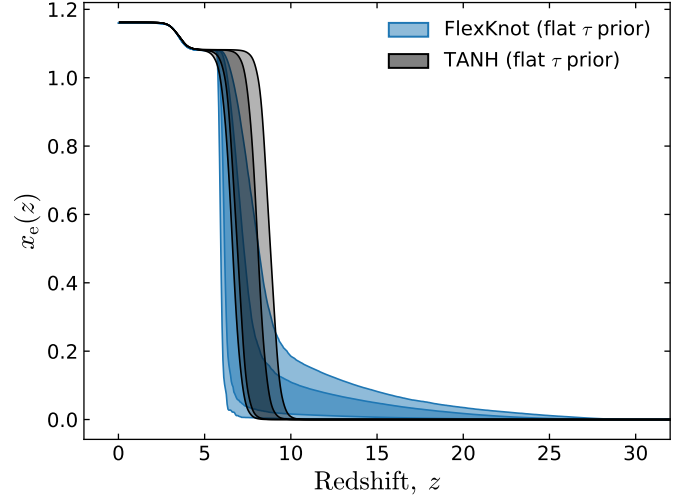


Fig. 45. Constraints on the free electron fraction, $x_e(z)$, from lowE alone, with $A_s e^{-2\tau}$ and other cosmological and instrumental parameters held fixed to their best-fit values from *Planck* TT,TE,EE, and with a flat prior on τ . The shaded bands are middle 68th and 95th percentiles (note that this does not correspond exactly to confidence intervals). The FlexKnot constraints show that any non-zero component of reionization above a redshift of about 15 is highly disfavoured.

anomalously large 21 cm signal from the EDGES experiment (Bowman et al. 2018). Some otherwise plausible explanations also lead, as a side-effect, to a significant number of ionizing photons being generated at high redshift, enough to contribute significantly to $\tau(15, 30)$. These models are now highly disfavoured by the *Planck* bound in their simplest forms (see e.g., Ewall-Wice et al. 2018).

CMB data also probe high-redshift reionization via the patchy kinetic Sunyaev-Zeldovich (kSZ) effect (Gruzinov & Hu 1998; Knox et al. 1998). *Planck* data, together with smaller-scale ACT and SPT data (which are even more sensitive to this effect), give upper bounds on the amplitude of the patchy kSZ power spectrum and thus on the duration of reionization (Zahn et al. 2012; Sievers et al. 2013; Planck Collaboration Int. XLVII 2016). We do not attempt to derive new constraints here, since it is not completely straightforward to turn a limit on the amplitude of the patchy kSZ signal into one on the duration of reionization, especially given the generic non-physical models for the ionization fraction that we use here. However, in the future kSZ should be a powerful probe of the details of reionization, in particular with low-noise small-scale temperature measurements over large fractions of the sky (Smith & Ferraro 2017; Ferraro & Smith 2018).

The lower panel of Fig. 44 compares the optical depth posteriors from different likelihoods. Results from the large-scale LFI polarization (Planck Collaboration V 2020) are in broad agreement with lowE, although with larger errors. The *Planck* lensing reconstruction data described in Sect. 2.3 can also provide a completely separate (although more model-dependent) determination of the value of τ ; lensing is directly sensitive to A_s , and hence can partially break the $A_s e^{-2\tau}$ degeneracy. By using the high- ℓ data in conjunction with the reconstructed lensing-potential power spectrum, both of which are sensitive to lensing, we can infer comparable constraints on τ . These are shown in the bottom panel of Fig. 44. Although the peak of the τ posterior lies at higher values in this case, the difference between the τ estimates from e.g., lowE and *Planck* TT,TE,EE+lensing is only 1.4σ (where we compute the difference in posterior mean with

respect to the Gaussian error bars combined in quadrature). The preference for higher τ is driven by the same features in the CMB power spectrum data that prefer more lensing in Λ CDM (giving $A_L > 1$; see Sect. 6.2): the lensing amplitude can be increased by increasing A_s , which at constant $A_s e^{-2\tau}$ also increases τ . Marginalizing over non- Λ CDM parameters, for example Ω_K (which can also increase lensing by having $\Omega_K < 0$), can reduce the pull to higher τ , but does not change $A_s e^{-2\tau}$ or the shape of the reionization bump significantly enough to affect the large-scale polarization result. This type of model-independence has motivated our focus on only large-scale polarization data in this section, although of course constraints on τ including higher- ℓ data (as are presented throughout the rest of this paper) are equally valid, bearing in mind which model is assumed. Also, results in other sections do not apply the lower bound from the Gunn-Peterson constraint, which reduces the posterior mean values, somewhat disguising the larger peak values of the optical depth.

Overall, the results in this section leave us with a picture of reionization that happened late and fast, and are consistent with reionization being driven by photons from massive stars in low mass galaxies (see e.g. Robertson et al. 2015; Parsa et al. 2018). Our results are also consistent with observations suggesting that the Universe is substantially neutral at redshift $z \gtrsim 7.5$ (Banados et al. 2018; Davies et al. 2018; Mason et al. 2018). The low value of the optical depth makes the *Planck* constraints very robust to the details of reionization modelling, with the simple TANH model adopted in this paper causing no significant biases in other parameters.

7.9. Dark-matter annihilation

CMB anisotropies are sensitive to energy injection in the intergalactic medium that could be a consequence, for example, of dark-matter (DM) annihilation (see discussion in Sect. 6.6. of PCP15 and references therein). The current CMB sensitivity to the annihilation cross section of weakly-interacting massive particles (WIMPs) is competitive with and complementary to that of indirect DM search experiments. The effective parameter constrained by CMB anisotropies is

$$p_{\text{ann}} \equiv f_{\text{eff}} \frac{\langle \sigma v \rangle}{m_\chi}, \quad (88)$$

where m_χ is the DM particle mass, $\langle \sigma v \rangle$ its thermally averaged annihilation cross-section (assumed here to be independent of temperature and redshift, as predicted for WIMPs annihilating in s-wave channels), and f_{eff} is the fraction of the energy released by the annihilation process that is transferred to the intergalactic medium (IGM) around the redshifts to which the CMB anisotropy data are most sensitive, namely $z \approx 600$ (Finkbeiner et al. 2012).

For each value of p_{ann} , we compute CMB anisotropies using the ExoClass branch (Stöcker et al. 2018) of class v2.6.3, with recombination solved by HyRec v2017 (Ali-Haïmoud & Hirata 2011). We assume that the energy injected by DM annihilation is immediately transferred to the IGM (the ‘‘on-the-spot’’ approximation), and splits between gas heating and hydrogen excitation/ionization, according to the calculations summarized in Table V of Galli et al. (2013). Helium ionization and beyond on-the-spot effects can be safely neglected here. Since CMB anisotropies are very weakly sensitive to the redshift dependence of the transferred energy fraction $f(z)$, we assume a constant fraction $f(z) = f_{\text{eff}}$.

We quote constraints on $p_{\text{ann}}^{28} \equiv p_{\text{ann}}/[10^{28} \text{ cm}^3 \text{ s}^{-1} \text{ GeV}^{-1}] = 17.8 p_{\text{ann}}/[10^6 \text{ m}^3 \text{ s}^{-1} \text{ kg}^{-1}]$:

$$p_{\text{ann}}^{28} < 3.5 \quad (95\%, \text{Planck TT,TE,EE+lowE}); \quad (89a)$$

$$p_{\text{ann}}^{28} < 3.3 \quad (95\%, \text{Planck TT,TE,EE+lowE+lensing}); \quad (89b)$$

$$p_{\text{ann}}^{28} < 3.2 \quad (95\%, \text{Planck TT,TE,EE+lowE+lensing+BAO}). \quad (89c)$$

The bound based on CMB temperature and polarization data improves by 17% compared to PCP15. The difference is driven by the new high- ℓ TT,TE,EE likelihood. This is consistent with the fact that in addition to changing the physics of recombination, and thus the scale and height of the acoustic peaks, DM annihilation enhances the freeze-out value of the ionization fraction of the Universe after recombination, and introduces a distinctive signature in the polarization spectrum for $\ell \leq 200$. The new bounds are not only stronger but also more robust, since polarization systematics in the *Planck* polarization spectra are now better understood. Adding *Planck* lensing and BAO further tightens the constraints.

In the baseline version of the Plik likelihood, the calibration parameters of the polarization data, which correct for polarization efficiencies, are fixed to the values computed assuming the base- Λ CDM model, as described in Sect. 2.2.1. This is not necessarily consistent when the ionization history is substantially modified by energy injection from DM or other mechanisms. We thus performed further analyses in which the polarization calibration parameters are varied, with a flat prior within the range 0.8–1.2. We found that our bounds remain unaffected by floating these additional nuisance parameters, which are not correlated with p_{ann} .

Figure 46 translates the bounds on p_{ann} into joint limits on the mass m_χ and annihilation cross-section $\langle \sigma v \rangle$ of DM, assuming twelve plausible WIMP s-wave annihilation channels. The value of f_{eff} for each mass and channel was computed⁴⁴ using the public DarkAges module of Stöcker et al. (2018), which relies on the energy transfer functions presented by Slatyer (2016a). We consistently account for corrections related to low-energy photons in the manner described in section V.B. of Slatyer (2016a). Finally, the DarkAges module defines f_{eff} by convolving $f(z)$ in redshift space with the weighting function recommended by Slatyer (2016b). Note that for the W^+W^- and Z^0Z^0 channels, the bounds assume on-shell 2-body processes and are cut sharply at the mass of the daughter particle, while in reality they would extend further to the left in Fig. 46.

As usual the strongest bounds are obtained assuming annihilation into electron-positron pairs. The case of annihilation purely into neutrinos is not shown here, since the constraints are orders of magnitude weaker in that case. Assuming a thermal cross-section (shown in Fig. 46), the 95% CL lower bounds on the DM mass range from $m_\chi \geq 9 \text{ GeV}$ for annihilation into tau/anti-tau, up to $m_\chi \geq 30 \text{ GeV}$ for annihilation in electron/positron. To compare with hints of DM annihilation in indirect DM search data, we first show the regions preferred by the AMS/PAMELA positron fraction and *Fermi*/H.E.S.S. electron-positron flux, assuming s-wave annihilation into muons and standard halo profiles. These regions, taken from Cirelli et al. (2009), have long been known to be in strong tension with CMB data.

We also indicate the regions suggested by the possible DM interpretation of several anomalies in indirect DM search data.

⁴⁴ Courtesy of P. Stöcker.

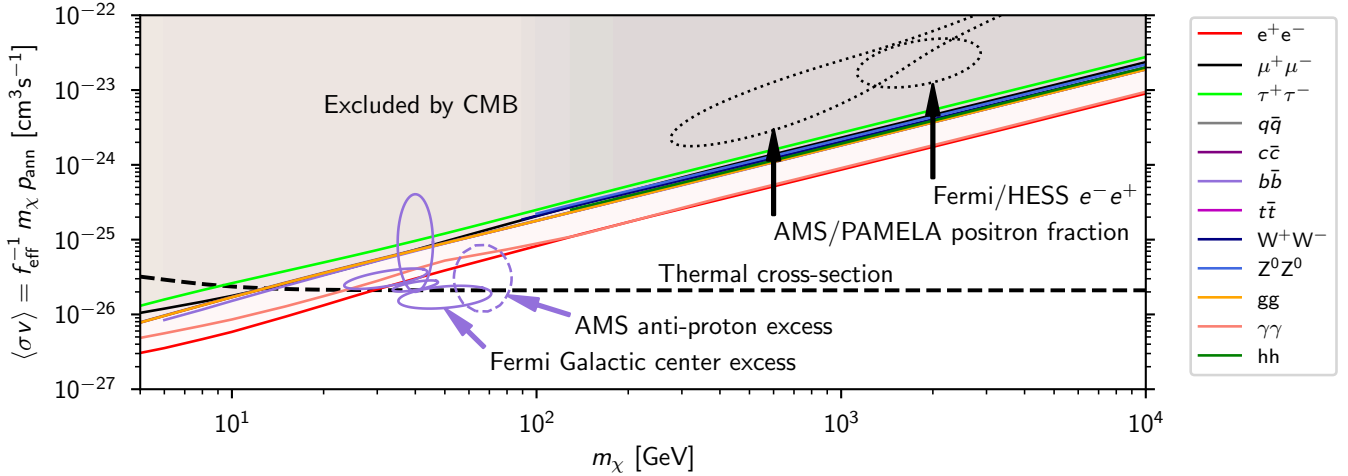


Fig. 46. *Planck* 2018 constraints on DM mass and annihilation cross-section. Solid straight lines show joint CMB constraints on several annihilation channels (plotted using different colours), based on $p_{\text{ann}} < 3.2 \times 10^{-28} \text{ cm}^3 \text{ s}^{-1} \text{ GeV}^{-1}$. We also show the 2σ preferred region suggested by the AMS proton excess (dashed ellipse) and the *Fermi* Galactic centre excess according to four possible models with references given in the text (solid ellipses), all of them computed under the assumption of annihilation into $b\bar{b}$ (for other channels the ellipses would move almost tangentially to the CMB bounds). We additionally show the 2σ preferred region suggested by the AMS/PAMELA positron fraction and *Fermi*/H.E.S.S. electron and positron fluxes for the leptophilic $\mu^+\mu^-$ channel (dotted contours). Assuming a standard WIMP-decoupling scenario, the correct value of the relic DM abundance is obtained for a “thermal cross-section” given as a function of the mass by the black dashed line.

The 95% CL preferred region for the AMS anti-proton excess is extracted from Cuoco et al. (2017a,b). The DM interpretation of the *Fermi* Galactic centre excess is very model-dependent and, as in Fig. 9 of Charles et al. (2016), we choose to show four results from the analyses of Gordon & Macias (2013), Abazajian et al. (2014), Calore et al. (2015), and Daylan et al. (2016). For the *Fermi* Galactic centre excess and the AMS anti-proton excess, we only show results assuming annihilation into $b\bar{b}$, in order to keep the figure readable. About 50% of the region found by Abazajian et al. (2014) is excluded by CMB bounds, while other regions are still compatible. The 95% CL preferred region for the AMS anti-proton excess is still compatible with CMB bounds for the $b\bar{b}$ channel shown in the figure, and we checked that this is also the case for other channels.

8. Conclusions

This is the final *Planck* collaboration paper on cosmological parameters and presents our best estimates of parameters defining the base- Λ CDM cosmology and a wide range of extended models. As in PCP13 and PCP15 we find that the base- Λ CDM model provides a remarkably good fit to the *Planck* power spectra and lensing measurements, with no compelling evidence to favour any of the extended models considered in this paper.

Compared to PCP15 the main changes in this analysis come from improvements in the *Planck* polarization analysis, both at low and high multipoles. The new *Planck* polarization maps provide a tight constraint on the reionization optical depth, τ , from large-scale polarization (and are consistent with the preliminary HFI polarization results presented in *Planck Collaboration Int. XLVI* 2016). This revision to the constraint on τ accounts for most of the (small) changes in parameters determined from the temperature power spectra in this paper compared to PCP15. We have characterized a number of systematic effects, neglected in PCP15, which affect the polarization spectra at high multipoles. Applying corrections for these systematics (principally arising from errors in polarization efficien-

cies and temperature-to-polarization leakage) we have produced high multipole TT,TE,EE likelihoods that provide substantially tighter constraints than using temperature alone. We have compared two TT,TE,EE likelihoods that use different assumptions to correct for polarization systematics and find consistency at the $\lesssim 0.5\sigma$ level. Although the TT,TE,EE likelihoods are not perfect, the *Planck* parameter results presented in this paper can be considered accurate to within their error bars.

Our main conclusions include the following.

- The 6-parameter base- Λ CDM model provides a good fit to the *Planck* TT, TE, and EE power spectra and to the *Planck* CMB lensing measurements, either individually or in combination with each other.
- The CMB angular acoustic scale is measured robustly at 0.03% precision to be $\theta_* = (0^\circ 5965 \pm 0^\circ 0002)$, and is one of the most accurately measured parameters in cosmology, of comparable precision to the measurement of the background CMB temperature (Fixsen 2009).
- The *Planck* best fit base- Λ CDM cosmology is in very good agreement with BAO, supernovae, redshift-space distortion measurements and BBN predictions for element abundance observations. There is some tension (at about 2.5σ) with high-redshift BAO measurements from quasar Ly α observations, but no standard extension of the base- Λ CDM cosmology improves the fit to these data.
- The new low- ℓ polarization likelihood tightens the reionization optical depth significantly compared to the 2015 analysis, giving $\tau = 0.054 \pm 0.007$, suggesting a mid-point reionization redshift of $z_{\text{re}} = 7.7 \pm 0.7$. This is consistent with astrophysical observations of quasar absorption lines and models in which reionization happened relatively fast and late. We investigated more general models of reionization and demonstrated that our cosmological parameter results are insensitive to residual uncertainties in the reionization history.
- The primordial fluctuations are consistent with Gaussian purely adiabatic scalar perturbations characterized by a power spectrum with a spectral index $n_s = 0.965 \pm 0.004$, consistent with the predictions of slow-roll, single-field, inflation. Combined with BAO, we find that the Universe is spatially flat to high

accuracy ($\Omega_K = 0.0007 \pm 0.0019$), consistent the predictions of simple inflationary models. Combining with BICEP-Keck 2015 data on B -mode polarization we find a 95% upper limit on the tensor-to-scalar ratio $r_{0.002} < 0.06$. Together with our measurement of n_s , these results favour concave over convex inflation potentials, suggesting a hierarchy between the slow-roll parameters measuring the slope and curvature of the potential.

– The *Planck* base- Λ CDM cosmology predicts a late-time clustering amplitude $\sigma_8 = 0.811 \pm 0.006$, and matter density parameter $\Omega_m = 0.315 \pm 0.007$. The parameter $S_8 \equiv \sigma_8 \Omega_m^{0.5} = 0.831 \pm 0.013$ is compatible with DES galaxy lensing, and joint *Planck*-DES lensing results, although in modest tension with DES results that also include galaxy clustering, which prefer a roughly 2.5σ lower value of S_8 . There is no obvious inconsistency between the *Planck* base- Λ CDM cosmology and counts of clusters (selected either through the thermal Sunyaev-Zeldovich effect or via X-ray luminosity) because of large uncertainties in the calibrations of cluster masses.

– The *Planck* base- Λ CDM cosmology requires a Hubble constant $H_0 = (67.4 \pm 0.5) \text{ km s}^{-1} \text{ Mpc}^{-1}$, in substantial 4.4σ tension with the latest local determination by Riess et al. (2019). The *Planck* measurement is in excellent agreement with independent inverse-distance-ladder measurements using BAO, supernovae, and element abundance results. None of the extended models that we have studied in this paper convincingly resolves the tension with the Riess et al. (2019) value of H_0 .

– Allowing for extra relativistic degrees of freedom, we measure the effective number of degrees of freedom in non-photon radiation density to be $N_{\text{eff}} = 2.89 \pm 0.19$ ($N_{\text{eff}} = 2.99 \pm 0.17$ including BAO data), consistent with the value 3.046 expected in the standard model. Light thermal relics that decoupled after the QCD phase transition are ruled out at the 2σ level. Allowing for larger N_{eff} can slightly reduce tension with the local H_0 measurement and be consistent with BAO; however, the marginalized constraint on H_0 remains in tension with Riess et al. (2019) at over 3σ and higher values of N_{eff} are not favoured by element abundance observations.

– Combining *Planck* data with Pantheon supernovae and BAO data, the equation of state of dark energy is tightly constrained to $w_0 = -1.03 \pm 0.03$, consistent with a cosmological constant. We have also investigated a variety of modified-gravity models, finding no significant evidence for deviations from Λ CDM.

– Allowing for a free degenerate active neutrino mass, and combining with BAO measurements, we obtain the tight 95% constraint on the sum of the masses $\sum m_\nu < 0.12 \text{ eV}$.

– We find good agreement between the predictions of BBN for the *Planck* base- Λ CDM parameters and element abundance observations. Uncertainties in nuclear rates currently dominate the error budget for the interpretation of deuterium abundances.

– We have investigated a number of models for massive sterile neutrinos and dark-matter annihilation, finding no evidence for deviations from base Λ CDM.

The overall picture from *Planck*, since our first results were presented in PCP13, is one of remarkable consistency with the 6-parameter Λ CDM cosmology. This consistency is strengthened with the addition of the polarization spectra presented in this paper. Nevertheless, there are a number of curious “tensions,” both internal to the *Planck* data (the tendency for *Planck* to favour $A_L > 1$, discussed in Sect. 6.2, is an example) and with some external data sets. Some of these tensions may reflect small systematic errors in the *Planck* data (though we have not found any evidence for errors that could significantly change our results) and/or systematic errors in external data.

However, none of these, with the exception of the discrepancy with direct measurements of H_0 , is significant at more than the $2\text{--}3\sigma$ level. Such relatively modest discrepancies generate interest, in part, because of the high precision of the *Planck* data set. We could, therefore, disregard these tensions and conclude that the 6-parameter Λ CDM model provides an astonishingly accurate description of the Universe from times prior to 380 000 years after the Big Bang, defining the last-scattering surface observed via the CMB, to the present day at an age of 13.8 billion years.

Nevertheless, it is important to bear in mind that the main ingredients of Λ CDM, namely inflation, dark energy, and dark matter are not understood at any fundamental level. There is, therefore, a natural tendency to speculate that “tensions” may be hints of new physics, especially given that the landscape of possible new physics is immense. In the post-*Planck* era, the CMB provides enormous potential for further discovery via high-sensitivity ground-based polarization experiments and possibly a fourth-generation CMB satellite. The next decade will see an ambitious programme of large BAO and weak lensing surveys, and new techniques such as deep 21-cm surveys and gravitational wave experiments. Uncovering evidence for new physics is therefore a realistic possibility. What we have learned, and the legacy from *Planck*, is that any signatures of new physics in the CMB must be small.

Acknowledgements. The Planck Collaboration acknowledges the support of: ESA; CNES, and CNRS/INSU-IN2P3-INP (France); ASI, CNR, and INAF (Italy); NASA and DoE (USA); STFC and UKSA (UK); CSIC, MINECO, JA, and RES (Spain); Tekes, AoF, and CSC (Finland); DLR and MPG (Germany); CSA (Canada); DTU Space (Denmark); SER/SSO (Switzerland); RCN (Norway); SFI (Ireland); FCT/MCTES (Portugal); ERC and PRACE (EU). A description of the Planck Collaboration and a list of its members, indicating which technical or scientific activities they have been involved in, can be found at <https://www.cosmos.esa.int/web/planck/planck-collaboration>. We additionally acknowledge support from the European Research Council under the European Union’s Seventh Framework Programme (FP/2007-2013)/ERC Grant Agreement No. [616170]. This project has received funding from the European Research Council (ERC) under the European Union’s Horizon 2020 research and innovation programme (grant agreement No 725456, CMBSPEC). We thank Ofelia Pisanti for providing updated numerical BBN results from the PARthENOPE code, Cyril Pitrou for producing some results from the PRIMAT code, and the DES team for sharing their likelihoods. We also thank Marco Crisostomi, Ignacy Sawicky, Alessandra Silvestri, and Filippo Vernizzi for discussions on the dark-energy and modified-gravity models. Some of the results in this paper have been derived using the HEALPIX package.

References

- Abazajian, K. N., Canac, N., Horiuchi, S., & Kaplinghat, M. 2014, *Phys. Rev. D*, **90**, 023526
- Abbott, B., et al. (LIGO Scientific Collaboration and Virgo Collaboration) 2017a, *Phys. Rev. Lett.*, **119**, 161101
- Abbott, B. P., Abbott, R., Abbott, T. D., et al. 2017b, *Nature*, **551**, 85
- Abe, K., Bronner, C., Haga, Y., et al. 2018, *Phys. Rev. D*, **97**, 072001
- Adamson, P., Aliaga, L., Ambrose, D., et al. 2017, *Phys. Rev. Lett.*, **118**, 231801
- Addison, G. E., Huang, Y., Watts, D. J., et al. 2016, *ApJ*, **818**, 132
- Addison, G. E., Watts, D. J., Bennett, C. L., et al. 2018, *ApJ*, **853**, 119
- Ade, P. A. R., Ahmed, Z., Aikin, R. W., et al. 2018, *Phys. Rev. Lett.*, **121**, 221301
- Adelberger, E. G., Balantekin, A. B., Bemmerer, D., et al. 2011, *Rev. Mod. Phys.*, **83**, 195
- Agafonova, N., Aleksandrov, A., Anokhina, A., et al. 2018, *JHEP*, **06**, 151
- Agrawal, P., Cyr-Racine, F. Y., Pinner, D., & Randall, L. 2019, ArXiv e-prints [arXiv:1904.01016]
- Aguiar-Arevalo, A., Auerbach, L. B., Burman, R. L., et al. 2001, *Phys. Rev. D*, **64**, 112007
- Aguiar-Arevalo, A. A., Brown, B. C., Bugel, L., et al. 2018, *Phys. Rev. Lett.*, **121**, 221801
- Akrami, Y., Kallosh, R., Linde, A., & Vardanyan, V. 2018, *JCAP*, **6**, 041
- Alam, S., Ata, M., Bailey, S., et al. 2017, *MNRAS*, **470**, 2617
- Alcock, C., & Paczynski, B. 1979, *Nature*, **281**, 358
- Ali-Haïmoud, Y., & Hirata, C. M. 2010, *Phys. Rev. D*, **82**, 063521
- Ali-Haïmoud, Y., & Hirata, C. M. 2011, *Phys. Rev. D*, **83**, 043513

- Allison, R., Caucal, P., Calabrese, E., Dunkley, J., & Louis, T. 2015, *Phys. Rev. D*, **92**, 123535
- Almazán, H., del Amo Sanchez, P., Bernard, L., et al. 2018, *Phys. Rev. Lett.*, **121**, 161801
- Amendola, L. 2000, *Phys. Rev. D*, **62**, 043511
- Amendola, L., Kunz, M., & Sapone, D. 2008, *JCAP*, **0804**, 013
- Anderson, L., Aubourg, E., Bailey, S., et al. 2014, *MNRAS*, **441**, 24
- Archidiacono, M., Gariazzo, S., Giunti, C., et al. 2016, *JCAP*, **1608**, 067
- Archidiacono, M., Hooper, D. C., Murgia, R., et al. 2019, *JCAP*, **1910**, 055
- Arnaud, M., Pratt, G. W., Piffaretti, R., et al. 2010, *A&A*, **517**, A92
- Ashenfelter, J., Balantekin, A. B., Baldenegro, C., et al. 2018, *Phys. Rev. Lett.*, **121**, 251802
- Ata, M., Baumgarten, F., Bautista, J., et al. 2018, *MNRAS*, **473**, 4773
- Aubourg, É., Bailey, S., Bautista, J. E., et al. 2015, *Phys. Rev. D*, **92**, 123516
- Audren, B., Lesgourgues, J., Benabed, K., & Prunet, S. 2013, *JCAP*, **1302**, 001
- Aver, E., Olive, K. A., & Skillman, E. D. 2015, *JCAP*, **1507**, 011
- Aylor, K., Hou, Z., Knox, L., et al. 2017, *ApJ*, **850**, 101
- Baker, T., Bellini, E., Ferreira, P. G., et al. 2017, *Phys. Rev. Lett.*, **119**, 251301
- Banados, E., Venemans, B. P., Mazzucchelli, C., et al. 2018, *Nature*, **553**, 473
- Bartelmann, M., & Schneider, P. 2001, *Phys. Rept.*, **340**, 291
- Baumann, D., Green, D., & Wallisch, B. 2018, *JCAP*, **1808**, 029
- Bautista, J. E., Busca, N. G., Guy, J., et al. 2017, *A&A*, **603**, A12
- Bautista, J. E., Vargas-Magaña, M., Dawson, K. S., et al. 2018, *ApJ*, **863**, 110
- Belgacem, E., Dirian, Y., Foffa, S., & Maggiore, M. 2018, *JCAP*, **1803**, 002
- Bellini, E., & Sawicki, I. 2014, *JCAP*, **7**, 050
- Ben Achour, J., Crisostomi, M., Koyama, K., et al. 2016, *JHEP*, **12**, 100
- Bennett, C. L., Halpern, M., Hinshaw, G., et al. 2003, *ApJS*, **148**, 1
- Bennett, C., Larson, D., Weiland, J. L., et al. 2013, *ApJS*, **208**, 20
- Bernal, J. L., Verde, L., & Riess, A. G. 2016, *JCAP*, **1610**, 019
- Betoule, M., Marriner, J., Regnault, N., et al. 2013, *A&A*, **552**, A124
- Betoule, M., Kessler, R., Guy, J., et al. 2014, *A&A*, **568**, A22
- Beutler, F., Blake, C., Colless, M., et al. 2011, *MNRAS*, **416**, 3017
- Beutler, F., Blake, C., Colless, M., et al. 2012, *MNRAS*, **423**, 3430
- Beutler, F., Seo, H.-J., Ross, A. J., et al. 2017a, *MNRAS*, **464**, 3409
- Beutler, F., Seo, H.-J., Saito, S., et al. 2017b, *MNRAS*, **466**, 2242
- BICEP2, Keck Array and Planck Collaborations 2015, *Phys. Rev. Lett.*, **114**, 101301
- Biffi, V., Borgani, S., Murante, G., et al. 2016, *ApJ*, **827**, 112
- Blake, C., Brough, S., Colless, M., et al. 2012, *MNRAS*, **425**, 405
- Blake, C., Baldry, I. K., Bland-Hawthorn, J., et al. 2013, *MNRAS*, **436**, 3089
- Blanchard, A., & Schneider, J. 1987, *A&A*, **184**, 1
- Blas, D., Lesgourgues, J., & Tram, T. 2011, *JCAP*, **1107**, 034
- Blomqvist, M., du Mas des Bourboux, H., Busca, N. G., et al. 2019, *A&A*, **629**, A86
- Böhringer, H., Chon, G., & Collis, C. A. 2014, *A&A*, **570**, A31
- Böhringer, H., Chon, G., Retzlaff, J., et al. 2017, *AJ*, **153**, 220
- Borsanyi, S., Fodor, Z., Kampert, K. H., et al. 2016, *Nature*, **539**, 69
- Bouwens, R. J., Illingworth, G. D., Oesch, P. A., et al. 2015, *ApJ*, **811**, 140
- Bowman, J. D., Rogers, A. E. E., Monsalve, R. A., Mozdzen, T. J., & Mahesh, N. 2018, *Nature*, **555**, 67
- Bridle, S., Elvin-Poole, J., Evans, J., et al. 2017, *Phys. Lett. B*, **764**, 322
- Brinckmann, T., & Lesgourgues, J. 2019, *Phys. Dark Univ.*, **24**, 100260
- Buen-Abad, M. A., Schmaltz, M., Lesgourgues, J., & Brinckmann, T. 2018, *JCAP*, **1801**, 008
- Calabrese, E., Slosar, A., Melchiorri, A., Smoot, G. F., & Zahn, O. 2008, *Phys. Rev. D*, **77**, 123531
- Calore, F., Cholis, I., McCabe, C., & Weniger, C. 2015, *Phys. Rev. D*, **91**, 063003
- Capozzi, F., Lisi, E., Marrone, A., & Palazzo, A. 2018, *Prog. Part. Nucl. Phys.*, **102**, 48
- Cardona, W., Kunz, M., & Pettorino, V. 2017, *JCAP*, **3**, 056
- Carron, J., Lewis, A., & Challinor, A. 2017, *JCAP*, **1705**, 035
- Carter, P., Beutler, F., Percival, W. J., et al. 2018, *MNRAS*, **481**, 2371
- Casas, S., Kunz, M., Martinelli, M., & Pettorino, V. 2017, *Phys. Dark Univ.*, **18**, 73
- Charles, E., Sanchez-Conde, M., Anderson, B., et al. 2016, *Phys. Rept.*, **636**, 1
- Chen, H.-Y., Fishbach, M., & Holz, D. E. 2018, *Nature*, **562**, 545
- Cheung, C., Fitzpatrick, A. L., Kaplan, J., Senatore, L., & Creminelli, P. 2008, *J. High Energy Phys.*, **3**, 014
- Chluba, J., & Sunyaev, R. A. 2006, *A&A*, **446**, 39
- Chluba, J., & Thomas, R. M. 2011, *MNRAS*, **412**, 748
- Chu, X., Dasgupta, B., & Kopp, J. 2015, *JCAP*, **1510**, 011
- Cirelli, M., Kadastik, M., Raidal, M., & Strumia, A. 2009, *Nucl. Phys. B*, **813**, 1; Erratum: *Nucl. Phys. B*, **873**, 530 (2013)
- Cole, S., Percival, W. J., Peacock, J. A., et al. 2005, *MNRAS*, **362**, 505
- Cooke, R., Pettini, M., Jorgenson, R. A., Murphy, M. T., & Steidel, C. C. 2014, *ApJ*, **781**, 31
- Cooke, R. J., Pettini, M., & Steidel, C. C. 2018, *ApJ*, **855**, 102
- Couchot, F., Henrot-Versillé, S., Perdureau, O., et al. 2017, *A&A*, **597**, A126
- Creminelli, P., & Vernizzi, F. 2017, *Phys. Rev. Lett.*, **119**, 251302
- Creminelli, P., D'Amico, G., Norena, J., & Vernizzi, F. 2009, *JCAP*, **0902**, 018
- Crisostomi, M., & Koyama, K. 2018, *Phys. Rev. D*, **97**, 084004
- Crites, A. T., Henning, J. W., Ade, P. A. R., et al. 2015, *ApJ*, **805**, 36
- Cuesta, A. J., Verde, L., Riess, A., & Jimenez, R. 2015, *MNRAS*, **448**, 3463
- Cuoco, A., Krämer, M., & Korsmeier, M. 2017a, *Phys. Rev. Lett.*, **118**, 191102
- Cuoco, A., Heisig, J., Korsmeier, M., & Krämer, M. 2017b, *JCAP*, **1710**, 053
- Dalal, N., Dore, O., Huterer, D., & Shirokov, A. 2008, *Phys. Rev. D*, **77**, 123514
- Das, S., Louis, T., Nolta, M. R., et al. 2014, *JCAP*, **4**, 14
- Davies, F. B., Hennawi, J. F., Bañados, E., et al. 2018, *ApJ*, **864**, 142
- Daylan, T., Finkbeiner, D. P., Hooper, D., et al. 2016, *Phys. Dark Univ.*, **12**, 1
- de Haan, T., Benson, B. A., Bleem, L. E., et al. 2016, *ApJ*, **832**, 95
- de Sainte Agathe, V., Balland, C., du Mas des Bourboux, H., et al. 2019, *A&A*, **629**, A85
- de Salas, P. F., & Pastor, S. 2016, *JCAP*, **1607**, 051
- de Salas, P. F., Lattanzi, M., Mangano, G., et al. 2015, *Phys. Rev. D*, **92**, 123534
- de Salas, P. F., Forero, D. V., Ternes, C. A., Tortola, M., & Valle, J. W. F. 2018a, *Phys. Lett. B*, **782**, 633
- de Salas, P. F., Gariazzo, S., Mena, O., Ternes, C. A., & Tórtola, M. 2018b, *Front. Astron. Space Sci.*, **5**, 36
- Defayette, C., Pujolas, O., Sawicki, I., & Vikman, A. 2010, *JCAP*, **1010**, 026
- Delubac, T., Bautista, J. E., Busca, N. G., et al. 2015, *A&A*, **574**, A59
- Dentler, M., Hernández-Cabezudo, Á., Kopp, J., Maltoni, M., & Schwetz, T. 2017, *JHEP*, **11**, 099
- Dentler, M., Hernández-Cabezudo, Á., Kopp, J., et al. 2018, *JHEP*, **08**, 010
- DES Collaboration 2018a, *MNRAS*, **480**, 3879
- DES Collaboration 2018b, *Phys. Rev. D*, **98**, 043526
- DES Collaboration 2019, *MNRAS*, **483**, 4866
- Di Valentino, E., Gustavino, C., Lesgourgues, J., et al. 2014, *Phys. Rev. D*, **90**, 023543
- Di Valentino, E., Bøehm, C., Hivon, E., & Bouchet, F. R. 2018, *Phys. Rev. D*, **97**, 043513
- Dima, A., & Vernizzi, F. 2018, *Phys. Rev. D*, **97**, 101302
- Dirian, Y. 2017, *Phys. Rev. D*, **96**, 083513
- Dirian, Y., Foffa, S., Kunz, M., Maggiore, M., & Pettorino, V. 2016, *JCAP*, **1605**, 068
- Dodelson, S., & Widrow, L. M. 1994, *Phys. Rev. Lett.*, **72**, 17
- du Mas des Bourboux, H., Le Goff, J. M., Blomqvist, M., et al. 2017, *A&A*, **608**, A130
- Efstathiou, G. 2014, *MNRAS*, **440**, 1138
- Efstathiou, G., & Bond, J. R. 1999, *MNRAS*, **304**, 75
- Efstathiou, G., & Gratton, S. 2019, ArXiv e-prints [arXiv:1910.00483]
- Einstein, A. 1917, *Sitzungsber. Preuss. Akad. Wiss. Berlin (Math. Phys.)*, **142**
- Eisenstein, D. J., Zehavi, I., Hogg, D. W., et al. 2005, *ApJ*, **633**, 560
- Elvin-Poole, J., Crocce, M., Ross, A. J., et al. 2018, *Phys. Rev. D*, **98**, 042006
- Erben, T., Hildebrandt, H., Miller, L., et al. 2013, *MNRAS*, **433**, 2545
- Ewall-Wice, A., Chang, T. C., Lazio, J., et al. 2018, *ApJ*, **868**, 63
- Ezquiaga, J. M., & Zumalacaregui, M. 2017, *Phys. Rev. Lett.*, **119**, 251304
- Fang, W., Hu, W., & Lewis, A. 2008, *Phys. Rev. D*, **78**, 087303
- Farhang, M., Bond, J. R., & Chluba, J. 2012, *ApJ*, **752**, 88
- Farhang, M., Bond, J. R., Chluba, J., & Switzer, E. R. 2013, *ApJ*, **764**, 137
- Feeney, S. M., Mortlock, D. J., & Dalmasso, N. 2018, *MNRAS*, **476**, 3861
- Feeney, S. M., Peiris, H. V., Williamson, A. R., et al. 2019, *Phys. Rev. Lett.*, **122**, 061105
- Ferrara, S., Kallosh, R., Linde, A., & Porrati, M. 2013, *Phys. Rev. D*, **88**, 085038
- Ferraro, S., & Smith, K. M. 2018, *Phys. Rev. D*, **98**, 123519
- Fields, B. D. 2011, *Annu. Rev. Nucl. Part. Sci.*, **61**, 47
- Fields, B. D., Molaro, P., & Sarkar, S. 2014, *Chin. Phys. C*, **38**, 339
- Finkbeiner, D. P., Galli, S., Lin, T., & Slatyer, T. R. 2012, *Phys. Rev. D*, **85**, 043522
- Fixsen, D. 2009, *ApJ*, **707**, 916
- Follin, B., & Knox, L. 2018, *MNRAS*, **477**, 4534
- Font-Ribera, A., Kirkby, D., Busca, N., et al. 2014, *JCAP*, **5**, 27
- Freedman, W. L., Madore, B. F., Gibson, B. K., et al. 2001, *ApJ*, **553**, 47
- Freedman, W. L., Madore, B. F., Scowcroft, V., et al. 2012, *ApJ*, **758**, 24
- Freedman, W. L., Madore, B. F., Hatt, D., et al. 2019, *ApJ*, **882**, 34
- Freedman, W. L., Madore, B. F., Hoyt, T., et al. 2020, *ApJ*, **891**, 57
- Galante, M., Kallosh, R., Linde, A., & Roest, D. 2015, *Phys. Rev. Lett.*, **114**, 141302
- Galli, S., Slatyer, T. R., Valdes, M., & Iocco, F. 2013, *Phys. Rev. D*, **88**, 063502
- Galli, S., Benabed, K., Bouchet, F., et al. 2014, *Phys. Rev. D*, **90**, 063504
- Gao, F., Braatz, J. A., Reid, M. J., et al. 2016, *ApJ*, **817**, 128
- Gariazzo, S., Giunti, C., Laveder, M., & Li, Y. F. 2018, *Phys. Lett. B*, **782**, 13
- George, E. M., Reichardt, C. L., Aird, K. A., et al. 2015, *ApJ*, **799**, 177
- Gil-Marín, H., Guy, J., Zarrouk, P., et al. 2018, *MNRAS*, **477**, 1604
- Gleyzes, J., Langlois, D., Piazza, F., & Vernizzi, F. 2013, *JCAP*, **8**, 025
- Gleyzes, J., Langlois, D., Piazza, F., & Vernizzi, F. 2015, *Phys. Rev. Lett.*, **114**, 211101

- Gnedin, N. Y., & Gnedin, O. Y. 1998, *ApJ*, 509, 11
- Gómez-Valent, A., & Amendola, L. 2018, *JCAP*, 2018, 051
- Gordon, C., & Macias, O. 2013, *Phys. Rev. D*, 88, 083521; Erratum: *Phys. Rev. D*, 89, 4, 049901 (2014)
- Grieb, J. N., Sánchez, A. G., Salazar-Albornoz, S., et al. 2017, *MNRAS*, 467, 2085
- Gruzinov, A., & Hu, W. 1998, *ApJ*, 508, 435
- Gubitosi, G., Piazza, F., & Vernizzi, F. 2013, *JCAP*, 2, 032
- Gustavino, C. 2017, in RICAP16, 6th Roma International Conference on Astroparticle Physics, Roma, Italy, eds. A. Morselli, A. Capone, & G. Rodriguez Fernandez, *EPJ Web Conf.*, 136, 01009
- Guth, A. H., Kaiser, D. I., & Nomura, Y. 2014, *Phys. Lett. B*, 733, 112
- Hamana, T., Shirasaki, M., Miyazaki, S., et al. 2020, *PASJ*, 72, 2020
- Handley, W., & Millea, M. 2019, *Entropy*, 21, 272
- Hannestad, S., Sloth Hansen, R., & Tram, T. 2013, *JCAP*, 4, 032
- Hanson, D., Challinor, A., & Lewis, A. 2010, *Gen. Rel. Grav.*, 42, 2197
- Hassan, S. F., Rosen, R. A., & Schmidt-May, A. 2012, *JHEP*, 02, 026
- Hazra, D. K., & Smoot, G. F. 2017, *JCAP*, 1711, 028
- Heavens, A., Jimenez, R., & Verde, L. 2014, *Phys. Rev. Lett.*, 113, 241302
- Heinrich, C., & Hu, W. 2018, *Phys. Rev. D*, 98, 063514
- Heinrich, C. H., Miranda, V., & Hu, W. 2017, *Phys. Rev. D*, 95, 023513
- Hellings, R. W., & Nordvedt, K. 1973, *Phys. Rev. D*, 7, 3593
- Henning, J. W., Sayre, J. T., Reichardt, C. L., et al. 2018, *ApJ*, 852, 97
- Heymans, C., Van Waerbeke, L., Miller, L., et al. 2012, *MNRAS*, 427, 146
- Hikage, C., Oguri, M., Hamana, T., et al. 2019, *PASJ*, 71, 43
- Hildebrandt, H., Choi, A., Heymans, C., et al. 2016, *MNRAS*, 463, 635
- Hildebrandt, H., Viola, M., Heymans, C., et al. 2017, *MNRAS*, 465, 1454
- Hildebrandt, H., Köhlinger, F., van den Busch, J. L., et al. 2020, *A&A*, 633, A69
- Hirata, C. M., & Seljak, U. 2004, *Phys. Rev. D*, 70, 063526; Erratum: *Phys. Rev. D*, 82, 049901 (2010)
- Hivon, E., Mottet, S., & Ponthieu, N. 2017, *A&A*, 598, A25
- Hoekstra, H., Herbonnet, R., Muzzin, A., et al. 2015, *MNRAS*, 449, 685
- Hojjati, A., Pogosian, L., & Zhao, G.-B. 2011, *JCAP*, 1108, 005
- Holz, D. E., & Hughes, S. A. 2005, *ApJ*, 629, 15
- Hou, Z., Aylor, K., Benson, B. A., et al. 2018, *ApJ*, 853, 3
- Howlett, C., Ross, A., Samushia, L., Percival, W., & Manera, M. 2015, *MNRAS*, 449, 848
- Hu, W., & Holder, G. P. 2003, *Phys. Rev. D*, 68, 023001
- Hu, W., Scott, D., Sugiyama, N., & White, M. 1995, *Phys. Rev. D*, 52, 5498
- Hu, B., Raveri, M., Frusciante, N., & Silvestri, A. 2014, *Phys. Rev. D*, 89, 103530
- Huang, Y., Addison, G. E., Weiland, J. L., & Bennett, C. L. 2018, *ApJ*, 869, 38
- Huterer, D., Shafer, D., Scolnic, D., & Schmidt, F. 2017, *JCAP*, 1705, 015
- Ijjas, A., & Steinhardt, P. J. 2016, *CQG*, 33, 044001
- Ijjas, A., Steinhardt, P. J., & Loeb, A. 2013, *Phys. Lett. B*, 723, 261
- Iliadis, C., Anderson, K., Coc, A., Timmes, F., & Starrfield, S. 2016, *ApJ*, 831, 107
- Izotov, Y. I., Thuan, T. X., & Guseva, N. G. 2014, *MNRAS*, 445, 778
- Jee, M. J., Tyson, J. A., Hilbert, S., et al. 2016, *ApJ*, 824, 77
- Jimenez, R., & Loeb, A. 2002, *ApJ*, 573, 37
- Joudaki, S., Blake, C., Johnson, A., et al. 2018, *MNRAS*, 474, 4894
- Joudaki, S., Hildebrandt, H., Traykova, D., et al. 2020, *A&A*, 368, L1
- Kalosh, R., Linde, A., & Roest, D. 2013, *J. High Energy Phys.*, 11, 198
- Kamionkowski, M., Kosowsky, A., & Stebbins, A. 1997, *Phys. Rev. D*, 55, 7368
- Kaplinghat, M., Chu, M., Haiman, Z., et al. 2003, *ApJ*, 583, 24
- Kazin, E. A., Koda, J., Blake, C., et al. 2014, *MNRAS*, 441, 3524
- Köhlinger, F., Viola, M., Joachimi, B., et al. 2017, *MNRAS*, 471, 4412
- Kholupenko, E. E., Ivanchik, A. V., & Varshalovich, D. A. 2007, *MNRAS*, 378, L39
- Knee, A. M., Contreras, D., & Scott, D. 2018, *JCAP*, 7, 39
- Knox, L., Scoccimarro, R., & Dodelson, S. 1998, *Phys. Rev. Lett.*, 81, 2004
- Komatsu, E., & Seljak, U. 2002, *MNRAS*, 336, 1256
- Krause, E., Eifler, T. F., Zuntz, J., et al. 2017, ArXiv e-prints [arXiv:1706.09359]
- Kreisch, C. D., Cyr-Racine, F. Y., & Doré, O. 2020, *Phys. Rev. D*, 101, 123505
- Kunz, M., & Sapone, D. 2006, *Phys. Rev. D*, 74, 123503
- Kuo, C. Y., Braatz, J. A., Reid, M. J., et al. 2013, *ApJ*, 767, 155
- Lancaster, L., Cyr-Racine, F.-Y., Knox, L., & Pan, Z. 2017, *JCAP*, 1707, 033
- Langlois, D., Mancarella, M., Noui, K., & Vernizzi, F. 2017, *JCAP*, 1705, 033
- Langlois, D., Saito, R., Yamauchi, D., & Noui, K. 2018, *Phys. Rev. D*, 97, 061501
- Larsen, P., Challinor, A., Sherwin, B. D., & Mak, D. 2016, *Phys. Rev. Lett.*, 117, 151102
- Lemos, P., Lee, E., Efstathiou, G., & Gratton, S. 2019, *MNRAS*, 483, 4803
- Lesgourgues, J., & Pastor, S. 2006, *Phys. Rept.*, 429, 307
- Lesgourgues, J., Mangano, G., Miele, G., & Pastor, S. 2013, *Neutrino Cosmology* (Cambridge)
- Lesgourgues, J., Marques-Tavares, G., & Schmaltz, M. 2016, *JCAP*, 1602, 037
- Lewis, A. 2008, *Phys. Rev. D*, 78, 023002
- Lewis, A. 2013, *Phys. Rev. D*, 87, 103529
- Lewis, A. 2019, ArXiv e-prints [arXiv:1910.13970]
- Lewis, A., & Bridle, S. 2002, *Phys. Rev. D*, 66, 103511
- Lewis, A., & Challinor, A. 2006, *Phys. Rept.*, 429, 1
- Lewis, A., Challinor, A., & Lasenby, A. 2000, *ApJ*, 538, 473
- Lin, M.-X., Benevento, G., Hu, W., & Raveri, M. 2019, *Phys. Rev. D*, 100, 063542
- Linde, A. 2018, *Found. Phys.*, 48, 1246
- Lombriser, L., & Taylor, A. 2016, *JCAP*, 1603, 031
- Louis, T., Addison, G. E., Hasselfield, M., et al. 2014, *JCAP*, 7, 016
- Louis, T., Grace, E., Hasselfield, M., et al. 2017, *JCAP*, 1706, 031
- LoVerde, M., & Afshordi, N. 2008, *Phys. Rev. D*, 78, 123506
- Mak, D. S. Y., Challinor, A., Efstathiou, G., & Lagache, G. 2017, *MNRAS*, 466, 286
- Maltoni, M. 2018, *Sterile Neutrinos: The Global Picture* (Heidelberg: Neutrino 2018 Conference)
- Mangano, G., Miele, G., Pastor, S., et al. 2005, *Nucl. Phys. B*, 729, 221
- Mantz, A. B., von der Linden, A., Allen, S. W., et al. 2015, *MNRAS*, 446, 2205
- Marcucci, L. E., Viviani, M., Schiavilla, R., Kievsky, A., & Rosati, S. 2005, *Phys. Rev. C*, 72, 014001
- Marcucci, L. E., Mangano, G., Kievsky, A., & Viviani, M. 2016, *Phys. Rev. Lett.*, 116, 102501; Erratum: *Phys. Rev. Lett.*, 117, 049901 (2016)
- Mason, C. A., Treu, T., Dijkstra, M., et al. 2018, *ApJ*, 856, 2
- McManus, R., Lombriser, L., & Peñarrubia, J. 2016, *JCAP*, 1611, 006
- Mead, A., Peacock, J., Heymans, C., Joudaki, S., & Heavens, A. 2015, *MNRAS*, 454, 1958
- Mead, A., Heymans, C., Lombriser, L., et al. 2016, *MNRAS*, 459, 1468
- Millea, M., & Bouchet, F. 2018, *A&A*, 617, A96
- Miranda, V., Lidz, A., Heinrich, C. H., & Hu, W. 2017, *MNRAS*, 467, 4050
- Mortonson, M. J., & Hu, W. 2008, *ApJ*, 672, 737
- Mosher, J., Guy, J., Kessler, R., et al. 2014, *ApJ*, 793, 16
- Motloch, P., & Hu, W. 2018, *Phys. Rev. D*, 97, 103536
- Muñoz, J. B., Grin, D., Dai, L., Kamionkowski, M., & Kovetz, E. D. 2016, *Phys. Rev. D*, 93, 043008
- Naess, S., Hasselfield, M., McMahon, J., et al. 2014, *JCAP*, 1410, 007
- Nagai, D., Kravtsov, A. V., & Vikhlinin, A. 2007, *ApJ*, 668, 1
- Nollett, K. M., & Burles, S. 2000, *Phys. Rev. D*, 61, 123505
- Nollett, K. M., & Holder, G. P. 2011, ArXiv e-prints [arXiv:1112.2683]
- Obied, G., Dvorkin, C., Heinrich, C., Hu, W., & Miranda, V. 2018, *Phys. Rev. D*, 98, 043518
- Oka, A., Saito, S., Nishimichi, T., Taruya, A., & Yamamoto, K. 2014, *MNRAS*, 439, 2515
- Okumura, T., Hikage, C., Totani, T., et al. 2016, *PASJ*, 68, 24
- Oldengott, I. M., Tram, T., Rampf, C., & Wong, Y. Y. Y. 2017, *JCAP*, 1711, 027
- Palanque-Delabrouille, N., Yèche, C., Baur, J., et al. 2015, *JCAP*, 1511, 011
- Parkinson, D., Riemer-Sorensen, S., Blake, C., et al. 2012, *Phys. Rev. D*, 86, 103518
- Parsa, S., Dunlop, J. S., & McLure, R. J. 2018, *MNRAS*, 474, 2904
- Patrignani, C. Particle Data Group 2016, *Chin. Phys.*, C40, 100001
- Peebles, P. J. E. 1968, *ApJ*, 153, 1
- Peebles, P. J. E., & Yu, J. T. 1970, *ApJ*, 162, 815
- Peel, A., Pettorino, V., Giocoli, C., Starck, J.-L., & Baldi, M. 2018, *A&A*, 619, A38
- Peimbert, A., Peimbert, M., & Luridiana, V. 2016, *Rev. Mex. Astron. Astrofis.*, 52, 419
- Peiris, H. V., Komatsu, E., Verde, L., et al. 2003, *ApJS*, 148, 213
- Peloton, J., Schmittfull, M., Lewis, A., Carron, J., & Zahn, O. 2017, *Phys. Rev. D*, 95, 043508
- Penna-Lima, M., Bartlett, J. G., Rozo, E., et al. 2017, *A&A*, 604, A89
- Percival, W. J., & White, M. 2009, *MNRAS*, 393, 297
- Percival, W. J., Baugh, C. M., Bland-Hawthorn, J., et al. 2001, *MNRAS*, 327, 1297
- Percival, W. J., Sutherland, W., Peacock, J. A., et al. 2002, *MNRAS*, 337, 1068
- Perlmutter, S., Aldering, G., Goldhaber, G., et al. 1999, *ApJ*, 517, 565
- Pettorino, V. 2013, *Phys. Rev. D*, 88, 063519
- Pettorino, V., & Baccigalupi, C. 2008, *Phys. Rev. D*, 77, 103003
- Pezzotta, A., de la Torre, S., Bel, J., et al. 2017, *A&A*, 604, A33
- Pierpaoli, E., Scott, D., & White, M. 2001, *MNRAS*, 325, 77
- Pisanti, O., Cirillo, A., Esposito, S., et al. 2008, *Comput. Phys. Commun.*, 178, 956
- Pitrou, C., Coc, A., Uzan, J.-P., & Vangioni, E. 2018, *Phys. Rept.*, 04, 005
- Planck Collaboration. 2018, *The Legacy Explanatory Supplement* (ESA), <https://www.cosmos.esa.int/web/planck/pla>
- Planck Collaboration XV. 2014, *A&A*, 571, A15
- Planck Collaboration XVI. 2014, *A&A*, 571, A16
- Planck Collaboration XVII. 2014, *A&A*, 571, A17

- Planck Collaboration XX. 2014, *A&A*, 571, A20
 Planck Collaboration XXII. 2014, *A&A*, 571, A22
 Planck Collaboration XXIV. 2014, *A&A*, 571, A24
 Planck Collaboration XXX. 2014, *A&A*, 571, A30
 Planck Collaboration I. 2016, *A&A*, 594, A1
 Planck Collaboration XI. 2016, *A&A*, 594, A11
 Planck Collaboration XIII. 2016, *A&A*, 594, A13
 Planck Collaboration XIV. 2016, *A&A*, 594, A14
 Planck Collaboration XV. 2016, *A&A*, 594, A15
 Planck Collaboration XVII. 2016, *A&A*, 594, A17
 Planck Collaboration XX. 2016, *A&A*, 594, A20
 Planck Collaboration XXIV. 2016, *A&A*, 594, A24
 Planck Collaboration I. 2020, *A&A*, 641, A1
 Planck Collaboration II. 2020, *A&A*, 641, A2
 Planck Collaboration III. 2020, *A&A*, 641, A3
 Planck Collaboration IV. 2020, *A&A*, 641, A4
 Planck Collaboration V. 2020, *A&A*, 641, A5
 Planck Collaboration VI. 2020, *A&A*, 641, A6
 Planck Collaboration VII. 2020, *A&A*, 641, A7
 Planck Collaboration VIII. 2020, *A&A*, 641, A8
 Planck Collaboration IX. 2020, *A&A*, 641, A9
 Planck Collaboration X. 2020, *A&A*, 641, A10
 Planck Collaboration XI. 2020, *A&A*, 641, A11
 Planck Collaboration XII. 2020, *A&A*, 641, A12
 Planck Collaboration Int. XLVI. 2016, *A&A*, 596, A107
 Planck Collaboration Int. XLVII. 2016, *A&A*, 596, A108
 Planck Collaboration Int. LI. 2017, *A&A*, 607, A95
 Polnarev, A. G. 1985, *Sov. Astron.*, 29, 607
 Poulin, V., Smith, T. L., Karwal, T., & Kamionkowski, M. 2019, *Phys. Rev. Lett.*, 122, 221301
 Prat, J., et al. 2018, *Phys. Rev. D*, 98, 042005
 Raveri, M., & Hu, W. 2019, *Phys. Rev. D*, 99, 043506
 Raveri, M., Hu, B., Frusciante, N., & Silvestri, A. 2014, *Phys. Rev. D*, 90, 043513
 Reid, M. J., Braatz, J. A., Condon, J. J., et al. 2013, *ApJ*, 767, 154
 Riess, A. G., Filippenko, A. V., Challis, P., et al. 1998, *AJ*, 116, 1009
 Riess, A. G., Macri, L., Casertano, S., et al. 2011, *ApJ*, 730, 119
 Riess, A. G., Macri, L. M., Hoffmann, S. L., et al. 2016, *ApJ*, 826, 56
 Riess, A. G., Casertano, S., Yuan, W., et al. 2018a, *ApJ*, 855, 136
 Riess, A. G., Casertano, S., Yuan, W., et al. 2018b, *ApJ*, 861, 126
 Riess, A. G., Casertano, S., Yuan, W., Macri, L. M., & Scolnic, D. 2019, *ApJ*, 876, 85
 Robertson, B. E., Ellis, R. S., Furlanetto, S. R., & Dunlop, J. S. 2015, *ApJ*, 802, L19
 Ross, A. J., Samushia, L., Howlett, C., et al. 2015, *MNRAS*, 449, 835
 Ross, A. J., Beutler, F., Chuang, C.-H., et al. 2017, *MNRAS*, 464, 1168
 Rosset, C., Tristram, M., Ponthieu, N., et al. 2010, *A&A*, 520, A13
 Rubiño-Martín, J. A., Chluba, J., Fendt, W. A., & Wandelt, B. D. 2010, *MNRAS*, 403, 439
 Saikawa, K., & Shirai, S. 2018, *JCAP*, 1805, 035
 Sakstein, J., & Jain, B. 2017, *Phys. Rev. Lett.*, 119, 251303
 Saltas, I. D., Sawicki, I., Amendola, L., & Kunz, M. 2014, *Phys. Rev. Lett.*, 113, 191101
 Saltas, I. D., Sawicki, I., & Lopes, I. 2018, *JCAP*, 1805, 028
 Salvati, L., Pagano, L., Consiglio, R., & Melchiorri, A. 2016, *JCAP*, 1603, 055
 Salvati, L., Douspis, M., & Aghanim, N. 2018, *A&A*, 614, A13
 Sánchez, A. G., Scoccimarro, R., Crocce, M., et al. 2017, *MNRAS*, 464, 1640
 Satpathy, S., Alam, S., Ho, S., et al. 2017, *MNRAS*, 469, 1369
 Saviano, N., Mirizzi, A., Pisanti, O., et al. 2013, *Phys. Rev. D*, 87, 073006
 Schellenberger, G., & Reiprich, T. H. 2017, *MNRAS*, 471, 1370
 Schmittfull, M. M., Challinor, A., Hanson, D., & Lewis, A. 2013, *Phys. Rev. D*, 88, 063012
 Scolnic, D., Casertano, S., Riess, A., et al. 2015, *ApJ*, 815, 117
 Scolnic, D. M., Jones, D. O., Rest, A., et al. 2018, *ApJ*, 859, 101
 Seager, S., Sasselov, D. D., & Scott, D. 1999, *ApJ*, 523, L1
 Seager, S., Sasselov, D. D., & Scott, D. 2000, *ApJS*, 128, 407
 Seljak, U. 1996, *ApJ*, 463, 1
 Seljak, U., & Zaldarriaga, M. 1997, *Phys. Rev. D Lett.*, 78, 2054
 Seljak, U., Sugiyama, N., White, M., & Zaldarriaga, M. 2003, *Phys. Rev. D*, 68, 083507
 Serebrov, A. P., Kolomensky, E. A., Fomin, A. K., et al. 2018, *Phys. Rev. C*, 97, 055503
 Serenelli, A., & Basu, S. 2010, *ApJ*, 719, 865
 Sereno, M., Covone, G., Izzo, L., et al. 2017, *MNRAS*, 472, 1946
 Shaw, J. R., & Chluba, J. 2011, *MNRAS*, 415, 1343
 Sievers, J. L., Hložek, R. A., Nolta, M. R., et al. 2013, *JCAP*, 1310, 060
 Sifón, C., Battaglia, N., Hasselfield, M., et al. 2016, *MNRAS*, 461, 248
 Slatyer, T. R. 2016a, *Phys. Rev. D*, 93, 023521
 Slatyer, T. R. 2016b, *Phys. Rev. D*, 93, 023527
 Smith, K. M., & Ferraro, S. 2017, *Phys. Rev. Lett.*, 119, 021301
 Smith, R. E., Peacock, J. A., Jenkins, A., et al. 2003, *MNRAS*, 341, 1311
 Smith, T. L., Muñoz, J. B., Smith, R., Yee, K., & Grin, D. 2017, *Phys. Rev. D*, 96, 083508
 Smoot, G. F., Bennett, C. L., Kogut, A., et al. 1992, *ApJ*, 396, L1
 Spergel, D. N., Flauger, R., & Hložek, R. 2015, *Phys. Rev. D*, 91, 023518
 Springob, C. M., Magoulas, C., Colless, M., et al. 2014, *MNRAS*, 445, 2677
 Stöcker, P., Krämer, M., Lesgourgues, J., & Poulin, V. 2018, *JCAP*, 1803, 018
 Story, K. T., Reichardt, C. L., Hou, Z., et al. 2013, *ApJ*, 779, 86
 Sunyaev, R. A., & Zeldovich, Y. B. 1970, *Ap&SS*, 7, 3
 Suyu, S. H., Auger, M. W., Hilbert, S., et al. 2013, *ApJ*, 766, 70
 Switzer, E. R., & Hirata, C. M. 2008, *Phys. Rev. D*, 77, 083006
 Takahashi, R., Sato, M., Nishimichi, T., Taruya, A., & Oguri, M. 2012, *ApJ*, 761, 152
 Troxel, M. A., Krause, E., Chang, C., et al. 2018a, *MNRAS*, 479, 4998
 Troxel, M. A., MacCrann, N., Zuntz, J., et al. 2018b, *Phys. Rev. D*, 98, 043528
 Valiviita, J. 2017, *JCAP*, 1704, 014
 van Uitert, E., Joachimi, B., Joudaki, S., et al. 2018, *MNRAS*, 476, 4662
 Vargas-Magaña, M., Ho, S., Cuesta, A. J., et al. 2018, *MNRAS*, 477, 1153
 Vázquez, J. A., Bridges, M., Hobson, M. P., & Lasenby, A. N. 2012, *JCAP*, 06, 006
 Viero, M. P., Wang, L., Zemcov, M., et al. 2013, *ApJ*, 772, 77
 Vikman, A. 2005, *Phys. Rev. D*, 71, 023515
 Villanueva-Domingo, P., Gariazzo, S., Gnedin, N. Y., & Mena, O. 2018, *JCAP*, 1804, 024
 von der Linden, A., Mantz, A., Allen, S. W., et al. 2014, *MNRAS*, 443, 197
 Weinberg, S. 1987, *Phys. Rev. Lett.*, 59, 2607
 Wong, W. Y., Moss, A., & Scott, D. 2008, *MNRAS*, 386, 1023
 Wong, K. C., Suyu, S. H., Chen, G. C. F., et al. 2019, ArXiv e-prints [arXiv:1907.04869]
 Yèche, C., Palanque-Delabrouille, N., Baur, J., & du Mas des Bourboux, H. 2017, *JCAP*, 1706, 047
 Yuan, W., Riess, A. G., Macri, L. M., Casertano, S., & Scolnic, D. 2019, *ApJ*, 886, 61
 Yue, A. T., Dewey, M. S., Gilliam, D. M., et al. 2013, *Phys. Rev. Lett.*, 111, 222501
 Zahn, O., Reichardt, C. L., Shaw, L., et al. 2012, *ApJ*, 756, 65
 Zaldarriaga, M., Spergel, D., & Seljak, U. 1997, *ApJ*, 488, 1
 Zarrouk, P., Burtin, E., Gil-Marín, H., et al. 2018, *MNRAS*, 477, 1639
 Zeldovich, Y. B., Kurt, V. G., & Syunyaev, R. A. 1968, *Zhurnal Eksperimentalnoi i Teoreticheskoi Fiziki*, 55, 278
 Zhang, P., Liguori, M., Bean, R., & Dodelson, S. 2007, *Phys. Rev. Lett.*, 99, 141302
 Zhang, B. R., Childress, M. J., Davis, T. M., et al. 2017, *MNRAS*, 471, 2254
 Zhao, G.-B., Pogosian, L., Silvestri, A., & Zylberberg, J. 2009, *Phys. Rev. D*, 79, 083513
 Zubeldía, I., & Challinor, A. 2019, *MNRAS*, 489, 401
 Zumalacárregui, M., & García-Bellido, J. 2014, *Phys. Rev. D*, 89, 064046

¹ AIM, CEA, CNRS, Université Paris-Saclay, Université Paris-Diderot, Sorbonne Paris Cité, 91191 Gif-sur-Yvette, France

² APC, AstroParticule et Cosmologie, Université Paris Diderot, CNRS/IN2P3, CEA/Irfu, Observatoire de Paris, Sorbonne Paris Cité, 10 rue Alice Domon et Léonie Duquet, 75205 Paris Cedex 13, France

³ African Institute for Mathematical Sciences, 6-8 Melrose Road, Muizenberg, Cape Town, South Africa

⁴ Aix Marseille Univ, CNRS, CNES, LAM, Marseille, France

⁵ Astrophysics Group, Cavendish Laboratory, University of Cambridge, J J Thomson Avenue, Cambridge, CB3 0HE, UK

⁶ Astrophysics & Cosmology Research Unit, School of Mathematics, Statistics & Computer Science, University of KwaZulu-Natal, Westville Campus, Private Bag X54001, Durban 4000, South Africa

⁷ CITA, University of Toronto, 60 St. George St., Toronto, ON M5S 3H8, Canada

⁸ CNRS, IRAP, 9 Av. colonel Roche, BP 44346, 31028 Toulouse Cedex 4, France

⁹ Cahill Center for Astronomy and Astrophysics, California Institute of Technology, Pasadena, CA 91125, USA

¹⁰ California Institute of Technology, Pasadena, California, USA

¹¹ Centre for Theoretical Cosmology, DAMTP, University of Cambridge, Wilberforce Road, Cambridge CB3 0WA, UK

¹² Computational Cosmology Center, Lawrence Berkeley National Laboratory, Berkeley, CA, USA

- ¹³ DTU Space, National Space Institute, Technical University of Denmark, Elektrovej 327, 2800 Kgs. Lyngby, Denmark
- ¹⁴ Département de Physique Théorique, Université de Genève, 24 quai E. Ansermet, 1211 Genève 4, Switzerland
- ¹⁵ Département de Physique, École normale supérieure, PSL Research University, CNRS, 24 rue Lhomond, 75005 Paris, France
- ¹⁶ Departamento de Astrofísica, Universidad de La Laguna (ULL), 38206 La Laguna, Tenerife, Spain
- ¹⁷ Departamento de Física, Universidad de Oviedo, C/ Federico García Lorca, 18, Oviedo, Spain
- ¹⁸ Department of Astrophysics/IMAPP, Radboud University, PO Box 9010, 6500 GL Nijmegen, The Netherlands
- ¹⁹ Department of Mathematics, University of Stellenbosch, Stellenbosch 7602, South Africa
- ²⁰ Department of Physics & Astronomy, University of British Columbia, 6224 Agricultural Road, Vancouver, BC, Canada
- ²¹ Department of Physics & Astronomy, University of the Western Cape, Cape Town 7535, South Africa
- ²² Department of Physics and Astronomy, University College London, London WC1E 6BT, UK
- ²³ Department of Physics and Astronomy, University of Sussex, Brighton BN1 9QH, UK
- ²⁴ Department of Physics, Gustaf Hällströmin katu 2a, University of Helsinki, Helsinki, Finland
- ²⁵ Department of Physics, Princeton University, Princeton, NJ, USA
- ²⁶ Department of Physics, University of California, Berkeley, CA, USA
- ²⁷ Department of Physics, University of California, One Shields Avenue, Davis, CA, USA
- ²⁸ Department of Physics, University of California, Santa Barbara, CA, USA
- ²⁹ Dipartimento di Fisica e Astronomia G. Galilei, Università degli Studi di Padova, via Marzolo 8, 35131 Padova, Italy
- ³⁰ Dipartimento di Fisica e Scienze della Terra, Università di Ferrara, Via Saragat 1, 44122 Ferrara, Italy
- ³¹ Dipartimento di Fisica, Università La Sapienza, P.le A. Moro 2, Roma, Italy
- ³² Dipartimento di Fisica, Università degli Studi di Milano, Via Celoria, 16, Milano, Italy
- ³³ Dipartimento di Fisica, Università degli Studi di Trieste, via A. Valerio 2, Trieste, Italy
- ³⁴ Dipartimento di Fisica, Università di Roma Tor Vergata, Via della Ricerca Scientifica, 1, Roma, Italy
- ³⁵ European Space Agency, ESAC, Planck Science Office, Camino bajo del Castillo, s/n, Urbanización Villafranca del Castillo, Villanueva de la Cañada, Madrid, Spain
- ³⁶ European Space Agency, ESTEC, Keplerlaan 1, 2201, AZ Noordwijk, The Netherlands
- ³⁷ Gran Sasso Science Institute, INFN, viale F. Crispi 7, 67100 L'Aquila, Italy
- ³⁸ HEP Division, Argonne National Laboratory, Lemont, IL 60439, USA
- ³⁹ Haverford College Astronomy Department, 370 Lancaster Avenue, Haverford, PA, USA
- ⁴⁰ Helsinki Institute of Physics, Gustaf Hällströmin katu 2, University of Helsinki, Helsinki, Finland
- ⁴¹ INAF – OAS Bologna, Istituto Nazionale di Astrofisica – Osservatorio di Astrofisica e Scienza dello Spazio di Bologna, Area della Ricerca del CNR, Via Gobetti 101, 40129 Bologna, Italy
- ⁴² INAF – Osservatorio Astronomico di Padova, Vicolo dell'Osservatorio 5, Padova, Italy
- ⁴³ INAF – Osservatorio Astronomico di Trieste, Via G.B. Tiepolo 11, Trieste, Italy
- ⁴⁴ INAF, Istituto di Radioastronomia, Via Piero Gobetti 101, 40129 Bologna, Italy
- ⁴⁵ INAF/IASF Milano, Via E. Bassini 15, Milano, Italy
- ⁴⁶ INFN – CNAF, viale Berti Pichat 6/2, 40127 Bologna, Italy
- ⁴⁷ INFN, Sezione di Bologna, viale Berti Pichat 6/2, 40127 Bologna, Italy
- ⁴⁸ INFN, Sezione di Ferrara, Via Saragat 1, 44122 Ferrara, Italy
- ⁴⁹ INFN, Sezione di Milano, Via Celoria 16, Milano, Italy
- ⁵⁰ INFN, Sezione di Roma 1, Università di Roma Sapienza, Piazzale Aldo Moro 2, 00185 Roma, Italy
- ⁵¹ INFN, Sezione di Roma 2, Università di Roma Tor Vergata, Via della Ricerca Scientifica, 1, Roma, Italy
- ⁵² IUCAA, Post Bag 4, Ganeshkhind, Pune University Campus, Pune 411 007, India
- ⁵³ Imperial College London, Astrophysics group, Blackett Laboratory, Prince Consort Road, London SW7 2AZ, UK
- ⁵⁴ Institut d'Astrophysique Spatiale, CNRS, Univ. Paris-Sud, Université Paris-Saclay, Bât. 121, 91405 Orsay Cedex, France
- ⁵⁵ Institut d'Astrophysique de Paris, CNRS (UMR7095), 98bis boulevard Arago, 75014 Paris, France
- ⁵⁶ Institut für Theoretische Teilchenphysik und Kosmologie, RWTH Aachen University, 52056 Aachen, Germany
- ⁵⁷ Institute Lorentz, Leiden University, PO Box 9506, Leiden 2300 RA, The Netherlands
- ⁵⁸ Institute of Astronomy, University of Cambridge, Madingley Road, Cambridge CB3 0HA, UK
- ⁵⁹ Institute of Theoretical Astrophysics, University of Oslo, Blindern, Oslo, Norway
- ⁶⁰ Instituto de Astrofísica de Canarias, C/Vía Láctea s/n, La Laguna, Tenerife, Spain
- ⁶¹ Instituto de Física de Cantabria (CSIC-Universidad de Cantabria), Avda. de los Castros s/n, Santander, Spain
- ⁶² Istituto Nazionale di Fisica Nucleare, Sezione di Padova, via Marzolo 8, 35131 Padova, Italy
- ⁶³ Jet Propulsion Laboratory, California Institute of Technology, 4800 Oak Grove Drive, Pasadena, CA, USA
- ⁶⁴ Jodrell Bank Centre for Astrophysics, Alan Turing Building, School of Physics and Astronomy, The University of Manchester, Oxford Road, Manchester M13 9PL, UK
- ⁶⁵ Kavli Institute for Cosmology Cambridge, Madingley Road, Cambridge CB3 0HA, UK
- ⁶⁶ Kavli Institute for the Physics and Mathematics of the Universe (Kavli IPMU, WPI), UTIAS, The University of Tokyo, Chiba 277-8583, Japan
- ⁶⁷ Laboratoire d'Océanographie Physique et Spatiale (LOPS), Univ. Brest, CNRS, Ifremer, IRD, Brest, France
- ⁶⁸ Laboratoire de Physique Subatomique et Cosmologie, Université Grenoble-Alpes, CNRS/IN2P3, 53 rue des Martyrs, 38026 Grenoble Cedex, France
- ⁶⁹ Laboratoire de Physique Théorique, Université Paris-Sud 11 & CNRS, Bâtiment 210, 91405 Orsay, France
- ⁷⁰ Lawrence Berkeley National Laboratory, Berkeley, CA, USA
- ⁷¹ Low Temperature Laboratory, Department of Applied Physics, Aalto University, Espoo 00076, Aalto, Finland
- ⁷² Max-Planck-Institut für Astrophysik, Karl-Schwarzschild-Str. 1, 85741 Garching, Germany
- ⁷³ Mullard Space Science Laboratory, University College London, Surrey RH5 6NT, UK
- ⁷⁴ NAOC-UKZN Computational Astrophysics Centre (NUCAC), University of KwaZulu-Natal, Durban 4000, South Africa
- ⁷⁵ National Centre for Nuclear Research, ul. L. Pasteura 7, 02-093 Warsaw, Poland
- ⁷⁶ Physics Department, Shahid Beheshti University, Velenjak, Tehran 19839, Iran
- ⁷⁷ Purple Mountain Observatory, No. 8 Yuan Hua Road, 210034 Nanjing, PR China
- ⁷⁸ SISSA, Astrophysics Sector, Via Bonomea 265, 34136 Trieste, Italy
- ⁷⁹ San Diego Supercomputer Center, University of California, San Diego, 9500 Gilman Drive, La Jolla, CA 92093, USA
- ⁸⁰ School of Chemistry and Physics, University of KwaZulu-Natal, Westville Campus, Private Bag X54001, Durban 4000, South Africa
- ⁸¹ School of Physical Sciences, National Institute of Science Education and Research, HBNI, Jatni 752050, Odisha, India
- ⁸² School of Physics and Astronomy, Cardiff University, Queens Buildings, The Parade, Cardiff CF24 3AA, UK

- ⁸³ School of Physics and Astronomy, Sun Yat-sen University, 2 Daxue Rd, Tangjia, Zhuhai, PR China
- ⁸⁴ School of Physics and Astronomy, University of Nottingham, Nottingham NG7 2RD, UK
- ⁸⁵ School of Physics, Indian Institute of Science Education and Research Thiruvananthapuram, Maruthamala PO, Vithura, Thiruvananthapuram 695551, Kerala, India
- ⁸⁶ School of Physics, The University of New South Wales, Sydney, NSW 2052, Australia
- ⁸⁷ Simon Fraser University, Department of Physics, 8888 University Drive, Burnaby, BC, Canada
- ⁸⁸ Sorbonne Université, Institut Lagrange de Paris (ILP), 98bis boulevard Arago, 75014 Paris, France
- ⁸⁹ Sorbonne Université, Observatoire de Paris, Université PSL, École normale supérieure, CNRS, LERMA, 75005 Paris, France
- ⁹⁰ Sorbonne Université, UMR7095, Institut d'Astrophysique de Paris, 98bis boulevard Arago, 75014 Paris, France
- ⁹¹ Space Research Institute (IKI), Russian Academy of Sciences, Profsoyuznaya Str, 84/32, Moscow 117997, Russia
- ⁹² Space Science Data Center – Agenzia Spaziale Italiana, Via del Politecnico snc, 00133 Roma, Italy
- ⁹³ Space Sciences Laboratory, University of California, Berkeley, CA, USA
- ⁹⁴ The Oskar Klein Centre for Cosmoparticle Physics, Department of Physics, Stockholm University, AlbaNova 106 91, Stockholm, Sweden
- ⁹⁵ Université de Toulouse, UPS-OMP, IRAP, 31028 Toulouse Cedex 4, France
- ⁹⁶ University of Heidelberg, Institute for Theoretical Physics, Philosophenweg 16, 69120 Heidelberg, Germany
- ⁹⁷ Warsaw University Observatory, Aleje Ujazdowskie 4, 00-478 Warszawa, Poland

Appendix A: Cosmological parameters from CamSpec

Section 2.2 summarized the two high-multipole likelihoods used in this paper. We stated that the two codes give very similar answers in *TT* but show some differences in *TE* and *EE*. We discuss these differences in more detail in this Appendix. Table 1 compares the base- Λ CDM parameters from *Planck* and CamSpec for the *Planck* TT,TE,EE+lowE+lensing likelihood combinations, showing that the two codes return cosmological parameters that agree to within a fraction of a standard deviation. Table A.1 is the equivalent of Table 2, but using the CamSpec likelihood in place of *Planck*. In *TT*, the parameters determined from the two codes agree to 0.2σ or better. The agreement is less good in *TE*; the most discrepant parameters are n_s , which is 1σ higher in CamSpec, and $A_s e^{-2\tau}$, which is 1.2σ higher in CamSpec. Both of these parameters are sensitive to the calibration of the polarization spectra which differ in the two codes. The other cosmological parameters agree to better than 0.5σ and the shifts in parameters between *TE* and *TT* are similar in both codes. In *EE*, the parameter shifts compared to *TT* are similar in both codes, although the *EE* parameters from the two codes typically differ by almost 1σ . Since *EE* from *Planck* is so noisy, the *EE* differences have little impact on the combined TT,TE,EE parameters.

The differences listed in Table 1 can be seen visually in Fig. A.1, which is the equivalent of Fig. 5 in Sect. 3, comparing base- Λ CDM parameters determined separately from TT, TE, and EE, and the combined result from the TT,TE,EE CamSpec likelihood. The two figures are remarkably similar, given the different methodologies and choices (e.g., polarization masks, multipole cuts, etc.) used to construct the polarization blocks of the likelihoods. For the base- Λ CDM cosmology, the two likelihoods are in such close agreement that it would make no difference to any of the science conclusions in this paper if we used CamSpec in place of *Planck*.

The small differences between the *Planck* and CamSpec TT likelihoods are probably due to underestimates of the modelling uncertainties because the foreground models in the two codes are almost identical. A more accurate impression of foreground-modelling uncertainties can be gleaned by comparing the default model with a heuristic foreground model applied to spectra, cleaned using the 545 GHz temperature maps, as described in Sect. 3.2 of PCP15. Since the low-frequency and high-frequency maps have different beams, the subtraction is actually done in the power spectrum domain:

$$\begin{aligned} \hat{C}^{T_{v_1} T_{v_2} \text{clean}} &= (1 + \alpha^{T_{v_1}})(1 + \alpha^{T_{v_2}})\hat{C}^{T_{v_1} T_{v_2}} \\ &\quad - (1 + \alpha^{T_{v_1}})\alpha^{T_{v_2}}\hat{C}^{T_{v_1} T_{v_1}} \\ &\quad - (1 + \alpha^{T_{v_2}})\alpha^{T_{v_1}}\hat{C}^{T_{v_2} T_{v_2}} + \alpha^{T_{v_1}}\alpha^{T_{v_2}}\hat{C}^{T_{v_1} T_{v_1}}, \end{aligned} \quad (\text{A.1})$$

(e.g., Spergel et al. 2015), where $\hat{C}^{T_{v_1} T_{v_2}}$ etc. are the mask-deconvolved beam-corrected power spectra at low frequencies and v_t is the frequency of the template map. The coefficients $\alpha^{T_{v_i}}$ are determined by minimizing

$$\sum_{\ell=\ell_{\min}}^{\ell_{\max}} \sum_{\ell'=\ell_{\min}}^{\ell_{\max}} \hat{C}_{\ell}^{T_{v_i} T_{v_i} \text{clean}} \left(\hat{M}_{\ell\ell'}^{T_{v_i} T_{v_i}} \right)^{-1} \hat{C}_{\ell'}^{T_{v_i} T_{v_i} \text{clean}}, \quad (\text{A.2})$$

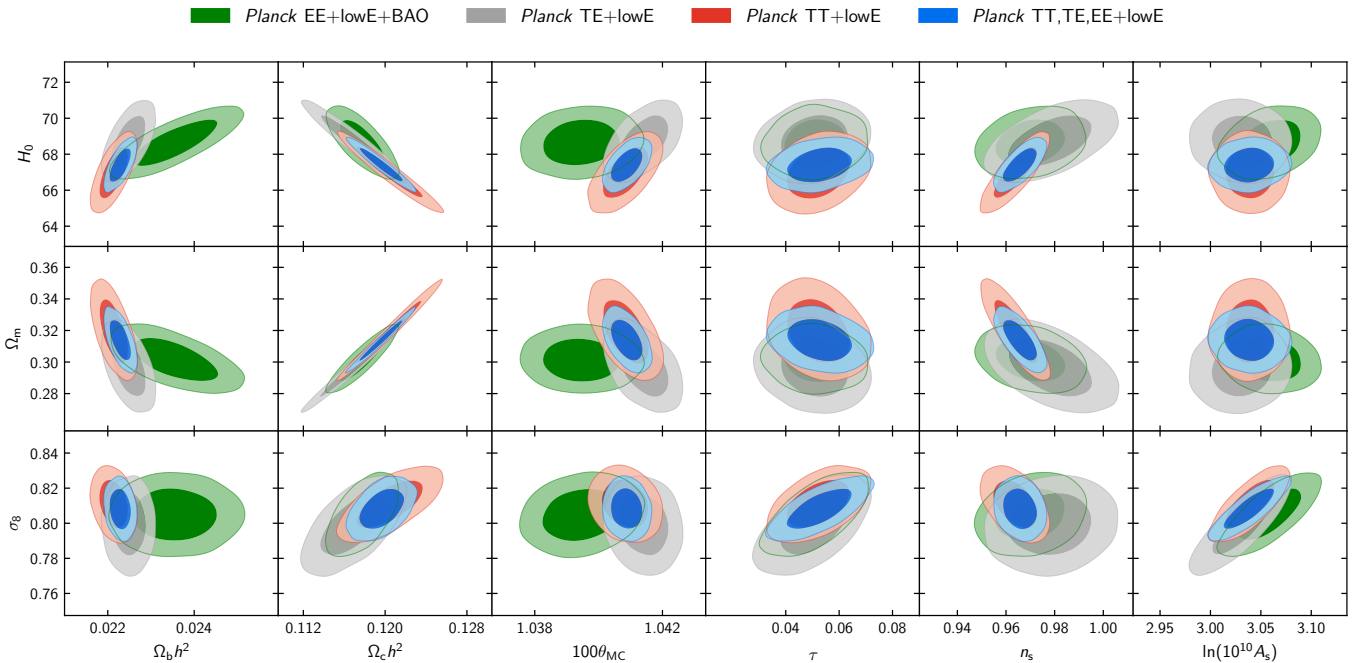
where $\hat{M}^{T_{v_i} T_{v_i}}$ is the covariance matrix of the estimates $\hat{C}^{T_{v_i} T_{v_i}}$. As in PCP15 we choose $\ell_{\min} = 100$ and $\ell_{\max} = 500$ and compute the spectra in Eq. (A.1) by cross-correlating half-mission maps using the 60% mask used to compute the 217×217 spectrum. The resulting cleaning coefficients are $\alpha_{143}^T = 0.00198$ and $\alpha_{217}^T = 0.00763$ (very close to the coefficients adopted in PCP15); note that all of the input maps here are in units of thermodynamic temperature. The cleaned half-mission 143×143 , 143×217 and 217×217 spectra are compared with uncleaned CamSpec spectra (using the same masks for both sets of spectra) and default foreground model in Fig. A.2.

To model residual foregrounds in the cleaned spectra, we assume that they follow power-laws, $A_f(\ell/1500)^{y_f}$ characterized by an amplitudes and spectral indices for each of the 143×143 , 143×217 and 217×217 spectra together with kinetic and thermal Sunyaev–Zeldovich templates, as in the default foreground model. We assume the default foreground model for the 100×100 spectrum. We then form a CamSpec “cleaned” likelihood (used in several places in the main body of this paper) using the same covariance matrices as those computed for the uncleaned likelihood. Comparing parameters for the TT+lowE likelihood combination, the cleaned and uncleaned cosmological parameters agree to a fraction of a standard deviation, with θ_{MC} and n_s from the cleaned likelihood each lower by 0.3σ . We conclude that systematics associated with modelling foregrounds do not introduce significant biases in cosmological parameter determinations.

Table A.2 gives CamSpec results for extensions to the base- Λ CDM cosmology, which is the equivalent to Table 4, but with the addition of results for the CamSpec cleaned TT+lowE likelihood. The CamSpec and *Planck* likelihoods give closely similar results for these extensions. The only noteworthy differences are the TT,TE,EE results for Ω_K , this being slightly closer to zero in the CamSpec likelihood (we find similar behaviour for the lensing consistency parameter A_L , as discussed in Sect. 6.2) and somewhat weaker constraints on Σm_ν and r . These differences give an indication of the sensitivity of our results to different methods and choices made in constructing the TT,TE,EE likelihoods and, in particular, to the schemes used to calibrate effective polarization efficiencies. A detailed description of CamSpec, including further justification of the methodology used to construct the polarization blocks of the likelihood, is given in Efstathiou & Gratton (2019).

Table A.1. Equivalent of Table 2, but using the CamSpec likelihood in place of Plik.

Parameter	TT+lowE 68% limits	TE+lowE 68% limits	EE+lowE 68% limits	TT,TE,EE+lowE 68% limits	TT,TE,EE+lowE+lensing 68% limits	TT,TE,EE+lowE+lensing+BAO 68% limits
$\Omega_b h^2$	0.02214 ± 0.00022	0.02248 ± 0.00026	0.0233 ± 0.0012	0.02229 ± 0.00016	0.02229 ± 0.00015	0.02234 ± 0.00014
$\Omega_c h^2$	0.1205 ± 0.0021	0.1169 ± 0.0021	0.1192 ± 0.0047	0.1196 ± 0.0014	0.1197 ± 0.0012	0.11907 ± 0.00094
$100\theta_{MC}$	1.04084 ± 0.00048	1.04141 ± 0.00051	1.03928 ± 0.00087	1.04088 ± 0.00032	1.04087 ± 0.00031	1.04095 ± 0.00030
τ	0.0521 ± 0.0080	0.0504 ± 0.0088	0.0504 ± 0.0088	0.0528 ± 0.0080	$0.0536^{+0.0069}_{-0.0077}$	$0.0552^{+0.0067}_{-0.0076}$
$\ln(10^{10} A_s)$	3.039 ± 0.016	3.031 ± 0.021	3.058 ± 0.022	3.039 ± 0.016	3.041 ± 0.015	$3.043^{+0.013}_{-0.015}$
n_s	0.9638 ± 0.0058	0.978 ± 0.011	0.967 ± 0.014	0.9658 ± 0.0045	0.9656 ± 0.0042	0.9671 ± 0.0038
H_0 [km s ⁻¹ Mpc ⁻¹]	66.98 ± 0.92	68.72 ± 0.93	67.9 ± 2.6	67.41 ± 0.62	67.39 ± 0.54	67.66 ± 0.42
Ω_Λ	0.680 ± 0.013	0.703 ± 0.012	$0.687^{+0.035}_{-0.028}$	0.6861 ± 0.0085	0.6858 ± 0.0074	0.6897 ± 0.0057
Ω_m	0.320 ± 0.013	0.297 ± 0.012	$0.313^{+0.028}_{-0.035}$	0.3139 ± 0.0085	0.3142 ± 0.0074	0.3103 ± 0.0057
$\Omega_m h^2$	0.1432 ± 0.0020	0.1400 ± 0.0020	0.1431 ± 0.0038	0.1426 ± 0.0013	0.1426 ± 0.0011	0.14205 ± 0.00090
$\Omega_m h^3$	0.09593 ± 0.00045	0.09622 ± 0.00054	$0.0971^{+0.0015}_{-0.0017}$	0.09610 ± 0.00031	0.09610 ± 0.00031	0.09611 ± 0.00031
σ_8	0.8110 ± 0.0089	0.799 ± 0.012	$0.809^{+0.019}_{-0.017}$	0.8083 ± 0.0076	0.8091 ± 0.0060	0.8083 ± 0.0060
$\sigma_8 (\Omega_m/0.3)^{0.5}$	0.837 ± 0.024	0.795 ± 0.025	0.825 ± 0.058	0.827 ± 0.016	0.828 ± 0.013	0.822 ± 0.011
$\sigma_8 \Omega_m^{0.25}$	0.610 ± 0.012	0.590 ± 0.013	0.604 ± 0.028	0.6050 ± 0.0083	0.6058 ± 0.0064	0.6033 ± 0.0057
z_{re}	$7.49^{+0.83}_{-0.75}$	$7.18^{+0.93}_{-0.75}$	$7.06^{+0.90}_{-0.76}$	$7.52^{+0.83}_{-0.75}$	7.61 ± 0.75	7.75 ± 0.73
$10^9 A_s$	2.089 ± 0.034	2.072 ± 0.042	2.130 ± 0.046	2.088 ± 0.034	$2.092^{+0.028}_{-0.031}$	$2.097^{+0.028}_{-0.032}$
$10^9 A_s e^{-2\tau}$	1.882 ± 0.014	1.873 ± 0.019	1.925 ± 0.024	1.879 ± 0.011	1.879 ± 0.011	1.877 ± 0.011
Age [Gyr]	13.825 ± 0.037	13.757 ± 0.039	13.75 ± 0.14	13.805 ± 0.025	13.805 ± 0.023	13.796 ± 0.020
z_e	1090.26 ± 0.41	1089.51 ± 0.42	$1088.8^{+1.6}_{-1.8}$	1089.99 ± 0.28	1089.99 ± 0.26	1089.88 ± 0.22
r_s [Mpc]	144.49 ± 0.48	145.15 ± 0.50	143.94 ± 0.66	144.58 ± 0.31	144.57 ± 0.28	144.70 ± 0.23
$100\theta_*$	1.04105 ± 0.00047	1.04158 ± 0.00050	1.03937 ± 0.00084	1.04107 ± 0.00031	1.04106 ± 0.00031	1.04114 ± 0.00030
z_{drag}	1059.43 ± 0.45	1059.98 ± 0.55	1061.9 ± 2.3	1059.73 ± 0.33	1059.74 ± 0.32	1059.79 ± 0.32
r_{drag} [Mpc]	147.23 ± 0.48	147.79 ± 0.52	146.31 ± 0.69	147.27 ± 0.31	147.26 ± 0.28	147.38 ± 0.25
k_D [Mpc ⁻¹]	0.14054 ± 0.00052	0.14021 ± 0.00060	0.1423 ± 0.0012	0.14061 ± 0.00034	0.14063 ± 0.00033	0.14054 ± 0.00031
z_{eq}	3408 ± 48	3331 ± 48	3405 ± 90	3392 ± 31	3393 ± 27	3379 ± 22
k_{eq} [Mpc ⁻¹]	0.01040 ± 0.00015	0.01017 ± 0.00014	0.01039 ± 0.00027	0.010352 ± 0.000095	0.010355 ± 0.000083	0.010314 ± 0.000066
$100\theta_{s,eq}$	0.4487 ± 0.0046	0.4565 ± 0.0047	0.4492 ± 0.0091	0.4503 ± 0.0030	0.4502 ± 0.0026	0.4515 ± 0.0021
f_{2000}^{143}	30.8 ± 3.0			29.8 ± 2.8	29.7 ± 2.8	29.5 ± 2.8
f_{2000}^{217}	107.6 ± 2.0			106.9 ± 1.9	106.9 ± 1.9	106.8 ± 1.9
$f_{2000}^{143 \times 217}$	33.0 ± 2.1			32.2 ± 2.0	32.2 ± 2.0	32.0 ± 2.0


Fig. A.1. Equivalent of Fig. 5 using CamSpec in place of Plik, showing constraints on parameters of the base- Λ CDM model using the high- ℓ TT, TE, and EE separately (with the EE results also including BAO), and the combined result from the TT,TE,EE likelihood.

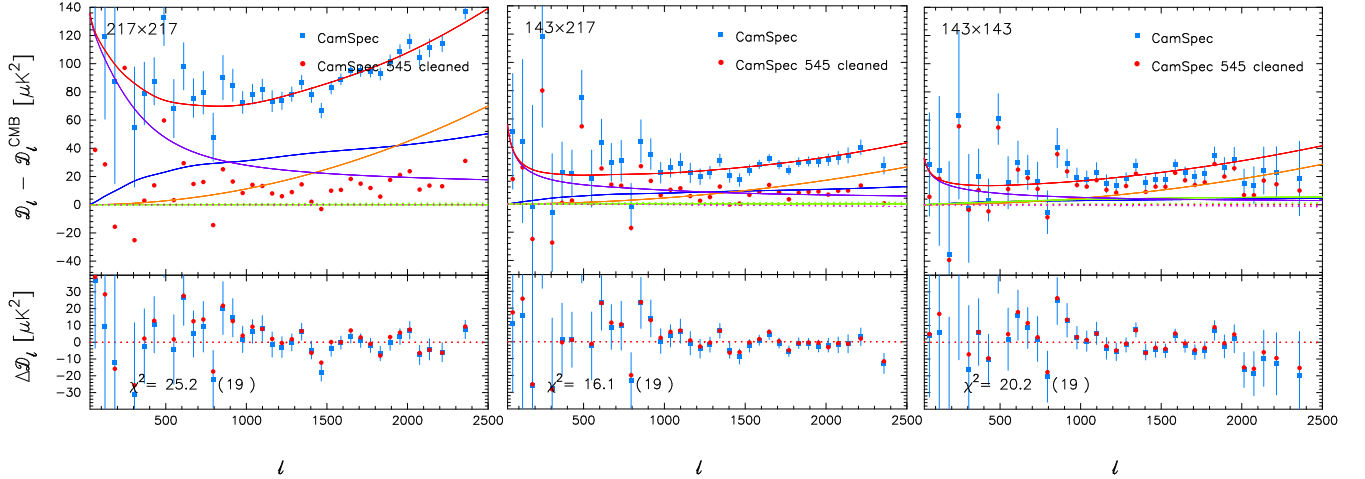


Fig. A.2. Residual plots illustrating the sensitivity of the TT spectra to foreground modelling. The blue points in the *upper panels* show the CamSpec half-mission cross-spectra after subtraction of the best-fit Λ CDM spectrum fit to TT +lowE. The residuals in the *upper panel* should be accurately described by the foreground model. Major foreground components are shown by the solid lines, colour coded as follows: total foreground spectrum (red); Poisson point sources (orange); clustered CIB (blue); thermal SZ (green); and Galactic dust (purple). Minor foreground components are shown by the dotted lines, colour coded as follows: kinetic SZ (green); and $tSZ \times CIB$ cross-correlation (purple). The red points in the upper panel show the 545 GHz-cleaned spectra (minus best-fit CMB, as subtracted from the uncleaned spectra) that are fit to a power-law residual foreground model, as discussed in the text. *Lower panels*: spectra after subtraction of the best-fit foreground models. The χ^2 values of the residuals of the blue points, and the number of band powers, are listed in the *lower panels*.

Table A.2. Constraints on 1-parameter extensions to the base- Λ CDM model using CamSpec at high ℓ , and also including *Planck* lensing and BAO.

Parameter	TT+lowE	TT ^{clean} +lowE	TT, TE, EE+lowE	TT, TE, EE+lowE+lensing	TT, TE, EE+lowE+lensing+BAO
Ω_K	$-0.058^{+0.046}_{-0.051}$	$-0.057^{+0.045}_{-0.051}$	$-0.037^{+0.032}_{-0.034}$	$-0.011^{+0.012}_{-0.013}$	$0.0005^{+0.0038}_{-0.0040}$
Σm_ν [eV] . . .	< 0.569	< 0.578	< 0.379	< 0.273	< 0.131
N_{eff}	$2.94^{+0.59}_{-0.56}$	$2.99^{+0.59}_{-0.57}$	$2.92^{+0.45}_{-0.43}$	$2.88^{+0.44}_{-0.42}$	$2.98^{+0.39}_{-0.38}$
Y_P	$0.242^{+0.040}_{-0.042}$	$0.246^{+0.042}_{-0.042}$	$0.246^{+0.035}_{-0.035}$	$0.244^{+0.034}_{-0.035}$	$0.248^{+0.032}_{-0.032}$
$dn_s/d \ln k$. . .	$-0.003^{+0.015}_{-0.015}$	$-0.005^{+0.015}_{-0.015}$	$-0.001^{+0.013}_{-0.013}$	$-0.001^{+0.013}_{-0.013}$	$0.000^{+0.013}_{-0.013}$
$r_{0.002}$	< 0.106	< 0.105	< 0.141	< 0.136	< 0.141
w_0	$-1.54^{+0.59}_{-0.48}$	$-1.55^{+0.60}_{-0.48}$	$-1.52^{+0.56}_{-0.45}$	$-1.54^{+0.51}_{-0.41}$	$-1.03^{+0.10}_{-0.11}$

Notes. This is equivalent to Table 4 for Pl1k, except that we have added results for the cleaned TT CamSpec likelihood in the third column. Note that we quote 95% limits here.